Technische Universität München
TUM School of Engineering and Design

Highly Efficient Energetic Synthesis of Coupled Steady-State Dynamic Systems

Rupert Ludwig Emanuel Ullmann

Vollständiger Abdruck der von der TUM School of Engineering and Design der Technischen Universität München zur Erlangung des akademischen Grades eines

Doktors der Ingenieurwissenschaften (Dr.-Ing.)

genehmigten Dissertation.

Vorsitz:

Prof. Dr.-Ing. habil. Fabian Duddeck

Prüfer*innen der Dissertation:

1. Prof. Dr.-Ing. habil. Gerhard Müller
2. Prof. Dr. ir. Elke Deckers

Die Dissertation wurde am 06.12.2022 bei der Technischen Universität München eingereicht und durch die TUM School of Engineering and Design am 05.04.2023 angenommen.

Zusammenfassung

Eine robuste virtuelle Entwicklung von Fahrzeugen bezüglich niederfrequenter vibroakustischer Eigenschaften benötigt die Anwendung von Methoden, welche eine Vielzahl an Modellauswertungen für wechselnde Eingangsparameter voraussetzen. Nachdem Finite-Elemente Modelle von Gesamtfahrzeugen Millionen von Unbekannten enthalten können, ist die Parametervariation solcher Modelle berechnungsintensiv und eine Anwendung entsprechender Methoden in der Praxis herausfordernd.

Um eine Anwendbarkeit dennoch zu ermöglichen, wird ein performantes Simulations-Framework im Rahmen der Arbeit entwickelt. Dieses stützt sich auf zwei Kernelemente. Zunächst wird ein vollmodularer Ansatz zur Gebietszerlegung und -kopplung eingeführt. Dieser ermöglicht eine Parallelisierung der Berechnungen, und zudem eine Hybridisierung der Modellierung durch Inklusion gemessener Subsysteme. Eine generalisierte Problembeschreibung wird hierzu eingeführt, die auf dem Konzept von Newton-Iterationen basiert und durch eine Flexibilisierung der Koppelbedingungen die Inklusion einer Vielzahl von Subsystemarten ermöglicht. Das modulare Konzept wird ebenfalls für eine effiziente Sensitivitätsberechnung in Subsystem-Netzwerken erweitert.

Die zweite Komponente stellt ein Ansatz zur parametrischen Modellreduktion von Subsystemen dar, welche die approximative Auswertung dieser um Größenordnungen beschleunigt. Eine Projektionsmethode wird verwendet, die auf einem globalen Basisansatz und affinen Matrixzerlegungen zur Berücksichtigung der hochdimensionalen Parametrik basiert. Ein neuer Ansatz zum Modelltraining für Frequenzgangsanalysen wird dazu eingeführt. Das Modelltraining basiert auf einem gängigen Momentenabgleich der Subsystem-Transferfunktionen mittels Krylov-Unterraummethoden und identifiziert die zu berücksichtigenden Parameter- und Frequenzpunkte mittels eines netzfreien Greedy-Verfahrens. Letzteres stützt sich auf Optimierungsprobleme, die für speziell zur bandbegrenzten Frequenzgangsanalyse entwickelte Fehlerschätzer formuliert werden und ein Training für hochdimensionale Parametrik großer industrieller Modelle ermöglichen.

Die Algorithmen werden an numerischen Referenzlösungen verifiziert. Die aus dem Framework resultierenden Potenziale werden final anhand einer globalisierten Optimierung sowohl eines akademischen zweidimensionalen Netzwerkbeispiels als

auch einer gekoppelten Fahrzeugstruktur veranschaulicht. Als Zielfunktion wird die frequenzbandintegrierte Leistung herangezogen, welche an der in das Fluid abstrahlenden Substruktur anliegt. Die korrekte Auswertung einer solchen energetischen Größe wurde dazu bei der Formulierung des numerischen Frameworks explizit berücksichtigt, als auch experimentelle Verfahren inklusive Phasenkorrektur zur Validierung diskutiert. Abschließend wird die relative Performanz der energetischen Zielfunktion gegenüber vereinfachten ingenieursmäßigen Ansätzen kritisch beleuchtet.

Abstract

Robust virtual development processes for low-frequency vehicle vibroacoustics require a significant amount of system evaluations for changing input parameter values. This need for extensive parameter evaluations is challenging as complete vehicle finite element models usually contain many states, and thus single parameter evaluations are computationally expensive.

As a remedy, a high-performance simulation framework is developed based on two main approaches. Firstly, a fully modular domain decomposition and coupling method is proposed allowing for parallel computations but also hybrid assemblies incorporating experimentally determined subsystems. Based on Newton iterations, a very general framework is found, with minimum limitations for the subsystems and, therefore, more extensive flexibility. At the same time, the framework provides a new, efficient formulation for sensitivity calculations in the network. Secondly, parametric model order reduction for structural components increases the computational efficiency of numeric subsystem evaluations by orders of magnitude. The reduced model is found by projection using a global basis with an affine system matrix decomposition. A new method for reduced model training is introduced suited for band-limited frequency-domain analyses. The training utilizes the concept of moment matching by Krylov-subspace methods in combination with a grid-free greedy sampling strategy for identifying expansion points in the parameter space. Local optimization problems for minimizing error estimates define the sampling strategy, enabling the reduction of large-scale industrial subsystems with high-dimensional input parameter spaces.

All numerical algorithms are verified against numerical reference solutions. The potentials of the proposed numerical framework are finally demonstrated for the case of a globalized optimization of both a generic coupled two-dimensional example and an industrial vehicle structure. The frequency band integrated power at the radiating subsystem interface is used for each example as the objective. The performance of such an energetic approach against more simplified engineering measures is discussed critically, and methods for experimental power determination are introduced, incorporating a phase correction.

Acknowledgments

This dissertation was written from 2015 to 2022 during my time at the BMW ProMotion program and my research at the Chair of Structural Mechanics of the TUM School of Engineering and Design.

I would like to express my gratitude to Univ.-Prof. Dr.-Ing. habil. Gerhard Müller for giving me the opportunity to write the thesis under his supervision and for the precious and open-minded discussions throughout the years, which provided me most important guidance. At the same time, I would like to thank him for the academic freedom in developing the thesis and the very friendly atmosphere during the collaboration.

Furthermore, I would like to thank Prof. Dr. ir. Elke Deckers for being my co-examiner, her interest in my thesis, and the work involved with this.

My special thanks go to Dr.-Ing. Stefan Sicklinger for initializing my thesis at the BMW Group and for his intense supervision all the time. I would like to thank him for his outstanding scientific and personal support, motivation, and friendship I highly appreciate. I also want to thank my managers at BMW Group Forschung, Neue Technologien, Innovationen Udo Ochner, Dr. Ralf Stroph, and Thomas Schmitt for their trust and support and for giving me the freedom to research during my years at the department. My gratitude also goes to the students who supported me during this time for their motivation, work, and fruitful discussions. Furthermore, I would like to express my thanks to all the colleagues at BMW for their support and introduction to vehicle development as well to the fellow Ph.D. candidates at the chair of Structural Mechanics and the BMW ProMotion program for their open mind and intense scientific discussions.

Finally, I would like to thank my family and friends for their patience over all the years and, most importantly, my wife Julia for all her indispensable support, motivation, and advice.

Rupert Ullmann
Technische Universität München
December 6, 2022

List of Symbols

Calligraphic letters

$\mathcal{A}$	event in probability theory
$\mathcal{B}$	event in probability theory
$\mathcal{I}_j()$	interface constraint operator for interface constraint j
$\mathcal{G}$	two-stage Krylov subspace
$\mathcal{K}$	one-stage Krylov subspace
$\mathcal{O}()$	time complexity
$\boldsymbol{\mathcal{R}}_j$	residual vector associated with input j
$\mathcal{R}_j$	residual associated with input j
$\mathcal{S}_j()$	operator of subsystem j
$\mathcal{T}$	search space
$\mathcal{C}$	constraint space
$\mathcal{Z}()$	operator for trapezoidal rule

Common sub-/superscripts and markers

$\overline{\square}$	averaged quantity
$\underline{\square}$	assembled quantity in subsystem coupling
$\square_{\mathrm{I}}$	quantity of a first-order system
${}^{j}\square$	quantity at iteration j

$\square_{\mathrm{R}}$ quantity of a reduced system

Greek letters

α Rayleigh damping coefficient

β Rayleigh damping coefficient

$\boldsymbol{\chi}$ snapshot matrix

Δ system ratio associated with power modal decomposition

δ_{ij} Kronecker-delta

η structural damping coefficient

κ expansion point

$\boldsymbol{\lambda}$ vector of Lagrange multipliers

Λ diagonal matrix of eigenvalues

λ eigenvalue

$\boldsymbol{\mu}_i$ adjoint matrix for Hessian calculation

μ mean value

$\boldsymbol{\nu}_i$ adjoint matrix for Hessian calculation

$\boldsymbol{\Omega}$ matrix of interpolation coefficients

ω angular frequency

$\boldsymbol{\Phi}$ modal matrix

π $\approx 3.141\,592\,653\,589\,793$

$\boldsymbol{\Psi}$ adjoint variable; power modal coordinate

ρ mass density

σ real part of Laplace variable; standard deviation

$\boldsymbol{\Theta}$ diagonal matrix of singular values

$\varepsilon_{\mathrm{rel}}^{\mathrm{lim}}$ relative error limit

$\varepsilon_{\mathrm{rel}}^{\mathrm{rlx}}$ relaxed relative error limit

ε_{H} error in transfer function matrix

$\varepsilon_{\mathrm{H,rel}}$ relative error in transfer function matrix

$\varepsilon_{\mathrm{H,rel}}^{\mathrm{max}}$ maximum relative error in transfer function matrix

$\Delta\varphi$ relative phase angle between two signals

$\Delta\varphi_{\mathrm{err}}$ error in the relative phase angle between two signals

φ angle

ϱ sound pressure quantity

$\boldsymbol{\Xi}$ vector of complex-valued phase correction factors

ξ modal damping ratio

Mathematical symbols and operators

$\square^*$ complex conjugate

$|\square|$ absolute value

$\square^H$ Hermitian transpose

$\square^+$ pseudo inverse

$\square^T$ transpose

arccos arcus cosinus

arctan arcus tangens

argmax argumentum maximi

$\bigcup_k$ vector-wise concatenation of k matrices

colsp column space of a matrix

cond conditioning

$\sim$ correlation

cos cosinus

d	total differential
diag	operator for constructing a (block) diagonal matrix
f	scalar function operator
$\Im$	operator to extract a complex number's imaginary part
$\circ\!\!-\!\!\bullet$	Laplace transform
$\log_{10}$	logarithmn with base ten
min	minimum
∇	divergence
Null	null space of matrix
∂	operator for partial derivative
$\propto$	proportionality
$\Re$	operator to extract a complex number's real part
sgn	signum operator
sgni	signum operator on a complex number's imaginary part
$\sum$	sum
span	span of vectors
subset	operator to extract a subset columns vectors for a matrix
$\succeq$	semi-definitness of a matrix
tr	trace operator
vec	operator to vectorize a matrix
$\mathbb{C}$	set of complex numbers
$\|\square\|$	norm
$\|\square\|_2$	Euclidean norm
$\|\square\|_\mathrm{F}$	Frobenius norm

$\mathbb{R}$ set of real numbers

Latin letters

$\boldsymbol{A}$ subsystem matrix (dynamic stiffness for second-order systems)

A acceleration quantity

a probability of a good outcome

$\boldsymbol{B}$ input map matrix of a (sub-)system in a MIMO setting

$\hat{\boldsymbol{B}}$ matrix operator for compatibility in subsystem coupling

$\boldsymbol{C}$ output map matrix of a (sub-)system in a MIMO setting

c coefficient of variation

$\boldsymbol{c}_\mathrm{e}$ equality constraints in optimization

$\boldsymbol{c}_\mathrm{i}$ inequality constraints in optimization

$\Delta\boldsymbol{c}$ corrector vector of the interface problem

$\boldsymbol{D}$ viscous damping matrix

d design parameter dimensionality of a (sub-)system

$\boldsymbol{D}_\mathrm{d}$ equivalent viscous damping matrix

E modulus of elasticity

E_kin kinetic energy

E_pot potential energy

E_tot total energy

$\boldsymbol{F}$ external input vector to a subsystem

F force quantity

f frequency of excitation

f_B frequency band

$\hat{\boldsymbol{f}}$ vector of basis functions for interpolation

$\boldsymbol{G}$	subsystem dual quantities from coupling effects
$\boldsymbol{H}$	transfer function matrix of a subsystem
H_{sw}	transfer function amplitude threshold value for relaxed error requirements
$\boldsymbol{I}$	identity matrix
i	complex variable
$\boldsymbol{J}$	interface Jacobian matrix
$\boldsymbol{K}$	stiffness matrix
$\boldsymbol{L}$	matrix operator for equilibrium in subsystem coupling
l	vector length
l_{defl}	deflation tolerance vector length
$\boldsymbol{M}$	mass matrix
$\boldsymbol{m}$	moment of Taylor series expansion
m	number of states of a reduced order model
n	number of states of a full order model
n_{int}	size of interface problem
n_{itMax}	maximum number of greedy iterations
n_{pre}	sample set size to determine the initial parameter point for optimization
n_{s}	number of subsystems in a network
n_{sam}	size of a-posteriori sample set
n_{skipMax}	required number of skipped iterations for lucky breakdown
n_{U}	number of a subsystem's inputs
n_{Y}	number of a subsystem's outputs
o	Krylov order

$\boldsymbol{P}$	continuation matrix for a Krylov sequence
$\boldsymbol{p}$	design parameter vector
$\tilde{\boldsymbol{p}}$	design parameter vector with frequency of excitation included
P	probability
${}^{j}\boldsymbol{p}_{\text{lopt}}$	resulting design parameter vector from one local optimization in a globalized optimization procedure
${}^{j}\boldsymbol{p}_{\text{opt}}$	resulting design parameter vector from optimization at greedy iteration j
$\boldsymbol{p}_{\text{gopt}}$	overall resulting design parameter vector from globalized optimization
${}^{j}\boldsymbol{p}_{0}$	initial design parameter vector at iteration j in greedy search
$\boldsymbol{p}_{0}$	initial design parameter vector for globalized optimization
$\boldsymbol{Q}$	starting matrix for a Krylov sequence
$\boldsymbol{q}$	vector of design objectives
$\boldsymbol{r}$	residuum vector
r	scalar residuum objective
$\boldsymbol{r}_{\text{B}}$	residuum vector introduced in the full order model using the reduced order model solution for the input map matrix as multi-column input
$\boldsymbol{r}_{\text{ge}}$	residuum vector of the governing equations
$\boldsymbol{S}$	structural damping matrix
s	Laplace variable
T	cycle time
t	thickness of a shell or beam; time
$\boldsymbol{U}$	input vector of a subsystem
V	velocity quantity

$\boldsymbol{V}$	projection matrix
$\boldsymbol{V}_{\mathrm{g}}$	projection matrix of a global basis approach
W	displacement quantity
$\boldsymbol{W}$	projection matrix
$\boldsymbol{X}$	state vector of a (sub-)system
$\boldsymbol{Y}$	output vector of a (sub)-system
$\boldsymbol{Z}$	transformation matrix
Z	impedance

Abbreviations

CGS	classical Gram Schmidt
CMS	component mode synthesis
DAQ	data aquisistion
DEIM	discrete empirical interpolation method
DOF	degree of freedom
DWR	dual weighted residual method
EIC	energy influence coefficient
EMA	experimental modal analysis
FBS	frequency based substructuring
FEM	finite element method
FETI	finite element tearing and interconnecting
FFT	fast Fourier transformation
FOM	full order model
GEP	generalized eigenvale problem
IH	impedance head

IJCSA interface-Jacobian-based co-simulation algorithm

IRKA iteratively corrected rational Krylov algorithm

LTI linear time-invariant

MAC modal assurance criterion

MGS modified Gram Schmidt

MIMO multiple input - multiple output

MOR model order reduction

MPC modal phase collinearity

MRC mixed residual coupling

OGPA optimization-based greedy parameter sampling

pMOR parametric model order reduction

POD proper orthogonal decomposition

pROM parametric reduced order model

ROM reduced order model

SEA statistical energy analysis

SISO single input - single output

SPL sound pressure level

SQP sequential quadratic programming

STFT short-time Fourier transformation

SVD singular value decomposition

SVDMOR singular value decompoition based input reduction for model order reduction

UQ uncertainty quantification

CONTENTS

CHAPTER 1

INTRODUCTION

1.1 Numerical Vehicle Vibroacoustics and some of its Challenges

The increasing cost and time pressure in the automotive industry, reinforced by an enlarging number of vehicle derivatives, leads to the growing importance of efficient development processes. At the same time, the importance of the acoustic quality of cars increases in its role as a key differentiator in the premium vehicle segment. Historically, the acoustic development of cars was mainly driven by the expert knowledge of single engineers and the results from several iterations in hardware experiments. Anyhow, such an approach requires the validity of expert experience from past projects, which may not be given for disruptive changes in the vehicle architecture; the switch from combustion drive trains to electric ones, for example. Expensive hardware prototypes are needed, which are available only at late development stages, in which no fundamental changes to the vehicle system are possible anymore. Virtual vehicle development and virtual testing are a remedy to that. An end-to-end virtual development process results in fewer hardware prototypes, thus enabling shorter

and significantly cheaper processes and more efficient vehicle modifications. There is no need to rely exclusively on expert experience, but numerical models are available at any stage of the development process for supporting decision-making.

In what follows, the focus is on structure-borne sound problems for the interior acoustic quality of linear time-invariant (LTI) vibroacoustic vehicle systems. The systems are considered to be in a steady state, thus, are analyzed in the band-limited frequency domain. In such a setting, vibration is transmitted from the source through the mechanical vehicle structure, radiates from the surfaces of the car body inside the passenger cabin, and results in sound pressure levels at the passenger ears positions, the relevant acoustic quantity for the customer. Unfortunately, the robust modeling and analysis by numerical methods is no trivial task for such an acoustic chain of effects. Vehicle structures are complex mechanical systems that involve many different subcomponents, materials, and contact types, like spot welds or gluing. Statistic variations in the manufacturing quality or material properties introduce aleatoric uncertainties in the model's input parameters. The unknown numerical modeling of subcomponents like rubber bushings or dampers introduces epistemic uncertainties in the transmission path through the structure. Epistemic uncertainties also play a significant role when it comes to the modeling of the radiator, thus the car body. The correct numerical representation of carpet coverings, plastic claddings, and their possible non-linear contact with the metal structures, for example, are still an open topic in industrial applications. Additional uncertainties arise in the early development stage, in which design details of the car body are not yet precisely known. Unfortunately, all these parameters of the radiator may significantly influence the sound pressure levels in the Helmholtz fluid of the interior cabin.

Even if there were no uncertainties, the numerical treatment of structure-borne sound problems remains challenging for complex vehicle structures. In synthesis, one has to find modifications with a high impact on the sound pressure on the one hand. This need for high-impact optimization is due to the logarithmic nature of human perception. On the other hand, one has to face highly non-convex optimization problems involving many design parameters to find cost and weight-effective modifications for better vibroacoustic performance. Although the considered vibroacoustic systems are linear in their states, the input parameters may have a highly non-linear influence

on the latter. At the same time, multiple and possibly interdisciplinary design constraints may need to be considered by synthesis.

These challenges are already significant in the lower frequency regime, which is the focus of the presented work. In the following, the lower frequency range is defined by a moderate number of significant resonant modes ($n_{\mathrm{res}} < 30$), the subcomponents of the coupled vehicle assembly exhibit in the analyzed frequency range. There are many sub-assemblies in vehicle systems, consisting of components that fulfill this property up to kilohertz frequencies. Wiper systems are one example or many assemblies which contain auxiliary units. For chassis systems, which are geometrically more complex and consist of dozens of components, the lower frequency range assumption is fulfilled at the component level typically up to several hundred hertz. Many acoustic phenomena like road-induced noise are present in this frequency range, which greatly impact acoustic vehicle quality.

During vehicle development, the systems are modeled deterministically in the low-frequency range, typically by the displacement-based finite element (FE) method. Vehicle FE models often have a fine discretization and complex modeling, which must be valid for different analysis types. Corresponding models, therefore, have many degrees of freedom (DOFs) in the range $n \approx 10^6$, making their evaluation computationally expensive. Furthermore, many different element types and connection techniques may be incorporated.

1.2 Possible Remedies

1.2.1 Probabilistic Energetic System Formulation

Many approaches have been developed to cope with the problem of robustness for vibroacoustic applications during the last decades. In such methods, probabilistic assumptions are introduced to enable robust analyses. In addition, popular methods analyze the wave transmission not based on the displacement-based system description, but the latter is reformulated entirely in terms of energetic quantities. Such energetic system formulations have a long history in vibroacoustics, especially in the high-frequency regime; consequently, an energetic system analysis seems to be a natural choice for vehicle networks.

Indeed, there are several methods that can be applied to complex industrial models. Statistical Energy Analysis (SEA) is probably the

most popular energy-based method in vibroacoustics. It allows for probabilistic system analysis in high-frequency ranges and requires only the evaluation of small systems of equations. The network concept is found in this method, and at the basis of averaging, robust levels and exchange of the subsystem energies of an assembly are calculated by solving energy balance equations. Classically, the SEA is derived by a modal approach, see Lyon et al. [158]. In this formulation, each subsystem is described by groups of *similar* modes. Similar modes are defined as modes of the same type, flexural or torsional, for example. A sufficiently high number of resonant modes is needed in each analyzed frequency band, at least three to six. These modes store the subsystem energy and exchange energy with resonant modes of other subsystems. The subsystem's capability to store energy is described by its modal density, the exchange by coupling loss factors. Both quantities must be determined depending on the single subsystem types, classically by analytic methods. In the classic SEA formulation, subsystems are weakly damped and coupled weakly. Indirect coupling of subsystems, which do not have a common interface, is impossible in most formulations. Some probability distribution over frequency is assumed for the modal parameters to approach the uncertainties of the system characteristics in the high-frequency range. Finally, results are obtained, which are averaged over frequency and spatially over the single subsystem domains. These results are interpreted as a statistical ensemble average of systems with similar properties.

There is the newer wave-based approach to SEA as an alternative, which is described in Le Bot [144], for example. Using the wave-based approach, one arrives at the same equations for the energy balance of the assembly. However, each subsystem is described not by a modal approach but by direct wave fields at each interface to other subsystems and a diffuse reverberant field. Each subsystem contains a single wave type. The direct fields of single interfaces do not interact, and the reverberant field is incoherent. In contrast to the modal derivation of SEA, the energy is stored in the reverberant field as a function of the subsystem modal density. An averaging is finally performed to cope with the uncertain wave properties.

The wave-based approach to SEA allows relating the latter to other energy-based methods. One of these methods is the energy-based finite element method (EFEM). In EFEM, the governing differential equations are formulated for the energy density as a variable and solved numerically by a finite element procedure. In the formulation

of Nefske et al. [180], the element formulation is obtained for the energy density, which is summed up incoherently from the energy of orthogonal waves, similar to wave-based SEA. An averaging is performed spatially over a wavelength and temporally over one period of vibration. Other formulations exist using far-field lossy plane waves, based on Wohlever et al. [274]. EFEM can be an attractive approach compared to SEA, as the spatial energy distribution in subsystems can be assessed, and FE modeling can be reused, at least in theory. Although the modeling can be reused, a new formulation must be found for any considered element type, and joint matrices are required at discontinuities. These joint matrices must be derived for different types of discontinuities a-priori.

Another concept for energy-based methods in the high-frequency regime is the Direct Energy Analysis (DEA), introduced in Tanner [243], respectively Discrete Flow Mapping. The concept of ray-tracing is followed to describe energy flows. However, densities of rays are tracked instead of single rays under the assumption of short wavelengths. As in EFEM, specific FE modeling can be reused, and energy fluxes through the single element boundaries are analyzed through ray densities. For automotive engineering, an application to a floor panel is demonstrated in Hartmann et al. [119].

Such energetic methods as introduced above, are a valuable approach for the solution of high-frequency-domain problems, but not necessarily for lower frequency ranges. All the above methods require a short wavelength assumption for meaningful results, thus a small ratio of the wavelength to subsystem dimensions, which defines the high-frequency regime. For compact subsystems in a vehicle assembly, this ratio is only fulfilled starting from several kilohertz. Hybrid methods were developed to relax that requirement for some subsystems of an assembly. The latter combine the above methods with a displacement-based finite element method and extend the applicability of the above methods to mid-frequency ranges (Mace et al. [161]). A popular approach for a (wave-based) SEA-FEM hybrid approach is found in Shorter et al. [225], for example. A combined EFEM-FEM approach is introduced in Vlahopoulos et al. [266]. However, the application for low-frequency analysis remains an open question. For many automotive structural assemblies, none of the subsystems fulfill the short-wavelength assumption up to several hundred hertz. Axle systems are one example, as discussed above.

Consequently, one could aim to extend or develop a method based on an energetic system formulation for robust analysis and high-impact optimization in the low-frequency range. However, several reasons contradict such an approach in practical use: Firstly, the above methods are non-parametric, meaning no direct link between the physical input parameters like a shell thickness and the outputs is available. As a result, a systematic sensitivity analysis or optimization of input parameters is challenging, at least in classic methods. Secondly, such an approach must be applicable in practice during the vehicle development process. During the latter, FE models of the single vehicle components are available, which are improved evolutionary through the product development process. Ideally, these models should be reused for the energetic analysis to avoid remodeling. The latter is expensive in time and money and may only be feasible in some development stages. However, industrial systems contain complex modeling, including many different element types and connection techniques. Therefore, reusing such modeling in a newly developed energetic system formulation is cumbersome and requires highly mature methods. This also applies to the approaches discussed above. The SEA requires completely different modeling, which must be built in parallel. EFEM and DEA can deal with FE modeling theoretically. However, formulations must be derived for any element type or connection technique used in the original FE model. Consequently, at least modifications of the modeling are required in practice, which result in a de facto remodeling.

1.2.2 Reusing the Deterministic Displacement-Based System Formulation

An alternative approach for the low-frequency range is followed here. No probabilistic models are developed, but the system analysis and synthesis are based on the displacement-based FE model, thus a purely deterministic system. For a deterministic system formulation, approaches to cope with the challenges of robustness and high-impact optimization are already available. Globalized optimization, utilizing random search algorithms (Zabinsky [280]), for example, enables high-impact synthesis in the presence of non-convex objective functions. For robustness of analysis, epistemic uncertainties can be reduced by inverse methods for parameter identification from validation data (Kennedy et al. [136]). Parametric methods for uncertainty quantifica-

tion (UQ) allow considering aleatoric uncertainties in the analysis. For an overview, refer to Ghanem et al. [96]. Nevertheless, all the above approaches are multi-query methods, meaning that repetitive deterministic system evaluations with varying input parameters are required. As the vehicle models contain up to hundreds of varying parameters, a large number of up to several million sampled system solutions may be needed to cover the high-dimensional parameter space. At the same time, corresponding numerical vehicle models have a vast number of DOFs; single parameter variations, thus, are computationally highly expensive. Consequently, the application of multi-query methods is challenging for such industrial models. One possible solution is reducing the input parameter space to the dominant directions. However, approaches to reducing the input parameter space are computationally expensive multi-query methods themselves. Global sensitivity analysis employing a variance-based approach (Saltelli et al. [218]), for example, requires extensive sampling, too.

This need for extensive sampling illustrates a central challenge when dealing with the industrial deterministic systems: one has to find a highly-efficient system evaluation scheme under the preservation of the system's numerous input parametric dependencies to speed up single parameter variations by some orders of magnitude. If such efficiency improvements can be provided for existing standard FE models, an enabler is found for multi-query methods and thus a robust virtual end-to-end development process for industrial vibroacoustic problems. No additional restrictions on the analytical system properties need to be introduced. No components need to be replaced by analytical surrogates, which simplify the complex mechanical properties which would not sufficiently reflect many geometrically complex vehicle structures. Enabling the standard FE models, the use in industrial development processes can also be ensured from the business process point of view.

Based on the deterministic system formulation, one may also evaluate energetic quantities as postprocessing of the displacement solution. Again, the mechanical structure can be considered a network of components, and energy exchange can be analyzed. Such an approach results in consistency with the analysis approach of high-frequency methods in Section 1.2.1; consequently, results from a parametric uncertainty quantification or other probabilistic methods in the low-frequency domain, which build on the deterministic system, can be compared against the ones of methods of Section 1.2.1. However, one

also may use energetic quantities for purely deterministic applications to gain additional insights into the transmission behavior of complex mechanical networks. In vibroacoustics, energetic quantities inside the mechanical structure were used for the analysis of single subsystem interactions in the design of resilient machine mounts in buildings, see Goyder et al. [103] for an early work, active vibration control (Gardonio [92, 93]) or the characterization of sound sources (Moorhouse [177]), respectively receiver (Jianxin et al. [132] and Weisser et al. [271]). In electrical engineering, energetic network analysis is an established analysis tool (see Bosse et al. [42] exemplary). Several studies in automotive design are also based on energetic quantities. Tadina et al. [239], Lenzi et al. [149] and Jund et al. [133] used energetic quantities for the evaluation of a body in white. Detailed analyses of smaller subcomponents were performed by Korta et al. [141] for an under-seat panel or by Ebert et al. [71] for a vehicle floor. In synthesis, one may use energetic quantities as a more robust objective than single sound pressure levels, as is discussed below.

In the past, approaches to speed up FE computations for an energetic analysis were already introduced, which, however, do not preserve parametric dependencies (Mace et al. [159, 160], Mourelatos et al. [178], and Tan [241]). These methods are based on the combination of domain decomposition and model order reduction by Component Mode Synthesis (CMS) methods; for more details on that approach, refer to Section 5.2.3.

1.3 Thesis Overview

1.3.1 Outline

Motivated by this, four main goals are followed with different emphasis in the proposed work:

1. **Development of an efficient numerical framework for multi-query applications.**
   The starting point is the deterministic displacement-based system formulation obtained from the standard FE modeling. In contrast to the above methods, particular emphasis is on preserving high-dimensional input parameter spaces for variation and efficient evaluation. The latter allows for multi-query appli-

cations like parametric uncertainty quantification or globalized optimization for large-scale industrial vibroacoustic models.

2. **Formulations and extensions for an energetic analysis.**
   An accurate evaluation of energetic quantities should be enabled during the postprocessing of the displacement-based system solution. As shown below, this results in the requirement of a systematic and accurate consideration of the model damping in numerical methods; and phase-accurate measurement approaches if experimental data should be combined into a hybrid network. Particular emphasis is on including structural damping and the necessary methodological extension for this purpose.

3. **Show-case demonstration of the numerical framework's potentials on a vibroacoustic large-scale vehicle system.**
   No explicit adaptions of the proposed framework are performed for one specific type of multi-query analysis to allow for general applicability. Anyhow, the potentials of the numerical framework should be presented on one element of an end-to-end development process explicitly: a globalized optimization of complete and fully coupled vibroacoustic systems. A complex industrial vehicle model is considered.

4. **Problem-specific discussion of the value of power as key performance indicator for vehicle systems.**
   It is evaluated if power can be a valuable and possibly more robust optimization objective for globalized optimization of vehicle systems. This is reflected problem-specific for the showcase systems.

The main focus of the proposed work is on the first goal of developing an efficient numerical framework with the preservation of parametric dependencies. The framework which is developed throughout Chapter 3 to Chapter 6 relies on two basic principles: the consideration of the vibroacoustic system as a modular network of substructures and a learning procedure based on parametric model order reduction (pMOR) of the latter ones.

A fully modular domain decomposition and coupling are introduced in Chapter 3, which allows for parallel computations. Anticipating the results of that chapter, modularity means the independent

calculation of subsystem outputs for certain inputs, followed by a synchronization of the subsystem inputs and outputs by evaluating an interface problem. Thus, instead of one large monolithic system, several small subsystems can be solved in parallel. Based on the concept of Newton iteration, a very general framework is found in a new formulation, with minimum limitations for the subsystems and, therefore, larger flexibility. Pure Neumann subsystems, for example, can be included in a systematic matter. Classic dual-domain decomposition methods can be considered a subcase of this more general framework. At the same time, an explicit link between domain decomposition and co-simulation is provided, as the framework is derived from a linearized version of a co-simulation method.

Complete vehicle models contain hundreds of design or uncertain model parameters. Modularity allows for efficient localized parameter variations on subsystem level, for which solely parts of the network need to be recalculated. In addition, localization is also possible for evaluating parameter sensitivities in the network. Consequently, the framework allows for a new, efficient formulation for sensitivity calculations, useful for optimization and UQ. This is discussed in Chapter 4.

The modular approach alone is not efficient enough for multi-query analyses of vibroacoustic problems. The structural subsystems still have many DOFs, which results in a computationally expensive evaluation of the subsystems for varying parameters. Parametric model order reduction is introduced to remedy that, allowing for highly efficient subsystem evaluations. Reduced-order models (ROMs) are found based on a projection of the full-order models (FOMs) utilizing Krylov subspaces, which are introduced in Chapter 5 for the non-parametric case first. The basic properties of Krylov subspaces are revisited in the context of subsystem coupling and energetic analysis. The standard theory is reformulated systematically for second-order systems with hysteretic damping, thus enabling an accurate damping modeling of the considered industrial models. Efficient code implementations are presented for the latter, including newly modified block-Arnoldi algorithms.

In Chapter 6, it is shown afterward how such subspaces can be utilized in a parametric model order approach. It is demonstrated that global basis methods are an attractive choice for the substructures considered in the thesis, which have a moderate number of resonant modes but show a highly non-linear dependence of the subsystem responses on the parameters. Based on that, a new approach is de-

veloped in the frequency domain, which utilizes a greedy sampling strategy to train the model in the parameter space. This training can be considered a learning process, as the essential system dynamics must be included in the reduced subspace. Due to the localized approach of parameter treatment provided by the coupling framework, a practical pMOR method does not need to preserve subsystem parameters for variation in the ROM in the order of hundreds. However, a high-dimensional parameter space still needs to be covered up to an order $d = 15$. This high-dimensional characteristic of parameter space imposes challenges for both the training of the reduced-order model and the later validation. As a remedy to the training challenge, the idea of a grid-free sampling through local optimization problems with error estimates as the objective is followed. For validation, a statistical approach using Bayesian inference is introduced.

As energetic quantities should be evaluated finally on the network, it is demonstrated already in Chapter 2, how energetic quantities can be evaluated in the mechanical network as postprocessing. Using such an energetic approach, one arrives at some similarities with SEA: energies are considered, which are exchanged by subsystems, network analysis is performed based on small systems of equations. However, the displacement-based deterministic system formulation is the basis instead of a probabilistic energetic one. Full coupling is considered through the Poincaré–Steklov operator, instead of a weak and direct coupling only.

Modularity through subsystem coupling does not only allow for parallel, distributed calculations but also provides a natural framework for hybridization. In the latter, parts of the numerical model are replaced by measured ones to meet the epistemic uncertainties in numerical modeling. It is sketched in Chapter 7, which additional challenges arise when measured subsystems should be used for energetic network analysis. It is demonstrated how concepts for phase correction enable validation measurements for energetic quantities. Conclusions are drawn from that for the measurement-based subsystem identification and are briefly discussed.

As a result, several different components are required for the proposed framework. Throughout Chapter 2 to Chapter 7 the main focus is on developing these individual components for an industrial application, each embedded in-situ in the context of existing methods and summarized at the end of each chapter. Only a few examples are occasionally provided in these chapters to illustrate the methods. Instead,

the interplay of all these components is illustrated on two extensive examples in Chapter 8. The globalized optimization of an academic two-dimensional showcase, as well as a numerical vehicle example, is demonstrated as part of an end-to-end virtual development process. The vehicle example consists of a rear axle and a car body, for which structure-borne sound transmission from road-induced noise is reduced through reducing power at the car body. The benefit of a globalized approach is discussed, which is enabled by the numerical framework. The value of power as a key performance indicator for the optimization of vehicle problems is evaluated: the underlying assumptions and the final performance of power are critically reflected based on the examples.

1.3.2 Requirements and Concepts for an Industrial Application

Before introducing the detailed methods, the basic properties of the systems considered in the thesis are summarized. Some general concepts can be derived from these, which form the background for developing the methods through the thesis. Large-scale mechanical networks are analyzed in a limited (low-) frequency band. The networks, which are considered in the presented work, consist of linear time-invariant subsystems. The numerical FE subsystems have the following properties:

- Many subsystem FE models have a large number of DOFs ($n \approx 10^6$), which results from the discretization of the underlying second-order system.
- A moderate number of resonant modes ($n_{\mathrm{res}} < 20$) is present in the analyzed frequency range per subsystem.
- Each subsystem has a limited but high-dimensional input parameter space up to a dimension of $d = 15$. The parameters have a potentially highly nonlinear influence on the subsystem outputs.
- Mainly small interfaces exist for the subsystems. Most interfaces between different subsystems are considered as discretized single points. Consequently, just a couple of inputs and outputs are present per interface.

- Complex FE modeling is used for the subsystems, including different element types and connection techniques.
- The damping modeling is complex. It comprises non-uniform spatial distributions with localized effects and different damping types. Structural damping, a standard engineering approach for damping modeling, is found in most subsystems.

Additionally, there may be subsystems from other sources than a FE model and may contain arbitrary structure (pure Neumann problems, for example). All methods, respectively algorithms developed during the presented work, must be able to handle such networks while providing a computational speed-up by some orders of magnitude as an enabler for (energetic) multi-query analyses. In particular, each algorithm must ensure

- scalability: the pMOR algorithms must work efficiently with large numbers of subsystem DOFs and the high-dimensional input parameter spaces. Subsystem coupling must provide favorable scaling with the number of parameter inputs and subsystems.
- generality: in subsystem coupling, the coupling method should introduce no restrictions on the subsystem properties. In pMOR, the theory behind algorithms should not be limited to special damping modelings, special element formulations, only specific input parameters, or the use in a specific multi-query method.
- non-intrusiveness: Assembly routines of commercial FE codes should be reused for subsystem discretization to ensure industrial applicability. Commercial FE programs, however, do not provide access to their code. Therefore, methods must not require any code modification but be based on available program output.

At the bottom line, the methods must enable the fast application to real industrial models. **Modularization** is one central principle to ensure such fast analyses, as discussed above. However, modularization is not only a prerequisite for efficient numerical evaluations but also reflects the vehicle development process. A modular principle is followed in automotive engineering to meet the ever-increasing number of vehicle derivatives in the presence of cost pressure. Many parts are

developed once and reused in many different vehicles. A corresponding numerical framework should reflect that. Subsystem coupling follows that principle. In the following, some basic approaches are discussed to preserve modularity when combined with model order reduction.

Localized and Decoupled pMOR

High computational costs arise mainly at two different stages of the subsystem coupling: at the calculation of the subsystem outputs and at the solution of the interface problem, which defines the network and synchronizes the subsystem outputs for the coupled response. As discussed above, model order reduction is applied to calculate the subsystem outputs. A local projection basis is found for every single subsystem, which should be reduced. This approach is called *localized* MOR in the following. The internal subsystem states are reduced, from which the outputs are calculated, but not the number of inputs and outputs. Thus, the structure of the interface problem is unaffected by MOR. Each local basis is found independently from the other subsystems or a specific assembly. The error control in the ROM generation is *decoupled* from later assemblies.

Thus, the interface problem is not reduced. The subsystem interfaces are small; consequently, the solution of the interface problem is not significant in the overall workflow when the proposed framework for subsystem coupling is used. Moreover, MOR on the interfaces problem contradicts the modularity approach, as a corresponding ROM cannot be reused for other assemblies and needs to be trained for the whole parameter space of the assembly, not the local subsystems' ones. As mechanical networks have up to hundreds of variable parameters, covering the whole parameter space would be infeasible.

Offline-online Phase Separation

Following a localized, decoupled pMOR approach, one can strictly separate between an offline and online phase. In the offline phase, the subsystems are pre-processed. Reduced-order models (ROM) are trained for the subsystem parameter spaces, or subsystem identification is performed based on measurements. In the online phase, the coupling of these subsystems is evaluated, and energetic quantities are calculated in the network for multi-query applications. From that

perspective, one could also call the offline phase a learning process, the online phase an execution process. This separation follows the principle of modularity: Any pre-processing, thus ROM generation is performed only once per subsystem. The results from the offline phase can be reused in different vehicle networks, different stages of development, and with different multi-query applications. This approach leads to a workflow as visualized in Figure 1.1.

As the resulting ROMs from the offline phase can be reused, calculations in the offline phase can be more demanding in terms of computational complexity. In the online phase, multi-query applications for high-dimensional parameter spaces require a vast number of repetitive system evaluations. Therefore, computational efficiency must be maximized at this stage, in contrast to the offline phase. No calculations should be included that require the evaluation of quantities except the ones of the ROMs.

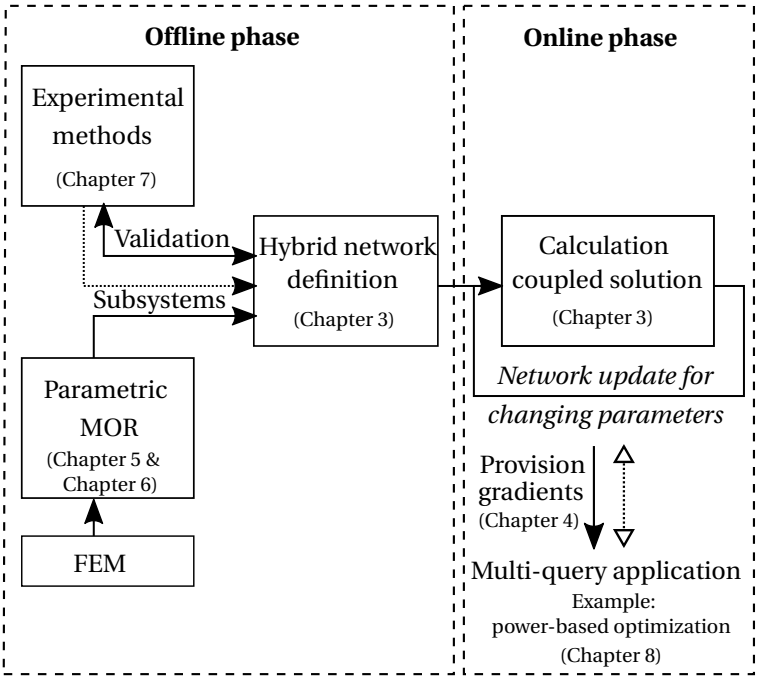

Figure 1.1: The workflow for the energetic network analysis based on the principle of an offline-online separation. References to the single chapters of the thesis are provided, while the measurement-based subsystem identification is only triggered.

CHAPTER 2

BASIC THEORY FOR THE NETWORK ANALYSIS

In the beginning, some basic mechanical and system theoretic concepts are introduced. The (sub-)system description and mechanical representation are discussed, and how energetic quantities can be evaluated for such systems.

2.1 System-Theoretic Preliminaries

2.1.1 Elements of Coupled Problems

A key concept of the coupling framework, which is proposed in Chapter 3, is a very general problem definition. The notation is adapted from the concept of Sicklinger [227] for this purpose. Assume a network consisting of $n_s \geq 2$ subsystems, of which one knows nothing except that they have the form

$$\boldsymbol{Y}_k = \mathcal{S}_k\left(\boldsymbol{U}_k, \boldsymbol{p}_k\right) \qquad k = 1, ..., n_s. \tag{2.1}$$

$\boldsymbol{U}_k$ the input vector, $\boldsymbol{Y}_k$ the output vector of the subsystem k. The inputs may be forces, the outputs displacements for mechanical systems

in classic approaches. In addition, there may be design parameters $\boldsymbol{p}_k$, stiffness or shell thickness values, for example. These form an additional class of inputs that cannot be used for the definition of the coupling operator. Equation (2.1) defines a subsystem simply as a transformation process of inputs to outputs; both provided on the subsystem interface for coupling. Thus, black-box subsystems are allowed, not exposing their inner structure. The only basic assumption so far is a linear relationship between inputs and outputs, as we deal with LTI systems. In addition, the subsystems may have internal state variables $\boldsymbol{X}_k$. The latter may be accessible together with the subsystem matrices for white-box subsystems but not for black-box ones. The subsystem formulation $\mathcal{S}_k$ also includes subsystem boundary conditions not related to coupling and external loads.

The coupling of subsystems is defined by interface constraint equations

$$\mathcal{I}_j\left(\boldsymbol{Y}_k, \boldsymbol{U}_k, k = 1, ..., n_\mathrm{s}\right) = 0 \qquad j = 1, ..., n_\mathrm{s}. \tag{2.2}$$

As a unique feature of the general formulation, Equation (2.2) can describe any coupling between inputs and outputs. In the following, no further assumptions are made on the form of the interface constraint equation $\mathcal{I}_j$, except that it is a linear combination of subsystem inputs and outputs

$$\mathcal{I}_j = \sum_\beta \boldsymbol{a}_{\beta\gamma} \boldsymbol{Y}_\beta + \sum_\gamma \boldsymbol{b}_{\beta\gamma} \boldsymbol{U}_\gamma. \tag{2.3}$$

The requirement of linear constraint equations is not obligatory for the concepts below; it could be relaxed by adapting the formulation of the coupling framework in Chapter 3. Anyhow, this linear form is sufficient for the vibroacoustic problems of the thesis. In addition, it allows interrelating the proposed framework to classic domain decomposition approaches. Equation (2.3) can incorporate any linear coupling between inputs and outputs. Inputs can be coupled to outputs $\mathcal{I} = \boldsymbol{a}_{\beta\gamma} \boldsymbol{Y}_\beta + \boldsymbol{b}_{\beta\gamma} \boldsymbol{U}_\gamma$, resulting in a Dirichlet-Neumann constraint equation. Dirichlet-Dirichlet constraint equations include a coupling of solely outputs $\mathcal{I} = \boldsymbol{a}_{\beta\gamma} \boldsymbol{Y}_\beta + \boldsymbol{b}_{\beta\gamma} \boldsymbol{Y}_\gamma$, Neumann-Neumann constraint equations a coupling of solely inputs $\mathcal{I} = \boldsymbol{a}_{\beta\gamma} \boldsymbol{U}_\beta + \boldsymbol{b}_{\beta\gamma} \boldsymbol{U}_\gamma$.

This general linear problem definition is used to develop a flexible and systematic subsystem coupling method for the definition of the interface problem in Chapter 3. Prior to that, however, the black-box

nature of the subsystems as defined by Equation (2.1) is unraveled for the vibroacoustic application. The known mechanical representation of the subsystems is discussed and how energies are calculated for the latter.

2.1.2 Second-Order Systems

The vibroacoustic subsystems, which are considered in the following, are spatially discretized and described by the equation of motion, a second-order ordinary differential equation in the time domain

$$\mathcal{S}_k : \begin{cases} \boldsymbol{K}_k\left(\boldsymbol{p}_k\right)\boldsymbol{X}_k(t) + \boldsymbol{D}_k\left(\boldsymbol{p}_k\right)\frac{\mathrm{d}\boldsymbol{X}_k(t)}{\mathrm{d}t} + \boldsymbol{M}_k\left(\boldsymbol{p}_k\right)\frac{\mathrm{d}^2\boldsymbol{X}_k(t)}{\mathrm{d}t^2} = \boldsymbol{F}(t) \\ \boldsymbol{Y}_k(t) = \boldsymbol{C}_k\boldsymbol{X}_k(t) \end{cases} \tag{2.4}$$

where the right hand side is

$$\boldsymbol{F}(t) = \boldsymbol{B}_k\left(\boldsymbol{F}_{\mathrm{ext},k}(t) + \boldsymbol{U}_k(t)\right). \tag{2.5}$$

A detailed description of the single variables involved in these equations is provided on the next page. The displacement-based finite element method provides the basis for the spatial discretization of all numerical subsystems in the following. In this variational method, the continuous spatial domain is divided into a mesh of finite elements. In the latter, the displacement solution is approximated locally by discrete DOFs and interpolating ansatz functions. For an in-depth overview of FE methods, refer to the textbooks of Zienkiewicz et al. [283] or Bathe [22].

Steady LTI systems do not need to be analyzed in the time domain but can be characterized efficiently in a transformed space. For generality, the Laplace transform $t \circ\!\!-\!\!\bullet\, s$ of the equation of motion is considered first, and the systems of equations are given as a function of the complex Laplace variable $s = \sigma + i\omega$, where $i = \sqrt{-1}$. The Laplace transform can account for any time-dependent load on an LTI system, and corresponding initial conditions can be introduced. In the following, zero initial conditions are chosen, which allow for the transfer function calculation below. This Laplace domain representation is the basis for the derivation of the model order reduction

technique in Chapter 5. As shown in Section 2.2, the harmonic analysis, which is performed in the frequency domain, can be deduced from this Laplace domain form in a second step.

Inner Representation

For zero initial conditions, the discretized equation of motion of subsystem k can be formulated in the Laplace domain as

$$\mathcal{S}_k : \begin{cases} \boldsymbol{A}_k\left(s, \boldsymbol{p}_k\right) \boldsymbol{X}_k(s) = \boldsymbol{B}_k\left(\boldsymbol{F}_{\text{ext},k}(s) + \boldsymbol{U}_k(s)\right) \\ \boldsymbol{Y}_k(s) = \boldsymbol{C}_k \boldsymbol{X}_k(s) \end{cases} \tag{2.6}$$

with the design parameter dependent dynamic stiffness matrix

$$\boldsymbol{A}_k\left(s, \boldsymbol{p}_k\right) = \boldsymbol{K}_k\left(\boldsymbol{p}_k\right) + i\,\text{sgni}(s)\,\boldsymbol{S}_k\left(\boldsymbol{p}_k\right) + s\boldsymbol{D}_k\left(\boldsymbol{p}_k\right) + s^2\boldsymbol{M}_k\left(\boldsymbol{p}_k\right).$$

$\boldsymbol{K}_k\left(\boldsymbol{p}_k\right) \in \mathbb{C}^{n\times n}$ is the stiffness matrix, $\boldsymbol{M}_k\left(\boldsymbol{p}_k\right) \in \mathbb{C}^{n\times n}$ the mass matrix. $\boldsymbol{D}_k\left(\boldsymbol{p}_k\right) \in \mathbb{C}^{n\times n}$ defines the viscous damping matrix of subsystem k. $\boldsymbol{S}_k\left(\boldsymbol{p}_k\right) \in \mathbb{C}^{n\times n}$ is the structural damping matrix, which is introduced in the Laplace transform in addition as discussed below. $\boldsymbol{X}_k(s) \in \mathbb{C}^{n\times 1}$ is the vector of internal states, respectively displacements. $\text{sgni}(s)$ is the abbreviation for the signum function of the imaginary part of s, $\text{sgn}\big(\Im(s)\big)$. The signum function is one, $\text{sgn}(\square) = 1$, for $\square > 0$, $\text{sgn}(\square) = -1$ for $\square < 0$, and $\text{sgn}(\square) = 0$ for $\square = 0$. The system formulation of Equation (2.6) allows for an explicit definition of the subsystem interfaces: $\boldsymbol{U}_k(s) \in \mathbb{C}^{n_\text{U}\times 1}$ is the vector of n_U inputs, respectively the forces resulting from the dynamic interaction of subsystems in a network. In addition, an external force excitation $\boldsymbol{F}_{\text{ext},k}(s)$ may be included in the subsystem definition. For brevity, the explicit notation of the variables' dependency on $\boldsymbol{p}_k$ and s is omitted in the following where not particularly relevant.

The inputs are mapped to the internal DOFs by the input map matrix $\boldsymbol{B}_k \in \mathbb{C}^{n\times n_\text{U}}$. $\boldsymbol{Y}_k \in \mathbb{C}^{n_\text{Y}\times 1}$ is the vector of n_Y outputs. The latter can be defined as any linear combination of states through the output matrix $\boldsymbol{C}_k \in \mathbb{C}^{n_\text{Y}\times n}$. In the case of a single-input-single-output (SISO) system, there is exactly one discrete input and one output. $\boldsymbol{C}_k$ and $\boldsymbol{B}_k$ become column, respectively row vectors in that case. However, the case of a multiple-input-multiple-output (MIMO) system is the common one in the thesis. If one further assumes that the same

combination of states defines the outputs and inputs, one obtains an interface-symmetric MIMO system. For an interface-symmetric system,

$$\boldsymbol{C}_k^H = \boldsymbol{B}_k \tag{2.7}$$

holds, while H is the Hermitian transpose. Interface-symmetric MIMO systems are assumed in the following for all subsystems.

A (FE) discretization of second-order systems usually results in system matrices ($\boldsymbol{K}_k$, $\boldsymbol{M}_k$, $\boldsymbol{S}_k$,$\boldsymbol{D}_k$), which are real valued and symmetric. The system matrices can become complex valued in a reduced system representation for several model order reduction techniques. For such setting, the system matrices are Hermitian, thus

$$\boldsymbol{D}_k = \boldsymbol{D}_k^H \quad \boldsymbol{M}_k = \boldsymbol{M}_k^H \quad \boldsymbol{K}_k = \boldsymbol{K}_k^H \quad \boldsymbol{S}_k = \boldsymbol{S}_k^H \tag{2.8}$$

which also covers the real-valued symmetric case. However, there are cases in which Equation (2.8) does not hold, mainly if the subsystem incorporates fluid-structure interaction and consequently includes some discretized Helmholtz fluid. In such a case, the state vector contains both displacement and acoustic pressure DOFs. Such subsystems do not necessarily contain symmetric (Hermitian) system matrices, depending on the fluid-structure interaction formulation (Sandberg et al. [219]).

As an alternative to the input-output form of Equation (2.6), subsystems can be rearranged in an inner representation as

$$\boldsymbol{A}_k \boldsymbol{X}_k = \boldsymbol{F}_k + \boldsymbol{G}_k \quad \longleftrightarrow \quad \begin{bmatrix} \boldsymbol{A}_{\mathrm{XX},k} & \boldsymbol{A}_{\mathrm{XY},k} \\ \boldsymbol{A}_{\mathrm{YX},k} & \boldsymbol{A}_{\mathrm{YY},k} \end{bmatrix} \begin{bmatrix} \dot{\boldsymbol{X}}_k \\ \boldsymbol{Y}_k \end{bmatrix} = \begin{bmatrix} \dot{\boldsymbol{F}}_{\mathrm{ext},k} \\ \boldsymbol{F}_{\mathrm{ext},k} \end{bmatrix} + \begin{bmatrix} \boldsymbol{0} \\ \boldsymbol{U}_k \end{bmatrix}. \tag{2.9}$$

This system formulation is more general as Equation (2.6) in the aspect that it includes an external load $\dot{\boldsymbol{F}}_{\mathrm{ext},k}$ applied to non-interface DOFs. It is set to zero for compatibility with Equation (2.6) in the following apart from some cases that explicitly include this quantity. At the same time, Equation (2.9) is less general as Equation (2.6). It neither allows to define a linear combination of states as output nor to split an input to several internal DOFs. One can argue that the latter distinction between the two system representations is artificial to a certain extent

when the subsystem is a white box; thus, one has full access to the internal states and system matrices. While the system of Equation (2.9) can be expressed in the form of Equation (2.6), a conversion the other way round is theoretically also possible. One can reformulate a subsystem of Equation (2.6) in the form Equation (2.9) by defining the outputs as $\mathring{\boldsymbol{Y}} = \boldsymbol{X}$ and the inputs as $\mathring{\boldsymbol{U}} = \boldsymbol{B}\boldsymbol{U}$ in this case. Nevertheless, such reformulation is often impractical as the interface structure of the subsystem changes when the subsystem coordinate system is changed. The proposed model order reduction technique is based on such (lossy) coordinate transformation of a system representation in the form of Equation (2.6), in which the states and the algebraic system of equations are transformed. As a result, after model order reduction, the interface problem would need to be reformulated after each step of model order reduction for a system formulation of Equation (2.9). Consequently, the form of Equation (2.6) is preferred over Equation (2.9) throughout the thesis.

Transfer Function Representation

In the inner representation, one has full access to the (sub-)system matrices and the states; thus, the subsystem is a white-box subsystem. This may not be the case in the transfer function representation, respectively outer form. In the latter, the subsystem is represented solely by its input-to-output behavior in the Laplace domain

$$\boldsymbol{H}_k = \frac{\boldsymbol{Y}_k}{\boldsymbol{U}_k}, \tag{2.10}$$

which is the rational transfer function matrix $\boldsymbol{H}_k \in \mathbb{C}^{n_\mathrm{Y} \times n_\mathrm{U}}$ of subsystem k. $\boldsymbol{H}_k$ is the Laplace transform of the impulse response function in the time domain. For interface-symmetric systems, the transfer function matrix is symmetric.

If the inner representation of the system is available (the realization of the transfer function), the transfer function is calculated as

$$\boldsymbol{H}_k = \boldsymbol{C}_k \boldsymbol{A}_k^{-1} \boldsymbol{B}_k = \boldsymbol{C}_k \left(\boldsymbol{K}_k + i\,\mathrm{sgni}(s)\, \boldsymbol{S}_k + s\boldsymbol{D}_k + s^2 \boldsymbol{M}_k \right)^{-1} \boldsymbol{B}_k \tag{2.11}$$

for second-order systems in the form of Equation (2.6). Rearranging Equation (2.9) for Equation (2.10), the transfer function is obtained for this alternative inner representation by

$$\boldsymbol{H}_k = \boldsymbol{A}_{k,\mathrm{Schur}}^{-1} = \left(\boldsymbol{A}_{\mathrm{YY},k} - \boldsymbol{A}_{\mathrm{XY},k} \boldsymbol{A}_{\mathrm{XX},k}^{-1} \boldsymbol{A}_{\mathrm{YX},k} \right)^{-1}, \tag{2.12}$$

which is the Schur complement (Schur [221]) of the dynamic stiffness. Although the transfer function could be obtained from the inversion of the whole dynamic stiffness, the inversion of the Schur-complement has better numerical properties in general (Badia et al. [18]).

Inner representations are not available in many applications, in using black-box code or many experimental methods for subsystem identification; the latter is discussed in Section 7.3 more in detail. For such a black-box subsystem, only sampled measurements of the transfer function matrix are available, often solely in the frequency domain. Corresponding subsystem coupling approaches must be capable of handling such subsystems.

Depending on the physical type of output and input, the transfer function matrix has different names in structural dynamics (see Harris et al. [118]). The transfer function matrix is also called receptance for a displacement output and force input. For an acceleration output, thus a scaling of Equation (2.11) by ω^2 in the frequency domain, $\boldsymbol{H}_k$ is referred to as accelerance. For a velocity output, alternative names are admittance or mobility. The inverse of a mobility matrix is named impedance matrix; the inverse of the accelerance is the apparent mass. All these representations can be considered transfer functions of correspondingly adapted subsystems in the general definition of Equation (2.1).

Damping modeling

The damping modeling for industrial second-order subsystems may be complex and highly localized in general. Thus, some modeling aspects are discussed explicitly on the matrix level in the following. In structural dynamics, the viscous damping often is assumed to be proportional. The latter terminology is used in different contexts. According to Caughey et al. [51], proportional damping is defined by a viscous damping matrix $\boldsymbol{D}_k$, which satisfies

$$\boldsymbol{K}_k \boldsymbol{M}_k^{-1} \boldsymbol{D}_k = \boldsymbol{D}_k \boldsymbol{M}_k^{-1} \boldsymbol{K}_k. \tag{2.13}$$

Rayleigh-Damping, $\boldsymbol{D}_k = \alpha \boldsymbol{M}_k + \beta \boldsymbol{K}_k$, is one common sub-case of such proportional damping definition. Often, the definition of Rayleigh damping itself is considered as the one of proportional damping. Proportional damping is defined here on the level of the global subsystem matrices. As a result, proportional damping is rarely obtained in real-world industrial FE models. Even if the model consists of one

homogeneous material with proportional damping and thus lacks localized damping, this can be the case. Connection techniques and finite element formulations introduce additional nondamped DOFs. As a result, no specific form of $\boldsymbol{D}_k$ can be assumed for most industrial models.

In addition, structural damping is systematically included in the Laplace domain representations Equation (2.6) to Equation (2.12). This additional form of damping is introduced, as viscous damping is insufficient to describe the damping behavior for many practical vibroacoustic systems. This deficiency led to the development of more general viscoelastic damping models, in which the viscous damping matrix can be frequency-dependent, $\boldsymbol{D}(\omega)$, see Crandall [62] and Ungar [257]. One particular case is a damping matrix $\boldsymbol{D}(\omega)$, whose elements have the form of $D_i = {}^{\text{const.}}/_{|\omega|}$, where $|\square|$ denotes the absolute value of a quantity. This form results in structural damping, a displacement-proportional damping. Such modeling is found in many industrial vibroacoustic models, especially for metal parts, and is realized via a complex material modulus of elasticity or complex springs. On the level of algebraic equations, structural damping is defined by the matrix $\boldsymbol{S}_k$ in Equation (2.6) in the frequency domain. Different names are available for that form of damping: (linear) hysteretic damping (Crandall [61] and Neumark [182]) or rate-independent damping (Chopra [57]), for example. Structural damping is defined typically in the frequency domain, a corresponding formulation can be introduced in the Laplace domain by the structural damping force as defined in Equation (2.6),

$$\boldsymbol{F}_{\text{d}} = i\,\text{sgni}(s)\,\boldsymbol{S}_k \boldsymbol{X}_K\,. \tag{2.14}$$

Employing the signum function on the imaginary part of s, the phase relation is preserved for both positive and negative frequencies ω and enables the passivity proof of Section 2.3.4. It leads to solutions of the characteristic equation of Equation (2.6), which appear in conjugate complex pairs with negative real parts for underdamped systems. Thus a stable second-order system without structural damping remains stable when structural damping is added as defined by Equation (2.14). The introduction in the Laplace domain is provided in an equivalent formulation by Chen et al. [54], or with some similar damping model by

Bonisoli et al. [40]. Converting Equation (2.14) to a frequency domain representation, the formulation changes to

$$\boldsymbol{F}_{\mathrm{d}} = i\,\mathrm{sgn}(\omega)\,\boldsymbol{S}_k \boldsymbol{X}_K\,, \tag{2.15}$$

which is the form as found in Crandall [62]. Note that this formulation of structural damping is not exclusively used in literature, but alternative definitions are available. Meerbergen [172], for example, omits the signum function, which does not take into account the above considerations for the negative frequency domain.

The time-domain equivalent of the frequency domain damping force, Equation (2.15), is a Hilbert transform of the time-dependent system states (Inaudi et al. [129]). The latter illustrates the problematic nature of structural damping in the time domain. As a Hilbert transform involves a convolution, such time-domain representation is not causal. The latter makes the use of structural damping questionable for time-domain analyses; consequently, this type of damping was not included in Equation (2.4). For a frequency domain, respectively Laplace domain analysis, however, structural damping is a common engineering approach to model many industry-relevant damping mechanisms. On material level, structural damping is usually introduced into models by a complex-valued modulus of elasticity

$$\hat{E} = E\left(1 + j\,\mathrm{sgni}(s)\eta\right),$$

where η is the structural damping coefficient. Correspondingly, complex-valued stiffness values may be introduced for discretized spring elements.

On the level of algebraic systems of equations, structural damping leads to necessarily complex-valued dynamic stiffness matrices in the Laplace domain. The formulation of model order reduction approaches needs to be adapted for such complex-valued matrices to be applied to metal part substructures in practice.

2.1.3 First-Order Systems

All mechanical subsystems in the vibroacoustic network are described by the second-order differential equation of Equation (2.4). Anyhow, first-order system representations have relevance throughout the thesis, as they are the historical starting point for the development of the model order reduction technique in Chapter 5. Considering zero

initial conditions again, the inner representation of a first-order subsystem without feedthrough is defined in the Laplace domain as

$$\mathcal{S}_{\mathrm{I},k}: \begin{cases} \boldsymbol{E}_k s\boldsymbol{X}_k(s) = \boldsymbol{A}_{\mathrm{I},k}\left(s,\boldsymbol{p}_k\right)\boldsymbol{X}_k + \boldsymbol{B}_{\mathrm{I},k}\boldsymbol{U}_k(s) \\ \boldsymbol{Y}_k(s) = \boldsymbol{C}_{\mathrm{I},k}\boldsymbol{X}_{\mathrm{I},k}(s) \end{cases} \tag{2.16}$$

with the parameter dependent state matrix $\boldsymbol{A}_{\mathrm{I},k}\left(s,\boldsymbol{p}_k\right) \in C^{n_\mathrm{I}\times n_\mathrm{I}}$ and $\boldsymbol{E}_k \in C^{n_\mathrm{I}\times n_\mathrm{I}}$. Equation (2.16) has the same structure as Equation (2.6): The first line is called state equation, the second line output equation. $\boldsymbol{B}_{\mathrm{I},k} \in \mathbb{C}^{n_\mathrm{I}\times n_\mathrm{U}}$ and $\boldsymbol{C}_{\mathrm{I},k} \in \mathbb{C}^{n_\mathrm{Y}\times n_\mathrm{I}}$ are the input and output matrices of the first-order system, which map the state DOFs $\boldsymbol{X}_{\mathrm{I},k} \in C^{n_\mathrm{I}\times 1}$ to the inputs $\boldsymbol{U}_k(s) \in C^{p\times 1}$ and outputs $\boldsymbol{Y}_k(s) \in C^{p\times 1}$.

The transfer function representation of the first-order system is found in the Laplace domain as

$$\boldsymbol{H}_{\mathrm{I},k} = \boldsymbol{C}_{\mathrm{I},k}(s\boldsymbol{E}_k - \boldsymbol{A}_{\mathrm{I},k})^{-1}\boldsymbol{B}_{\mathrm{I},k}. \tag{2.17}$$

Any second-order system can be transformed to a first-order representation by linearization. Compared to the second-order form, the number of unknowns in the state vector is doubled $n_\mathrm{I} = 2n$ in this case. Such linearization is not unique (Tisseur et al. [245]); depending on the choice of the state vector, different formulations for linearization are available. A common choice for the state vector is

$$\boldsymbol{X}_{\mathrm{I},k} = \begin{bmatrix} \boldsymbol{X}_k \\ \frac{\mathrm{d}\boldsymbol{X}_k}{\mathrm{d}t} \end{bmatrix},$$

which results in the the following linearized system matrices

$$\begin{aligned} \boldsymbol{E}_k &= \begin{bmatrix} \boldsymbol{D}_k & \boldsymbol{M}_k \\ \boldsymbol{M}_k & \boldsymbol{0} \end{bmatrix} \quad \boldsymbol{A}_{\mathrm{I},k} = \begin{bmatrix} -\boldsymbol{K}_k - i\,\mathrm{sgni}(s)\,\boldsymbol{S}_k & \boldsymbol{0} \\ \boldsymbol{0} & \boldsymbol{M}_k \end{bmatrix}. \\ \boldsymbol{B}_{\mathrm{I},k} &= \begin{bmatrix} \boldsymbol{B}_k \\ \boldsymbol{0} \end{bmatrix} \qquad \boldsymbol{C}_{\mathrm{I},k} = \begin{bmatrix} \boldsymbol{C}_k & \boldsymbol{0} \end{bmatrix} \end{aligned} \tag{2.18}$$

Using the linearization of Equation (2.18), the symmetry of the system matrices is preserved in the first-order representation. For symmetric system matrices of the second-order system, $\boldsymbol{K}_k$, $\boldsymbol{M}_k$, $\boldsymbol{S}_k$,$\boldsymbol{D}_k$, the

first-order system matrices $\boldsymbol{A}_k$ and $\boldsymbol{E}_k$ are symmetric, too. For other linearization schemes, refer to Tisseur et al. [245] or Salimbahrami [217].

The state matrix does not depend on the Laplace variable s in standard first-order representations, in contrast to the dynamic stiffness in second-order systems. Anyhow, the inclusion of structural damping introduces such dependency, as evident from Equation (2.18). Thus, the introduction of structural damping requires the critical review of established algorithms applied to a system in state-space form.

2.2 Harmonic Analysis of Linear Systems

As steady systems are assumed, harmonic analyses are performed throughout the thesis. A steady system is characterized in the time domain by its particular response

$$\boldsymbol{X}(t) = \boldsymbol{X}_0 \cos\left(\omega t + \varphi_{\mathrm{X}}\right) \quad \text{resp.} \quad \boldsymbol{Y}(t) = \boldsymbol{Y}_0 \cos\left(\omega t + \varphi_{\mathrm{Y}}\right), \tag{2.19}$$

which is calculated by solving Equation (2.4) for a harmonic excitation $\boldsymbol{F}(t) = \boldsymbol{F}_0 \cos\left(\omega t + \varphi_{\mathrm{F}}\right)$ with $\omega = 2\pi f$. f is the frequency of excitation. These harmonic functions can be reformulated in a complex notation using Euler's formula, as shown exemplarily for the state

$$\boldsymbol{X}(t) = \frac{1}{2}\left(\boldsymbol{X}_0 e^{i\varphi_{\mathrm{X}}} e^{i\omega t} + \boldsymbol{X}_0 e^{-i\varphi_{\mathrm{X}}} e^{-i\omega t}\right) = \frac{1}{2}\left(\boldsymbol{X} e^{i\omega t} + \boldsymbol{X}^* e^{i\omega t}\right). \tag{2.20}$$

$\square^*$ denotes the conjugate complex and $\boldsymbol{X}$ the signal's complex-valued amplitude. The latter contains the phase and amplitude information of the signal of Equation (2.19)

$$\boldsymbol{X}_0 = |\boldsymbol{X}| \qquad \varphi_X = \arctan\left(\frac{\Im(\boldsymbol{X})}{\Re(\boldsymbol{X})}\right),$$

where $|\square|$ is the absolute value. The Euler representation consists of a positive and negative frequency component. Anyhow, only one component needs to be considered to solve Equation (2.4) for the complex-valued state vector of the complete solution, respectively output vector and thus for the required amplitude and phase information (Bosse et al. [42]). There is no uniform convention in vibroacoustics on whether to take the positive or negative-valued frequency

component (Maysenhölder [169]). In the following, all expressions are based on considering the positive-valued components. Thus, one uses analytic signals as ansatz function in the time-domain

$$\hat{\boldsymbol{X}}(t) = \boldsymbol{X}\, e^{i\omega t} \quad \text{resp.} \quad \hat{\boldsymbol{Y}}(t) = \boldsymbol{Y}\, e^{i\omega t} \tag{2.21}$$

for an excitation of the same form, $\hat{\boldsymbol{F}}(t) = \boldsymbol{F}\, e^{i\omega t}$. This corresponds to an addition of a sine-imaginary part to the cosine function of Equation (2.19)

$$\hat{\boldsymbol{X}}(t) = \boldsymbol{X}_0 \cos\left(\omega t + \varphi_{\mathrm{X}}\right) + i\boldsymbol{X}_0 \sin\left(\omega t + \varphi_{\mathrm{X}}\right). \tag{2.22}$$

The time-dependent analytic signals are complex valued, for which only the real part is physical $\boldsymbol{X}(t) = \Re\left(\hat{\boldsymbol{X}}(t)\right)$. However, they allow to calculate $\boldsymbol{X}$ and $\boldsymbol{Y}$, and thus the required amplitude and phase vectors directly from the solution of the system with the analytic ansatz functions. The described procedure corresponds to a Fourier transformation of the time-domain representation of the steady system, Equation (2.4), which is evaluated for the positive frequency content only, and for which the complete solution is recovered afterward. Therefore, the required frequency-domain representations are obtained by substituting $s = i\omega$ in the Laplace domain formulations of Equation (2.6), respectively Equation (2.11).

Performing a harmonic analysis, the involved variables are complex-valued and frequency-dependent. The notation of the latter is omitted for brevity in the following. If variables do not depend on frequency, this is stated explicitly.

2.3 Energetic Network Analysis for Coupled Deterministic Systems

The above system formulations are based on displacement DOFs, and, in the case of first-order system, their time derivatives. For such discretized subsystems, the evaluation of energetic quantities is a postprocessing step after the system solution. Before suitable postprocessing is presented, it is clarified below what energetic quantities are available for an evaluation and how they are related.

2.3.1 Energetic Quantities of a Subsystem

Therefore, the interrelation between the different energetic quantities of a subsystem is derived. These relationships have been thoroughly

investigated; refer to Alfredsson [3] and Alfredsson et al. [4], for example. The following paragraph follows closely Ullmann et al. [253, 255]. A continuum mechanic formulation is followed below for illustration, which results in formulas for discrete systems in Section 2.3.2. The indices for indicating subsystem k are dropped during the section for brevity.

Energy conservation is a fundamental principle of mechanical systems. Starting from the wave equation, a corresponding corollary can be derived for source-free volumes as

$$\frac{\partial E_{\mathrm{totV}}(t)}{\partial t} + \nabla \boldsymbol{i}(t) = -D(t) \tag{2.23}$$

where E_{totV} is the total energy density, $\boldsymbol{i}$ is the vector of (acoustic) energy fluence rate or simply instantaneous intensity, and D is the dissipated energy per volume. No external body forces are considered. For solid structures, a derivation can be found in Maysenhölder [169], for Helmholtz fluids in Kirchhoff [140]. The corollary is known as Poynting's theorem in electrodynamics. Integrating (2.23) over the subsystem volume V an expression in the form of the first law of thermodynamics is obtained and, thus, can be interpreted as the law of (acoustic) energy conservation

$$\frac{\partial}{\partial t} \underbrace{\int_V E_{\mathrm{totV}}(t)\,\mathrm{d}V}_{E_{\mathrm{tot}}(t)} + \underbrace{\int_S \boldsymbol{i}(t)\cdot\boldsymbol{n}\,\mathrm{d}S}_{P(t)} = \underbrace{-\int_V D(t)\,\mathrm{d}V}_{P_{\mathrm{diss}}(t)}. \tag{2.24}$$

S is the overall surface of the subsystem volume, $\boldsymbol{n}$ the surface normal vector. Further assuming external excitation solely at the connecting interfaces, the integration over S can be reduced to integration over the subsystem interfaces, which are considered a subset of S. $E_{\mathrm{tot}}(t)$ is the time-dependent total subsystem energy, which is the sum of potential and kinetic energy,

$$E_{\mathrm{tot}}(t) = \int_V E_{\mathrm{totV}}(t)\mathrm{d}V = \int_V E_{\mathrm{potV}}(t)\mathrm{d}V + \int_V E_{\mathrm{kinV}}(t)\mathrm{d}V. \tag{2.25}$$

For linear elastic solids, the total energy is obtained by

$$E_{\mathrm{tot}}(t) = \int_V \frac{1}{2}\boldsymbol{\rho}\,\boldsymbol{v}(t)\,\boldsymbol{v}(t)\mathrm{d}V + \int_V \frac{1}{2}\boldsymbol{\varepsilon}(t)\,\boldsymbol{\sigma}(t)\mathrm{d}V \tag{2.26}$$

where $\boldsymbol{v}(t) = \frac{\mathrm{d}\boldsymbol{w}}{\mathrm{d}t}$ is the velocity vector, $\boldsymbol{\varepsilon}(t)$ the strain tensor, $\boldsymbol{\sigma}(t)$ the stress tensor.

$P_{\mathrm{diss}}(t)$ is the instantaneous dissipated power. $P(t)$ is the instantaneous power calculated by the surface integral of the scalar product of the intensity and the surface normal vector $\boldsymbol{n}$. The intensity vector itself is obtained by the multiplication of the stress tensor and the velocity vector

$$P(t) = \int_S \boldsymbol{i}(t)^T \boldsymbol{n}\,\mathrm{d}S = \int_S \boldsymbol{n}^T \boldsymbol{\sigma}(t)\,\boldsymbol{v}(t)\,\mathrm{d}S. \tag{2.27}$$

The above formulas in the time domain are valid for any time-dependent system response. However, usually, not the instantaneous values but the cycle-averaged energetic values are of interest for harmonic analysis. On cycle average, the change of the total energy is zero for a harmonic excitation

$$\frac{1}{T}\int_0^T E_{\mathrm{tot}}(t)\mathrm{d}t = 0, \tag{2.28}$$

where T is the cycle time. The cycle-averaged mean power is obtained from Equation (2.24) by

$$\overline{P} = \frac{1}{T}\int_0^T P(t)\mathrm{d}t = \frac{1}{T}\int_0^T P_{\mathrm{diss}}(t)\mathrm{d}t. \tag{2.29}$$

To obtain the cycle averaged form of the energy conservation law (Equation (2.24)) in the frequency domain, a valuable auxiliary is given by the following relationship for two functions $a(t)$ and $b(t)$, which oscillate harmonically at the same frequency

$$\frac{1}{T}\int_0^T \Re\big(a(t)\big)\Re\big(b(t)\big)\mathrm{d}t = \frac{1}{2}\Re\big(a\,b^*\big) = \frac{1}{2}\Re\big(S_{\mathrm{ab}}\big). \tag{2.30}$$

The time average of the product of the two real parts of $a(t)$ and $b(t)$ is obtained by the real part of the complex conjugate multiplication of the two complex-valued quantities in the frequency domain. $a\,b^*$ is a cross-power spectrum S_{ab}, which corresponds to a convolution in the time domain. The energy conservation, Equation (2.24), thus is obtained in the frequency domain as

$$2\,i\,\omega(\overline{E}_{\mathrm{pot}} - \overline{E}_{\mathrm{kin}}) + P_{\mathrm{c}} = \overline{P}_{\mathrm{diss}} \tag{2.31}$$

where $\overline{E}_{\text{pot}}$ is the cycle averaged potential energy,

$$\overline{E}_{\text{pot}} = \frac{1}{4}\Re\left(\int_V \boldsymbol{\varepsilon}^* \boldsymbol{\sigma}\, \mathrm{d}V\right) \tag{2.32}$$

$\overline{E}_{\text{kin}}$ the cycle averaged kinetic energy

$$\bar{E}_{\text{kin}} = \frac{1}{4}\Re\left(\int_V \rho\, \boldsymbol{v}^* \boldsymbol{v}\, \mathrm{d}V\right). \tag{2.33}$$

P_{c} is the complex power, which is complex valued and is obtained according to Alfredsson et al. [4], Maysenhölder [169], and Pavic [195] as

$$P_{\text{c}} = \frac{1}{2}\int_S \boldsymbol{n}^T \boldsymbol{\sigma}\, \boldsymbol{v}^*\, \mathrm{d}S. \tag{2.34}$$

Based on the reformulated mechanical energy conservation, Equation (2.31), the real and imaginary parts of the complex power can be related to cycle-averaged values (Alfredsson [3]):

$$\Re\left(P_{\text{c}}\right) = \overline{P} = \overline{P}_{\text{diss}} \tag{2.35}$$

$$\Im\left(P_{\text{c}}\right) = 2\omega(\overline{E}_{\text{pot}} - \overline{E}_{\text{kin}}). \tag{2.36}$$

The real part of the complex power quantity is equal to the vibration cycle-averaged dissipated power, $\overline{P}_{\text{diss}}$; it is referred to shortly as mean power in the following. The imaginary part is proportional to the product of the circular frequency of excitation ω and the Lagrangian $\overline{E}_{\text{pot}} - \overline{E}_{\text{kin}}$. It is called reactive power in literature (Jacobsen [130]) and is equal to the magnitude of that part of instantaneous power, whose cyclic mean value is zero. As reactive power is proportional to the difference in mean energies, reactive power is considered as a measure of oscillating energy in electrical networks (Bosse et al. [42]). For mechanical systems, the use of reactive power as an indicator for several different effects is discussed critically, especially in the context of intensity methods, refer to Fahy [75], Jacobsen [130], Maysenhölder [169], and Rossing [210].

2.3.2 Evaluation of Energetic Quantities in Discretized Subsystems

These energetic quantities can be evaluated in networks of coupled, discretized subsystems. For the derivations of this section assume

a displacement-based subsystem formulation as provided by Equation (2.6) or Equation (2.11). The subsystem inputs are forces $\boldsymbol{U}_k : F$, the outputs, respectively states are displacements $\boldsymbol{Y}_k, \boldsymbol{X}_k : W$ and may contain both translational and rotational DOFs. Such system formulation is not a requirement for the evaluation of energetic quantities. However, the formulas below need to be reformulated otherwise. Furthermore, an interface-symmetric subsystem in the form of Equation (2.6) is required, which is defined by $\boldsymbol{C}_k^H = \boldsymbol{B}_k$

A discretized version of the energy conservation in the frequency domain, Equation (2.31), is obtained directly by pre-multiplying Equation (2.6) with the Hermitian of the velocity vector $\boldsymbol{V} = i\omega\boldsymbol{X}$. Starting from that, the relationship for the energetic quantities of discretized systems can be found. A discretized version of Equation (2.34) is obtained for the calculation of power in accordance with Alfredsson [3] and Mace et al. [160]. In Ullmann et al. [255], the evaluation of power in arbitrary cutting sections of FE models was demonstrated. The complex power, Equation (2.34), can be further split into two parts: one part, which results from the energy exchange between the subsystems of a network, and the input power as another part, which is supplied by external forces. The first part, the complex power of a discretized subsystem resulting from the interaction in the network and summed up over all the subsystem's interfaces, is given by

$$P_k = \frac{i\omega}{2}\boldsymbol{U}_k^H \boldsymbol{Y}_k = \frac{i\omega}{2}\boldsymbol{U}_k^H \boldsymbol{H}_k \boldsymbol{U}_k. \tag{2.37}$$

Consequently, the mean power is obtained from

$$\overline{P}_k = \frac{\omega}{2}\Re\left(i\boldsymbol{U}_k^H \boldsymbol{Y}_k\right) = \frac{\omega}{2}\Re\left(i\boldsymbol{U}_k^H \boldsymbol{H}_k \boldsymbol{U}_k\right) = -\frac{\omega}{2}\Im\left(\boldsymbol{U}_k^H \boldsymbol{H}_k \boldsymbol{U}_k\right), \tag{2.38}$$

the reactive power from

$$R_k = \frac{\omega}{2}\Im\left(i\boldsymbol{U}_k^H \boldsymbol{Y}_k\right) = \frac{\omega}{2}\Im\left(i\boldsymbol{U}_k^H \boldsymbol{H}_k \boldsymbol{U}_k\right) = \frac{\omega}{2}\Re\left(\boldsymbol{U}_k^H \boldsymbol{H}_k \boldsymbol{U}_k\right). \tag{2.39}$$

The subsystem input power, which results from external forces, is given by

$$P_{\text{ext},k} = \frac{i\omega}{2}\boldsymbol{F}_{\text{ext},k}^H \boldsymbol{Y}_k = \frac{i\omega}{2}\boldsymbol{F}_{\text{ext},k}^H \boldsymbol{H}_k \boldsymbol{F}_{\text{ext},k}, \tag{2.40}$$

and the real and imaginary parts correspondingly to Equation (2.38) and Equation (2.39). The energy exchange of single subsystems through

partial interfaces are obtained by modifying Equation (2.37), respectively Equation (2.38) or Equation (2.39) for the partial input and output vector.

The cycle-averaged total energy can be calculated from the sum of kinetic and potential energy $\overline{E}_{\mathrm{tot},k} = \overline{E}_{\mathrm{P},k} + \overline{E}_{\mathrm{P},k}$ for discretized systems. For the latter, the kinetic energy is obtained at any frequency by

$$\overline{E}_{\mathrm{kin},k} = \frac{1}{4}\omega^2 \boldsymbol{X}_k^H \boldsymbol{M}_k \boldsymbol{X}_k, \tag{2.41}$$

the potential energy by

$$\overline{E}_{\mathrm{pot},k} = \frac{1}{4}\boldsymbol{X}_k^H \boldsymbol{K}_k \boldsymbol{X}_k. \tag{2.42}$$

Real-valued symmetric, respectively complex-valued Hermitian matrices $\boldsymbol{K}_k$ and $\boldsymbol{M}_k$ are assumed for Equation (2.41) and Equation (2.42).

2.3.3 Availability of Energetic Quantities for Network Evaluations

Different methods for an energetic network characterization are available, which utilize different energetic measures as the quantity of interest. A first approach is to evaluate the subsystem mean kinetic and potential energies, like in a SEA method (Le Bot [144] and Lyon et al. [158]). An additional scaling of the subsystem energies by the system input power is possible, resulting in energy influence coefficients (EIC, Mace et al. [160])

$$a_{kl} = \frac{\overline{E}_{\mathrm{tot},kl}}{\bar{P}_l} \tag{2.43}$$

where $E_{\mathrm{tot},kl}$ is the total energy in subsystem k due to an external input power at subsystem l. EICs showed up to give valuable insights into the dynamics of coupled systems for deterministic low-frequency systems, as demonstrated for a vehicle floor by Müller et al. [179]. Energy influence coefficients can be further used to estimate SEA (like) coupling loss factors, see Thite et al. [244].

However, the evaluation of energies is not possible for hybrid networks, which include any experimentally or generically determined

black-box subsystem. Calculating the subsystem energy by Equation (2.41) and Equation (2.42) requires the inner representation of the second-order system, Equation (2.6). The subsystem state vector $\boldsymbol{X}_k$, mass and stiffness matrix $\boldsymbol{M}_k$, respectively $\boldsymbol{K}_k$, must be available. In a measurement-based subsystem identification, the transfer function is often measured at distinct frequency samples, without reconstruction of an inner representation. As a possible remedy, energies can be estimated from the observation of the sampled subsystem inputs and outputs, which does not require an inner representation (see Section 7.1.2). However, such approaches are an error-prone approximation without general applicability.

As a result, power quantities but not subsystem energies can be evaluated in hybrid networks: the calculation of power solely needs knowledge of the subsystem inputs and outputs, which are available in any subsystem coupling scenario by construction. If not explicitly stated, mean power quantities are evaluated exclusively in the following; they contribute to the temporal mean of power and are thus directly connected to the energy dissipated in the mechanical network and the energy flow.

2.3.4 Requirements for Accurate Power Quantities

If power should be analyzed in the network as postprocessing, there are additional requirements for both numerical and experimental network characterization methods. First, the discussion on these is based on a SISO setting with unidirectional input and output - without losing generality. Again, the subsystem input is a force $U_k : F$, the output is a displacement $Y_k : W$. Rewriting Equation (2.37) in a trigonometric form as

$$\overline{P} = \frac{1}{2}|U_k||Y_k|\sin(\Delta\varphi_{\mathrm{YU}}) = \frac{1}{2}|U_k|^2|H|\sin(\Delta\varphi_{\mathrm{H}}) \tag{2.44}$$

emphasizes that besides the amplitudes of forces and velocities, the relative phase between these signals, $\Delta\varphi_{\mathrm{UY}}$, is included in the power calculation. $H_{\mathrm{v}} = sH$ is the SISO transfer function, which was defined for a velocity output for brevity, thus the mobility. Accordingly, the required phase is given by

$$\Delta\varphi_{\mathrm{H}} = \Delta\varphi_{\mathrm{UY}} = \arctan\frac{\Im\left(S_{\mathrm{UY}}\right)}{\Re\left(S_{\mathrm{UY}}\right)}, \tag{2.45}$$

where $S_{\mathrm{UY}} = U_k^* Y_k$ is the cross power spectrum between output and input.

Phase Accuracy and Damping Modeling

The accuracy of the relative phase in Equation (2.45) can become a crucial requirement for meaningful power quantities. To illustrate this, the paragraphs below follow closely Ullmann et al. [256] and the sensitivity of power with respect to perturbations in the input and output quantities is discussed. As examined in Chapter 7, experimental methods may introduce an distortion not proportional to the original non-distorted value. The absolute conditioning of the power quantity,

$$\mathrm{cond}(\overline{P}, \gamma) = \left| \frac{\partial \overline{P}(\gamma)}{\partial \gamma} \right| \frac{1}{|\overline{P}(\gamma)|}, \tag{2.46}$$

is evaluated for this, which differs from the standard conditioning in that it omits the scaling by $|\gamma|$. $\partial \overline{P}(\gamma)/\partial \gamma$ is the partial derivative of the mean power $\overline{P}$ with respect to γ. γ is the input, for which the mean power's sensitivity should be analyzed; here, the amplitudes of the two required quantities, the force and the velocity, and the relative phase between them are chosen, $\gamma = |U_k|, |Y_k|, \Delta\varphi_{\mathrm{UY}}$. As the amplitudes of the subsystem input and output are linear inputs to the mean power, the conditioning results in

$$\mathrm{cond}(\overline{P}, |U_k|) = \frac{1}{U_k} \quad \text{resp.} \quad \mathrm{cond}(\overline{P}, |Y_k|) = \frac{1}{Y_k}, \tag{2.47}$$

which illustrates that the influence of a fixed error of the input or output scales inversely to the amplitude of the corresponding quantity. However, the conditioning for the relative phase is

$$\mathrm{cond}(\overline{P}, \Delta\varphi_{\mathrm{UY}}) = |\tan^{-1}(\Delta\varphi_{\mathrm{UY}})|. \tag{2.48}$$

Equation (2.48) is evaluated in Figure 2.1. The latter illustrates that $\Delta\varphi_{\mathrm{UY}}$ has a significantly higher conditioning for values around $a \cdot \pi$, with $a \in \mathbb{Z}$ than provided by the conditioning of the amplitudes in Equation (2.47). This result indicates a high sensitivity of mean power, and even small errors in the relative phase may significantly influence the resulting power. In contrast, for values of $\Delta\varphi_{\mathrm{UY}}$ that are around

$(2a-1)\pi/2$, the conditioning is small. A phase of $(2a-1)\pi/2$ corresponds to a resonance of the undamped system, where power has a small sensitivity with respect to phase errors as a result. Undamped systems

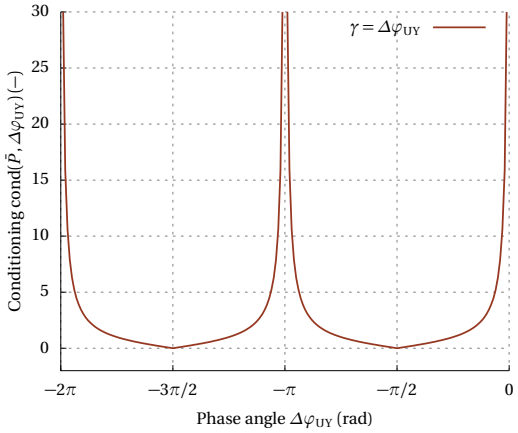

Figure 2.1: Conditioning of the mean power, Equation (2.46), for the relative phase angle $\Delta\varphi_{UY}$.

have a relative phase of $a\pi$, $a \in \mathbb{Z}$ at non-resonant frequencies. The less a system is damped, the more the relative phase approaches such value in these frequency ranges. The phase lag from $a\pi$, $a \in \mathbb{Z}$, which is introduced by the (light) damping, is small for such systems but must be determined very accurately for accurate power values due to the high conditioning in these phase ranges.

Example 2.1 (Two-DOF system)

This sensitivity to the relative phase can be illustrated using a two-DOF system with variable structural damping value η, as defined by Figure 2.2 and Table 2.1.

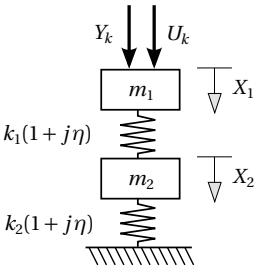

Figure 2.2: Schema of the two-DOF example for evaluating the phase sensitivity of energetic quantities.

Quantity	k_1	k_2	m_1	m_2	F_0
Value	100	10	0.06	0.05	1

Table 2.1: Parameters for the two-DOF example.

The system has resonances at $f_1 = 1.49\,\mathrm{Hz}$ and $f_2 = 9.78\,\mathrm{Hz}$. A SISO setting is considered with an evaluation at the point of load input. To illustrate the results of Figure 2.1, a numerical experiment is performed. A random relative phase error between $\Delta\varphi_{\mathrm{err}} \in [-1°, 1°]$ is introduced on $\Delta\varphi_{\mathrm{UY}}$ and the coefficient of variation

$$c = \frac{\sigma\left(\overline{P}\right)}{\mu\left(\overline{P}\right)} \tag{2.49}$$

is repetitively evaluated per frequency for fixed damping values η. $\sigma\left(\overline{P}\right)$ is the standard deviation of mean power for different phase errors and $\mu\left(\overline{P}\right)$ the corresponding mean value. The results are provided in Figure 2.3 and are in line with the ones of Figure 2.1: The relative phase approaches $a \cdot \pi/2$ for non-resonant frequencies. This results in power quantities, which are highly sensitive to $\Delta\varphi_{\mathrm{err}}$, and consequently in $c \geq 10$. In contrast, the mean power is insensitive to $\Delta\varphi_{\mathrm{err}}$ for frequency values close to the system resonances at $f_1 = 1.49\,\mathrm{Hz}$ or $f_2 = 9.78\,\mathrm{Hz}$. As evident from Figure 2.3, there is another, third frequency range around $f_{\mathrm{A}} = 7.71\,\mathrm{Hz}$ in which power is insensitive. The frequency f_{A} is identified as anti-resonance; thus, the frequency value at which the system has its maximum input impedance. Furthermore, Figure 2.3 shows the influence of the (sub)system damping on the evaluation of power: the higher the damping, the lower the coefficient of variation becomes for non-resonant frequencies. This is because the difference in the relative phase from $\pi/2$ is increased out of resonance.

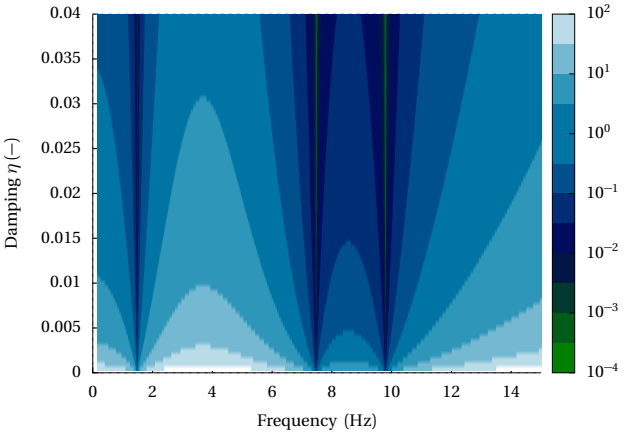

Figure 2.3: Variation coefficient of the two-DOF example's mean input power for an uncertain $\Delta\varphi_{\mathrm{UY}}$, illustrated on a logarithmic scale as a function of the structural damping coefficient.

As a result, experimental methods to measure power directly or to provide a subsystem identification based on a transfer function representation should be phase accurate for subsystems with light damping in particular. At least, the qualitative phase errors introduced by the experimental setup must be known to evaluate the results for power. Considering an inner system representation, the relative phase is directly linked with the system damping. Therefore, numerical methods that work on these representations should have a particular emphasis on correct damping modeling.

Passivity of Subsystems

In order to evaluate the quantitative phase error and thus the validity of power quantities, the true phase values of the transfer function matrix need to be known. This is usually not given for experimental methods in which the latter just should be determined. Anyhow, another approach is available for a baseline quality measure of experimental or numerical methods concerning phase accuracy. This approach can be performed for any symmetric MIMO transfer function and is based on the passivity of the single subsystems in the mechanical network. In system theory, the passivity of subsystems is defined by the supplied work $\int_0^T \boldsymbol{Y}(t)^T \boldsymbol{U}(t)\mathrm{d}t$ to be lower bounded for any integration time T. The increase in energy over time does not exceed the work supplied by the external source, thus is linked to a time-integrated version of Equation (2.24). The passivity is ensured for linear systems if they possess a positive real transfer function. Assuming interface symmetry ($\boldsymbol{C} = \boldsymbol{B}^H$) and thus a symmetric matrix of transfer functions $\boldsymbol{H}$ in the Laplace domain and using the positive real lemma, a positive real transfer function is provided if the following three conditions hold (see Curtain [63] and Wohlers [273], for example):

1. $\boldsymbol{H}_k(s)$ is analytic in $\Re(s) > 0$
2. $\boldsymbol{H}_k(s^*) = \boldsymbol{H}_k(s)^H$ for all $s \in \mathbb{C}$
3. $\Re\left(\boldsymbol{W}^H \boldsymbol{H}_k(s) \boldsymbol{W}\right) \geq 0$ for any $\boldsymbol{W} \in \mathbb{C}^{n\times 1}$ while $s \in \mathbb{C}$ and $\Re(s) > 0$

The first condition is the requirement of stability and is fulfilled for stable systems. Thus, passivity includes stability. The second condition holds for the interface-symmetric second-order systems of the thesis

with Hermitian system matrices, which can be shown in a straightforward manner

$$\begin{aligned}\boldsymbol{H}_k(s)^H &= \left(\boldsymbol{C}_k\left(\boldsymbol{K}_k + i\,\mathrm{sgni}(s)\,\boldsymbol{S}_k + s\boldsymbol{D}_k + s^2\boldsymbol{M}_k\right)^{-1}\boldsymbol{B}_k\right)^H \\ &= \boldsymbol{B}_k^H\left(\boldsymbol{K}_k^H + i\,\mathrm{sgni}\left(s^*\right)\boldsymbol{S}_k^H + s\boldsymbol{D}_k^H + s^{2*}\boldsymbol{M}_k^H\right)^{-1}\boldsymbol{C}_k^H = \boldsymbol{H}_k(s^*).\end{aligned}$$

For rational transfer functions, the third conditions is equivalent to the requirement, that the matrix $\boldsymbol{H}(i\omega)+\boldsymbol{H}(i\omega)^H$ needs to be positive semi-definite, thus

$$\boldsymbol{W}^H\left(\boldsymbol{H}(i\omega)+\boldsymbol{H}(i\omega)^H\right)\boldsymbol{W} \geq 0 \tag{2.50}$$

holds for all $\boldsymbol{W} \in \mathbb{C}^{n\times 1}$ and $\omega \in (R)$, while poles of $\boldsymbol{H}(s)$ on the imaginary axis need to be simple and need to have a nonnegative definite residuum (Anderson et al. [12]). Poles on the imaginary axis of the complex plane would be obtained for undamped systems. It turns out that Equation (2.50) states nothing except that the mean power balance at the subsystem interface must be larger or equal to zero for passive subsystems without internal sources for any input vector. In other words, the mechanical subsystems themselves do not produce any energy but only dissipate. For a modified system definition of Equation (2.6), respectively Equation (2.11) with velocity output $\boldsymbol{Y} : V$, the mean power balance is reformulated as

$$\begin{aligned}\overline{P}_k &= \frac{\omega}{2}\Re\left(i\left(\boldsymbol{U}_k^H + \boldsymbol{F}_{\mathrm{ext},k}^H\right)\boldsymbol{H}_k\left(\boldsymbol{U}_k + \boldsymbol{F}_{\mathrm{ext},k}\right)\right) = \frac{1}{2}\Re\left(\dot{\boldsymbol{U}}_k^H\,\boldsymbol{H}_{\mathrm{V},k}\,\dot{\boldsymbol{U}}_k\right) \\ &= \frac{1}{4}\dot{\boldsymbol{U}}^H\left(\boldsymbol{H}_{\mathrm{V},k} + \boldsymbol{H}_{\mathrm{V},k}^H\right)\dot{\boldsymbol{U}} \geq 0.\end{aligned} \tag{2.51}$$

$\boldsymbol{H}_{\mathrm{V},k} = s\boldsymbol{H}_k$ is the mobility, thus the transfer function matrix for the velocity output and $\dot{\boldsymbol{U}}_k = \boldsymbol{U}_k + \boldsymbol{F}_{\mathrm{ext},k}$. Equation (2.51) takes the same form of Equation (2.50). Consequently, when the subsystem's passivity is preserved for any subsystem identification method, based on hardware measurements or on the (manipulation of) numerical modeling, physically meaningful energetic network analysis can be ensured in the sense that no artificial energy sources are added.

For black-box subsystems, which provide only an outer representation sampled at distinct frequency points, the condition of Equation (2.50) can be evaluated for the mobility at these frequency samples. As $\left(\boldsymbol{H}_{\mathrm{V},k}(i\omega)+\boldsymbol{H}_{\mathrm{V},k}(i\omega)^H\right) = 2\Re\left(\boldsymbol{H}_{\mathrm{V},k}(i\omega)\right)$ holds for interface

symmetry, Equation (2.50) is equal to the condition of a positive semi-definite real part of $\boldsymbol{H}_{\mathrm{V},k}$,

$$\Re\left(\boldsymbol{H}_{\mathrm{V},k}\right) \succeq 0, \tag{2.52}$$

for all frequency samples. The diagonal entries of the sampled $\boldsymbol{H}_{\mathrm{V},k}$ thus must have a positive real part. This requirement is equal to a negative semi-definite imaginary part of the transfer function for a displacement output $\boldsymbol{H}_k$, and a positive semi-definite imaginary part for the transfer function with an acceleration output. Positive frequencies ω are assumed in all cases.

The definiteness of matrices is closely related to the possible phase angles between vectors and their images. For a positive semi-definite mobility (in the sense of a positive real part of the complex power, Equation (2.51)), the angle between $\boldsymbol{W}$ and $\boldsymbol{H}_{\mathrm{V},k}\boldsymbol{W}$

$$\Delta\varphi_{\boldsymbol{W},\boldsymbol{H}_{\mathrm{V}}\boldsymbol{W}} = \arccos\left(\frac{\Re\left(\boldsymbol{W}^H\boldsymbol{H}_{\mathrm{V},k}\boldsymbol{W}\right)}{\|\boldsymbol{W}\|\left\|\boldsymbol{H}_{\mathrm{V},k}\boldsymbol{W}\right\|}\right)$$

must be between $\Delta\varphi_{\boldsymbol{W},\boldsymbol{H}_{\mathrm{V}}\boldsymbol{W}} \in \left[-\frac{\pi}{2},\frac{\pi}{2}\right]$ for any $\boldsymbol{W} \in \mathbb{C}^{n\times 1}$. As a result, valid angles for the complex-valued diagonal entries of the transfer function matrix can be derived

$$\varphi_{\boldsymbol{H}_{ii}} \in \begin{cases} [-\pi,0] & \text{for} \quad \boldsymbol{Y}:W \\ \left[-\frac{\pi}{2},\frac{\pi}{2}\right] & \text{for} \quad \boldsymbol{Y}:V \\ [0,\pi] & \text{for} \quad \boldsymbol{Y}:A. \end{cases} \tag{2.53}$$

For the measurement-based identification of passive subsystems, these passivity indicators provide a quality check for the measured input-to-output behavior in the frequency domain, which is used by Allen et al. [6] and Häußler [121], for example.

The preservation of passivity is relevant not only for experimental methods but a baseline requirement also for numerical methods, which work on the inner representation. Requirements for preservation of passivity can be deduced for such methods, model order reduction, for example. Equation (2.8) states, that real-valued symmetric or complex-valued Hermitian subsystem matrices $\boldsymbol{K}$, $\boldsymbol{M}$, $\boldsymbol{D}$, $\boldsymbol{S}$ are assumed for the inner representation of a second-order system (Equation (2.6)). Thus, the second condition for passivity is fulfilled by definition. The third condition, the requirement of positive power

balances, needs extra consideration. While dropping the subsystem indices $\square_k$ for brevity and with the subsystem's mobility as transfer function

$$\boldsymbol{H}_{\mathrm{V}}(s) = s\boldsymbol{B}^H\left(s^2\boldsymbol{M} + s\boldsymbol{D} + \boldsymbol{K} + i\,\mathrm{sgni}(s)\,\boldsymbol{S}\right)\boldsymbol{B},$$

the third condition can be rewritten as

$$\begin{aligned}
&\boldsymbol{W}^H\boldsymbol{B}^H\Big[s\left(s^2\boldsymbol{M} + s\boldsymbol{D} + \boldsymbol{K} + i\,\mathrm{sgni}(s)\,\boldsymbol{S}\right)^{-1} + \\
&s^*\left(s^{*2}\boldsymbol{M}^H + s^*\boldsymbol{D}^H + \boldsymbol{K}^H + i\,\mathrm{sgni}\left(s^*\right)\boldsymbol{S}^H\right)^{-1}\Big]\boldsymbol{B}\boldsymbol{W} \\
=&\boldsymbol{W}^H\boldsymbol{B}^H\left(s^*\boldsymbol{M}^H + \boldsymbol{D}^H + \frac{\boldsymbol{K}^H + i\,\mathrm{sgni}(s^*)\,\boldsymbol{S}^H}{s^*}\right)^{-1} \\
&\left[s^*\boldsymbol{M}^H + \boldsymbol{D}^H + \frac{\boldsymbol{K}^H + i\,\mathrm{sgni}(s^*)\,\boldsymbol{S}^H}{s^*} + s\boldsymbol{M} + \boldsymbol{D} + \frac{\boldsymbol{K} + i\,\mathrm{sgni}(s)\,\boldsymbol{S}}{s}\right] \\
&\left(s\boldsymbol{M} + \boldsymbol{D} + \frac{\boldsymbol{K} + i\,\mathrm{sgni}(s)\,\boldsymbol{S}}{s}\right)^{-1}\boldsymbol{B}\boldsymbol{W} \geq 0
\end{aligned} \tag{2.54}$$

This reformulation follows the concept of Salimbahrami et al. [215] closely but is changed to a complex-valued formulation and the inclusion of structural damping. Assuming that $\boldsymbol{M}$, $\boldsymbol{K}$, $\boldsymbol{D}$ and $\boldsymbol{S}$ are Hermitian, as stated by Equation (2.8), and substituting

$$\tilde{\boldsymbol{W}} = \left(s^2\boldsymbol{M} + s\boldsymbol{D} + \boldsymbol{K} + i\,\mathrm{sgni}(s)\,\boldsymbol{S}\right)^{-1}\boldsymbol{B}\boldsymbol{W},$$

one arrives at

$$\tilde{\boldsymbol{W}}^H\left[2\sigma\boldsymbol{M} + \boldsymbol{D}^H + \boldsymbol{D} + \frac{2\sigma}{\sigma^2+\omega^2}\boldsymbol{K} + \frac{2|\omega|}{\sigma^2+\omega^2}\boldsymbol{S}\right]\tilde{\boldsymbol{W}} \geq 0. \tag{2.55}$$

Equation (2.55) is fulfilled if the matrix in brackets is positive semi-definite. For symmetric subsystems and $\sigma \geq 0$, this is ensured again if the subsystem matrices are Hermitian and positive semi-definite

$$\begin{aligned}
&\boldsymbol{D}_k + \boldsymbol{D}_k^H \succeq 0 \quad \boldsymbol{M}_k = \boldsymbol{M}_k^H \succeq 0 \quad \boldsymbol{K}_k = \boldsymbol{K}_k^H \succeq 0 \quad \boldsymbol{S}_k = \boldsymbol{S}_k^H \succeq 0 \\
&\boldsymbol{C}_k = \boldsymbol{B}_k^H.
\end{aligned} \tag{2.56}$$

Thus, any numerical method rendering system matrices, which do not fulfill these requirements of Equation (2.56), are not passivity preserving. Note, the signum function in the definition of the structural damping, Equation (2.14), is essential for the concept of this proof. Without

the signum function introduced (Meerbergen [172], for example), the part of the structural damping in Equation (2.55) would become a complex expression, $2i\sigma \mathbf{s}/\sigma^2+\omega^2$. As a result, the semi-definiteness of the matrix in brackets could not be proved as above.

2.4 Chapter Summary

The system theoretic preliminaries for the energetic analysis and synthesis of mechanical networks were introduced. Two elements define the corresponding subsystem coupling problem: firstly, a very general subsystem definition, which only requires the subsystems to provide outputs for inputs at an interface. The second element is the use of linear interface constraint equations, which allow for a free definition of a Neumann-Neumann, Dirichlet-Dirichlet, and Neumann-Dirichlet coupling of the subsystem inputs and outputs. The inner and outer (transfer function) representation in the Laplace domain with zero initial conditions were introduced for the underlying second-order systems. In particular, it was discussed how structural damping, which provides a displacement-proportional damping force and is needed for many industrial models, can be introduced in these representations. Different energetic quantities were discussed, which can be evaluated for subsystems. While this was discussed from a continuum mechanics point of view, corresponding formulas were presented for discretized systems. It was pointed out that mean power provides a measure for the energy flow due to dissipation and can be calculated solely from the subsystem inputs and outputs; thus, it is available for any hybrid network setup. Based on a two-degrees-of-freedom system, it was shown that the accuracy in the phase shift introduced by the system damping can be essential for evaluating power quantities for lightly damped systems, in particular. Thus, one needs to model damping correctly in numerical methods and to ensure phase correct experimental approaches. The concept of subsystem passivity was introduced to provide a baseline quality measure for damping and phase modeling. It was shown that passivity implies non-negative power balances at the subsystem level and thus provides physically meaningful energy flow analyses. Conditions for the inner and the transfer function representation were finally derived to ensure passivity for second-order systems.

CHAPTER 3

FULLY MODULAR RESIDUAL BASED SUBSYSTEM COUPLING FRAMEWORK

Subsystem coupling is mainly used for hybridization in vehicle vibroacoustics so far. However, there is another motivation for subsystem coupling, which is not much considered yet in this domain. It provides modularity, which allows for the massively parallel computation of subsystem solutions in the online phase, thus for a significant computational speedup. For multi-query applications, the latter is further increased by modularity, as single input parameters usually can be linked to single subsystems; this allows for recycling of large parts of the network calculations if only a few parameters are changed. For this, modularity is the central concept for this thesis's numerical framework, and an efficient and truly modular approach to subsystem coupling is presented on the level of algebraic systems of equations. It builds on the very general subsystem definition of Section 2.1.1. As a result, minimum requirements for the coupling definition and the subsystem properties are needed. Singular or black-box subsystems can be coupled. Furthermore, the presented approach provides a unifying framework for classic domain decomposition methods on

the level of algebraic equations and an explicit link between domain decomposition and co-simulation.

3.1 Existing Methods and Limitations

Classic domain decomposition methods are available for such efficient parallelized evaluation of vibroacoustic systems in the online phase. For this purpose, domain decomposition approaches partition the monolithic problem into (a network of) subdomains, followed by a coupling step, thus domain integration. The latter involves the independent and thus parallelizable solution of the subsystems and a final synchronization step solving an interface problem.

For the first time, domain decomposition methods were introduced for overlapping subdomains by Schwarz [222] in the nineteenth century. In recent decades, domain decomposition methods with non-overlapping subdomains gained popularity, in the iterative solution of coupled problems, for example (see Toselli et al. [247] for an overview). The case of non-overlapping subsystems is considered in the following, while the focus is not on the first step of the domain partitioning, thus exactly where and how to split. Focus is on the second step of the subsystem coupling instead. Nevertheless, the way of subsystem coupling, of course, is linked to the possible domain partitioning, as discussed below.

The presented study on subsystem coupling is not restricted to a particular partial differential equation. No reference to underlying continuous operators is given here, but the problem of subsystem coupling is discussed on the level of the algebraic systems of equations, as they arise from discretization methods. To review classic domain decomposition methods, assume a class of problems that render the following algebraic system of equations which define the coupled network of s subsystems

$$\begin{cases} \boldsymbol{A}\boldsymbol{X} = \boldsymbol{F} + \boldsymbol{G} \\ \hat{\boldsymbol{B}}\boldsymbol{X} = 0 \\ \boldsymbol{L}^T\boldsymbol{G} = 0 \end{cases} . \tag{3.1}$$

$\boldsymbol{A}$ is the block diagonal matrix of the single subsystem matrices, $\boldsymbol{A} = \mathrm{diag}\left(\boldsymbol{A}_1, \boldsymbol{A}_2, ..., \boldsymbol{A}_s\right)$, which are typically the dynamic stiffness matrices of the subsystems for structural dynamics. $\boldsymbol{X}$ contains the subsystem primal quantities (states), which may be coupled to other

subsystems or not, $\boldsymbol{F}$ the subsystem dual quantities that arise from external excitation, $\boldsymbol{G}$ the subsystem dual quantities from coupling effects between the different subsystems. In structural mechanics, $\boldsymbol{X}$ classically contains displacements, $\boldsymbol{F}$ and $\boldsymbol{G}$ forces.

$$\boldsymbol{X} = \begin{bmatrix} \boldsymbol{X}_1 \\ \vdots \\ \boldsymbol{X}_s \end{bmatrix} \qquad \boldsymbol{G} = \begin{bmatrix} \boldsymbol{G}_1 \\ \vdots \\ \boldsymbol{G}_s \end{bmatrix} \qquad \boldsymbol{F} = \begin{bmatrix} \boldsymbol{F}_1 \\ \vdots \\ \boldsymbol{F}_s \end{bmatrix}.$$

The coupling between the subsystems is defined firstly by the compatibility of the subsystem primal quantities in the second line of Equation (3.1), which is expressed as a weighted linear combination of the entries of $\boldsymbol{X}$ as defined by the mapping matrix $\hat{\boldsymbol{B}} \in \mathbb{R}^{n_i \times n}$. Secondly, by the equilibrium of dual quantities in the third line of Equation (3.1), which again is a weighted linear mapping, now of the entries of $\boldsymbol{G}$ as given by the mapping matrix $\boldsymbol{L} \in \mathbb{R}^{n_i \times n}$.

Starting from that formulation, two popular approaches for domain decomposition methods can be introduced briefly on the level of the algebraic equations. For a more detailed overview of classic domain decomposition methods, refer to Mathew [168] and Toselli et al. [247]. The basic idea is to transform $\boldsymbol{X}$, respectively $\boldsymbol{G}$ to fulfill either the compatibility or equilibrium by construction. A key ingredient is that the class of networks, which is considered in such methods, renders a matrix operator for compatibility $\hat{\boldsymbol{B}}$, which forms the null space of the one for equilibrium $\boldsymbol{L}$

$$\hat{\boldsymbol{B}} = \text{Null}(\boldsymbol{L}) \qquad \hat{\boldsymbol{B}}^T = \text{Null}\left(\boldsymbol{L}^T\right), \tag{3.2}$$

and vice versa.

Primal Methods In the first approach of primal methods, a transformed vector of primal quantities $\underline{\boldsymbol{X}}$ is introduced, with $\boldsymbol{X} = \boldsymbol{L}\underline{\boldsymbol{X}}$. $\underline{\boldsymbol{X}}$ ensures the compatibility by definition

$$\hat{\boldsymbol{B}}\boldsymbol{X} = \hat{\boldsymbol{B}}\boldsymbol{L}\underline{\boldsymbol{X}} = 0,$$

as Equation (3.2) holds. Simply spoken, two directly coupled states, which consequently must take the same value, are replaced by only one unknown in $\underline{\boldsymbol{X}}$. Thus, Equation (3.1) reduces to

$$\begin{cases} \boldsymbol{A}\,\boldsymbol{L}\underline{\boldsymbol{X}} = \boldsymbol{F} + \boldsymbol{G} \\ \boldsymbol{L}^T\,\boldsymbol{G} = 0 \end{cases} . \tag{3.3}$$

One could call $\underline{\boldsymbol{X}}$ an assembled quantity, which is denoted by $\underline{\square}$ in the following. In the general formulation, $\underline{\boldsymbol{X}}$ can contain both primal quantities, that are coupled to other subsystems, and uncoupled ones. To solve the coupling problem, anyhow, only the coupled interface quantities are required of each subsystem k, thus $\boldsymbol{Y}_k$ and $\boldsymbol{U}_k$. For subsystems in the form Equation (2.9), the uncoupled quantities $\dot{\boldsymbol{X}}_k$ can be condensed by the subsystems' Schur complement form

$$\boldsymbol{A}_{\mathrm{Schur},k}\,\boldsymbol{Y}_k = \boldsymbol{F}_{\mathrm{Schur},k} + \boldsymbol{U}_k, \tag{3.4}$$

which results in

$$\left(\boldsymbol{A}_{\mathrm{YY},k} - \boldsymbol{A}_{\mathrm{YX},k}\boldsymbol{A}_{\mathrm{XX},k}^{-1}\boldsymbol{A}_{\mathrm{XY},k}\right)\boldsymbol{Y}_k = \dot{\boldsymbol{F}}_{\mathrm{ext},k} - \boldsymbol{A}_{\mathrm{YX},k}\boldsymbol{A}_{\mathrm{XX},k}^{-1}\boldsymbol{F}_{\mathrm{ext},k} + \boldsymbol{U}_k. \tag{3.5}$$

Using Schur complement forms, a reduced form of Equation (3.3) is obtained

$$\begin{cases} \boldsymbol{A}_{\mathrm{Schur}}\,\boldsymbol{L}_{\mathrm{Y}}\underline{\boldsymbol{Y}} = \boldsymbol{F}_{\mathrm{Schur}} + \boldsymbol{U} \\ \boldsymbol{L}_{\mathrm{Y}}^T\,\boldsymbol{U} = 0 \end{cases} \tag{3.6}$$

with $\boldsymbol{L}_{\mathrm{Y}}$ being the mapping matrix for the equilibrium of the subsystem inputs, $\boldsymbol{Y} = \boldsymbol{L}_{\mathrm{Y}}\underline{\boldsymbol{Y}}$ and

$$\boldsymbol{Y} = \left[\boldsymbol{Y}_1^T,\, \boldsymbol{Y}_2^T,\, \ldots,\, \boldsymbol{Y}_s^T\right]^T \qquad \boldsymbol{U} = \left[\boldsymbol{U}_1^T,\, \boldsymbol{U}_2^T,\, \ldots,\, \boldsymbol{U}_s^T\right]^T.$$

Eliminating $\boldsymbol{U}$ in the first line of Equation (3.6) by a left hand multiplication with $\boldsymbol{L}_{\mathrm{Y}}^T$, one renders an interface problem to solve for the unknown primal variables, the subsystem outputs, as

$$\boldsymbol{L}_{\mathrm{Y}}^T\boldsymbol{A}_{\mathrm{Schur}}\boldsymbol{L}_{\mathrm{Y}}\underline{\boldsymbol{Y}} = \boldsymbol{L}_{\mathrm{Y}}^T\boldsymbol{F}_{\mathrm{Schur}}. \tag{3.7}$$

Equation (3.7) is also called Schur-complement system, which is equal to the discretized Poincaré-Steklov operator. In structural dynamics,

any FE assembly can be considered a primal assembly; without condensation of non-coupled quantities. More distinct subsystem coupling approaches are provided by primal assemblies, which are combined with non-parametric model order reduction in the approach of Component Mode Synthesis (Craig et al. [58] and Hurty [126]). Again, the internal uncoupled states usually are not condensed in such an approach.

Dual Methods Dual approaches are an alternative. A vector of Lagrange multipliers $\boldsymbol{\lambda}$ can be introduced for the dual quantities resulting from coupling, while $\boldsymbol{G} = -\hat{\boldsymbol{B}}^T \boldsymbol{\lambda}$ holds. This choice of transformation ensures that the equilibrium condition,

$$\boldsymbol{L}^T \boldsymbol{G} = -\boldsymbol{L}^T \hat{\boldsymbol{B}}^T \boldsymbol{\lambda} = 0,$$

is fulfilled by definition for systems where Equation (3.2) holds. Thus, Equation (3.1) reduces to

$$\begin{cases} \boldsymbol{A}\boldsymbol{X} = \boldsymbol{F} - \hat{\boldsymbol{B}}^T \boldsymbol{\lambda} \\ \hat{\boldsymbol{B}}\boldsymbol{X} = 0 \end{cases} . \tag{3.8}$$

Eliminating $\boldsymbol{X}$ in the first line of Equation (3.8), one arrives at an interface problem for determining the dual quantities for coupling by

$$\left(\hat{\boldsymbol{B}}\boldsymbol{A}^{-1}\hat{\boldsymbol{B}}^T\right)\boldsymbol{\lambda} = \hat{\boldsymbol{B}}\boldsymbol{A}^{-1}\boldsymbol{F}. \tag{3.9}$$

Again, it is sufficient to use only coupled states for constructing the interface problem

$$\left(\hat{\boldsymbol{B}}_\mathrm{U}\boldsymbol{A}_\mathrm{Schur}^{-1}\hat{\boldsymbol{B}}_\mathrm{U}^T\right)\boldsymbol{\lambda} = \hat{\boldsymbol{B}}_\mathrm{U}\boldsymbol{A}_\mathrm{Schur}^{-1}\boldsymbol{F}_\mathrm{Schur} \tag{3.10}$$

with $\boldsymbol{U} = -\hat{\boldsymbol{B}}_\mathrm{U}^T\boldsymbol{\lambda}$, $\boldsymbol{A}_\mathrm{Schur}$ and $\boldsymbol{F}_\mathrm{Schur}$ according to Equation (3.4). Dual approaches are used in many different disciplines. They are popular in iterative domain decomposition approaches, like for the finite element tearing and interconnecting (FETI) method (Farhat et al. [76, 77]). Preconditioned iterative algorithms are used in such an approach to solving the interface problem of Equation (3.9). Especially for FETI, many different variants of dual methods were developed through the last decades; see Gosselet et al. [102] for an overview. In structural dynamics, dual approaches are applied through the Frequency-Based

Substructuring (FBS) formulation for Lagrange Multipliers (de Klerk [66]). Just recently, FBS gained popularity in vehicle vibroacoustics in order to include experimentally identified subsystems (Häußler [121] and Van Der Seijs [260], for example).

All the above methods have in common that a homogeneous domain decomposition is required. The latter is defined as an assembly according to Equation (3.1) which incorporates solely subsystems of the same form (for second-order systems in the Laplace domain Equation (2.9) or Equation (2.6)). Subsystem primal variables are coupled to primal variables, dual quantities to dual ones. While this restriction sounds natural from a theory point of view, it imposes unnecessary restrictions in practice, as shown below. In dual methods, the single subsystem matrices $\boldsymbol{A}_k$ need to be invertible, see Equation (3.9); therefore, the systematic incorporation of singular subsystems is challenging. This inclusion requires the construction of coarse problems in FETI methods, which differ between the single FETI formulations. A discussion for incorporating singular subsystems for FBS, which can be achieved by pseudo inverses or merging with other subsystems, is provided in Allen et al. [6].

3.2 Mixed Residual Based Coupling (MRC) Framework

A valuable observation is that co-simulation algorithms also aim at subsystem coupling. Although derived in a different context, there is clearly a strong theoretical connection to domain decomposition methods. Sicklinger [227] presented the Interface-Jacobian-based Co-Simulation Algorithm (IJCSA), a very general formulation for the co-simulation of non-linear problems. It is based on the concept of Newton iterations and includes the definition of a Jacobi matrix for the interface problem.

In the following, a very flexible coupling methodology for linear subsystems is derived on the level of algebraic systems of equations, which is based on a linearization of the IJCSA. This development results in the novel framework of mixed residual coupling (MRC). Two essential ingredients are forming the framework, which are discussed below. Firstly, the idea of subsystem coupling using the ordinary Newton method is presented for the general problem definition of Section 2.1.1. For the latter, the notation of the parametric dependency of quantities is dropped for brevity in the following. This concept is fol-

lowed from the IJCSA framework with modifications for purely linear systems. It is discussed how singular subsystems can be included in such an approach. Secondly, a novel coordinate transformation is introduced, resulting in a mixed input vector, which provides efficiency enhancements and relates classic domain decomposition methods to the MRC framework.

3.2.1 The Concept of Subsystem Coupling with Newton's Method

The general subsystem and network definition of Section 2.1.1 is one enabler for the MRC framework. Basically, the interface constraint equations, Equation (2.2), need to be fulfilled to obtain a coupling between the subsystems of the network. Consequently, the residuum vector

$$\boldsymbol{r} = \left[\boldsymbol{\mathcal{R}}_1, \boldsymbol{\mathcal{R}}_2, \ldots, \boldsymbol{\mathcal{R}}_{n_\mathrm{s}}\right]^T, \tag{3.11}$$

which is formed of the interface constraints

$$\boldsymbol{\mathcal{R}}_j = \mathcal{I}_j\left(\boldsymbol{Y}_k, \boldsymbol{U}_k, k = 1, ..., n_\mathrm{s}\right)$$

must become zero. For the limitation on arbitrary but linear coupling between inputs and outputs (see Equation (2.3)), a matrix notation can be found for the residuum

$$\boldsymbol{r} = \frac{\partial \boldsymbol{\mathcal{I}}}{\partial \boldsymbol{Y}}\boldsymbol{Y} + \frac{\partial \boldsymbol{\mathcal{I}}}{\partial \boldsymbol{U}}\boldsymbol{U}, \tag{3.12}$$

with the matrices $\frac{\partial \boldsymbol{\mathcal{I}}}{\partial \boldsymbol{Y}} \in \mathbb{R}^{n_\mathrm{r} \times n_\mathrm{Y}}$ and $\frac{\partial \boldsymbol{\mathcal{I}}}{\partial \boldsymbol{U}} \in \mathbb{R}^{n_\mathrm{r} \times n_\mathrm{U}}$; here n_Y is the overall number of subsystem outputs in the whole network, n_U is the overall number of subsystem inputs, n_r is the number of the required interface constraint equations to define the network. Due to the assumed subsystems' interface symmetry, there are as many subsystem outputs as inputs in the overall network, and $n_\mathrm{Y} = n_\mathrm{U} = n_\mathrm{r}$ holds for the basic formulation of the method in this section. Symmetric subsystems are not required for the proposed method of MRC, but the MRC framework can be applied to a setting of subsystems with non-symmetric interfaces, too. Solely the notation needs to be adapted slightly in this case.

To visualize the MRC approach of system definition, one can write the coupling problem similar to Equation (3.1) as

$$\begin{cases} \boldsymbol{Y}_k = \mathcal{S}_k\left(\boldsymbol{U}_k\right) & k = 1, ..., n_\mathrm{s} \\ \boldsymbol{r} = \frac{\partial \boldsymbol{\mathcal{I}}}{\partial \boldsymbol{Y}} \boldsymbol{Y} + \frac{\partial \boldsymbol{\mathcal{I}}}{\partial \boldsymbol{U}} \boldsymbol{U} = 0 \end{cases} .$$

Compared to the form of common domain decomposition methods in Section 3.1, this problem definition is more general. It is not restricted to a homogeneous domain decomposition as the linear subsystems can have any form as long as they provide an interface by $\boldsymbol{Y}_k$ and $\boldsymbol{U}_k$. Any interface quantities can be coupled in any linear combination. This flexibility allows handling a non-homogeneous domain decomposition, in which the single subsystem outputs of the network are not necessarily the same physical quantity, respectively the inputs.

An initial guess for the subsystem inputs usually does not result in a zero residuum vector $\boldsymbol{r} = 0$. Following the idea of IJCSA in Sicklinger [227], the ordinary Newton method is chosen to achieve a zero residuum vector and thus a coupled system solution. Starting with an initial guess of ${}^0\boldsymbol{U}$, an input vector $\boldsymbol{U}$ is found iteratively, which ensures $\boldsymbol{r} = 0$. During iteration m, the input vector ${}^m\boldsymbol{U}$ is updated with a corrector ${}^m\Delta\boldsymbol{c}$. Following Newton's method, the latter is determined from the interface problem

$${}^m\boldsymbol{J} \cdot {}^m\Delta\boldsymbol{c} = -{}^m\boldsymbol{r}. \tag{3.13}$$

${}^m\boldsymbol{J}$ is the Jacobian matrix of the residuum (Equation (3.11)) in iteration m. It contains the first derivative of the interface constraint equations with respect to $\boldsymbol{U}$ and can be written as

$$\begin{aligned} {}^m\boldsymbol{J} &= \frac{\partial \boldsymbol{\mathcal{I}}}{\partial \boldsymbol{\mathcal{S}}} \cdot {}^m\frac{\partial \boldsymbol{\mathcal{S}}}{\partial \boldsymbol{U}} + \frac{\partial \boldsymbol{\mathcal{I}}}{\partial \boldsymbol{U}} = \frac{\partial \boldsymbol{\mathcal{I}}}{\partial \boldsymbol{Y}} \cdot {}^m\frac{\partial \boldsymbol{Y}}{\partial \boldsymbol{U}} + \frac{\partial \boldsymbol{\mathcal{I}}}{\partial \boldsymbol{U}} \\ &= \begin{bmatrix} \frac{\partial \mathcal{I}_1}{\partial \boldsymbol{Y}_1} \cdot {}^m\frac{\partial \boldsymbol{Y}_1}{\partial \boldsymbol{U}_1} + \frac{\partial \mathcal{I}_1}{\partial \boldsymbol{U}_1} & \cdots & \frac{\partial \mathcal{I}_1}{\partial \boldsymbol{Y}_{n_\mathrm{s}}} \cdot {}^m\frac{\partial \boldsymbol{Y}_{n_\mathrm{s}}}{\partial \boldsymbol{U}_{n_\mathrm{s}}} + \frac{\partial \mathcal{I}_1}{\partial \boldsymbol{U}_{n_\mathrm{s}}} \\ \vdots & \ddots & \vdots \\ \frac{\partial \mathcal{I}_r}{\partial \boldsymbol{Y}_1} \cdot {}^m\frac{\partial \boldsymbol{Y}_1}{\partial \boldsymbol{U}_1} + \frac{\partial \mathcal{I}_s}{\partial \boldsymbol{U}_1} & \cdots & \frac{\partial \mathcal{I}_r}{\partial \boldsymbol{Y}_{n_\mathrm{s}}} \cdot {}^m\frac{\partial \boldsymbol{Y}_s}{\partial \boldsymbol{U}_{n_\mathrm{s}}} + \frac{\partial \mathcal{I}_{n_\mathrm{s}}}{\partial \boldsymbol{U}_{n_\mathrm{s}}} \end{bmatrix}. \end{aligned} \tag{3.14}$$

The Jacobian includes the same matrices as Equation (3.12); additionally, the derivatives of the subsystem inputs with respect to their

outputs are incorporated, which can formally be written as a block diagonal matrix

$$\frac{\partial \boldsymbol{\mathcal{S}}}{\partial \boldsymbol{U}} = \frac{\partial \boldsymbol{Y}}{\partial \boldsymbol{U}} = \operatorname{diag}\left(\frac{\partial \boldsymbol{Y}_1}{\partial \boldsymbol{U}_1}, \frac{\partial \boldsymbol{Y}_2}{\partial \boldsymbol{U}_2}, \ldots, \frac{\partial \boldsymbol{Y}_{n_\mathrm{s}}}{\partial \boldsymbol{U}_{n_\mathrm{s}}} \right).$$

Equation (3.13) and Equation (3.14) hold for networks incorporating both linear and non-linear subsystems. For the case of coupling solely linear subsystems, as considered here, further simplifications are possible. The necessary steps for coupling linear subsystems are given by Algorithm 3.1. The frames n in Algorithm 3.1 can be frequency samples for a harmonic analysis or time steps for analyses in the time domain.

Algorithm 3.1: Subsystem coupling of linear assemblies by Newton's Method in matrix notation form.

```
    //  select starting values
1   ⁰U_i = 0
    //  loop over frames
2   for n = 0, ... n_f do
        //  solve all subsystems in parallel
3       ⁰Y_i^n = S_i(⁰U_i^n)
        //  initialize assembly operators
4       (∂I/∂U)^n , (∂I/∂Y)^n
        //  evaluate residuum
5       ⁰r^n = (∂I/∂Y)^n ⁰Y^n + (∂I/∂U)^n ⁰U^n
        //  calculate input/output relation of subsystems
6       (∂Y/∂U)^n = Y_i / U_i
        //  assemble the Jacobian
7       J^n = (∂I/∂Y)^n (∂Y/∂U)^n + (∂I/∂U)^n
        //  get corrector
8       J^n Δc^n = −⁰r^n
        //  apply corrector
9       ¹U_i^n = ⁰U_i^n + Δc_i^n
        //  solve all subsystems in parallel
10      ¹Y_i^n = S_i(¹U_i^n)
```

Compared to the classic formulation of the IJCSA by Sicklinger [227], Algorithm 3.1 involves two major simplifications for linear systems: Most prominently, networks of purely linear systems only need one Newton iteration for convergence. Thus the input corrector has to be determined once, and ${}^1\boldsymbol{r} = 0$ is fulfilled by definition.

In addition, the derivatives of the subsystem outputs with respect to the subsystem inputs are determined directly by the subsystem's input-to-output-behavior

$$\frac{\partial \boldsymbol{Y}_k}{\partial \boldsymbol{U}_k} = \frac{\boldsymbol{Y}_k}{\boldsymbol{U}_k}. \tag{3.15}$$

As the required derivatives are provided by the transfer function of the linear system (compare Equation (2.10)), $\partial \boldsymbol{Y}_k / \partial \boldsymbol{U}_k$ could be directly replaced by $\boldsymbol{H}_k$. Anyhow, the notation $\partial \boldsymbol{Y}_k / \partial \boldsymbol{U}_k$ is preferred over $\boldsymbol{H}_k$ in this and the following chapter for consistency with IJCSA.

Note that a frame-independent $\partial \boldsymbol{\mathcal{I}} / \partial \boldsymbol{U}^n = \partial \boldsymbol{\mathcal{I}} / \partial \boldsymbol{U}$ and $\partial \boldsymbol{\mathcal{I}} / \partial \boldsymbol{Y}^n = \partial \boldsymbol{\mathcal{I}} / \partial \boldsymbol{Y}$ can be usually ensured. In this case, the corresponding step four in 3.1 can be extracted from the loop for further simplifications.

Further note that only the subsystem inputs and outputs, coupled to each other, are considered in $\boldsymbol{Y}$ and $\boldsymbol{U}$ in the following. There may be the case that a subsystem would formally provide more inputs and outputs for coupling, as used for the actual network. In such case, one would slightly reformulate Equation (2.6) as

$$\begin{aligned} \boldsymbol{A}_k \boldsymbol{X}_k = \begin{bmatrix} \boldsymbol{B}_{\mathrm{X},k} & \boldsymbol{B}_{\mathrm{U},k} \end{bmatrix} \left(\begin{bmatrix} \boldsymbol{F}_{\mathrm{X},k} \\ \boldsymbol{F}_{\mathrm{U},k} \end{bmatrix} + \begin{bmatrix} \boldsymbol{0} \\ \boldsymbol{U}_k \end{bmatrix} \right), \\ \begin{bmatrix} \tilde{\boldsymbol{Y}}_k \\ \boldsymbol{Y}_k \end{bmatrix} = \begin{bmatrix} \boldsymbol{C}_{\mathrm{X},k} \\ \boldsymbol{C}_{\mathrm{Y},k} \end{bmatrix} \boldsymbol{X}_k \end{aligned}, \tag{3.16}$$

and only that part of the transfer function which is coupled defines the required input-to-output behavior

$$\frac{\partial \mathbf{Y}_k}{\partial \boldsymbol{U}_k} = \boldsymbol{C}_{\mathrm{Y},k} \boldsymbol{A}_k^{-1} \boldsymbol{B}_{\mathrm{U},k}. \tag{3.17}$$

Example 3.1 (Homogeneous Three Subsystem Example)

The concept of Newton iterations for subsystem coupling can be visualized by means of the example in Figure 3.1. Three subsystems define the mechanical network, each forming a spring-mass system. The single subsystems are connected via point interfaces to each other. The example is used throughout the whole chapter to illustrate the different formulations of the presented MRC framework.

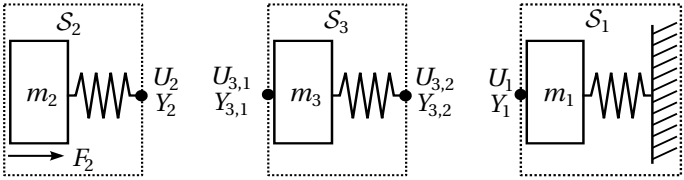

Figure 3.1: Three subsystem example. Each subsystem consists of a coupled mass and spring.

Consider a homogeneous domain decomposition for a first setting. All subsystem outputs are displacements, all inputs are forces (see Table 3.1). All subsystems are of the form of Equation (2.9):

$$
\begin{aligned}
Y_1 &= \mathcal{S}_1(U_1) && (k_1-\omega^2 m_1)Y_1 = U_1 \\
\boldsymbol{Y}_2 &= \mathcal{S}_2(\boldsymbol{U}_2) && \begin{bmatrix} k_2-\omega^2 m_2 & -k_2 \\ -k_2 & k_2 \end{bmatrix} \begin{bmatrix} X_2 \\ Y_2 \end{bmatrix} = \begin{bmatrix} F_2 \\ U_2 \end{bmatrix} \\
\boldsymbol{Y}_3 &= \mathcal{S}_3(\boldsymbol{U}_3) && \begin{bmatrix} k_3-\omega^2 m_3 & -k_3 \\ -k_3 & k_3 \end{bmatrix} \boldsymbol{Y}_3 = \boldsymbol{U}_3.
\end{aligned}
$$

Subsystem $\mathcal{S}$	$\boldsymbol{Y}$	$\boldsymbol{U}$
1	W	F
2	W	F
3	W	F

Table 3.1: Input/output configuration of the subsystems for the homogeneous decomposition of the three subsystem example.

The homogeneous domain decomposition requires solely Dirichlet-Dirichlet and Neumann-Neumann interface constraints to define the coupling. This results in a residuum vector of

$$\boldsymbol{r} = \begin{bmatrix} Y_2 - Y_{3,1} \\ U_2 + U_{3,1} \\ Y_1 - Y_{3,2} \\ U_1 + U_{3,2} \end{bmatrix} = \frac{\partial \boldsymbol{\mathcal{I}}}{\partial \boldsymbol{Y}} \boldsymbol{Y} + \frac{\partial \boldsymbol{\mathcal{I}}}{\partial \boldsymbol{U}} \boldsymbol{U}$$

with

$$\boldsymbol{Y} = \begin{bmatrix} Y_1 \\ Y_2 \\ Y_{3,1} \\ Y_{3,2} \end{bmatrix} \quad \boldsymbol{U} = \begin{bmatrix} U_1 \\ U_2 \\ U_{3,1} \\ U_{3,2} \end{bmatrix}$$

and

$$\frac{\partial \boldsymbol{\mathcal{I}}}{\partial \boldsymbol{Y}} = \begin{bmatrix} 0 & 1 & -1 & 0 \\ 0 & 0 & 0 & 0 \\ 1 & 0 & 0 & -1 \\ 0 & 0 & 0 & 0 \end{bmatrix} \quad \frac{\partial \boldsymbol{\mathcal{I}}}{\partial \boldsymbol{U}} = \begin{bmatrix} 0 & 0 & 0 & 0 \\ 0 & 1 & 1 & 0 \\ 0 & 0 & 0 & 0 \\ 1 & 0 & 0 & 1 \end{bmatrix}.$$

Assume values of $k_1 = k$, $m_1 = 2m$, $k_2 = 5k$, $m_2 = 2m$, $k_3 = 3k$, and $m_3 = m$ for the example throughout the whole chapter. For the initial solution of zero subsystem inputs

$$^0\boldsymbol{U} = \begin{bmatrix} 0 & 0 & 0 & 0 \end{bmatrix}^T \qquad ^0\boldsymbol{Y} = \begin{bmatrix} 0 & -\frac{F_2}{2m\omega^2} & 0 & 0 \end{bmatrix}^T$$

a non-zero residuum is obtained

$$^0\boldsymbol{r} = \begin{bmatrix} -\frac{F_2}{2m\omega^2} & 0 & 0 & 0 \end{bmatrix}^T.$$

The interface Jacobian matrix needs to be formed to construct the interface problem of Equation (3.13). This involves the evaluation of the subsystem derivatives according to Equation (3.15), thus the determination of the transfer functions for the linear subsystems. While this is obtained by an inversion of the subsystem matrix $\boldsymbol{A}_k$ of Equation (2.9) for $\mathcal{S}_1$ and $\mathcal{S}_3$, $\mathcal{S}_2$ has an internal uncoupled state. Consequently, the Schur complement is formed for $\partial Y_2/\partial U_2$ according to Equation (2.12):

$$\frac{\partial Y_2}{\partial U_2} = A^{-1}_{2,\text{Schur}} = \left(5k - \frac{25k^2}{5k - 2\omega^2 m}\right)^{-1} = \frac{2\omega^2 m - 5k}{10km\omega^2}.$$

This results in

$$\frac{\partial \boldsymbol{\mathcal{S}}}{\partial \boldsymbol{U}} = \text{diag}\left(\frac{\partial Y_1}{\partial U_1}, \frac{\partial Y_2}{\partial U_2}, \frac{\partial \boldsymbol{Y}_3}{\partial \boldsymbol{U}_3}\right) = \text{diag}\left(A_1^{-1}, A^{-1}_{2,\text{Schur}}, \boldsymbol{A}_3^{-1}\right)$$
$$= \begin{bmatrix} \frac{1}{k-\omega^2 2m} & 0 & 0 & 0 \\ 0 & \frac{2\omega^2 m - 5k}{10km\omega^2} & 0 & 0 \\ 0 & 0 & \frac{-1}{\omega^2 m} & \frac{-1}{\omega^2 m} \\ 0 & 0 & \frac{-1}{\omega^2 m} & \frac{-\omega^2 m + 3k}{3k\omega^2 m} \end{bmatrix}$$

and the interface Jacobian matrix as

$$\boldsymbol{J} = \frac{\partial \boldsymbol{\mathcal{I}}}{\partial \boldsymbol{\mathcal{S}}} \frac{\partial \boldsymbol{\mathcal{S}}}{\partial \boldsymbol{U}} + \frac{\partial \boldsymbol{\mathcal{I}}}{\partial \boldsymbol{U}} = \begin{bmatrix} 0 & -\frac{-\omega^2 2m + 5k}{10k\omega^2 m} & \frac{1}{\omega^2 m} & \frac{1}{\omega^2 m} \\ 0 & 1 & 1 & 0 \\ \frac{-1}{k-\omega^2 2m} & 0 & \frac{1}{\omega^2 m} & \frac{-\omega^2 m + 3k}{3k\omega^2 m} \\ 1 & 0 & 0 & 1 \end{bmatrix}.$$

The solution of the interface problem of Equation (3.13) provides a corrector for the inputs of

$$\Delta \boldsymbol{c} = t \cdot \begin{bmatrix} 15F_2k^2\left(-2m\omega^2+k\right) \\ -5F_2k\left(2m^2\omega^4-10km\omega^2+3k^2\right) \\ 5F_2k\left(2m^2\omega^4-10km\omega^2+3k^2\right) \\ -15F_2k^2\left(-2m\omega^2+k\right) \end{bmatrix}$$

with $t = \left(-4\,m^3\omega^6+50\,km^2\omega^4-96\,k^2m\omega^2+15\,k^3\right)^{-1}$. Applying the corrector ${}^1\boldsymbol{U} = \Delta \boldsymbol{c}$, the update of the subsystem outputs results in the final coupled solution

$${}^1\boldsymbol{Y} = t \cdot \begin{bmatrix} 15k^2F_2 \\ 10F_2k(-m\omega^2+2k) \\ 10F_2k(-m\omega^2+2k) \\ 15k^2F_2 \end{bmatrix}.$$

■

Using the above concept of subsystem coupling for a homogeneous domain decomposition, the resulting interface problem has some similarities with the one of three-field approaches. Three-field approaches were initially developed to couple subsystems with non-conforming meshes and incorporate another output field (Aminpour et al. [9]), but were also used for mixed assemblies in structural dynamics (Voormeeren et al. [268]). Both approaches use Dirichlet-Dirichlet and Neumann-Neumann constraint equations concurrently to form the interface problem. This is in contrast to the interface problems of the primal approach (Equation (3.7)) or dual approach (Equation (3.7)), for which one of the constraints is fulfilled a-priori by a suitable coordinate transformation.

The duality of the Dirichlet-Dirichlet and Neumann-Neumann residuum equations results in redundancies in the corrector. As illustrated by the example, the single entries of $\Delta \boldsymbol{c}$ differ pairwise only by their sign for a homogeneous domain decomposition and a one-to-one coupling of DOFs. This redundancy leads to an interface problem,

which is of double size compared to a classical domain decomposition. This motivates to combine the concept of Newton iterations with a coordinate transformation similar to classic domain decomposition methods. Introducing a mixed input vector below, this is achieved. But before, it is shown how one can use the framework's flexibility to incorporate singular subsystems.

3.2.2 Handling of Singular Subsystems

The flexibility of the above MRC framework allows to incorporate singular subsystems in a direct and straightforward matter, which is not possible in classic domain decomposition approaches. Singular subsystems arise from floating substructures in structural mechanics or mass-less subsystems in structural dynamics. Mass-less subsystems can be a result of an early prototyping stage or experimental procedures for mount characterization; for an automotive application of the latter refer to Almirón et al. [7]. The proposed procedure for inclusion is illustrated through a massless subsystem, which contains a one-dimensional spring (Figure 3.2).

Figure 3.2: A one-dimensional spring subsystem.

The subsystem is defined in the form of Equation (2.9) as

$$\boldsymbol{Y}_k = \mathcal{S}_k(\boldsymbol{U}_k) \qquad \boldsymbol{A}_k \boldsymbol{Y}_k = \boldsymbol{U}_k \quad \longleftrightarrow \quad \begin{bmatrix} k & -k \\ -k & k \end{bmatrix} \begin{bmatrix} Y_{k,1} \\ Y_{k,2} \end{bmatrix} = \begin{bmatrix} U_{k,1} \\ U_{k,2} \end{bmatrix}, \tag{3.18}$$

thus has forces as inputs and displacements as outputs. The inversion of the subsystem matrix $\boldsymbol{A}_k$ is not possible without using a pseudo-inverse, as $\boldsymbol{A}_k$ is singular. Such problem is also called a pure-Neumann problem (see Bochev et al. [36]).

The flexible framework of the MRC presents a systematic and straightforward possibility to handle such subsystem, given that intrusive access to $\boldsymbol{A}_k$ is provided. No pseudo inverses are needed and the

spring can remain an independent subsystem. To avoid the inversion of the full $\boldsymbol{A}_k$ some of the inputs and outputs can be switched. Corresponding to the rank deficiency z of the subsystem system matrix $\boldsymbol{A}_k$, z inputs and outputs need to be interchanged. For this, a system of the form of Equation (2.9) is rewritten as

$$\begin{bmatrix} \boldsymbol{A}_{\mathrm{LL}} & \boldsymbol{A}_{\mathrm{LY}} \\ \boldsymbol{A}_{\mathrm{YL}} & \boldsymbol{A}_{\mathrm{YY}} \end{bmatrix} \begin{bmatrix} \boldsymbol{L}_{\mathrm{Y}} \\ \boldsymbol{Y}_{\mathrm{sw}} \end{bmatrix} = \begin{bmatrix} \boldsymbol{L}_{\mathrm{U}} \\ \boldsymbol{U}_{\mathrm{sw}} \end{bmatrix}$$

while $\square_{\mathrm{sw}}$ indicates the subset of inputs and outputs, which are switched in the following. $\boldsymbol{L}_{\mathrm{Y}} = \begin{bmatrix} \tilde{\boldsymbol{X}} & \boldsymbol{Y}_{\mathrm{nosw}} \end{bmatrix}^T$ contains the outputs not to be switched and uncoupled internal states. $\boldsymbol{L}_{\mathrm{U}} = \begin{bmatrix} \boldsymbol{0} & \boldsymbol{U}_{\mathrm{nosw}} \end{bmatrix}^T$ is formed accordingly by the subset of inputs $\boldsymbol{U}_{\mathrm{nosw}}$, which are not switched. The index k for indicating subsystem k is omitted for brevity. Switching the inputs and outputs

$$\begin{bmatrix} \boldsymbol{A}_{\mathrm{LL}} & \boldsymbol{A}_{\mathrm{LY}} \\ \boldsymbol{A}_{\mathrm{YL}} & \boldsymbol{A}_{\mathrm{YY}} \end{bmatrix} \begin{bmatrix} \boldsymbol{L}_{\mathrm{Y}} \\ \mathring{\boldsymbol{U}}_{\mathrm{sw}} \end{bmatrix} = \begin{bmatrix} \boldsymbol{L}_{\mathrm{U}} \\ -\mathring{\boldsymbol{Y}}_{\mathrm{sw}} \end{bmatrix}, \tag{3.19}$$

one can rearrange the subsystem as

$$\begin{bmatrix} -\boldsymbol{A}_{\mathrm{LY}}\boldsymbol{A}_{\mathrm{YY}}^{-1}\boldsymbol{A}_{\mathrm{YL}} + \boldsymbol{A}_{\mathrm{LL}} & -\boldsymbol{A}_{\mathrm{LY}}\boldsymbol{A}_{\mathrm{YY}}^{-1} \\ -\boldsymbol{A}_{\mathrm{YY}}^{-1}\boldsymbol{A}_{\mathrm{LY}} & -\boldsymbol{A}_{\mathrm{YY}}^{-1} \end{bmatrix} \begin{bmatrix} \boldsymbol{L}_{\mathrm{Y}} \\ \mathring{\boldsymbol{Y}}_{\mathrm{sw}} \end{bmatrix} = \begin{bmatrix} \boldsymbol{L}_{\mathrm{U}} \\ \mathring{\boldsymbol{U}}_{\mathrm{sw}} \end{bmatrix}.$$

The symmetry of the original subsystem matrix $\boldsymbol{A}$ can be preserved by this scheme of switching, resulting in

$$\frac{\partial \mathbf{Y}_k}{\partial \boldsymbol{U}_k} = \begin{bmatrix} \boldsymbol{A}_{\mathrm{LL}}^{-1} & -\boldsymbol{A}_{\mathrm{LL}}^{-1}\boldsymbol{A}_{\mathrm{LY}} \\ -\boldsymbol{A}_{\mathrm{YL}}\boldsymbol{A}_{\mathrm{LL}}^{-1} & \boldsymbol{A}_{\mathrm{YL}}\boldsymbol{A}_{\mathrm{LL}}^{-1}\boldsymbol{A}_{\mathrm{LY}} - \boldsymbol{A}_{\mathrm{YY}} \end{bmatrix}. \tag{3.20}$$

The basic idea of input-output switching is a concept many engineers are used to as they were taught manual methods for specific kinds of impedance coupling in their undergraduate studies. The MRC framework here provides a systematic framework for such switching concepts in general subsystem coupling applications.

For the spring subsystem, the rank deficiency of $\boldsymbol{A}_k$ is one. Changing one input and output

$$\begin{bmatrix} k & -k \\ -k & k \end{bmatrix} \begin{bmatrix} \mathring{U}_{i,1} \\ Y_{i,2} \end{bmatrix} = \begin{bmatrix} -\mathring{Y}_{i,1} \\ U_{i,2} \end{bmatrix},$$

one arrives at

$$\begin{bmatrix} -\frac{1}{k} & 1 \\ 1 & 0 \end{bmatrix} \begin{bmatrix} \mathring{Y}_{i,1} \\ Y_{i,2} \end{bmatrix} = \begin{bmatrix} \mathring{U}_{i,1} \\ U_{i,2} \end{bmatrix} \tag{3.21}$$

and

$$\frac{\partial \mathbf{Y}_i}{\partial \boldsymbol{U}_i} = \begin{bmatrix} 0 & 1 \\ 1 & \frac{1}{k} \end{bmatrix}. \tag{3.22}$$

A mandatory non-homogeneous domain decomposition is obtained by interchanging inputs and outputs partially. The inputs contain different physical quantities, forces and displacements for the spring example, the outputs accordingly. Thus, the interface constraint equations have to be adapted. Coupling constraint equations, which were of Neumann-Neumann and Dirichlet-Dirichlet type before switching, are changed to Dirichlet-Neumann.

The stiffer the spring is, the worse conditioned Equation (3.22) and Equation (3.22) become. As alternative an even simpler possibility is to switch all subsystem inputs and outputs. Particular caution is required in this case, as the natural boundary conditions of a subsystem are not fulfilled anymore by default. In structural mechanics, for example, a full switch results in a zero displacement boundary condition for a zero (uncoupled) input, but not a zero force. As consequence, either additional residuum equations need to be defined to constrain the uncoupled inputs and outputs, or the system must be in Schur-complement form

$$\boldsymbol{A}_{k,\mathrm{Schur}} \mathring{\boldsymbol{U}}_k = \mathring{\boldsymbol{Y}}_k. \tag{3.23}$$

In this case,

$$\frac{\partial \mathring{\mathbf{Y}}_k}{\partial \mathring{\boldsymbol{U}}_k} = \boldsymbol{A}_{k,\mathrm{Schur}}. \tag{3.24}$$

The subsystem's $\boldsymbol{A}_{k,\text{Schur}}$ is not modified by switching all inputs and outputs. However, all interface constraint equations involving the switched subsystem need to be adapted.

Example 3.2 (Non-Homogeneous Three Subsystem Example)

Continuing the example of Section 3.2.1, interface switching to include singular subsystems in the MRC framework is demonstrated. Assume that the three subsystem network should be enabled for a zero mass of subsystem $\mathcal{S}_3$.

In a first setting, the approach of a full switch of the interface of subsystem $\mathcal{S}_3$ is discussed for this and $\mathcal{S}_3$ takes the form of

$$\boldsymbol{Y}_3 = \mathcal{S}_3(\boldsymbol{U}_3) \qquad \begin{bmatrix} k_3 - \omega^2 m_3 & -k_3 \\ -k_3 & k_3 \end{bmatrix} \boldsymbol{U}_3 = \boldsymbol{Y}_3.$$

Subsystem $\mathcal{S}$	$\boldsymbol{Y}$	$\boldsymbol{U}$
1	W	F
2	W	F
3	F	W

Table 3.2: Input/output configuration of the subsystems for the non-homogeneous decomposition of the three subsystem example. A full switch of $\mathcal{S}_3$ is considered.

As a result, all inputs of subsystem $\mathcal{S}_3$ are displacements, all outputs forces. A non-homogeneous domain decomposition is obtained according to Table 3.2. As all interface constraint equations involve the interface quantities of $\mathcal{S}_3$, the whole coupling definition needs to be changed to Dirichlet-Neumann type equations

$$\boldsymbol{r} = \begin{bmatrix} Y_2 - \mathring{U}_{3,1} \\ U_2 + \mathring{Y}_{3,1} \\ Y_1 - \mathring{U}_{3,2} \\ U_1 + \mathring{Y}_{3,2} \end{bmatrix},$$

which results in

$$\frac{\partial \boldsymbol{\mathcal{I}}}{\partial \boldsymbol{Y}} = \begin{bmatrix} 0 & 1 & 0 & 0 \\ 0 & 0 & 1 & 0 \\ 1 & 0 & 0 & 0 \\ 0 & 0 & 0 & 1 \end{bmatrix} \qquad \frac{\partial \boldsymbol{\mathcal{I}}}{\partial \boldsymbol{U}} = \begin{bmatrix} 0 & 0 & -1 & 0 \\ 0 & 1 & 0 & 0 \\ 0 & 0 & 0 & -1 \\ 1 & 0 & 0 & 0 \end{bmatrix}.$$

With

$$\begin{aligned} \frac{\partial \boldsymbol{\mathcal{S}}}{\partial \boldsymbol{U}} &= \operatorname{diag}\left(A_1^{-1}, A_{2,\text{Schur}}^{-1}, \boldsymbol{A}_3\right) \\ &= \begin{bmatrix} \frac{1}{k-\omega^2 2m} & 0 & 0 & 0 \\ 0 & \frac{2\omega^2 m-5k}{10km\omega^2} & 0 & 0 \\ 0 & 0 & 3k-\omega^2 m & -3k \\ 0 & 0 & -3k & 3k \end{bmatrix}, \end{aligned}$$

the interface Jacobian now becomes

$$\boldsymbol{J} = \frac{\partial \boldsymbol{\mathcal{I}}}{\partial \boldsymbol{\mathcal{S}}} \frac{\partial \boldsymbol{\mathcal{S}}}{\partial \boldsymbol{U}} + \frac{\partial \boldsymbol{\mathcal{I}}}{\partial \boldsymbol{U}} = \begin{bmatrix} 0 & \frac{2m\omega^2-5k}{10km\omega^2} & -1 & 0 \\ 0 & 1 & -\omega^2+3k & -3k \\ \frac{1}{-2m\omega^2+k} & 0 & 0 & -1 \\ 1 & 0 & -3k & 3k \end{bmatrix}.$$

The values of ${}^0\boldsymbol{U}$, ${}^0\boldsymbol{Y}$ and ${}^0\boldsymbol{r}$ do not change compared to Section 3.2.1. Solving the corresponding interface problem, the following corrector is obtained

$$\Delta\tilde{\boldsymbol{c}} = t \cdot \begin{bmatrix} 15F_2k^2\left(k-2m\omega^2\right) \\ -5kF_2\left(2m^2\omega^4-10km\omega^2+3k^2\right) \\ 10F_2k\left(2k-m\omega^2\right) \\ 15F_2k^2 \end{bmatrix}.$$

Updating the subsystems for the inputs ${}^1\boldsymbol{U} = \Delta\boldsymbol{c}$, the coupled subsystem outputs are

$${}^1\boldsymbol{Y} = t \cdot \begin{bmatrix} 15k^2F_2 \\ 10kF_2\left(-m\omega^2+2k\right) \\ 5kF_2\left(2m^2\omega^4-10km\omega^2+3k^2\right) \\ -15F_2k^2\left(k-2m\omega^2\right) \end{bmatrix}.$$

As alternative strategy for input switching, a partial switch is already sufficient and the first output and input of subsystem $\mathcal{S}_3$ are switched in a second setting. The modified subsystem takes the form of

$$\boldsymbol{Y}_3 = \mathcal{S}_3(\boldsymbol{U}_3) \quad \begin{bmatrix} k_3-\omega^2 m_3 & -k_3 \\ -k_3 & k_3 \end{bmatrix} \begin{bmatrix} U_{3,1} \\ Y_{3,2} \end{bmatrix} = \begin{bmatrix} -Y_{3,1} \\ U_{3,2} \end{bmatrix}$$

$$\rightarrow \begin{bmatrix} -\frac{1}{3k-\omega^2 m} & \frac{3k}{3k-\omega^2 m} \\ \frac{3k}{3k-\omega^2 m} & 3k-\frac{9k^2}{3k-\omega^2 m} \end{bmatrix} \begin{bmatrix} Y_{3,1} \\ Y_{3,2} \end{bmatrix} = \begin{bmatrix} U_{3,1} \\ U_{3,2} \end{bmatrix}.$$

The input $\mathring{U}_{3,1}$ is now a displacement, while $U_{3,2}$ is still a force. In contrast to the first setting, only the first two constraint equations involving $\mathring{U}_{3,1}$ and $\mathring{Y}_{3,1}$ have to be changed to Dirichlet-Neumann type. The remaining two interface equations are still of Dirichlet-Dirichlet and Neumann-Neumann type:

$$\boldsymbol{r} = \begin{bmatrix} Y_2 - \mathring{U}_{3,1} \\ U_2 - \mathring{Y}_{3,1} \\ Y_1 - Y_{3,2} \\ U_1 + U_{3,2} \end{bmatrix}.$$

With

$$\frac{\partial \boldsymbol{\mathcal{I}}}{\partial \boldsymbol{Y}} = \begin{bmatrix} 0 & 1 & 0 & 0 \\ 0 & 0 & -1 & 0 \\ 1 & 0 & 0 & -1 \\ 0 & 0 & 0 & 0 \end{bmatrix} \qquad \frac{\partial \boldsymbol{\mathcal{I}}}{\partial \boldsymbol{U}} = \begin{bmatrix} 0 & 0 & -1 & 0 \\ 0 & 1 & 0 & 0 \\ 0 & 0 & 0 & 0 \\ 1 & 0 & 0 & 1 \end{bmatrix}$$

and

$$\frac{\partial \boldsymbol{\mathcal{S}}}{\partial \boldsymbol{U}} = \operatorname{diag}\left(A_1^{-1}, A_{2,\text{Schur}}^{-1}, \boldsymbol{A}_{3,\text{mod}}^{-1}\right) = \begin{bmatrix} \frac{1}{k-\omega^2 2m} & 0 & 0 & 0 \\ 0 & \frac{2\omega^2 m-5k}{10km\omega^2} & 0 & 0 \\ 0 & 0 & \omega^2 m & 1 \\ 0 & 0 & 1 & \frac{1}{3k} \end{bmatrix},$$

the Jacobian results in

$$\boldsymbol{J} = \frac{\partial \boldsymbol{\mathcal{I}}}{\partial \boldsymbol{\mathcal{S}}}\frac{\partial \boldsymbol{\mathcal{S}}}{\partial \boldsymbol{U}} + \frac{\partial \boldsymbol{\mathcal{I}}}{\partial \boldsymbol{U}} = \begin{bmatrix} 0 & \frac{2m\omega^2-5k}{10km\omega^2} & -1 & 0 \\ 0 & 1 & -m\omega^2 & -1 \\ \frac{1}{-2m\omega^2+k} & 0 & -1 & -\frac{1}{3k} \\ 1 & 0 & 0 & 1 \end{bmatrix}.$$

Again, ${}^0\boldsymbol{U}$, ${}^0\boldsymbol{Y}$ and ${}^0\boldsymbol{r}$ do not change compared to Section 3.2.1, which results in the converged inputs

$${}^1\boldsymbol{U} = \Delta\tilde{\boldsymbol{c}} = t \cdot \begin{bmatrix} 15F_2k^2\left(k-2m\omega^2\right) \\ -5kF_2\left(2m^2\omega^4-10km\omega^2+3k^2\right) \\ 10F_2k\left(2k-m\omega^2\right) \\ -15F_2k^2\left(k-2m\omega^2\right) \end{bmatrix}$$

and outputs

$${}^1\boldsymbol{Y} = t \cdot \begin{bmatrix} 15k^2F_2 \\ 10kF_2\left(-m\omega^2+2k\right) \\ 5kF_2\left(2m^2\omega^4-10km\omega^2+3k^2\right) \\ 15k^2F_2 \end{bmatrix}.$$

For both settings, a zero mass $m_3 = 0$ is now possible, resulting in $\mathcal{S}_3$ being a simple spring subsystem.

3.2.3 Efficiency Enhancements by a Mixed Input Vector

As discussed above, the duality of Dirichlet-Dirichlet and Neumann-Neumann residuum equations in the definition of the interface problem leads to a redundancy in the input corrector. Considering both, Dirichlet-Dirichlet and Neumann-Neumann constraints explicitly in the interface problem may be beneficial for iterative solutions of the interface problem in Equation (3.13). However, this redundancy is not required in a direct solution of Equation (3.13) for linear subsystems. Motivated by this, a novel coordinate transformation is introduced as second key ingredient of the MRC framework, resulting in a mixed input vector that avoids redundancy. Similar to a classic dual domain decomposition method, the Neumann-Neumann constraint equations should be fulfilled implicitly by that coordinate transformation for efficiency, while preserving the full flexibility, which was achieved above.

The approach is illustrated in a first step with a set of minimum assumptions on the problem definition. Shorter formula are presented for a subclass of coupling problems in a second step. Without the introduction of further assumptions on the interface definition, $\boldsymbol{r}$ and $\boldsymbol{U}$ is formally resorted such that

$$\frac{\partial \hat{\boldsymbol{\mathcal{I}}}}{\partial \hat{\boldsymbol{U}}} = \begin{bmatrix} \frac{\partial_{\mathrm{Dx}} \boldsymbol{\mathcal{I}}}{\partial_{\mathrm{DN}} \boldsymbol{U}} & \mathbf{0} \\ \mathbf{0} & \frac{\partial_{\mathrm{NN}} \boldsymbol{\mathcal{I}}}{\partial_{\mathrm{NN}} \boldsymbol{U}} \end{bmatrix} \tag{3.25}$$

with

$$\boldsymbol{\mathcal{I}} = \boldsymbol{Z}_{\mathcal{I}} \hat{\boldsymbol{\mathcal{I}}} = \boldsymbol{Z}_{\mathcal{I}} \begin{bmatrix} {}_{\mathrm{Dx}}\boldsymbol{\mathcal{I}} \\ {}_{\mathrm{NN}}\boldsymbol{\mathcal{I}} \end{bmatrix} \qquad \boldsymbol{U} = \boldsymbol{Z}_{\mathrm{U}} \hat{\boldsymbol{U}} = \boldsymbol{Z}_{\mathrm{U}} \begin{bmatrix} {}_{\mathrm{DN}}\boldsymbol{U} \\ {}_{\mathrm{NN}}\boldsymbol{U} \end{bmatrix}.$$

$\boldsymbol{Z}_{\mathrm{U}}$ and $\boldsymbol{Z}_{\mathcal{I}}$ are boolean mappers to the initial ordering of interface constraint equations and inputs. ${}_{\mathrm{Dx}}\boldsymbol{\mathcal{I}}$ are the constraint equations, which are of Dirichlet-Neumann or Dirichlet-Dirichlet type; ${}_{\mathrm{Dx}}\boldsymbol{U}$ are the inputs which are involved in these interface constraints. ${}_{\mathrm{NN}}\boldsymbol{\mathcal{I}}$ are the Neumann-Neumann constraint equations and ${}_{\mathrm{NN}}\boldsymbol{U}$ the inputs, which are constrained solely by these constraint equations. Once the null space of $\partial_{\mathrm{NN}}\boldsymbol{\mathcal{I}}/\partial_{\mathrm{NN}}\boldsymbol{U}$ is found, the following coordinate transformation can be defined

$${}_{\mathrm{NN}}\boldsymbol{U} = \mathrm{Null}\left(\frac{\partial_{\mathrm{NN}}\boldsymbol{\mathcal{I}}}{\partial_{\mathrm{NN}}\boldsymbol{U}}\right) {}_{\mathrm{NN}}\underline{\boldsymbol{U}}. \tag{3.26}$$

While ${}_{\mathrm{NN}}\boldsymbol{U}$ contains pairwise correlated inputs for the example of a one-to-one coupling, which solely differ by their sign, the *assembled* version ${}_{\mathrm{NN}}\underline{\boldsymbol{U}}$ contains only one inputs for these pairs. This concept is equal to the introduction of Lagrange-Multipliers in dual domain decomposition methods. Using the assembled inputs provided by the transformation of Equation (3.26), one can show that the corresponding Neumann-Neumann constraint equations result in a zero residuum by definition

$$ {}_{\mathrm{NN}}\boldsymbol{r} = \frac{\partial\, {}_{\mathrm{NN}}\boldsymbol{\mathcal{I}}}{\partial\, {}_{\mathrm{NN}}\boldsymbol{U}}\, {}_{\mathrm{NN}}\boldsymbol{U} = \frac{\partial\, {}_{\mathrm{NN}}\boldsymbol{\mathcal{I}}}{\partial\, {}_{\mathrm{NN}}\boldsymbol{U}} \mathrm{Null}\left(\frac{\partial\, {}_{\mathrm{NN}}\boldsymbol{\mathcal{I}}}{\partial\, {}_{\mathrm{NN}}\boldsymbol{U}} \right) {}_{\mathrm{NN}}\underline{\boldsymbol{U}} = \boldsymbol{0} \cdot {}_{\mathrm{NN}}\underline{\boldsymbol{U}}. \quad (3.27) $$

By the introduction of the transformation matrix

$$ \boldsymbol{V} = \boldsymbol{Z}_{\boldsymbol{U}} \begin{bmatrix} {}_{\mathrm{DN}}\boldsymbol{T} & \boldsymbol{0} \\ \boldsymbol{0} & \mathrm{Null}\left(\frac{\partial\, {}_{\mathrm{NN}}\boldsymbol{\mathcal{I}}}{\partial\, {}_{\mathrm{NN}}\boldsymbol{U}} \right) \end{bmatrix}, \quad (3.28) $$

the full input vector can be transformed

$$ \boldsymbol{U} = \boldsymbol{V}\, \tilde{\boldsymbol{U}}. $$

$\tilde{\boldsymbol{U}}$ is called the mixed input vector, accounting for the fact that it contains unique *assembled* inputs ${}_{\mathrm{NN}}\underline{\boldsymbol{U}}$ as well as *non-assembled* inputs ${}_{\mathrm{DN}}\tilde{\boldsymbol{U}}$

$$ \tilde{\boldsymbol{U}} = \begin{bmatrix} {}_{\mathrm{DN}}\tilde{\boldsymbol{U}} \\ {}_{\mathrm{NN}}\underline{\boldsymbol{U}} \end{bmatrix}. $$

${}_{\mathrm{DN}}\boldsymbol{T}$ which is contained in Equation (3.28) is an arbitrary linear transformation matrix of the inputs, which are constrained by Dirichlet-Neumann interface conditions ${}_{\mathrm{DN}}\boldsymbol{U} = {}_{\mathrm{DN}}\boldsymbol{T} \cdot {}_{\mathrm{DN}}\tilde{\boldsymbol{U}}$. The matrix ${}_{\mathrm{DN}}\boldsymbol{T}$ may be chosen as the identity matrix, alternatively any resorting or sign switching of the inputs can be realized.

In line with Equation (3.27), only the Dirichlet-Neumann respectively Dirichlet-Dirichlet residuum equations ${}_{\mathrm{Dx}}\boldsymbol{r}$ need to be evaluated for a mixed input vector

$$\begin{aligned}\hat{\boldsymbol{r}} &= \frac{\partial \hat{\boldsymbol{\mathcal{I}}}}{\partial \boldsymbol{Y}}\boldsymbol{Y} + \frac{\partial \hat{\boldsymbol{\mathcal{I}}}}{\partial \hat{\boldsymbol{U}}}\hat{\boldsymbol{U}} \\ &= \left[\frac{\partial_{\mathrm{Dx}}\boldsymbol{\mathcal{I}}}{\partial \boldsymbol{Y}}\boldsymbol{0}\right]\boldsymbol{Y} + \begin{bmatrix} \frac{\partial_{\mathrm{Dx}}\boldsymbol{\mathcal{I}}}{\partial_{\mathrm{DN}}\boldsymbol{U}} & \boldsymbol{0} \\ \boldsymbol{0} & \frac{\partial_{\mathrm{NN}}\boldsymbol{\mathcal{I}}}{\partial_{\mathrm{NN}}\boldsymbol{U}} \end{bmatrix} \begin{bmatrix} {}_{\mathrm{DN}}\boldsymbol{T} & \boldsymbol{0} \\ \boldsymbol{0} & \mathrm{Null}\left(\frac{\partial_{\mathrm{NN}}\boldsymbol{\mathcal{I}}}{\partial_{\mathrm{NN}}\boldsymbol{U}}\right) \end{bmatrix} \tilde{\boldsymbol{U}} \\ &= \begin{bmatrix} \frac{\partial_{\mathrm{Dx}}\boldsymbol{\mathcal{I}}}{\partial \boldsymbol{Y}} \\ \boldsymbol{0} \end{bmatrix}\boldsymbol{Y} + \begin{bmatrix} \frac{\partial_{\mathrm{Dx}}\boldsymbol{\mathcal{I}}}{\partial_{\mathrm{DN}}\boldsymbol{U}}\,{}_{\mathrm{DN}}\boldsymbol{T} & \boldsymbol{0} \\ \boldsymbol{0} & \boldsymbol{0} \end{bmatrix} \tilde{\boldsymbol{U}} = \begin{bmatrix} {}_{\mathrm{Dx}}\boldsymbol{r} \\ \boldsymbol{0} \end{bmatrix},\end{aligned}$$

which leads to an interface problem of reduced size

$$\tilde{\boldsymbol{J}}\,\Delta\tilde{\boldsymbol{c}} = -{}^{0}_{\mathrm{Dx}}\boldsymbol{r}. \tag{3.29}$$

$\Delta\tilde{\boldsymbol{c}}$ provides the corrector for the mixed input vector $\tilde{\boldsymbol{U}}$, while the subsystem inputs are obtained by

$${}^{1}\boldsymbol{U} = {}^{0}\boldsymbol{U} + \boldsymbol{V}\,\Delta\tilde{\boldsymbol{c}}.$$

The Jacobian matrix of the correspondingly reduced interface problem is given by

$$\tilde{\boldsymbol{J}} = \frac{\partial_{\mathrm{Dx}}\boldsymbol{\mathcal{I}}}{\partial \mathbf{Y}}\frac{\partial \mathbf{Y}}{\partial \tilde{\boldsymbol{U}}} + \frac{\partial_{\mathrm{Dx}}\boldsymbol{\mathcal{I}}}{\partial \tilde{\boldsymbol{U}}} = \left(\frac{\partial_{\mathrm{Dx}}\boldsymbol{\mathcal{I}}}{\partial \mathbf{Y}}\frac{\partial \mathbf{Y}}{\partial \boldsymbol{U}} + \frac{\partial_{\mathrm{Dx}}\boldsymbol{\mathcal{I}}}{\partial \boldsymbol{U}}\right)\boldsymbol{V}. \tag{3.30}$$

The approach to introduce a mixed input vector can be simplified for some additional assumptions on the interface definition; a set of assumptions corresponding to Equation (3.2) stated for classic domain decomposition methods. Assume that the Dirichlet-Dirichlet interface constraint equations are formulated in a way that they span the required null space

$$\left(\frac{\partial_{\mathrm{DD}}\boldsymbol{\mathcal{I}}}{\partial_{\mathrm{DD}}\boldsymbol{Y}}\right)^{T} = \mathrm{Null}\left(\frac{\partial_{\mathrm{NN}}\boldsymbol{\mathcal{I}}}{\partial_{\mathrm{NN}}\boldsymbol{U}}\right), \tag{3.31}$$

while the inputs and outputs are collocated

$$\boldsymbol{Y} = \boldsymbol{Z}_{\mathrm{U}}\hat{\boldsymbol{Y}} = \boldsymbol{Z}_{\mathrm{U}}\begin{bmatrix} {}_{\mathrm{DN}}\boldsymbol{Y} \\ {}_{\mathrm{DD}}\boldsymbol{Y} \end{bmatrix}. \tag{3.32}$$

Collocation means that the outputs ${}_{\mathrm{DD}}\boldsymbol{Y}$, which are constrained by Dirichlet-Dirichlet interface conditions, must be at same position in $\boldsymbol{Y}$ as the inputs ${}_{\mathrm{NN}}\boldsymbol{U}$ in $\boldsymbol{U}$. This condition is fulfilled for network definitions of mechanical subsystems in the same coordinate system, for example. Further assume, that $\partial_{\mathrm{DN}}\boldsymbol{\mathcal{I}}/\partial_{\mathrm{DN}}\boldsymbol{Y}$ is of full rank, so the transformation matrix is directly given by

$$\boldsymbol{V} = \left(\frac{\partial_{\mathrm{Dx}}\boldsymbol{\mathcal{I}}}{\partial \boldsymbol{Y}} \right)^T . \tag{3.33}$$

Then, the interface Jacobian matrix of Equation (3.30) can be rewritten as

$$\tilde{\boldsymbol{J}} = \frac{\partial_{\mathrm{Dx}}\boldsymbol{\mathcal{I}}}{\partial \mathbf{Y}} \frac{\partial \mathbf{Y}}{\partial \boldsymbol{U}} \left(\frac{\partial_{\mathrm{Dx}}\boldsymbol{\mathcal{I}}}{\partial \boldsymbol{Y}} \right)^T + \frac{\partial_{\mathrm{Dx}}\boldsymbol{\mathcal{I}}}{\partial \boldsymbol{U}} \left(\frac{\partial_{\mathrm{Dx}}\boldsymbol{\mathcal{I}}}{\partial \boldsymbol{Y}} \right)^T . \tag{3.34}$$

The resulting calculation steps for this subcase of MRC are summarized in Algorithm 3.2 on the next page.

Analyzing Equation (3.34), the coordinate transformation can result in a symmetric interface Jacobian matrix. The first summand renders a symmetric matrix for a symmetric $\partial \mathbf{Y}/\partial \boldsymbol{U}$. The second summand is symmetric for

$$\frac{\partial_{\mathrm{DN}}\boldsymbol{\mathcal{I}}}{\partial \boldsymbol{U}} \left(\frac{\partial_{\mathrm{DN}}\boldsymbol{\mathcal{I}}}{\partial \boldsymbol{Y}} \right)^T = \frac{\partial_{\mathrm{DN}}\boldsymbol{\mathcal{I}}}{\partial \boldsymbol{Y}} \left(\frac{\partial_{\mathrm{DN}}\boldsymbol{\mathcal{I}}}{\partial \boldsymbol{U}} \right)^T . \tag{3.35}$$

Thus, defining the Dirichlet-Neumann interface constraints correspondingly, symmetry is ensured and $\boldsymbol{J}$ is self-adjoint. This is beneficial for the calculation of sensitivities in particular, as shown in Section 4.1.

Example 3.3 (Non-Homogeneous Three Subsystem Example)

Again, the concept of coordinate transformation can be visualized for the three subsystem example. The mixed input vector is introduced for the second setting of switched inputs as defined in Section 3.2. In this setting, one Neumann-Neumann constraint equation is contained

$$\mathcal{I}_4 = U_1 + U_{3,2},$$

Algorithm 3.2: Mixed input vector based subsystem coupling of linear networks, which fulfill Equation (3.31) and Equation (3.32).

// select starting values

1 ${}^{0}\tilde{\boldsymbol{U}}_i^0 = {}^{\text{ini}}\tilde{\boldsymbol{U}}_i$

// loop over frames

2 **for** $n = 0, \ldots n_\text{f}$ **do**

// initialize assembly operators

3 $\frac{\partial_{\text{Dx}}\boldsymbol{\mathcal{I}}^n}{\partial \boldsymbol{U}}$, $\frac{\partial_{\text{Dx}}\boldsymbol{\mathcal{I}}^n}{\partial \boldsymbol{Y}}$

// choose initial input vector

4 ${}^{0}\boldsymbol{U}^n = \left(\frac{\partial_{\text{Dx}}\boldsymbol{\mathcal{I}}^n}{\partial \boldsymbol{Y}}\right)^T \cdot {}^{0}\tilde{\boldsymbol{U}}^n$

// solve all subsystems in parallel

5 ${}^{0}\boldsymbol{Y}_i^n = \mathcal{S}_i\left({}^{0}\boldsymbol{U}_i^n\right)$

// evaluate residuum (without Neumann-Neumann conditions)

6 ${}^{0}_{\text{Dx}}\boldsymbol{r}^n = \frac{\partial_{\text{Dx}}\boldsymbol{\mathcal{I}}^n}{\partial \boldsymbol{Y}} {}^{0}\boldsymbol{Y}^n + \frac{\partial_{\text{Dx}}\boldsymbol{\mathcal{I}}^n}{\partial \boldsymbol{U}} {}^{0}\boldsymbol{U}^n$

// calculate input/output relation of subsystems

7 $\frac{\partial \boldsymbol{Y}}{\partial \boldsymbol{U}}^n$

// assemble the Jacobian

8 $\tilde{\boldsymbol{J}}^n = \frac{\partial_{\text{Dx}}\boldsymbol{\mathcal{I}}^n}{\partial \boldsymbol{Y}} \frac{\partial \boldsymbol{Y}}{\partial \boldsymbol{U}}^n \left(\frac{\partial_{\text{Dx}}\boldsymbol{\mathcal{I}}^n}{\partial \boldsymbol{Y}}\right)^T + \frac{\partial_{\text{Dx}}\boldsymbol{\mathcal{I}}^n}{\partial \boldsymbol{U}} \left(\frac{\partial_{\text{Dx}}\boldsymbol{\mathcal{I}}^n}{\partial \boldsymbol{Y}}\right)^T$

// get corrector

9 $\tilde{\boldsymbol{J}}^n \Delta\tilde{\boldsymbol{c}}^n = -{}^{0}_{\text{Dx}}\boldsymbol{r}^n$

// apply and transform corrector

10 ${}^{1}\boldsymbol{U}_i^n = \left(\frac{\partial_{\text{Dx}}\boldsymbol{\mathcal{I}}^n}{\partial \boldsymbol{Y}}\right)^T \left({}^{0}\tilde{\boldsymbol{U}}_i^n + \Delta\tilde{\boldsymbol{c}}_i^n\right)$

// solve all subsystems in parallel

11 ${}^{1}\boldsymbol{Y}_i^n = \mathcal{S}_i\left({}^{1}\boldsymbol{U}_i^n\right)$

which can be removed from the interface problem by coordinate transformation. Fulfilling that interface constraint a-priori by construction, only ${}_{\text{Dx}}\boldsymbol{r}$ must be evaluated

$$ {}_{\text{Dx}}\boldsymbol{r} = \begin{bmatrix} Y_2 - \mathring{U}_{3,1} \\ U_2 - \mathring{Y}_{3,1} \\ Y_1 - Y_{3,2} \end{bmatrix} = \frac{\partial_{\text{Dx}}\boldsymbol{\mathcal{I}}}{\partial \boldsymbol{Y}} \boldsymbol{Y} + \frac{\partial_{\text{Dx}}\boldsymbol{\mathcal{I}}}{\partial \boldsymbol{U}} \boldsymbol{U} $$

with

$$\frac{\partial_{\mathrm{Dx}}\boldsymbol{\mathcal{I}}}{\partial \boldsymbol{Y}} = \begin{bmatrix} 0 & 1 & 0 & 0 \\ 0 & 0 & -1 & 0 \\ 1 & 0 & 0 & -1 \end{bmatrix} \qquad \frac{\partial_{\mathrm{Dx}}\boldsymbol{\mathcal{I}}}{\partial \boldsymbol{U}} = \begin{bmatrix} 0 & 0 & -1 & 0 \\ 0 & 1 & 0 & 0 \\ 0 & 0 & 0 & 0 \end{bmatrix}.$$

The assumptions in Equation (3.31) and Equation (3.32) hold for the three subsystem example and $\partial_{\mathrm{DN}}\boldsymbol{\mathcal{I}}/\partial_{\mathrm{DN}}\boldsymbol{Y}$ is of full rank. Thus, the transformation matrix is given by

$$\boldsymbol{V} = \left(\frac{\partial_{\mathrm{Dx}}\boldsymbol{\mathcal{I}}}{\partial \boldsymbol{Y}}\right)^T.$$

As $\partial \boldsymbol{\mathcal{S}}/\partial \boldsymbol{U}$ is symmetric (see Section 3.2) and Equation (3.35) holds, a symmetric interface Jacobian matrix is obtained by

$$\begin{aligned} \tilde{\boldsymbol{J}} &= \left(\frac{\partial_{\mathrm{Dx}}\boldsymbol{\mathcal{I}}}{\partial \boldsymbol{\mathcal{S}}}\frac{\partial \boldsymbol{\mathcal{S}}}{\partial \boldsymbol{U}} + \frac{\partial_{\mathrm{Dx}}\boldsymbol{\mathcal{I}}}{\partial \boldsymbol{U}}\right)\left(\frac{\partial_{\mathrm{Dx}}\boldsymbol{\mathcal{I}}}{\partial \boldsymbol{Y}}\right)^T \\ &= \begin{bmatrix} \frac{2m\omega^2-5k}{10km\omega^2} & 1 & 0 \\ 1 & m\omega^2 & 1 \\ 0 & 1 & \frac{1}{-2m\omega^2+k}+\frac{1}{3k} \end{bmatrix}. \end{aligned}$$

For the initial mixed input and (non-mixed) output vector

$${}^0\tilde{\boldsymbol{U}} = \begin{bmatrix} 0 & 0 & 0 \end{bmatrix}^T \qquad {}^0\boldsymbol{Y} = \begin{bmatrix} 0 & -\frac{F_2}{2m\omega^2} & 0 & 0 \end{bmatrix}^T,$$

the Dirichlet residuum results in

$${}^0_{\mathrm{Dx}}\boldsymbol{r} = \begin{bmatrix} -\frac{F_2}{2m\omega^2} & 0 & 0 \end{bmatrix}^T.$$

Solving Equation (3.29) for the corrector for a zero ${}^1_{\mathrm{Dx}}\boldsymbol{r}$, one obtains

$$\Delta\tilde{\boldsymbol{c}} = t \cdot \begin{bmatrix} -5kF_2\left(2m^2\omega^4 - 10km\omega^2 + 3k^2\right) \\ -10kF_2\left(2k - m\omega^2\right) \\ 15k^2F_2\left(k - 2m\omega^2\right) \end{bmatrix}.$$

After the application of the transformation ${}^1\boldsymbol{U} = \Delta\boldsymbol{c} = (\partial_{\mathrm{Dx}}\mathcal{I}/\partial\boldsymbol{Y})^T\,\Delta\tilde{\boldsymbol{c}}$, the same subsystem inputs are provided as in Section 3.2.

■

3.2.4 Dual Domain Decomposition as a Special Case of MRC Framework

The introduction of a mixed input vector does not only allow for smaller interface problems. It also enables one to relate the MRC framework to classic domain decomposition methods of Section 3.1. Thus, it provides an explicit link between domain decomposition and co-simulation approaches. A homogeneous domain decomposition has to be assumed for this, all outputs and inputs of the subsystems are the same physical quantity. For such a setting, it is straightforward to show the MRC framework's connection to dual domain decomposition on the level of the algebraic system of equations.

Further assume the general form of Equation (3.16) for all subsystems. Depending on the publication, the classic dual domain decomposition interface problem may be constructed from the inversion of the full subsystem matrices $\boldsymbol{A}_k$ according to Equation (3.9) or may exclude non-coupled states by using the inverted subsystems' Schur-complements as in Equation (3.10). The more general formulation found in literature is based on Equation (3.9); thus, the MRC formulas are modified in the following for the overall subsystem state vector $\boldsymbol{X}$ and $\boldsymbol{G}$ as defined in Equation (3.1). For a corresponding mapping, $\boldsymbol{C}_{\mathrm{Y},k}$ relates the subsystem outputs to the overall subsystem state variable vector as stated by Equation (3.16), $\boldsymbol{Y}_k = \boldsymbol{C}_{\mathrm{Y},k}\boldsymbol{X}_k$. The subsystems are again assumed to be symmetric in their inputs and outputs. Thus, $\boldsymbol{C}_{\mathrm{Y},k} = \boldsymbol{B}_{\mathrm{U},k}^T$ holds for the case of real-valued $\boldsymbol{C}_{\mathrm{Y},k}, \boldsymbol{B}_{\mathrm{U},k} \in \mathbb{R}$, which is assumed in this section to be in line with the definition of classic methods in Section 3.1. Accordingly, one can construct a vector of the coupled subsystem inputs in the size of the system states by $\boldsymbol{U}_k = \boldsymbol{C}_{\mathrm{Y},k}^{T+}\boldsymbol{G}_k$. $\square^+$ indicates a pseudo inverse in the sense that $\boldsymbol{C}_{\mathrm{Y},k}^{T+}\boldsymbol{C}_{\mathrm{Y},k}^{T} = \boldsymbol{I}$ holds.

Using that mapping, the residuum Equation (3.12) is rewritten as

$$\boldsymbol{r} = \frac{\partial\mathcal{I}}{\partial\boldsymbol{Y}}\boldsymbol{Y} + \frac{\partial\mathcal{I}}{\partial\boldsymbol{U}}\boldsymbol{U} = \frac{\partial\mathcal{I}}{\partial\boldsymbol{Y}}\boldsymbol{C}\boldsymbol{X} + \frac{\partial\mathcal{I}}{\partial\boldsymbol{U}}\boldsymbol{C}^{T+}\boldsymbol{G} \tag{3.36}$$

with the block diagonal matrix

$$\boldsymbol{C} = \mathrm{diag}\left(\boldsymbol{C}_{\mathrm{Y},1}, \boldsymbol{C}_{\mathrm{Y},2}, \ldots \boldsymbol{C}_{\mathrm{Y},n_\mathrm{s}}\right).$$

As a result of the homogeneous domain decomposition, all outputs are constrained by Dirichlet-Dirichlet interface constraint equations, all inputs by Neumann-Neumann ones

$$\boldsymbol{Y} = {}_{\mathrm{DD}}\boldsymbol{Y} \qquad \boldsymbol{U} = {}_{\mathrm{NN}}\boldsymbol{U}.$$

The indices for $\boldsymbol{Y}$ and $\boldsymbol{U}$ indicating the type of coupling are omitted for brevity in the following. Resorting the residuum vector according to Equation (3.25), the absence of Dirichlet-Neumann constraints is evident

$$\hat{\boldsymbol{r}} = \frac{\partial \hat{\boldsymbol{\mathcal{I}}}}{\partial \boldsymbol{Y}}\boldsymbol{Y} + \frac{\partial \hat{\boldsymbol{\mathcal{I}}}}{\partial \boldsymbol{U}}\boldsymbol{U} = \begin{bmatrix} \frac{\partial_{\mathrm{DD}}\boldsymbol{\mathcal{I}}}{\partial \boldsymbol{Y}}\boldsymbol{C} \\ \boldsymbol{0} \end{bmatrix} \boldsymbol{X} + \begin{bmatrix} \boldsymbol{0} \\ \frac{\partial_{\mathrm{NN}}\boldsymbol{\mathcal{I}}}{\partial \boldsymbol{U}}\boldsymbol{C}^{T+} \end{bmatrix} \boldsymbol{G} = \begin{bmatrix} {}_{\mathrm{DD}}\boldsymbol{r} \\ {}_{\mathrm{NN}}\boldsymbol{r} \end{bmatrix}. \tag{3.37}$$

Following Section 3.2.3, a mixed input vector is introduced, while the assumptions in Equation (3.31) and Equation (3.32) hold for the corresponding class of considered problems. $\partial_{\mathrm{DN}}\boldsymbol{\mathcal{I}}/\partial_{\mathrm{DN}}\boldsymbol{Y}$ is of zero dimension as the problem does not involve any Dirichlet-Neumann constraint equations. As a result, the coordinate transformation is given by

$$\boldsymbol{G} = \boldsymbol{C}^T\boldsymbol{U} = \boldsymbol{C}^T\boldsymbol{V}\tilde{\boldsymbol{U}} = \boldsymbol{C}^T\left(\frac{\partial_{\mathrm{DD}}\boldsymbol{\mathcal{I}}}{\partial \boldsymbol{Y}}\right)^T \underline{\boldsymbol{U}}. \tag{3.38}$$

The mixed input vector contains solely *assembled* quantities $\tilde{\boldsymbol{U}} = \underline{\boldsymbol{U}}$. As the Neumann-Neumann residuum equations are zero by construction for this transformation

$${}_{\mathrm{NN}}\boldsymbol{r} = \frac{\partial_{\mathrm{NN}}\boldsymbol{\mathcal{I}}}{\partial \boldsymbol{U}}\boldsymbol{C}^{T+}\boldsymbol{G} = \frac{\partial_{\mathrm{NN}}\boldsymbol{\mathcal{I}}}{\partial \boldsymbol{U}}\boldsymbol{C}^{T+}\boldsymbol{C}^T\left(\frac{\partial_{\mathrm{DD}}\boldsymbol{\mathcal{I}}}{\partial \boldsymbol{Y}}\right)^T \underline{\boldsymbol{U}} = 0, \tag{3.39}$$

the residuum is determined purely by Dirichlet-Dirichlet constraint equations

$${}_{\mathrm{Dx}}\boldsymbol{r} = {}_{\mathrm{DD}}\boldsymbol{r} = \frac{\partial_{\mathrm{DD}}\boldsymbol{\mathcal{I}}}{\partial \boldsymbol{Y}}\boldsymbol{C}\boldsymbol{X}, \tag{3.40}$$

resulting in

$$\tilde{\boldsymbol{J}}\Delta\tilde{\boldsymbol{c}} = -{}_{\mathrm{DD}}\boldsymbol{r}. \tag{3.41}$$

Considering a block version of Equation (3.17)

$$\frac{\partial \boldsymbol{Y}}{\partial \boldsymbol{U}} = \boldsymbol{C}\boldsymbol{A}^{-1}\boldsymbol{C}^T,$$

the Jacobian matrix is given by

$$\begin{aligned}\tilde{\boldsymbol{J}} &= \left(\frac{\partial_{\mathrm{DD}}\boldsymbol{\mathcal{I}}}{\partial \boldsymbol{Y}}\frac{\partial \boldsymbol{Y}}{\partial \boldsymbol{U}} + \frac{\partial_{\mathrm{DD}}\boldsymbol{\mathcal{I}}}{\partial \boldsymbol{U}}\right)\left(\frac{\partial_{\mathrm{DD}}\boldsymbol{\mathcal{I}}}{\partial \boldsymbol{Y}}\right)^T \\ &= \left(\frac{\partial_{\mathrm{DD}}\boldsymbol{\mathcal{I}}}{\partial \boldsymbol{Y}}\boldsymbol{C}\boldsymbol{A}^{-1}\boldsymbol{C}^T + \boldsymbol{0}\right)\left(\frac{\partial_{\mathrm{DD}}\boldsymbol{\mathcal{I}}}{\partial \boldsymbol{Y}}\right)^T.\end{aligned} \tag{3.42}$$

$\boldsymbol{A}^{-1}$ is the inverse of the block diagonal matrix of the subsystem matrices. In the case that the subsystems can be represented in the form of Equation (3.6), $\boldsymbol{C}\boldsymbol{A}^{-1}\boldsymbol{C}^T$ is equal to the block diagonal matrix of inverse subsystem Schur complements.

It can be shown in a straightforward manner, that the classic dual domain decomposition renders the same interface problem as given by Equation (3.41). Therefore, the dual domain decomposition interface problem of Equation (3.9) is derived once again from Equation (3.8). Inserting the relation Equation (3.38) and replacing the compatibility equation by the equivalent Dirichlet-Dirichlet residuum equations Equation (3.40),

$$\begin{cases} \boldsymbol{A}\boldsymbol{X} = \boldsymbol{F} + \left(\frac{\partial_{\mathrm{DD}}\boldsymbol{\mathcal{I}}}{\partial \boldsymbol{Y}}\boldsymbol{C}\right)^T \underline{\boldsymbol{U}} \\ {}_{\mathrm{DD}}\boldsymbol{r} = \frac{\partial_{\mathrm{DD}}\boldsymbol{\mathcal{I}}}{\partial \boldsymbol{Y}}\boldsymbol{C}\boldsymbol{X} = 0 \end{cases} \tag{3.43}$$

is obtained. The interface problem of the dual domain decomposition is obtained by eliminating $\boldsymbol{X}$ in the first line of Equation (3.43)

$$\left(\frac{\partial_{\mathrm{DD}}\boldsymbol{\mathcal{I}}}{\partial \boldsymbol{Y}}\boldsymbol{C}\boldsymbol{A}^{-1}\boldsymbol{C}^T\left(\frac{\partial_{\mathrm{DD}}\boldsymbol{\mathcal{I}}}{\partial \boldsymbol{Y}}\right)^T\right)\underline{\boldsymbol{U}} = \frac{\partial_{\mathrm{DD}}\boldsymbol{\mathcal{I}}}{\partial \boldsymbol{Y}}\boldsymbol{C}\boldsymbol{A}^{-1}\boldsymbol{F}. \tag{3.44}$$

Equation (3.44) is equal to Equation (3.41). The right hand side of Equation (3.44) can be interpreted as the non-zero Dirichlet-Dirichlet residuum

$$\begin{aligned}{}_{\mathrm{DD}}\boldsymbol{r} &= \frac{\partial_{\mathrm{DD}}\boldsymbol{\mathcal{I}}}{\partial \boldsymbol{Y}}\boldsymbol{C}\boldsymbol{X} = \frac{\partial_{\mathrm{DD}}\boldsymbol{\mathcal{I}}}{\partial \boldsymbol{Y}}\boldsymbol{C}\boldsymbol{A}^{-1}\left(\boldsymbol{F} + \boldsymbol{C}^T\left(\frac{\partial_{\mathrm{DD}}\boldsymbol{\mathcal{I}}}{\partial \boldsymbol{Y}}\right)^T {}^0\underline{\boldsymbol{U}}\right) \\ &= \frac{\partial_{\mathrm{DD}}\boldsymbol{\mathcal{I}}}{\partial \boldsymbol{Y}}\boldsymbol{C}\boldsymbol{A}^{-1}\boldsymbol{F}\end{aligned}$$

with ${}^0\underline{\boldsymbol{U}} = \boldsymbol{0}$. The expression in brackets on the left hand side of Equation (3.44) is the reduced interface Jacobian, see Equation (3.42). Furthermore, $\underline{\boldsymbol{U}} = {}^0\underline{\boldsymbol{U}} + \Delta\tilde{\boldsymbol{c}} = \Delta\tilde{\boldsymbol{c}}$ holds.

On an algebraic level, therefore, the dual domain decomposition can be interpreted as a special case of the MRC framework for a homogeneous domain decomposition.

Comparing the interface problem of Equation (3.44) to the classic notation for dual approaches, Equation (3.8), one can relate the quantities used in classic approaches to the ones of the MRC explicitly. The vector of assembled inputs used in the MRC equals the Lagrange multipliers in dual approaches, $\underline{\boldsymbol{U}} = -\boldsymbol{\lambda}$. The matrix $\hat{\boldsymbol{B}}$, which is used in classic approaches, is equal to

$$\hat{\boldsymbol{B}} = \frac{\partial_{\mathrm{DD}}\boldsymbol{\mathcal{I}}}{\partial\,\boldsymbol{Y}}\boldsymbol{C}.$$

3.2.5 The Primal Assembly as a Special Case of MRC Framework

In principle, the flexibility of the MRC framework allows to express even primal assemblies, like an FE assembly, as a special case of the MRC framework. To emphasize the generality of the MRC framework, it is briefly discussed how MRC can render the interface problem Equation (3.7).

Consider all subsystems are of the form of Equation (3.6) and their non-coupled states were condensed by calculating their respective Schur-complement form, Equation (3.4). Consequently, all inputs and outputs of all subsystems can be switched according to Equation (3.23) without violating the natural boundary conditions of the underlying physical problem. Again, a homogeneous domain decomposition is required, resulting in purely Dirichlet-Dirichlet and Neumann-Neumann constraint equations. Full input switching results in a setting in which the former inputs are constrained by Dirichlet-Dirichlet constraints, the former outputs by Neumann-Neumann ones. Again, a mixed input vector is introduced by

$$\mathring{\boldsymbol{U}} = \boldsymbol{V}\,\tilde{\boldsymbol{U}} = \left(\frac{\partial_{\mathrm{DD}}\boldsymbol{\mathcal{I}}}{\partial\,\mathring{\boldsymbol{Y}}}\right)^T \underline{\boldsymbol{U}}.$$

In structural mechanics, $\underline{\boldsymbol{U}}$ now may represent *assembled* displacements. Assembling the reduced interface problem, only ${}_{\mathrm{DD}}\boldsymbol{\mathcal{I}}$ con-

straints need to be considered in Equation (3.29) due to the homogeneous domain decomposition. Using Equation (3.24) to calculate $\partial \mathring{\boldsymbol{Y}} / \partial \mathring{\boldsymbol{u}}$ for the Jacobian matrix, one obtains a reduced interface problem of

$$\frac{\partial_{\mathrm{DD}} \boldsymbol{\mathcal{I}}}{\partial \mathring{\boldsymbol{Y}}} \boldsymbol{A}_{\mathrm{Schur}} \left(\frac{\partial_{\mathrm{DD}} \boldsymbol{\mathcal{I}}}{\partial \mathring{\boldsymbol{Y}}} \right)^T \Delta \tilde{\boldsymbol{c}} = - \frac{\partial_{\mathrm{DD}} \boldsymbol{\mathcal{I}}}{\partial \mathring{\boldsymbol{Y}}} \left(\boldsymbol{0} - \boldsymbol{F}_{\mathrm{Schur}} \right).$$

This interface problem is equal to Equation (3.7) as $\boldsymbol{L}_{\mathrm{C}}^T = \partial_{\mathrm{DD}} \boldsymbol{\mathcal{I}} / \partial \mathring{\boldsymbol{Y}}$ holds. Thus, one could render the same interface problem with the MRC framework as for a primal assembly. Note that the possibility to formulate the same interface equations mainly originates from the general coupling problem definition. This flexibility allows to modify all subsystems, thus to redefine the primal interface problem in a dual manner. Anyhow, the required switch of inputs and outputs requires intrusive changes in all subsystem definitions; this results in a less practical relevance of this setting.

3.3 Chapter Summary

For the first time, the mixed residual coupling framework was proposed for coupling linear, non-overlapping subsystems. Two essential components characterize the method.

Firstly, it is based on a very general problem definition. Subsystems can have any form, and any linear interface constraints can be defined; thus, non-homogeneous domain decompositions are possible. Based on a linearized version of the Interface-Jacobian-based Co-Simulation Algorithm, the coupling interface problem is constructed and solved using the ordinary Newton method. The latter provides a corrector for the subsystem inputs to ensure zero interface constraints.

Secondly, a mixed input vector was introduced by a coordinate transformation as a novelty, reducing the interface problem's size. The mixed residual coupling framework combines both efficiency and increased flexibility for coupling compared to classic domain decomposition methods. Dirichlet-Neumann interface constraints can be defined, and very general subsystem definitions are possible. This flexibility allows for truly hybrid assemblies and straightforward inclusion of Neumann-only subsystems by input switching. Two approaches for such switching were discussed.

The coordinate transformation for the mixed input vector does not only improve efficiency. It also provides the relation between the framework and common domain decomposition methods. Dual-domain decomposition methods were shown to be a special case of the proposed framework. At the same time, an explicit link between Newton-based co-simulation and classic domain decomposition is provided. This link provides a starting point to incorporate approaches from co-simulation for including non-linear subsystems, for example.

The method was derived on a purely algebraic level. Thus, it is not limited to a specific physical domain or particular discretization method. Anyhow, examples were provided context-driven for harmonic analysis in structural mechanics.

CHAPTER 4

MODULAR CALCULATION OF SENSITIVITIES FOR COUPLED PROBLEMS

The mechanical network evaluation in the online phase often incorporates the calculation of gradients for optimization or uncertainty propagation applications. Thus, besides an efficient subsystem coupling approach, the gradient calculation in the network must also be computationally cheap. In the following, the modular approach of the MRC framework of Chapter 3 is extended to a new sensitivity calculation scheme for this purpose, which retains modularity.

4.1 Modular Calculation of Gradients for Coupled Problems

4.1.1 Basics for Monolithic Problems

The approaches to sensitivity calculation are briefly discussed for a monolithic problem as a basis in a first step. For this, Section 4.1.1 is adapted from Martins et al. [167].

A real-valued objective is defined in optimization or uncertainty applications

$$\boldsymbol{q}\left(\boldsymbol{p}, \boldsymbol{X}(\boldsymbol{p})\right), \tag{4.1}$$

which depends on the variable design parameters $\boldsymbol{p}$ and the system state $\boldsymbol{X}$. Sensitivities with respect to a parameter p_j contained in $\boldsymbol{p}$

$$\frac{\mathrm{d}\boldsymbol{q}}{\mathrm{d}p_j} = \frac{\partial \boldsymbol{q}}{\partial p_j} + \frac{\partial \boldsymbol{q}}{\partial \boldsymbol{X}} \frac{\mathrm{d}\boldsymbol{X}}{\mathrm{d}p_j} \tag{4.2}$$

need to be provided for such applications. The evaluation of Equation (4.2) requires the calculation of the total derivative $\mathrm{d}\boldsymbol{X}/\mathrm{d}p_j$. Besides the objective in Equation (4.1), a second equation is available for this, which is given by the residuum of the problem's governing equations

$$\boldsymbol{r}_{\mathrm{ge}}\left(\boldsymbol{p}, \boldsymbol{X}(\boldsymbol{p})\right) = 0. \tag{4.3}$$

As Equation (4.3) is fulfilled for any parameter vector $\boldsymbol{p}$, the total derivative of Equation (4.3) with respect to a design parameter p_j is calculated as

$$\frac{\mathrm{d}\boldsymbol{r}_{\mathrm{ge}}}{\mathrm{d}p_j} = \frac{\partial \boldsymbol{r}_{\mathrm{ge}}}{\partial p_j} + \frac{\partial \boldsymbol{r}_{\mathrm{ge}}}{\partial \boldsymbol{X}} \frac{\mathrm{d}\boldsymbol{X}}{\mathrm{d}p_j} = 0. \tag{4.4}$$

The total derivative of the system states $\mathrm{d}\boldsymbol{X}/\mathrm{d}p_j$ is obtained from this expression by

$$\frac{\mathrm{d}\boldsymbol{X}}{\mathrm{d}p_j} = \left(\frac{\partial \boldsymbol{r}_{\mathrm{ge}}}{\partial \boldsymbol{X}}\right)^{-1} \left(-\frac{\partial \boldsymbol{r}_{\mathrm{ge}}}{\partial p_j}\right). \tag{4.5}$$

Inserting Equation (4.5) in Equation (4.2)

$$\frac{\mathrm{d}\boldsymbol{q}}{\mathrm{d}p_j} = \frac{\partial \boldsymbol{q}}{\partial p_j} - \underbrace{\frac{\partial \boldsymbol{q}}{\partial \boldsymbol{X}} \overbrace{\left(\frac{\partial \boldsymbol{r}_{\mathrm{ge}}}{\partial \boldsymbol{X}}\right)^{-1}}^{-\frac{\mathrm{d}\boldsymbol{X}}{\mathrm{d}p_j}}}_{-\boldsymbol{\psi}^T} \frac{\partial \boldsymbol{r}_{\mathrm{ge}}}{\partial p_j}, \tag{4.6}$$

it can be illustrated, that there are two ways of calculating sensitivities. The first one is given by the *direct approach*. In a direct approach, one calculates $\mathrm{d}\boldsymbol{X}/\mathrm{d}p_j$ directly from Equation (4.5) by solving a linear

system of equations for the right hand side $\partial \boldsymbol{r}_{\mathrm{ge}}/\partial p_j$. Thus, a system solution is required for each design parameter. As an alternative, the *adjoint approach* is provided by reformulating Equation (4.6) as

$$\frac{\mathrm{d}\boldsymbol{q}}{\mathrm{d}p_j} = \frac{\partial \boldsymbol{q}}{\partial p_j} + \boldsymbol{\Psi}^T \frac{\partial \boldsymbol{r}_{\mathrm{ge}}}{\partial p_j}. \tag{4.7}$$

$\boldsymbol{\Psi}$ is the adjoint variable and is given by

$$\left(\frac{\partial \boldsymbol{r}_{\mathrm{ge}}}{\partial \boldsymbol{X}}\right)^T \boldsymbol{\Psi} = -\left(\frac{\partial \boldsymbol{q}}{\partial \boldsymbol{X}}\right)^T. \tag{4.8}$$

With this reformulation, Equation (4.8) needs to be solved for the right hand side $(\partial \boldsymbol{q}/\partial \boldsymbol{x})^T$ instead of Equation (4.5). Consequently, one system solution is required per objective. The adjoint approach is preferred over the direct one in settings with more design parameters than objectives and vice versa.

4.1.2 Sensitivities for Coupled Problems

These approaches can be adapted systematically for coupled problems, as demonstrated in the following. A framework for efficient sensitivity analysis of coupled problems is derived based on the above formula. Again, the two available equations for sensitivity calculations, the objective function and the residuum of the problem's governing equations, are the starting point for deriving the formula. These equations now do not depend on the system states, but on the subsystem interface quantities, thus finally on the inputs.

The reformulation of Equation (4.1) with respect to subsystem interface quantities results in

$$\boldsymbol{q}\left(\boldsymbol{p}, \mathcal{S}_k\left(\boldsymbol{U}_k(\boldsymbol{p}), \boldsymbol{p}\right), \boldsymbol{U}_k(\boldsymbol{p}), k = 1...n_{\mathrm{s}}\right), \tag{4.9}$$

and for Equation (4.3) correspondingly in

$$\boldsymbol{r}_{\mathrm{ge}}\left(\boldsymbol{p}, \mathcal{S}_k\left(\boldsymbol{U}_k(\boldsymbol{p}), \boldsymbol{p}\right), \boldsymbol{U}_k(\boldsymbol{p}), k = 1...n_{\mathrm{s}}\right) = 0. \tag{4.10}$$

In contrast to the notation in Section 2.1.1, the parametric dependency of the single subsystem quantities is expressed more explicitly in the above formula in order to support the following derivations: also the inputs $\boldsymbol{U}(\boldsymbol{p})$ are parameter-dependent, as they result from the network interaction, which changes if the parameters change.

Formulation for Non-Transformed Input Vector

For the derivation of the sensitivity formula, assume no coordinate transformation of $\boldsymbol{U}$ and thus no mixed input vector for the first. The total derivative of the objective function, Equation (4.9), has the form of

$$\begin{aligned}\frac{\mathrm{d}\boldsymbol{q}}{\mathrm{d}p_j} &= \frac{\partial \boldsymbol{q}}{\partial p_j} + \frac{\partial \boldsymbol{q}}{\partial \boldsymbol{\mathcal{S}}}\left(\frac{\partial \boldsymbol{\mathcal{S}}}{\partial p_j} + \frac{\mathrm{d}\boldsymbol{\mathcal{S}}}{\mathrm{d}\boldsymbol{U}}\frac{\partial \boldsymbol{U}}{\partial p_j}\right) + \frac{\partial \boldsymbol{q}}{\partial \boldsymbol{U}}\frac{\mathrm{d}\boldsymbol{U}}{\mathrm{d}p_j} \\ &= \left(\frac{\partial \boldsymbol{q}}{\partial p_j} + \frac{\partial \boldsymbol{q}}{\partial \boldsymbol{\mathcal{S}}}\frac{\partial \boldsymbol{\mathcal{S}}}{\partial p_j}\right) + \left(\frac{\partial \boldsymbol{q}}{\partial \boldsymbol{\mathcal{S}}}\frac{\partial \boldsymbol{\mathcal{S}}}{\partial \boldsymbol{U}} + \frac{\partial \boldsymbol{q}}{\partial \boldsymbol{U}}\right)\frac{\mathrm{d}\boldsymbol{U}}{\mathrm{d}p_j}.\end{aligned} \tag{4.11}$$

The residuum equation of the governing equations, Equation (4.10), is again required for the calculation of $\mathrm{d}\boldsymbol{U}/\mathrm{d}p$. This is provided by the converged interface residuum for subsystem coupling

$$\boldsymbol{r}_{\mathrm{ge}} = {}^{1}\boldsymbol{r} = 0. \tag{4.12}$$

According to Equation (4.10), the derivative of Equation (4.12) is calculated as

$$\frac{\mathrm{d}\boldsymbol{r}_{\mathrm{ge}}}{\mathrm{d}p_j} = \frac{\partial \boldsymbol{\mathcal{I}}}{\partial p_j} + \frac{\partial \boldsymbol{\mathcal{I}}}{\partial \boldsymbol{\mathcal{S}}}\left(\frac{\partial \boldsymbol{\mathcal{S}}}{\partial p_j} + \frac{\mathrm{d}\boldsymbol{\mathcal{S}}}{\mathrm{d}\boldsymbol{U}}\frac{\partial \boldsymbol{U}}{\partial p_j}\right) + \frac{\partial \boldsymbol{\mathcal{I}}}{\partial \boldsymbol{U}}\frac{\mathrm{d}\boldsymbol{U}}{\mathrm{d}p_j} = 0, \tag{4.13}$$

and is rearranged for the total derivative of the subsystem inputs with respect to the design parameter as

$$\frac{\mathrm{d}\boldsymbol{U}}{\mathrm{d}p_j} = -\left(\frac{\partial \boldsymbol{\mathcal{I}}}{\partial \boldsymbol{\mathcal{S}}}\frac{\partial \boldsymbol{\mathcal{S}}}{\partial \boldsymbol{U}} + \frac{\partial \boldsymbol{\mathcal{I}}}{\partial \boldsymbol{U}}\right)^{-1}\left(\frac{\partial \boldsymbol{\mathcal{I}}}{\partial \boldsymbol{\mathcal{S}}}\frac{\partial \boldsymbol{\mathcal{S}}}{\partial p_j} + \frac{\partial \boldsymbol{\mathcal{I}}}{\partial p_j}\right). \tag{4.14}$$

Comparing the inverted matrix to Equation (3.14), it turns out, that the expression is the MRC interface Jacobian matrix, thus Equation (4.14) can be reformulated as

$$\frac{\mathrm{d}\boldsymbol{U}}{\mathrm{d}p_j} = -\boldsymbol{J}^{-1}\left(\frac{\partial \boldsymbol{\mathcal{I}}}{\partial \boldsymbol{\mathcal{S}}}\frac{\partial \boldsymbol{\mathcal{S}}}{\partial p_j} + \frac{\partial \boldsymbol{\mathcal{I}}}{\partial p_j}\right). \tag{4.15}$$

Inserting Equation (4.15) into Equation (4.11), the total derivative of the objective is finally obtained by

$$\frac{\mathrm{d}\boldsymbol{q}}{\mathrm{d}p} = \left(\frac{\partial \boldsymbol{q}}{\partial \boldsymbol{\mathcal{S}}}\frac{\partial \boldsymbol{\mathcal{S}}}{\partial p_j} + \frac{\partial \boldsymbol{q}}{\partial p_j}\right) - \left(\frac{\partial \boldsymbol{q}}{\partial \boldsymbol{\mathcal{S}}}\frac{\partial \boldsymbol{\mathcal{S}}}{\partial \boldsymbol{U}} + \frac{\partial \boldsymbol{q}}{\partial \boldsymbol{U}}\right)\boldsymbol{J}^{-1}\left(\frac{\partial \boldsymbol{\mathcal{I}}}{\partial \boldsymbol{\mathcal{S}}}\frac{\partial \boldsymbol{\mathcal{S}}}{\partial p_j} + \frac{\partial \boldsymbol{\mathcal{I}}}{\partial p_j}\right).$$

(4.16)

Although Equation (4.16) involves several matrices, only a few of them have to be computed in an expensive procedure in addition to the solution of the interface problem itself in Chapter 3: the matrices $\partial \mathcal{I}/\partial \mathcal{S}$ and $\partial \mathcal{S}/\partial \mathcal{U}$ are already used during the subsystem coupling, as well as the factorization of the interface Jacobian $\mathcal{J}^{-1}$. $\partial \mathcal{Q}/\partial \mathcal{S}$, $\partial \mathcal{Q}/\partial p_j$ and $\partial \mathcal{Q}/\partial \mathcal{U}$ usually can be extracted cheaply from the objective function definition without expensive numerical calculations. The same holds for $\partial \mathcal{I}/\partial p$, which is implicitly given by the interface definition. The only quantity which renders significant additional numerical effort is the calculation of the block diagonal matrix $\partial \mathcal{S}/\partial p_j$. However, the modular nature of the MRC framework is also present here. Parameters are usually localized in the network and are allocated to one single subsystem k. In this case, $\partial \mathcal{S}/\partial p$ is mainly zero-valued, and only that block diagonal part needs to be evaluated, which belongs to $\partial \mathcal{S}_k/\partial p$. In summary, only a few additional computations of localized quantities are necessary, leading to highly efficient sensitivity calculations.

As discussed for the monolithic case, there are again two practical approaches for sensitivity calculations as defined in Equation (4.16). The direct approach now has the form of

$$\frac{\mathrm{d}\mathcal{Q}}{\mathrm{d}p_j} = \left(\frac{\partial \mathcal{Q}}{\partial \mathcal{S}}\frac{\partial \mathcal{S}}{\partial p_j} + \frac{\partial \mathcal{Q}}{\partial p_j}\right) + \left(\frac{\partial \mathcal{Q}}{\partial \mathcal{S}}\frac{\partial \mathcal{S}}{\partial \mathcal{U}} + \frac{\partial \mathcal{Q}}{\partial \mathcal{U}}\right)\frac{\mathrm{d}\mathcal{U}}{\mathrm{d}p_j}; \tag{4.17}$$

with the system of equations

$$\mathcal{J}\,\frac{\mathrm{d}\mathcal{U}}{\mathrm{d}p_j} = -\left(\frac{\partial \mathcal{I}}{\partial \mathcal{S}}\frac{\partial \mathcal{S}}{\partial p_j} + \frac{\partial \mathcal{I}}{\partial p_j}\right), \tag{4.18}$$

which needs to be solved for the total derivative of the subsystem inputs in addition. The factorization of $\mathcal{J}$, which was calculated for the interface problem, can be reused for the solution of Equation (4.18).

The adjoint approach results in

$$\frac{\mathrm{d}\mathcal{Q}}{\mathrm{d}p_j} = \left(\frac{\partial \mathcal{Q}}{\partial \mathcal{S}}\frac{\partial \mathcal{S}}{\partial p_j} + \frac{\partial \mathcal{Q}}{\partial p_j}\right) + \Psi^T\left(\frac{\partial \mathcal{I}}{\partial \mathcal{S}}\frac{\partial \mathcal{S}}{\partial p_j} + \frac{\partial \mathcal{I}}{\partial p_j}\right) \tag{4.19}$$

with the additional system of equations

$$\mathcal{J}^T\Psi = -\left(\frac{\partial \mathcal{Q}}{\partial \mathcal{S}}\frac{\partial \mathcal{S}}{\partial \mathcal{U}} + \frac{\partial \mathcal{Q}}{\partial \mathcal{U}}\right)^T \tag{4.20}$$

for determining the adjoint variable. Here, the factorization of the Jacobian matrix $\boldsymbol{J}$ can be reused for a self-adjoint $\boldsymbol{J}$. Requirements for such a symmetric $\boldsymbol{J}$ were discussed above: symmetric subsystem transfer functions $\partial \mathbf{Y}/\partial \boldsymbol{U}$ and the validity of Equation (3.35).

Interpreting the formula in Equation (4.17) and Equation (4.19) from a physical point of view, the first part of the equations provides the local, direct part of the sensitivity. This part is non-zero if the objective directly involves subsystem quantities and the design parameter is linked to the same subsystem(s). The second part propagates the sensitivity over the whole coupled problem, thus includes the indirect fraction caused by the coupling.

Formulation for Mixed Input Vector

The above sensitivity formula can be extended for a mixed input vector $\tilde{\boldsymbol{U}}$, thus for the efficiency enhancements in Section 3.2.3. Therefore, $\tilde{\boldsymbol{U}}$ is substituted for $\boldsymbol{U}$ in the derivative, Equation (4.11),

$$\frac{\mathrm{d}\boldsymbol{q}}{\mathrm{d}p_j} = \frac{\partial \boldsymbol{q}}{\partial p_j} + \frac{\partial \boldsymbol{q}}{\partial \boldsymbol{\mathcal{S}}}\left(\frac{\partial \boldsymbol{\mathcal{S}}}{\partial p_j} + \frac{\mathrm{d}\boldsymbol{\mathcal{S}}}{\mathrm{d}\tilde{\boldsymbol{U}}}\frac{\partial \tilde{\boldsymbol{U}}}{\partial p_j}\right) + \frac{\partial \boldsymbol{q}}{\partial \tilde{\boldsymbol{U}}}\frac{\mathrm{d}\tilde{\boldsymbol{U}}}{\mathrm{d}p_j}. \tag{4.21}$$

According to Section 3.2.3, the residuum is fully determined by the Dirichlet-Dirichlet/Dirichlet-Neumann part

$$\tilde{\boldsymbol{r}}_{\mathrm{ge}} = {}^{1}_{\mathrm{Dx}}\boldsymbol{r} = 0. \tag{4.22}$$

Equation (4.14) thus can be rewritten as

$$\frac{\mathrm{d}\tilde{\boldsymbol{U}}}{\mathrm{d}p_j} = -\left(\frac{\partial\, {}_{\mathrm{Dx}}\boldsymbol{\mathcal{I}}}{\partial \boldsymbol{\mathcal{S}}}\frac{\partial \boldsymbol{\mathcal{S}}}{\partial \tilde{\boldsymbol{U}}} + \frac{\partial\, {}_{\mathrm{Dx}}\boldsymbol{\mathcal{I}}}{\partial \tilde{\boldsymbol{U}}}\right)^{-1}\left(\frac{\partial\, {}_{\mathrm{Dx}}\boldsymbol{\mathcal{I}}}{\partial \boldsymbol{\mathcal{S}}}\frac{\partial \boldsymbol{\mathcal{S}}}{\partial p_j} + \frac{\partial\, {}_{\mathrm{Dx}}\boldsymbol{\mathcal{I}}}{\partial p_j}\right), \tag{4.23}$$

Equation (4.16) as

$$\begin{aligned}\frac{\mathrm{d}\boldsymbol{q}}{\mathrm{d}p_j} = &\left(\frac{\partial \boldsymbol{q}}{\partial \boldsymbol{\mathcal{S}}}\frac{\partial \boldsymbol{\mathcal{S}}}{\partial p_j} + \frac{\partial \boldsymbol{q}}{\partial p_j}\right) \\ &-\left(\frac{\partial \boldsymbol{q}}{\partial \boldsymbol{\mathcal{S}}}\frac{\partial \boldsymbol{\mathcal{S}}}{\partial \boldsymbol{U}} + \frac{\partial \boldsymbol{q}}{\partial \boldsymbol{U}}\right)\boldsymbol{V}\,\tilde{\boldsymbol{J}}^{-1}\left(\frac{\partial\, {}_{\mathrm{Dx}}\boldsymbol{\mathcal{I}}}{\partial \boldsymbol{\mathcal{S}}}\frac{\partial \boldsymbol{\mathcal{S}}}{\partial p_j} + \frac{\partial\, {}_{\mathrm{Dx}}\boldsymbol{\mathcal{I}}}{\partial p_j}\right).\end{aligned} \tag{4.24}$$

$\tilde{\boldsymbol{J}}$ is the Jacobian matrix of the reduced interface problem according to Equation (3.30), $\boldsymbol{V}$ the transformation matrix of Equation (3.28).

With the direct approach, the sensitivities of the transformed coupled problem are obtained by

$$\frac{\mathrm{d}\boldsymbol{q}}{\mathrm{d}p_j} = \left(\frac{\partial \boldsymbol{q}}{\partial \boldsymbol{\mathcal{S}}}\frac{\partial \boldsymbol{\mathcal{S}}}{\partial p_j} + \frac{\partial \boldsymbol{q}}{\partial p_j}\right) + \left(\frac{\partial \boldsymbol{q}}{\partial \boldsymbol{\mathcal{S}}}\frac{\partial \boldsymbol{\mathcal{S}}}{\partial \boldsymbol{U}} + \frac{\partial \boldsymbol{q}}{\partial \boldsymbol{U}}\right)\boldsymbol{V}\frac{\mathrm{d}\tilde{\boldsymbol{U}}}{\mathrm{d}p_j} \tag{4.25}$$

while

$$\tilde{\boldsymbol{J}}\frac{\mathrm{d}\tilde{\boldsymbol{U}}}{\mathrm{d}p_j} = \left(\frac{\partial_{\mathrm{Dx}}\boldsymbol{\mathcal{I}}}{\partial \boldsymbol{\mathcal{S}}}\frac{\partial \boldsymbol{\mathcal{S}}}{\partial p_j} + \frac{\partial_{\mathrm{Dx}}\boldsymbol{\mathcal{I}}}{\partial p_j}\right). \tag{4.26}$$

The adjoint approach takes the form of

$$\frac{\mathrm{d}\boldsymbol{q}}{\mathrm{d}p_j} = \left(\frac{\partial \boldsymbol{q}}{\partial \boldsymbol{\mathcal{S}}}\frac{\partial \boldsymbol{\mathcal{S}}}{\partial p_j} + \frac{\partial \boldsymbol{q}}{\partial p_j}\right) + \tilde{\boldsymbol{\Psi}}^T\left(\frac{\partial_{\mathrm{Dx}}\boldsymbol{\mathcal{I}}}{\partial \boldsymbol{\mathcal{S}}}\frac{\partial \boldsymbol{\mathcal{S}}}{\partial p_j} + \frac{\partial_{\mathrm{Dx}}\boldsymbol{\mathcal{I}}}{\partial p_j}\right) \tag{4.27}$$

with

$$\tilde{\boldsymbol{J}}^T\tilde{\boldsymbol{\Psi}} = -\left(\left(\frac{\partial \boldsymbol{q}}{\partial \boldsymbol{\mathcal{S}}}\frac{\partial \boldsymbol{\mathcal{S}}}{\partial \boldsymbol{U}} + \frac{\partial \boldsymbol{q}}{\partial \boldsymbol{U}}\right)\boldsymbol{V}\right)^T. \tag{4.28}$$

Reformulation for Classic Domain Decomposition Methods

The mixed formulation provides a systematic and modular approach to sensitivity analysis not only for the MRC framework but also for its special case of classic dual methods. Assuming $\partial\boldsymbol{\mathcal{I}}/\partial p_j = 0$, which holds for a classic approach, the above equations are reformulated in the notation of Section 3.1 for the sake of clarity.

The direct approach is given for the classic dual domain decomposition by

$$\frac{\mathrm{d}\boldsymbol{q}}{\mathrm{d}p_j} = \left(\frac{\partial \boldsymbol{q}}{\partial \boldsymbol{X}}\frac{\partial\left(\boldsymbol{A}^{-1}\right)}{\partial p_j}(\boldsymbol{F}+\boldsymbol{G}) + \frac{\partial \boldsymbol{q}}{\partial p_j}\right) + \left(\frac{\partial \boldsymbol{q}}{\partial \boldsymbol{X}}\boldsymbol{A}^{-1} + \frac{\partial \boldsymbol{q}}{\partial \boldsymbol{G}}\right)\hat{\boldsymbol{B}}^T\frac{\mathrm{d}\boldsymbol{\lambda}}{\mathrm{d}p_j}$$

with the system of equations for determining the total derivative $\mathrm{d}\boldsymbol{\lambda}/\mathrm{d}p_j$

$$\left(\hat{\boldsymbol{B}}\boldsymbol{A}^{-1}\hat{\boldsymbol{B}}^T\right)\frac{\mathrm{d}\boldsymbol{\lambda}}{\mathrm{d}p_j} = -\hat{\boldsymbol{B}}\frac{\partial\left(\boldsymbol{A}^{-1}\right)}{\partial p_j}(\boldsymbol{F}+\boldsymbol{G}).$$

The adjoint formula can be rewritten as

$$\frac{\mathrm{d}\boldsymbol{q}}{\mathrm{d}p_j} = \left(\frac{\partial \boldsymbol{q}}{\partial \boldsymbol{X}}\frac{\partial\left(\boldsymbol{A}^{-1}\right)}{\partial p_j}(\boldsymbol{F}+\boldsymbol{G}) + \frac{\partial \boldsymbol{q}}{\partial p_j}\right) + \tilde{\boldsymbol{\Psi}}^T\hat{\boldsymbol{B}}\frac{\partial\left(\boldsymbol{A}^{-1}\right)}{\partial p_j}(\boldsymbol{F}+\boldsymbol{G})$$

with

$$\left(\hat{\boldsymbol{B}}\boldsymbol{A}^{-1}\hat{\boldsymbol{B}}^T\right)^T\tilde{\boldsymbol{\Psi}} = -\hat{\boldsymbol{B}}\left(\frac{\partial \boldsymbol{q}}{\partial \boldsymbol{X}}\boldsymbol{A}^{-1} + \frac{\partial \boldsymbol{q}}{\partial \boldsymbol{G}}\right)^T.$$

Example 4.1 (Three Subsystem Example)

The three subsystem example is continued using the setting of Section 3.2.3 to illustrate the modular approach to sensitivity calculation. The internal state of subsystem $\mathcal{S}_2$ is chosen as objective, $q = X_2$. The mass of subsystem $\mathcal{S}_3$ is defined as design parameter $p = m_3$.

The adjoint approach is presented in the following, which is often of particular relevance. In a first step, the objective can be rewritten in terms of the subsystem's $\mathcal{S}_2$ inputs

$$q = X_2 = -\frac{F_2}{\omega^2 m_2} - \frac{U_2}{\omega^2 m_2},$$

resulting in the associated partial derivatives

$$\frac{\partial q}{\partial p} = \frac{\partial X_2}{\partial m_3} = 0 \qquad \frac{\partial q}{\partial \boldsymbol{U}} = \begin{bmatrix} 0 & -\frac{1}{\omega^2 m_2} & 0 & 0 \end{bmatrix} \qquad \frac{\partial q}{\partial \mathcal{S}} = \boldsymbol{0}$$

which are required for the sensitivity calculation. The interface constraint equations do not involve the design parameter $p = m_3$ explicitly, thus

$$\frac{\partial\, {}_{\mathrm{Dx}}\mathcal{I}}{\partial m_3} = \begin{bmatrix} 0 & 0 & 0 \end{bmatrix}^T.$$

Inserting these values into Equation (4.28) for determining the adjoint variable results in

$$\tilde{\boldsymbol{J}}^T\tilde{\boldsymbol{\Psi}} = -\left(\frac{\partial \boldsymbol{q}}{\partial \boldsymbol{U}}\boldsymbol{V}\right)^T = \begin{bmatrix} \frac{1}{2\omega^2 m} & 0 & 0 \end{bmatrix}^T,$$

which provides the adjoint variable as

$$\tilde{\boldsymbol{\Psi}} = t \cdot \begin{bmatrix} -5k\left(2m^2\omega^4 - 10km\omega^2 + 3k^2\right) \\ -10k\left(2k - m\omega^2\right) \\ 15k^2\left(k - 2m\omega^2\right) \end{bmatrix}.$$

$\partial \boldsymbol{\mathcal{S}}/\partial p$ needs to be determined additionally. As the parameter is linked to subsystem $\mathcal{S}_3$ exclusively, only the component $\frac{\partial \boldsymbol{\mathcal{S}}_3}{\partial p}$ is non-zero. This results in

$$\begin{aligned}\frac{\partial \boldsymbol{\mathcal{S}}}{\partial m_3} &= \operatorname{diag}\left(\frac{\partial^2 Y_1}{\partial U_1 \partial m_3}, \frac{\partial^2 Y_2}{\partial U_2 \partial m_3}, \frac{\partial^2 \boldsymbol{Y}_3}{\partial \boldsymbol{U}_3 \partial m_3}\right) \boldsymbol{V} \Delta\tilde{\boldsymbol{c}} \\ &= \operatorname{diag}\left(0, 0, \frac{\partial^2 \boldsymbol{Y}_3}{\partial \boldsymbol{U}_3 \partial m_3}\right) \boldsymbol{V} \Delta\tilde{\boldsymbol{c}} = \begin{bmatrix} 0 \\ 0 \\ t 10 k \omega^2 \left(-m\omega^2 + 2k\right) F_2 \\ 0 \end{bmatrix}.\end{aligned}$$

According to Equation (4.27), the total derivative of X_2 with respect to m_3 is finally obtained by

$$\begin{aligned}\frac{\mathrm{d}X_2}{\mathrm{d}m_3} &= \left(\frac{\partial q}{\partial \boldsymbol{\mathcal{S}}} \frac{\partial \boldsymbol{\mathcal{S}}}{\partial m_3} + \frac{\partial X_2}{\partial m_3}\right) + \tilde{\boldsymbol{\Psi}}^T \left(\frac{\partial_{\mathrm{Dx}} \boldsymbol{\mathcal{I}}}{\partial \boldsymbol{\mathcal{S}}} \frac{\partial \boldsymbol{\mathcal{S}}}{\partial m_3} + \frac{\partial_{\mathrm{Dx}} \boldsymbol{\mathcal{I}}}{\partial m_3}\right) \\ &= 0 + \tilde{\boldsymbol{\Psi}}^T \left(\frac{\partial_{\mathrm{Dx}} \boldsymbol{\mathcal{I}}}{\partial \boldsymbol{\mathcal{S}}} \frac{\partial \boldsymbol{\mathcal{S}}}{\partial m_3} + \frac{\partial_{\mathrm{Dx}} \boldsymbol{\mathcal{I}}}{\partial m_3}\right) \\ &= t^2 100 \omega^2 F_2 k^2 \left(-m\omega^2 + 2k\right)^2.\end{aligned}$$

Note, as the objective and the design parameter were not directly linked by a single subsystem, the first part of the total derivative is zero.

■

4.2 Derivatives for Mean Power as Objective Function in Harmonic Analyses

It is discussed in the following how derivatives can be calculated for power quantities, the spatially integrated power at the interface of subsystem k in particular. As for the remaining thesis, it is assumed that the subsystem inputs are forces $\boldsymbol{U} : F$, the outputs, respectively states are displacements $\boldsymbol{Y}, \boldsymbol{X} : W$.

Following Equation (2.37), the spatially integrated complex power at the interface of subsystem k is a function of the subsystem inputs and outputs

$$P = \frac{1}{2}\left(\boldsymbol{F}_k^H \boldsymbol{V}_k\right) = \frac{\omega}{2}\left(i\,\boldsymbol{U}_k^H \boldsymbol{Y}_k\right).$$

For a harmonic analysis, the power, input, and output quantities can be complex valued in general, $P : \mathbb{C}^n \to \mathbb{C}$. Such formulation of power is not holomorphic, and thus the complex derivative of P with respect to $\boldsymbol{U}_k$, respectively $\boldsymbol{Y}_k$ does not exist. These derivatives, however, are required for the above framework for sensitivity analysis.

Anyhow, real differentiability can be ensured for the real-valued mean power. For this, the latter has to be formulated in terms of real-only quantities. The latter are obtained by rearranging the complex-valued $\boldsymbol{U}_k$ and $\boldsymbol{Y}_k$ in real-valued vectors of double size. This enlarges the number of subsystem states, inputs and outputs by a factor of two

$$\hat{\boldsymbol{Y}} = \begin{bmatrix} \boldsymbol{Y}_\Re \\ \boldsymbol{Y}_\Im \end{bmatrix} \qquad \hat{\boldsymbol{U}} = \begin{bmatrix} \boldsymbol{U}_\Re \\ \boldsymbol{U}_\Im \end{bmatrix}$$

with $\square_\Re = \Re(\square)$ and $\square_\Im = \Im(\square)$. Consequently, the whole framework for subsystem coupling can be reformulated in real only quantities with the double number of equations at each stage. In such formulation, the mean power can be rewritten as

$$\overline{P} = \frac{\omega}{2}\left(\boldsymbol{U}_{\Im,k}^T \boldsymbol{Y}_{\Re,k} - \boldsymbol{U}_{\Re,k}^T \boldsymbol{Y}_{\Im,k}\right), \tag{4.29}$$

which involves real quantities only, $\overline{P} : \mathbb{R}^{2n} \to \mathbb{R}$. The derivative of Equation (4.29) with respect to a parameter p_j is given by

$$\frac{\mathrm{d}\overline{P}}{\mathrm{d}p_j} = \frac{\omega}{2}\left(\boldsymbol{U}_{\Im,k}^T \frac{\mathrm{d}\boldsymbol{Y}_{\Re,k}}{\mathrm{d}p_j} + \frac{\mathrm{d}\boldsymbol{U}_{\Im,k}^T}{\mathrm{d}p_j}\boldsymbol{Y}_{\Re,k} - \boldsymbol{U}_{\Re,k}^T \frac{\mathrm{d}\boldsymbol{Y}_{\Im,k}}{\mathrm{d}p_j} - \frac{\mathrm{d}\boldsymbol{U}_{\Re,k}^T}{\mathrm{d}p_j}\boldsymbol{Y}_{\Im,k}\right). \tag{4.30}$$

As changing the whole framework to a real-only reformulation is not efficient from an implementation point of view, one can evaluate Equation (4.30) using the complex-valued variables. Performing

a coefficient comparison, one can show that the derivative of Equation (4.30) can be calculated by

$$\frac{\mathrm{d}\overline{P}}{\mathrm{d}p} = \frac{\omega}{2}\Re\left(i\,\boldsymbol{U}_k^H \left(\frac{\partial\,\boldsymbol{Y}_k}{\partial\,p} + \frac{\partial\,\boldsymbol{Y}_k}{\partial\,\boldsymbol{U}_k}\frac{\mathrm{d}\boldsymbol{U}_k}{\mathrm{d}p} \right) - i\,\boldsymbol{Y}_k^H \frac{\mathrm{d}\boldsymbol{U}_k}{\mathrm{d}p} \right). \tag{4.31}$$

Defining the substitute quantity $\mathring{P}$ from which the mean power is obtained by

$$\frac{\mathrm{d}\overline{P}}{\mathrm{d}p} = \frac{\omega}{2}\Re\left(\frac{\mathrm{d}\mathring{P}}{\mathrm{d}p} \right), \tag{4.32}$$

the above framework for sensitivity calculations can be used to calculate

$$\frac{\mathrm{d}\mathring{P}}{\mathrm{d}p} = i\,\boldsymbol{U}_k^H \left(\frac{\partial\,\boldsymbol{Y}_k}{\partial\,p} + \frac{\partial\,\boldsymbol{Y}_k}{\partial\,\boldsymbol{U}_k}\frac{\mathrm{d}\boldsymbol{U}_k}{\mathrm{d}p} \right) - i\,\boldsymbol{Y}_k^H \frac{\mathrm{d}\boldsymbol{U}_k}{\mathrm{d}p}. \tag{4.33}$$

In the following, this is demonstrated without the adaptions for a mixed input vector for readability and exemplary in the adjoint framework. For the use with a mixed input vector, $\tilde{\boldsymbol{U}}$ can be substituted for $\boldsymbol{U}$ in the equations below. Rearranging Equation (4.33) in the formulation of Equation (4.19) and Equation (4.20), $\mathrm{d}\mathring{P}/\mathrm{d}p$ is obtained by

$$\frac{\mathrm{d}\mathring{P}}{\mathrm{d}p} = \left(\frac{\partial\,\mathring{P}}{\partial\,\boldsymbol{\mathcal{S}}}\frac{\partial\,\boldsymbol{\mathcal{S}}}{\partial\,p} + 0 \right) + \boldsymbol{\Psi}^T \left(\frac{\partial\,\boldsymbol{\mathcal{I}}}{\partial\,\boldsymbol{\mathcal{S}}}\frac{\partial\,\boldsymbol{\mathcal{S}}}{\partial\,p} + \frac{\partial\,\boldsymbol{\mathcal{I}}}{\partial\,p} \right). \tag{4.34}$$

The adjoint variable is determined by

$$\boldsymbol{J}^T\boldsymbol{\Psi} = -\left(\frac{\partial\,\mathring{P}}{\partial\,\boldsymbol{\mathcal{S}}}\frac{\partial\,\boldsymbol{\mathcal{S}}}{\partial\,\boldsymbol{U}} + \frac{\partial\,\mathring{P}}{\partial\,\boldsymbol{U}} \right)^T \tag{4.35}$$

while

$$\frac{\mathrm{d}\mathring{P}}{\mathrm{d}\boldsymbol{\mathcal{S}}_j} = \begin{cases} i\,\boldsymbol{U}_j^H & \text{for} \quad j = k \\ 0 & \text{else} \end{cases} \tag{4.36}$$

and

$$\frac{\mathrm{d}\mathring{P}}{\mathrm{d}\boldsymbol{U}_j} = \begin{cases} -i\,\boldsymbol{Y}_j^H & \text{for} \quad j = k \\ 0 & \text{else} \end{cases}. \tag{4.37}$$

Further, a zero partial derivative $\partial\boldsymbol{\mathcal{I}}/\partial\,p = 0$ is obtained for the mechanical networks of the thesis, when $p \neq \boldsymbol{U}_j, \boldsymbol{Y}_j$, which allows for a simplification of the above formula.

4.3 Chapter Summary

The Mixed Residual Coupling framework approach was extended to calculate sensitivities in coupled networks. Efficient formulas were presented for direct and adjoint calculation schemes. It was discussed that only a few additional matrix quantities need to be computed for a sensitivity calculation in the framework, which are further modular and localized. Thus, the concept of modularity can also be followed for sensitivity calculation. Corresponding formulas were provided not only in the MRC framework's notation but also for common dual-domain decomposition methods. Furthermore, the sensitivity calculation for mean power at subsystem interfaces was discussed.

CHAPTER 5

KRYLOV-SUBSPACE LEARNING FOR FE SUBSYSTEMS: BASICS

The subsystem coupling framework allows for parallelized and distributed calculations. Nevertheless, the computational costs for calculating the energy flow through the network of full order models (FOMs) may still be infeasible for multi-query methods in the online phase (Algorithm 3.1 on page 53 lines 3 and 10). As initially stated, learning the essential subsystem dynamics employing model order reduction (MOR) techniques is a remedy to that. Therefore, MOR is performed on a subsystem-local and decoupled level to follow the principles of modularity and offline-online separation. As shown below, Krylov-Subspace methods are an attractive choice for subsystem coupling and evaluating power quantities in particular. This method found applications to structural dynamics just recently, and there are many open points for an industrial application. In the following, these topics are addressed, and an application to large-scale industrial subsystem models is finally enabled.

5.1 Refined Requirements for Model Order Reduction (MOR)

Subsystem Coupling In the context of Chapter 3, the requirements of Section 1.3.2 for a MOR method for subsystem coupling applications can be refined. MOR must provide an optimal fitting of the input-to-output behavior $\frac{\partial \boldsymbol{Y}}{\partial \boldsymbol{U}}$ of floating and non-floating subsystems. For the vibroacoustic analysis in the frequency domain, this is equal to the transfer function matrix of the linear subsystem (see Equation (3.15)). Neither optimal fitting of internal states is significant, nor physical states must be preserved for coupling. As a harmonic analysis and synthesis is performed for a limited number of frequencies and thus in a limited frequency range

$$f_\mathrm{B} \in \left[f_\mathrm{l}, f_\mathrm{u}\right],$$

efficient MOR algorithms provide an accurate approximation in f_B, but not in the whole frequency domain.

Energetic Analysis As the energy should be finally analyzed in the network, MOR must enable to evaluate power accurately. A sufficient phase accuracy of the approximated transfer function matrix must be ensured for this, as discussed in Section 2.3.4. Firstly, this highlights the need for a sufficiently accurate approximation of the subsystem damping. The possibly localized and complex damping modeling of the industrial FOM must be considered accurately. Secondly, MOR must preserve the passivity of the subsystems as a baseline requirement for phase accuracy. MOR must introduce no artificial energy sources.

Subsystem Form Thus, no specific form of the damping matrices $\boldsymbol{S}$ and $\boldsymbol{D}$, like a Rayleigh damping approach, can be assumed (see Section 2.1.2), but MOR must be developed for general industrial subsystems in the second-order form. Structural damping must be considered, which imposes an additional challenge. This kind of damping is lacking in many second-order system formulations and thus in most approaches for MOR. Both, the real-valued FOM subsystem matrices (Equation (2.8)), as well as their interface (Equation (2.7)) are assumed to be symmetric.

MOR algorithms need to be capable of models with a large number of state unknowns and complex modeling techniques, as already stated in Section 1.3.2. This complex modeling also leads to the requirement of non-intrusiveness in the context of MOR: the algorithms should directly work on subsystem matrices, which were obtained from an arbitrary FE discretizer.

Multi-query Application The reduced-order model (ROM) must retain parametric dependencies for later variation. This preservation of parameters is addressed in Chapter 6. For the first, however, parametric dependency is omitted, and the basics of MOR are introduced. Note that the method development of the thesis follows the principle of generality as initially stated. Thus, MOR is not tailored for a distinct online application but general multi-query methods.

For readability, subscripts k indicating single subsystems, as well as the notation of parametric dependencies, are dropped in Chapter 5 and Chapter 6. Nevertheless, all derivations refer to a single subsystem in these chapters. Furthermore, the wording *system* is used for a subsystem for brevity.

5.2 Projection-based MOR

Well-established concepts for MOR can be used in order to reduce single subsystems. Many of these approaches, among the basic method followed in the thesis, rely on projection, which is introduced firstly. The introduction is limited to the main concepts required by the proposed MOR approach. More general projection theory can be found in Saad [213].

5.2.1 The Concept of Projection

Using projection, the state vector $\boldsymbol{X} \in \mathbb{C}^{n\times 1}$ of a second-order or first-order subsystem (see Equation (2.6), respectively Equation (2.16)) can be transformed to a new coordinate system by

$$\boldsymbol{X} = \boldsymbol{Z}\boldsymbol{X}_{\mathrm{T}}. \tag{5.1}$$

$\boldsymbol{X}_\mathrm{T}$ is the transformed state vector. $\boldsymbol{Z} \in \mathbb{C}^{n\times n}$ is the transformation matrix, whose columns span the subspace $\mathcal{N}$ providing the new coordinate system

$$\mathrm{colsp}(\boldsymbol{Z}) = \mathcal{N}. \tag{5.2}$$

$\mathrm{colsp}(\square)$ is the column space of a matrix $\square$, which is the span of the columns of $\square$; thus, the set of all possible linear combinations of the column vectors of $\square$. No information is lost in the case of a full-rank $\boldsymbol{Z}$. The basic idea of projection-based model order reduction is to find a lower-dimensional subspace of the original one, on which the system state is projected,

$$\boldsymbol{X} \approx \boldsymbol{V}\boldsymbol{X}_\mathrm{R}, \tag{5.3}$$

while $m \ll n$ for $\boldsymbol{X}_\mathrm{R} \in \mathbb{C}^{m\times 1}$ and $\boldsymbol{V} \in \mathbb{C}^{n\times m}$. $\square_\mathrm{R}$ indicates a projected, thus reduced quantity. $\boldsymbol{V}$ spans the subspace $\mathcal{T}$, $\mathrm{colsp}(\boldsymbol{V}) = \mathcal{T}$, which is called search space or trial space in literature (see Bui-Thanh et al. [46] and Grimme [105] exemplary). As the subspace is lower-dimensional, information is truncated, and the state is just approximated. In order to provide sufficient accuracy of the approximation, MOR needs to find a sufficiently small subspace, which contains the most significant patterns of system state $\boldsymbol{X}$ at the same time.

Inserting that approximated state into the system of equations in Equation (2.6), the following is obtained:

$$\begin{cases} \left(\boldsymbol{K} + i\,\mathrm{sgni}(s)\boldsymbol{S} + s\boldsymbol{D} + s^2\boldsymbol{M}\right)\boldsymbol{V}\boldsymbol{X}_\mathrm{R} = \boldsymbol{B}\boldsymbol{U} + \boldsymbol{r} \\ \boldsymbol{Y} = \boldsymbol{C}\boldsymbol{V}\boldsymbol{X}_\mathrm{R} \end{cases} \tag{5.4}$$

The approximated system state vector $\boldsymbol{X}_\mathrm{R}$ usually introduces an error, as $\boldsymbol{X}$ is not fully contained in $\mathcal{T}$ and a residual $\boldsymbol{r}$ is introduced

$$\boldsymbol{r} = \boldsymbol{B}\boldsymbol{U} - \left(\boldsymbol{K} + i\,\mathrm{sgni}(s)\boldsymbol{S} + s\boldsymbol{D} + s^2\boldsymbol{M}\right)\boldsymbol{V}\boldsymbol{X}_\mathrm{R}. \tag{5.5}$$

Equation (5.4) is overdetermined as n equations are provided for m unknowns. A left-hand side projection is introduced for the system of equations to obtain a unique solution. In addition to the subspace $\mathcal{T}$ on which the state is approximated, a direction of projection must be specified via constraints for the projection. A constraint space achieves this $\mathcal{C}$ with $\mathrm{colsp}(\boldsymbol{W}) = \mathcal{C}$. An alternative name for $\mathcal{C}$ is test

space (see Bui-Thanh et al. [46] and Hesthaven et al. [122], for example). A common choice for constraints is to ensure a vanishing residual in Equation (5.4), as the residual is unknown a-priori. A zero residual is obtained by choosing $\boldsymbol{W}^H$ orthogonal to $\boldsymbol{r}$, resulting in $\boldsymbol{W}^H\boldsymbol{r} = 0$. The latter is called the Petrov-Galerkin condition. Consequently, the residual solely exists in the subspace which contains the truncated basis vectors. Under the additional assumption of bi-orthogonality of $\boldsymbol{W}$ and $\boldsymbol{V}$, $\boldsymbol{W}^H\boldsymbol{V} = \boldsymbol{I}$, while $\boldsymbol{I}$ is the identity matrix, one finally results in a well-defined system of equations for a subsystem

$$\mathcal{S}_\mathrm{R}: \begin{cases} \boldsymbol{W}^H\left(\boldsymbol{K} + i\,\mathrm{sgn}i(s)\boldsymbol{S} + s\boldsymbol{D} + s^2\boldsymbol{M}\right)\boldsymbol{V}\boldsymbol{X}_\mathrm{R} = \boldsymbol{W}^H\boldsymbol{B}\boldsymbol{U} + \boldsymbol{0} \\ \boldsymbol{Y} = \boldsymbol{C}\boldsymbol{V}\boldsymbol{X}_\mathrm{R} \end{cases}, \tag{5.6}$$

or shortly

$$\mathcal{S}_\mathrm{R}: \begin{cases} \left(\boldsymbol{K}_\mathrm{R} + i\,\mathrm{sgn}i(s)\boldsymbol{S}_\mathrm{R} + s\boldsymbol{D}_\mathrm{R} + s^2\boldsymbol{M}_\mathrm{R}\right)\boldsymbol{X}_\mathrm{R} = \boldsymbol{B}_\mathrm{R}\boldsymbol{U} \\ \boldsymbol{Y} = \boldsymbol{C}_\mathrm{R}\boldsymbol{X}_\mathrm{R} \end{cases} \tag{5.7}$$

with

$$\begin{aligned} &\boldsymbol{K}_\mathrm{R} = \boldsymbol{W}^H\boldsymbol{K}\boldsymbol{V} \quad \boldsymbol{S}_\mathrm{R} = \boldsymbol{W}^H\boldsymbol{S}\boldsymbol{V} \quad \boldsymbol{D}_\mathrm{R} = \boldsymbol{W}^H\boldsymbol{D}\boldsymbol{V} \quad \boldsymbol{M}_\mathrm{R} = \boldsymbol{W}^H\boldsymbol{M}\boldsymbol{V} \\ &\boldsymbol{C}_\mathrm{R} = \boldsymbol{C}\boldsymbol{V} \quad \boldsymbol{B}_\mathrm{R} = \boldsymbol{W}^H\boldsymbol{B}. \end{aligned} \tag{5.8}$$

Equation (5.7) defines the reduced-order model (ROM), which is obtained from the original FOM by Equation (5.8). Solving the projected system for the projected state by Equation (5.7), the Petrov-Galerkin condition is always fulfilled.

A corresponding representation can be found for first-order systems as

$$\mathcal{S}_\mathrm{I,R}: \begin{cases} \boldsymbol{E}_\mathrm{R}s\boldsymbol{X}_\mathrm{R} = \boldsymbol{A}_\mathrm{I,R}\boldsymbol{X}_\mathrm{I,R} + \boldsymbol{B}_\mathrm{I,R}\boldsymbol{U}_\mathrm{R} \\ \boldsymbol{Y}_\mathrm{R} = \boldsymbol{C}_\mathrm{I,R}\boldsymbol{X}_\mathrm{I,R} \end{cases}, \tag{5.9}$$

with

$$\boldsymbol{E}_\mathrm{R} = \boldsymbol{W}_\mathrm{I}^H\boldsymbol{E}\boldsymbol{V}_\mathrm{I} \quad \boldsymbol{A}_\mathrm{I,R} = \boldsymbol{W}_\mathrm{I}^H\boldsymbol{A}_\mathrm{I,R}\boldsymbol{V}_\mathrm{I} \quad \boldsymbol{C}_\mathrm{I,R} = \boldsymbol{C}_\mathrm{I}\boldsymbol{V}_\mathrm{I} \quad \boldsymbol{B}_\mathrm{I,R} = \boldsymbol{W}_\mathrm{I}^H\boldsymbol{B}_\mathrm{I}.$$

(5.10)

In the special case of $\mathcal{T} = \mathcal{C}$, the projection is orthogonal: The direction of projection on $\mathcal{T}$ is perpendicular to $\mathcal{T}$ itself. For that case, the Petrov-Galerkin conditions are often called Galerkin or Bubnov-Galerkin conditions, and $\boldsymbol{W} = \boldsymbol{V}$ can be chosen. Otherwise, the projection is called oblique.

5.2.2 Useful Properties of Projection-Based MOR

A projection-based MOR ensures specific subsystem properties, which are helpful in the following method development and thus should be discussed upfront.

Structure-Preserving Properties

The following matrix properties can be preserved by projection by employing a Bubnov-Galerkin projection ($\boldsymbol{W} = \boldsymbol{V}$). On the level of subsystem matrices, the explicit projection of a Hermitian matrix $\boldsymbol{A} = \boldsymbol{A}^H \in \mathbb{C}^{n\times n}$ by a Bubnov-Galerkin projection renders again a Hermitian matrix $\boldsymbol{A}_\mathrm{R}$

$$\boldsymbol{A}_\mathrm{R}^H = \left(\boldsymbol{V}^H \boldsymbol{A} \boldsymbol{V}\right)^H = \boldsymbol{V}^H \boldsymbol{A}^H \boldsymbol{V} = \boldsymbol{V}^H \boldsymbol{A} \boldsymbol{V} = \boldsymbol{A}_\mathrm{R}. \tag{5.11}$$

Based on this formula, different cases of complex and non-complex $\boldsymbol{V}$ as well as $\boldsymbol{A}$ are defined, where $\boldsymbol{A}_\mathrm{R}$ has the property as defined in Table 5.1. As a result, using a Bubnov-Galerkin projection with a complex-valued projection matrix $\boldsymbol{V}$ is not structure-preserving in a classical sense, as real-valued symmetric FOM system matrices become complex-valued Hermitian in the space of the ROM.

	$\boldsymbol{A} = \boldsymbol{A}^H \in \mathbb{C}^{n\times n}$	$\boldsymbol{A} = \boldsymbol{A}^T \in \mathbb{R}^{n\times n}$
$\boldsymbol{V} \in \mathbb{C}^{n\times m}$	$\boldsymbol{A}_\mathrm{R} = \boldsymbol{A}_\mathrm{R}^H \in \mathbb{C}^{m\times m}$	$\boldsymbol{A}_\mathrm{R} = \boldsymbol{A}_\mathrm{R}^H \in \mathbb{C}^{m\times m}$
$\boldsymbol{V} \in \mathbb{R}^{n\times m}$	$\boldsymbol{A}_\mathrm{R} = \boldsymbol{A}_\mathrm{R}^H \in \mathbb{C}^{m\times m}$	$\boldsymbol{A}_\mathrm{R} = \boldsymbol{A}_\mathrm{R}^T \in \mathbb{R}^{m\times m}$

Table 5.1: The property of $\boldsymbol{A}_\mathrm{R}$ according to Equation (5.11) in dependence of $\boldsymbol{V}$ and $\boldsymbol{A}$.

In addition, the definiteness of matrices is preserved for a Bubnov-Galerkin projection. Exemplary assume a positive (semi-) definite

matrix $\boldsymbol{A}$, $\boldsymbol{U}^H \boldsymbol{A}\boldsymbol{U} \geq 0$, then its projected counterpart $\boldsymbol{A}_\mathrm{R}$ is positive (semi-) definite again

$$\boldsymbol{U}^H \boldsymbol{A}_\mathrm{R} \boldsymbol{U} = \boldsymbol{U}^H \boldsymbol{V}^H \boldsymbol{A}\boldsymbol{V}\boldsymbol{U} = \tilde{\boldsymbol{U}}^H \boldsymbol{A}\tilde{\boldsymbol{U}} \geq 0 \quad \text{for any } \tilde{\boldsymbol{U}} \in \mathbb{C}^{m\times 1} \tag{5.12}$$

while $\tilde{\boldsymbol{U}} = \boldsymbol{V}\boldsymbol{U}$. The same proof is possible for negative (semi-) definite matrices.

Preservation of Passivity

These properties of a Bubnov-Galerkin projection-based MOR method are helpful for the energetic network analysis, as they allow for the preservation of FOM's passivity in its ROM, even though a complex-valued projection matrix $\boldsymbol{V}$ does not provide a structure-preserving MOR technique in a classical sense. The passivity requirement, which is derived in Section 2.3.4, states that a passive second-order subsystem with a symmetric interface ($\boldsymbol{C} = \boldsymbol{B}^H$) requires system matrices, which are Hermitian and positive semi-definite as defined in Equation (2.56). Employing Equation (5.11) and Equation (5.12), one can state that these requirements for passivity preservation are met by construction for such systems using a Bubnov-Galerkin projection-based MOR method. Any interface-symmetric FOM system in the form of Equation (2.6) with positive semi-definite system matrices, which are either complex-valued Hermitian or real-valued symmetric, provides a ROM ensuring Equation (2.56).

Invariance Property

Another important property of projection-based methods is the reduced model's independence of the actual choice of $\boldsymbol{V}$ and $\boldsymbol{W}$, but the exclusive dependence on the information contained in the subspaces (Salimbahrami et al. [216]). This is called invariance property in the following. If one substitutes the projection matrices by alternative ones, $\hat{\boldsymbol{V}}$ and $\hat{\boldsymbol{W}}$, this leads to the same ROM in another realization if the same subspace is spanned

$$\mathrm{colsp}(\boldsymbol{V}) = \mathrm{colsp}\left(\hat{\boldsymbol{V}}\right) \qquad \mathrm{colsp}(\boldsymbol{W}) = \mathrm{colsp}\left(\hat{\boldsymbol{W}}\right).$$

Consider a change of basis by multiplication with the non-singular matrices $\boldsymbol{T}_1$, $\boldsymbol{T}_2 \in \mathbb{C}^{m\times m}$

$$\hat{\boldsymbol{V}} = \boldsymbol{V}\boldsymbol{T}_1 \qquad \hat{\boldsymbol{W}} = \boldsymbol{W}\boldsymbol{T}_2,$$

resulting in the reduced model $\hat{\mathcal{S}}_\mathrm{R}$ with changed system matrices

$$\begin{aligned}&\hat{\boldsymbol{K}}_\mathrm{R} = \hat{\boldsymbol{W}}^H \boldsymbol{K}\, \hat{\boldsymbol{V}} \quad \hat{\boldsymbol{S}}_\mathrm{R} = \hat{\boldsymbol{W}}^H \boldsymbol{S}\, \hat{\boldsymbol{V}} \quad \hat{\boldsymbol{D}}_\mathrm{R} = \hat{\boldsymbol{W}}^H \boldsymbol{D}\, \hat{\boldsymbol{V}} \quad \hat{\boldsymbol{M}}_\mathrm{R} = \hat{\boldsymbol{W}}^H \boldsymbol{M}\, \hat{\boldsymbol{V}} \\ &\hat{\boldsymbol{C}}_\mathrm{R} = \boldsymbol{C}\, \hat{\boldsymbol{V}} \quad \hat{\boldsymbol{B}}_\mathrm{R} = \hat{\boldsymbol{W}}^H \boldsymbol{B}.\end{aligned} \tag{5.13}$$

The proof is straightforward, showing that the transfer function $\hat{\boldsymbol{H}}_\mathrm{R}$ resulting from $\hat{\mathcal{S}}_\mathrm{R}$ is equal to $\boldsymbol{H}_\mathrm{R}$ from $\mathcal{S}_\mathrm{R}$:

$$\begin{aligned}\hat{\boldsymbol{H}}_\mathrm{R} &= \boldsymbol{C}\, \hat{\boldsymbol{V}} \left[\hat{\boldsymbol{W}}^H \boldsymbol{A}\, \hat{\boldsymbol{V}}\right]^{-1} \hat{\boldsymbol{W}}^H \boldsymbol{B} = \\ &= \boldsymbol{C}\, \boldsymbol{V}\, \boldsymbol{T}_1 \left[\boldsymbol{T}_2^H \boldsymbol{W}^H \boldsymbol{A}\, \boldsymbol{V}\, \boldsymbol{T}_1\right]^{-1} \boldsymbol{T}_2^H \boldsymbol{W}^H \boldsymbol{B} \\ &= \boldsymbol{C}\, \boldsymbol{V}\, \boldsymbol{T}_1 \boldsymbol{T}_1^{-1} \left[\boldsymbol{W}^H \boldsymbol{A}\boldsymbol{V}\right]^{-1} \boldsymbol{T}_2^{-H} \boldsymbol{T}_2^H \boldsymbol{W}^H \boldsymbol{B} = \boldsymbol{H}_\mathrm{R}\end{aligned} \tag{5.14}$$

while $\boldsymbol{A} = \boldsymbol{K} + i\,\mathrm{sgni}(s)\boldsymbol{S} + s\boldsymbol{D} + s^2\boldsymbol{M}$. Consequently, although the system realization changes, and thus the state $\hat{\boldsymbol{X}}_\mathrm{R}$ is different as $\boldsymbol{X}_\mathrm{R}$ for $\boldsymbol{T}_1 \neq \boldsymbol{I}$, the transfer function is unchanged. In fact, Equation (5.14) states nothing except that infinitely many realizations exist for a transfer function. This invariance is valuable as it allows the flexibility to modify the projection matrices within algorithms. While such a changed algorithm does not influence $\boldsymbol{H}_\mathrm{R}$ in exact arithmetic, more robust results can be obtained in the presence of finite-precision arithmetic, as discussed below.

5.2.3 Some Methods for Basis Generation

Different model order reduction techniques exist to determine the projection matrices $\boldsymbol{V}$ and possibly $\boldsymbol{W}$. In the following, a short overview is given, sketching the basic concept of some methods for linear systems from different disciplines. The methods are discussed in the scope of the above-introduced requirements, and the final choice for a MOR method is motivated.

System-Theoretic Methods

The class of system-theoretic methods is attractive from a theoretical point of view - although less common in structural dynamics. Balanced truncation is one popular approach of this class, classically developed for first-order systems. Performing a system balancing allows finding a transformed system that has states that are difficult

(respectively easy) to reach *and* observe. The observability and reachability gramians are used for this, which are measures for the energy required to reach a specific system state, respectively the energy obtained from observing it. This transformed system representation allows for truncating states which require high energy to reach and provide litte energy in observing at the same time, which is the basic idea of balanced truncation; see Pernebo et al. [200] for one of the first applications. As important advantage of balanced truncation, error bounds exist (Enns [74] and Glover [100]). However, Lyapunov equations need to be solved to obtain the required gramians, which is computationally demanding. As a consequence, Balanced Truncation is difficult to apply to large-scale systems (see Antoulas [15], for example) and requires the introduction of additional low-rank approximations for the solution of the Lyapunov equations (Stykel [236]). Second-order systems, in addition, need to be transformed to a first-order representation, losing second-order structure and increasing computational effort. Alternatively, different variants were developed for the direct application to second-order systems but without the advantage of error bounds or preservation of stability (Reis et al. [207]). In addition, classic balanced truncation methods need to be reformulated for an approximation that is particularly accurate in a band-limited frequency range, see Benner et al. [33], for example. Another system-theoretic method is the Hankel-Norm Approximation, in which model order reduction is optimal with respect to the Hankel-norm of the system. Refer to Antoulas [15] for an overview.

Data-Driven Methods

In contrast to system-theoretic approaches, there is a fundamentally different class of data-driven methods. These methods do not utilize any information from the inner representation of the underlying subsystem but work on samples of the system outputs or states. The starting point is a manifold of samples $\boldsymbol{x}_1$, often called snapshots

$$\boldsymbol{\chi} = \begin{bmatrix} \boldsymbol{x}_1 \, \boldsymbol{x}_2 \, ... \, \boldsymbol{x}_k \end{bmatrix}. \tag{5.15}$$

From a data point of view, the task is to find the m principal directions - the dominant patterns - in that data set matrix Equation (5.15). These principal directions finally form the projection matrix for the corresponding subspace. An optimal approximation $\hat{\boldsymbol{\chi}}$ for $\boldsymbol{\chi}$ can be

sought in a least-squares sense for the m-dimensional approximation to the n-dimensional data set

$$\underset{\hat{\boldsymbol{\chi}}\,\text{while}\,\text{rank}(\hat{\boldsymbol{\chi}})=m}{\text{argmin}} \left\| \boldsymbol{\chi} - \hat{\boldsymbol{\chi}} \right\|_{\text{F}}, \tag{5.16}$$

with $\|\square\|_{\text{F}}$ is indicating the Frobenius norm of a matrix, which is the square roots of the sum of all squared matrix elements (Golub et al. [101]). An optimality in the context of Equation (5.16) is provided by the Eckart-Young-Mirsky-(Schmidt)-theorem (Eckart et al. [72]). The latter provides an optimal matrix approximation $\hat{\boldsymbol{\chi}}$ by a singular value decomposition (SVD) of $\boldsymbol{\chi}$ truncated after m singular values.

$$\boldsymbol{\chi} = \begin{bmatrix} \boldsymbol{V} & \boldsymbol{V}_{\text{tr}} \end{bmatrix} \begin{bmatrix} \boldsymbol{\Theta} & \boldsymbol{0} \\ \boldsymbol{0} & \boldsymbol{\Theta}_{\text{tr}} \end{bmatrix} \begin{bmatrix} \boldsymbol{N} \\ \boldsymbol{N}_{\text{tr}} \end{bmatrix} \tag{5.17}$$

with $\boldsymbol{V} \in \mathbb{C}^{n \times m}$ is the required projection matrix, the diagonal matrix $\boldsymbol{\Theta} \in \mathbb{C}^{m \times m}$ contains the m largest singular values and $\boldsymbol{N} \in \mathbb{C}^{m \times m}$. Then, the optimal approximation of the dataset is given by

$$\hat{\boldsymbol{\chi}} = \boldsymbol{V}\boldsymbol{\Theta}\boldsymbol{N}^{H}. \tag{5.18}$$

No more accurate basis $\boldsymbol{V}$ exists for approximating $\boldsymbol{\chi}$ with rank m. The same holds when the Frobenius norm in Equation (5.16) is replaced by the spectral norm $\left\| \boldsymbol{\chi} - \hat{\boldsymbol{\chi}} \right\|_2$. The spectral norm of a matrix is a p-norm of order two and corresponds to the maximum singular value of that matrix, thus $\|\square\|_2 = \max(\|\square \cdot \boldsymbol{X}\|_2 / \|\boldsymbol{X}\|_2)$ for arbitrary vectors $\boldsymbol{X} \neq 0$ (Golub et al. [101]).

The SVD-based method has different names in different disciplines. It is referred to as Proper Orthogonal Decomposition (POD), especially if such a data set approximates the solution of a known or unknown partial differential equation by a separation ansatz. Instead of using a-priori determined functions like Fourier-modes as ansatz functions, respectively, as a basis, the data-driven POD approach generates basis vectors directly from samples resulting in Equation (5.17). The POD was initially developed in the spatial-time-continuous domain and Equation (5.15) contains state vectors for different time samples (see Berkooz et al. [34] and Sirovich [230]). In structural dynamics, the POD is used mainly in the non-linear regime; refer to Kerschen et al. [137] for examples. For linear(ized) systems, frequency-domain versions exist, in which the basis is generated from samples of

harmonic solutions in the frequency domain (Kim [139]). POD bases are also used in many approaches related to the reduced basis method. The latter can preserve input parameters of the FOM in the ROM; see Haasdonk et al. [110] for an example. Karhunen-Loève expansion (Karhunen [135] and Loève [155]) is another name for POD, and it is also known under slight modifications as principal component analysis (Hotelling [124]), empirical orthogonal functions (Lorenz [156]) or factor analysis (Harman [117]).

Summarizing the data-driven approach, its advantage is that it can be applied without any additional knowledge of the inner system representation or prerequisites on system properties but can solely work on the system's outputs. Thus, there are no restrictions on the inner subsystem representation and its damping modeling, and it does not require intrusiveness. This, however, is a disadvantage at the same time. If the inner representation of Equation (2.6) is accessible for the MOR algorithm, not all the knowledge is used which would be available. Naturally, this results in either less effective reduced models or more expensive algorithms to find such ROM.

All the approaches mentioned so far, the system-theoretic and data-driven methods, have in common that an SVD is used at some stage of the algorithm. Antoulas [15] summarizes these methods consequently under the category of SVD-based methods.

Modal Reduction

The probably best-known model order reduction technique for basis generation in structural dynamics, modal reduction, is related to that class of methods as an eigenvalue problem is solved, which is closely linked to an SVD. A common approach in structural dynamics is to solve the eigenvalue problem for the non-damped second-order system

$$\left(\boldsymbol{K} - \omega_{\mathrm{r},j}^2 \boldsymbol{M}\right)\boldsymbol{\Phi}_j = \boldsymbol{0}, \tag{5.19}$$

which has the form of a generalized eigenvalue problem (GEP)

$$\boldsymbol{K}\boldsymbol{\Phi}_j = \lambda_j \boldsymbol{M}\boldsymbol{\Phi}_j. \tag{5.20}$$

$\lambda_j = \omega_{\mathrm{r},j}^2$ provides the squared resonant frequency and the corresponding column j in $\boldsymbol{\Phi}$ the associated mode shape or eigenmode, which is real valued for a real-valued $\boldsymbol{K}$ and $\boldsymbol{M}$. Modal methods are

part of standard textbooks on structural dynamics, refer to Craig et al. [60], Géradin et al. [94], and Hambric et al. [115]. Choosing the most significant mode shapes, one obtains the desired projection matrix $\boldsymbol{V} = \boldsymbol{\Phi}_{\text{sel}} = \text{subset}(\boldsymbol{\Phi})$. The questions on how to select $\boldsymbol{\Phi}_{\text{sel}}$, however, is no trivial task if the ROM should be accurate in a limited frequency band of interest in particular. In engineering practice, often, the mode shapes corresponding to the lowest resonant frequencies are chosen up to a user-specified frequency threshold as heuristics. Other selection strategies are available; see Varga [264] for an overview.

The diagonalization of the reduced system matrices $\boldsymbol{K}_{\text{R}}$ and $\boldsymbol{M}_{\text{R}}$ is a valuable property of the modal reduction approach when applied to a non-damped system representation. Under the assumption of a mass orthonormalization,

$$\boldsymbol{\Phi}^T \boldsymbol{M} \boldsymbol{\Phi} = \delta_{ij} \qquad \boldsymbol{\Phi}^T \boldsymbol{K} \boldsymbol{\Phi} = \delta_{ij} \omega_j \tag{5.21}$$

holds, where δ_{ij} is the Kronecker-delta. This results in a ROM with decoupled DOFs, which can be solved independently from each other. In this case, the method is called modal superposition (Tisseur et al. [245]).

When a damped system should be represented by a modal basis obtained from the undamped eigenvalue problem in Equation (5.20), there are different cases to distinguish. For proportional viscous damping as defined by Equation (2.13), the viscous damping matrix $\boldsymbol{D}$ is also diagonalized by the modal basis (which is basically the motivation behind Equation (2.13)). From a data point of view, all system information is already covered by projection with the real-valued mode shapes of the non-damped system; no additional damping information is needed but contained in the complex eigenvalues. The same observation is made for the discussion of structural damping if $\boldsymbol{S}$ is diagonalized by the modal basis.

The other case is a general non-proportional system damping, due to localized damping, for example. Using mode shapes of the undamped system as projection matrix leads to coupled degrees of freedom in the ROM on the one hand. On the other hand, the quality of the projection basis in such cases is questionable, as information of the potentially complex damping modeling is missing in the subspace of the ROM. To include such damping modeling, a quadratic

eigenvalue problem has to be solved instead of Equation (5.20), which has the following form if structural damping is omitted:

$$\left(\boldsymbol{K}+\lambda_j\boldsymbol{D}+\lambda_j^2\boldsymbol{M}\right)\boldsymbol{\Phi}_j=\boldsymbol{0}. \tag{5.22}$$

In order to solve that quadratic eigenvalue problem, the system can be transformed to a first-order system representation, and a generalized eigenvalue problem can be solved (Tisseur et al. [245]). Using the linearization scheme of Equation (2.18), the GEP is obtained as

$$\boldsymbol{A}_{\mathrm{I}}\boldsymbol{\Phi}_{\mathrm{I},j}=\lambda_{\mathrm{I},j}\boldsymbol{E}\boldsymbol{\Phi}_{\mathrm{I},j} \tag{5.23}$$

with

$$\boldsymbol{\Phi}_{\mathrm{I}}=\begin{bmatrix}\boldsymbol{\Phi}\\ \lambda\boldsymbol{\Phi}\end{bmatrix}. \tag{5.24}$$

This GEP has the double number of unknowns compared to Equation (5.20). Mode shapes are complex valued, as well as the $2n$ eigenvalues, which occur in complex conjugate pairs for underdamped systems, respectively, for modes below critical damping. Complex modal superposition methods are possible as in the real case but in first-order form, see Xu et al. [276]. A similar GEP can be found for the inclusion of general structural damping by substituting $\boldsymbol{K}$ by $\bar{\boldsymbol{K}}=\boldsymbol{K}+i\,\mathrm{sgni}\left(\lambda_j\right)\boldsymbol{S}$ in the above equations. However, a modified solver is needed, as the matrices become complex valued, and a case separation is needed for positive and negative imaginary parts of λ.

A modal reduction is an attractive approach for engineers, as the modes contained in the projection matrix allow for an immediate physical interpretation. Consequently, this approach may be the most popular MOR technique in industry, and modal procedures are standard solvers in most commercial FE programs. However, modal bases are not necessarily a good choice from the subsystem coupling point of view. Modal reduction relies solely on the system matrices and is independent of a specific subsystem input and output definition; thus, no input-output optimal fit is obtained.

Component Mode Synthesis

Different methods were developed for enriching modal subsystem projection matrices to address that. This class of methods is known

as Component Mode Synthesis and includes two popular procedures: the Craig-Bampton and the Craig-Chang method. The Craig-Bampton method constructs a basis from eigenmodes for the subsystem with fixed coupling interfaces and constraints modes (Craig et al. [58]). These constraints modes correspond to static displacement shapes for a unit displacement at the single interface DOFs. In the Craig-Chang method, the projection matrix is constructed from eigenmodes for the subsystem with free coupling interfaces, the rigid-body modes of the substructure, and inertia relief attachment modes (Craig et al. [59]). Again, inertia relief attachment modes are static displacement modes for unit displacement at the interface DOFs, but with no other boundary conditions applied at the interface. For floating substructures, as followed in the thesis, a singular system must be solved for the rigid body modes, which need to be considered in the basis in addition; see Géradin et al. [94] for details. Since a part of the subspace spanned by these free-interface modes is already included in the static displacement modes, the corresponding parts are removed, leading to residual inertia relief attachment modes. Conceptually, the methods of Rubin [211] and MacNeal [162] employ the information for the projection matrix; the latter method differs solely in the projection of the mass matrix, for which only the free interface modes are considered. Classic Component Mode Synthesis Methods are usually formulated in the form of Equation (2.9). In such a form, the spatial interface DOFs are directly contained in the state vector $\boldsymbol{X}$ and can be directly coupled, the internal states $\dot{\boldsymbol{X}}$ are modal coordinates. Such representation is also called superelement, which can be directly considered in a primal assembly with standard FE parts. For dual coupling, there are distinct formulations of Component Mode Synthesis methods, dual Craig-Bampton, which incorporates an additional interface weakening, for example (see Rixen [209]). While a Craig-Bampton method is a remedy for a better input-output fitting, it shares the problem of modal approaches concerning the limited damping modeling in the ROM.

Condensation Methods

The Craig-Bampton method can also be seen as a condensation approach enriched by a modal basis. In condensation methods, the

reduced space is exclusively formed by (primarily physical) interface DOFs, but no internal states like generalized coordinates

$$\begin{bmatrix} \dot{\boldsymbol{X}} \\ \boldsymbol{Y} \end{bmatrix} = \boldsymbol{V}\,\boldsymbol{Y}.$$

Thus, the internal states are reconstructed from a ROM that is reduced to the interface quantities only. Condensation methods have a long history in structural dynamics. The most basic form is Guyan reduction (Guyan [109]) with a projection matrix $\boldsymbol{V} = \left[\boldsymbol{I}, \left(\boldsymbol{K}_{\mathrm{XX}}^{-1}\boldsymbol{K}_{\mathrm{XY}}\right)^T\right]^T$, which corresponds to a Schur complement system of the static system. As any mass and damping information is missing in this projection matrix, many extensions were developed during the last decades (Friswell et al. [85], Leung [150], and O'Callahan et al. [184]). However, the full damping information is considered in none of the methods for general damping modeling.

The characteristics of the discussed methods are found in Table 5.2, while the approaches are considered in their classic formulations, and only properties are listed, which are relevant for the thesis.

	BT	SVD	MM	CMS	CM	KM
Optimal IO fit	+	o	-	o	o	+
Frequency-band fit	-	+	o	o	-	+
General damping	o	+	-	-	-	+
Adaption to 2$^{\mathrm{nd}}$ order form	-	-	+	+	+	+
Efficiency for large $\boldsymbol{X}$	-	+	+	+	+	+

Table 5.2: Thesis-relevant characteristics of model order reduction methods in their classic formulations. BT: Balanced Truncation; SVD: SVD-based methods; MM: Modal methods; CMS: Component Mode Synthesis methods; CM: Condensation methods; KM: Krylov subspace methods. The weighting is as follows. -: no; o: partly; +: yes.

5.3 The Concept of Moment Matching

There is another class of MOR methods, which is based on moment matching. Moment matching approaches a direct fit of the input-to-

output behavior of subsystems, thus the transfer function - locally targeted in the domain of interest. It is an attractive concept for the subsystem coupling application as a consequence. As shown below, they allow for the inclusion of arbitrary damping modeling, in addition, thus potentially providing accurate power quantities. Moment matching methods were initially developed for first-order systems for applications in control theory. For this reason, moment matching is introduced for first-order systems firstly and is extended for second-order systems in Section 5.4.2 afterward. Consider the first-order system of Equation (2.16) with the Laplace domain transfer function according to Equation (2.17). The latter can be rewritten via a Taylor series expansion around $s = \kappa$ as

$$\boldsymbol{H}_{\mathrm{I}}(s) = \sum_{j=0}^{\infty} \frac{1}{j!} \frac{\partial \boldsymbol{H}_{\mathrm{I}}(s)}{\partial s^j}\bigg|_{s=\kappa} (s-\kappa)^{j-1} = \sum_{j=0}^{\infty} -\boldsymbol{m}_j (s-\kappa)^{j-1}, \tag{5.25}$$

where

$$\boldsymbol{m}_j = \boldsymbol{C}_{\mathrm{I}} \left(\left(\boldsymbol{A}_{\mathrm{I}} - \kappa \boldsymbol{E}_{\mathrm{I}} \right)^{-1} \boldsymbol{E}_{\mathrm{I}} \right)^j (\boldsymbol{A}_{\mathrm{I}} - \kappa \boldsymbol{E}_{\mathrm{I}})^{-1} \boldsymbol{B}_{\mathrm{I}} \tag{5.26}$$

is called the j-th (block) moment $\boldsymbol{m} \in \mathbb{C}^{q \times p}$ of the subsystem around κ in the Laplace domain; κ is the expansion point. The basic idea of moment matching is to find a ROM $\mathcal{S}_{\mathrm{I,R}}$ which shares the first o moments with the original FOM Equation (2.16) at κ. Thus the transfer functions of the two systems have the same o derivatives at κ; o is called the order in the following. The moments are called Markov parameters for an expansion point of $\kappa \to \infty$. If the moment matching is performed around $\kappa = 0$, it is named Padé approximation (Baker [21]). In that case, $\boldsymbol{A}$ must be nonsingular. A matching around k expansion points is possible, at each point o_k moments are matched as a result.

Conceptually different numerical approaches exist to perform such moment matching. There are explicit approaches that do not perform a projection of the subsystem's inner representation and, thus, are not projection-based MOR methods. Instead, the moments are calculated explicitly in such an approach and a surrogate reduced-order frequency response is directly forced to match these moments. Such approaches were used for circuit design for several decades, see Hwang et al. [127], for example, as well as the newer methods Asymptotic Waveform Evaluation (AWE, Pillage et al. [202]) or Complex Frequency Hopping (CFH, Chiprout et al. [56]). As no projection is

performed, the passivity is not preserved automatically (compare Section 5.2.2). In addition, there are several numerical issues when using these approaches; refer to Gallivan et al. [88] for a discussion.

5.4 Basics of Krylov Subspace Construction for MOR

A numerically more robust method is provided by implicit moment matching, which is based on the calculation of a block Krylov subspace of order o

$$\mathcal{K}_o(\boldsymbol{P},\boldsymbol{Q}) = \operatorname{span}\left\{\boldsymbol{Q},\boldsymbol{P}\boldsymbol{Q},...,\boldsymbol{P}^{r-1}\boldsymbol{Q}\right\}, \tag{5.27}$$

where $\boldsymbol{Q}$ is called start matrix and $\boldsymbol{P}$ continuation matrix in the following. $\operatorname{span}\{\boldsymbol{X}_1,...,\boldsymbol{X}_n\}$ defines the span of the vectors $\boldsymbol{X}_1$ to $\boldsymbol{X}_n$. The wording *block* is omitted if $\boldsymbol{Q}$ is a vector, not a matrix. Initially, Krylov [142] introduced the sequence for eigenvalue calculations in 1931. Implicit moment matching using Krylov subspaces became popular starting in the 1990s by Padé approximation via the Lanczos process (PVL, Feldmann et al. [79] and Freund [84]) and others; these methods, however, were not yet projection based. For the first time, Odabasioglu et al. [185] introduced an explicit projection of the system matrices of the inner representation as defined by Equation (5.8), respectively Equation (5.10). This approach, named the passive reduced-order interconnect macromodeling algorithm (PRIMA), thus enabled a passivity-preserving MOR method. Just recently, methods building on these basic approaches found applications to structural dynamics; see Lehner et al. [148], Soppa [234], van de Walle [259], and van Ophem [262] for examples.

Hereinafter the idea of rational interpolation at n_s expansion points is followed for the explicit projection, for which the projection matrices $\boldsymbol{V}_\mathrm{I}$ and $\boldsymbol{W}_\mathrm{I}$ are chosen as a combination of Krylov subspaces with a start and continuation matrix as follows

$$\bigcup_k \mathcal{K}_{o_\mathrm{b}(k)}\left(\left(\boldsymbol{A}_\mathrm{I}-\kappa_k\boldsymbol{E}\right)^{-1}\boldsymbol{E};\left(\boldsymbol{A}_\mathrm{I}-\kappa_k\boldsymbol{E}\right)^{-1}\boldsymbol{B}_\mathrm{I}\right) \subseteq \operatorname{colsp}(\boldsymbol{V}_\mathrm{I}) \tag{5.28}$$

and

$$\bigcup_k \mathcal{K}_{o_\mathrm{c}(k)}\left(\left(\boldsymbol{A}_\mathrm{I}-\kappa_k\boldsymbol{E}\right)^{-H}\boldsymbol{E}^H;\left(\boldsymbol{A}_\mathrm{I}-\kappa_k\boldsymbol{E}\right)^{-H}\boldsymbol{C}_\mathrm{I}^H\right) \subseteq \operatorname{colsp}(\boldsymbol{W}_\mathrm{I}). \tag{5.29}$$

$\bigcup_k$ indicates the vector-wise concatenation of k matrices, here of the Krylov sequences at the single k expansion points, each of order $o(k)$,

in one matrix. Equation (5.28) is called input Krylov subspace, Equation (5.29) output Krylov subspace. For this choice of Krylov subspaces, one can show that in total $\sum_k o_\mathrm{b}(k) + o_\mathrm{c}(k)$ moments are matched in the projected ROM by the Petrov-Galerkin projection. A corresponding proof can be found in Grimme [105]. For a Bubnov-Galerkin projection, thus either using exclusively the input or output Krylov subspace, only $\sum_k o_\mathrm{b}(k)$ respectively $\sum_k o_\mathrm{c}(k)$ moments are matched in the general case.

Krylov subspaces of the form Equation (5.27) are called *one-stage* in the following. In literature a common name is first-order Krylov subspace. The contrary naming convention of the thesis is motivated by the nature of Equation (5.27). As shown below in Section 5.4.3, also moment-matching of certain second-order systems can be performed using one-stage approaches. As a consequence, the different naming convention was chosen to avoid any confusion between the chosen Krylov subspaces and the order of the subsystem, which should be reduced.

5.4.1 Basic Algorithms

Calculating the sequence of Equation (5.27) directly, the repetitive multiplication of $\left(\boldsymbol{A}-\kappa_k \boldsymbol{E}\right)^{-1} \boldsymbol{E}$ may again lead to numerical difficulties, as pointed out by Grimme et al. [104]. The practical experience tells that - among other factors - such numerical issues occur more likely the more large-scale the FOM is. As a remedy, robust and well-developed numerical algorithms exist to calculate the union of the subspaces as defined in Equation (5.28), respectively in Equation (5.29). Such algorithms utilize the invariance property of Equation (5.14) and perform several orthonormalization steps during the sequence construction.

Before Krylov subspace methods were used in MOR applications, they already had a long history in the iterative solution of linear systems (refer to Golub et al. [101] for an overview) or eigenvalue extraction (Lanczos [143], Ruhe [212], and Sorensen [235]). In the scope of these applications, many algorithmic approaches emerged, which can be adapted for a projection matrix calculation. Corresponding algorithms are clustered in two basic groups, Lanczos-type algorithms (Lanczos [143]) and Arnoldi-type algorithms (Arnoldi [16]).

In a Lanczos procedure for MOR, one calculates $\boldsymbol{W}$ and $\boldsymbol{V}$ to be bi-orthogonal, $\boldsymbol{W}^H \boldsymbol{V} = \boldsymbol{I}$. Following Arnoldi algorithms, the two pro-

jection matrices are separately calculated while ensuring $\boldsymbol{W}^H \boldsymbol{W} = \boldsymbol{I}$ and $\boldsymbol{V}^H \boldsymbol{V} = \boldsymbol{I}$. While the classic Lanczos method orthogonalizes candidate vectors against the two previous vectors in the projection matrix, the new candidate is orthogonalized against all previous vectors in an Arnoldi approach, which is potentially computationally more costly.

Nevertheless, classic Lanczos-type algorithms suffer from numerical drawbacks and, therefore, increased implementation efforts. The basic formulation is limited to single-input single-output (SISO) systems as found in Gugercin [108] and Salimbahrami [217], for example. The development of versions for multiple-input multiple-output (MIMO) systems is difficult for the general case (Gugercin [108]). The bi-orthogonality is lost gradually, which requires re-orthogonalization (Simon [228], for example). Breakdowns occur for a zero-length of the candidate vector of one iteration without the possibility of continuing in a classic formulation. Typically, both projection matrices are calculated, $\boldsymbol{W}$ and $\boldsymbol{V}$, despite the Petrov-Galerkin or Bubnov-Galerkin approach. Salimbahrami et al. [214] introduced a Lanczos algorithm with full orthogonalization and therefore increased computational costs. Gallivan et al. [89] introduced a rational Lanczos procedure for model order reduction.

Arnoldi-type algorithms are numerically more robust and, therefore, easier to implement (Salimbahrami et al. [214]). A basic SISO version is provided in Algorithm 5.1 on the next page. Principal directions in the basis can be identified straightforwardly due to the orthogonality of the projection matrix, as shown below. Implementations for the block subspace in Equation (5.27), which can handle MIMO systems, are straightforward to derive for Arnoldi-type methods. As a consequence, Arnoldi-type algorithms are used within that work. There are two approaches to handling starting matrices instead of vectors, thus enabling the reduction of MIMO systems: vector-wise and block-wise implementations. The latter mainly relies on reformulating vector-vector by matrix-matrix operations and an additional QR-factorization. Another idea followed by vector-wise implementations is the modification of Algorithm 5.1 on the following page by introducing an additional loop over the multiple starting vectors. Both approaches are discussed by Gugercin [108].

Also Arnoldi-type iterations can break down if $\left\| {}^{j+1}\boldsymbol{V} \right\|_2 = 0$ (Algorithm 5.1, line 6). This zero-length terminates the iteration in the case of SISO systems. In a MIMO setting, corresponding columns of the

candidate matrix are deflated, thus removed, and the iteration can be continued. Deflation can be considered by just slight modifications of Algorithm 5.1, an implementation is introduced in Section 5.4.3.

A simple Gram-Schmidt orthogonalization, as introduced in Algorithm 5.1, is not accurate enough in many cases to ensure sufficient orthogonality of the basis vectors and must be replaced for numerical stability. This is discussed more in detail in Section 5.5, as well as additional normalization steps.

Many other modifications of Arnoldi algorithms exist besides for orthogonalization. For example, refer to the global Arnoldi method in which the standard inner product is replaced by the Frobenius inner product $\langle \boldsymbol{V}, \boldsymbol{W} \rangle_F = \mathrm{tr}(\boldsymbol{V}^H \boldsymbol{W})$, where $\mathrm{tr}(\square)$ is the trace operator. The basis vectors are therefore called F-orthonormal in such an algorithm (Bonin et al. [39]).

The Arnoldi algorithm is executed independently for the calculation of each of the projection matrices $\boldsymbol{V}$ (Equation (5.28)) and $\boldsymbol{W}$ (Equation (5.29)). Following the idea of a multi-point interpolation, Algorithm 5.1 is executed once for each expansion point κ_k, and the single local projection matrices are concatenated. Again, different approaches exist, which basically differ in the approach of concatenation and the choice of the starting matrix $\boldsymbol{Q}$ for each of the expansion points (Skoogh [232], for example). In the case $\boldsymbol{Q} = \boldsymbol{B}$ is chosen for any expansion point, the algorithm is called *restarting*.

Algorithm 5.1: Basic Arnoldi algorithm.

Input : Continuation matrix $\boldsymbol{P}$, start vector $\boldsymbol{q}$
Output : Projection matrix $\boldsymbol{V}$

```
1 Function BasicOneStageArnoldi(P,q):
2     V = [q]
3     for j = 1,2,...k do
          //  calculate next mode
4         W = P · ^jV
          //  orthogonalize
5         ^jH = V^H W
6         ^{j+1}V = W − V H_j
          //  add to basis
7         V = [V, ^{j+1}V]
8     return V
```

5.4.2 Efficient Extension to Second-Order Systems

The concept of moment matching through Krylov subspaces can be transferred to second-order systems. For the derivation of corresponding expressions, the second-order system is linearized. A non-unique linearization is given by Equation (2.18) and is repeated here for convenience

$$\boldsymbol{E} = \begin{bmatrix} \boldsymbol{D} & \boldsymbol{M} \\ \boldsymbol{M} & \boldsymbol{0} \end{bmatrix} \quad \boldsymbol{A}_{\mathrm{I}} = \begin{bmatrix} \tilde{\boldsymbol{K}} & \boldsymbol{0} \\ \boldsymbol{0} & \boldsymbol{M} \end{bmatrix} \quad \boldsymbol{B}_{\mathrm{I}} = \begin{bmatrix} \boldsymbol{B} \\ \boldsymbol{0} \end{bmatrix} \qquad \boldsymbol{C}_{\mathrm{I}} = \begin{bmatrix} \boldsymbol{C} & \boldsymbol{0} \end{bmatrix}$$

with $\tilde{\boldsymbol{K}} = -\boldsymbol{K} - i\,\mathrm{sgn}i(s)\,\boldsymbol{S}$. For brevity and without the loss of generality, assume a moment matching at the zero expansion point $\kappa = 0$ for the following derivations. Inserting the linearized system matrices into Equation (5.28), one obtains the input Krylov subspace as

$$\begin{aligned} &\mathcal{K}_r\left(\begin{bmatrix} \tilde{\boldsymbol{K}} & \boldsymbol{0} \\ \boldsymbol{0} & \boldsymbol{M} \end{bmatrix}^{-1} \begin{bmatrix} \boldsymbol{D} & \boldsymbol{M} \\ \boldsymbol{M} & \boldsymbol{0} \end{bmatrix}, \begin{bmatrix} \tilde{\boldsymbol{K}} & \boldsymbol{0} \\ \boldsymbol{0} & \boldsymbol{M} \end{bmatrix}^{-1} \begin{bmatrix} \boldsymbol{B} \\ \boldsymbol{0} \end{bmatrix}\right) = \\ &\mathcal{K}_r\left(\begin{bmatrix} \tilde{\boldsymbol{K}}^{-1}\boldsymbol{D} & \tilde{\boldsymbol{K}}^{-1}\boldsymbol{M} \\ \boldsymbol{I} & \boldsymbol{0} \end{bmatrix}, \begin{bmatrix} \tilde{\boldsymbol{K}}^{-1}\boldsymbol{B} \\ \boldsymbol{0} \end{bmatrix}\right) \subseteq \mathrm{colsp}(\boldsymbol{V}_{\mathrm{I}}). \end{aligned} \tag{5.30}$$

Starting from other linearizations than the non-unique form of Equation (2.18), one arrives at the same expression for the input space (Salimbahrami et al. [214]). The output space can be rewritten correspondingly to Equation (5.30) as

$$\mathcal{K}_r\left(\begin{bmatrix} \tilde{\boldsymbol{K}}^{-H}\boldsymbol{D}^H & \tilde{\boldsymbol{K}}^{-H}\boldsymbol{M}^H \\ \boldsymbol{I} & \boldsymbol{0} \end{bmatrix}, \begin{bmatrix} -\tilde{\boldsymbol{K}}^{-H}\boldsymbol{C}^H \\ \boldsymbol{0} \end{bmatrix}\right) \subseteq \mathrm{colsp}(\boldsymbol{W}_{\mathrm{I}}). \tag{5.31}$$

One straightforward option is to stay in the first-order framework to obtain ROMs of second-order systems. The one-stage subspaces are then calculated numerically according to Equation (5.30) and Equation (5.31) by corresponding algorithms from the preceding Section 5.4.1. Refer to Freund [83] or Vandendorpe et al. [263] for such approaches. The block-structure of the first-order system matrices of

Equation (2.18) can be preserved after projection by rearranging $\boldsymbol{V}_\mathrm{I}$ and $\boldsymbol{W}_\mathrm{I}$ in block-diagonal matrices,

$$\mathrm{colsp}(\boldsymbol{Z}) = \mathrm{colsp}\left(\begin{bmatrix}\boldsymbol{Z}_1\\ \boldsymbol{Z}_2\end{bmatrix}\right) \subseteq \mathrm{colsp}\left(\begin{bmatrix}\boldsymbol{Z}_1 & \boldsymbol{0}\\ \boldsymbol{0} & \boldsymbol{Z}_2\end{bmatrix}\right). \tag{5.32}$$

However, as the second-order system is reformulated in a first-order form, the number of states is doubled, increasing computational effort.

There are more economical approaches to generating Krylov subspaces for second-order systems. The starting point for the derivation of such algorithms is the observation that the matrices of both subspaces, Equation (5.30) and Equation (5.31) exhibit a form of

$$\mathcal{K}_r\left(\begin{bmatrix}\boldsymbol{P}_1 & \boldsymbol{P}_2\\ \boldsymbol{I} & \boldsymbol{0}\end{bmatrix}, \begin{bmatrix}\boldsymbol{Q}\\ \boldsymbol{0}\end{bmatrix}\right). \tag{5.33}$$

This form with zero and identity matrices in the second row leads to a Krylov sequence of the form

$$\begin{bmatrix}\boldsymbol{R}_0 & \boldsymbol{R}_1 & \ldots & \boldsymbol{R}_{r-1}\\ \boldsymbol{0} & \boldsymbol{R}_0 & \ldots & \boldsymbol{R}_{j-2}\end{bmatrix} = \begin{bmatrix}\boldsymbol{Z}_\mathrm{u}\\ \boldsymbol{Z}_\mathrm{l}\end{bmatrix} \tag{5.34}$$

with

$$\begin{aligned}&\boldsymbol{R}_0 = \boldsymbol{Q}\\ &\boldsymbol{R}_1 = \boldsymbol{P}_1\boldsymbol{R}_0\\ &\boldsymbol{R}_j = \boldsymbol{P}_1\boldsymbol{R}_{j-1} + \boldsymbol{P}_2\boldsymbol{R}_{l-2} \text{ for } j \geq 2.\end{aligned} \tag{5.35}$$

It is obvious from Equation (5.34) that

$$\mathrm{colsp}(\boldsymbol{Z}_\mathrm{l}) \subseteq \mathrm{colsp}(\boldsymbol{Z}_\mathrm{u}), \tag{5.36}$$

and the overall Krylov subspace is determined by $\boldsymbol{Z}_\mathrm{u}$. The latter can be constructed by introducing a two-stage Krylov subspace

$$\mathcal{G}_o\left(\boldsymbol{P}_1, \boldsymbol{P}_2; \boldsymbol{Q}\right) = \mathrm{span}\left\{\boldsymbol{R}_0, \boldsymbol{R}_1, \ldots \boldsymbol{R}_{o-1}\right\} = \mathrm{colsp}\left(\boldsymbol{Z}_\mathrm{u}\right). \tag{5.37}$$

Corresponding numerical implementations are based on Arnoldi-like procedures and mainly differ in the orthonormalization strategy, refer to Bai et al. [19, 20], Lu et al. [157], and Salimbahrami et al. [214] for different examples. The subspaces are called second-order Krylov subspaces in these publications. This different naming is motivated by the discussion above.

It follows from Equation (5.36) in combination with Equation (5.32) that a Krylov subspace for a second-order system, which is generated by linearization and a one-stage algorithm can be embedded in the two-stage Krylov subspace

$$\mathcal{K}_r\left(\begin{bmatrix}\boldsymbol{P}_1 & \boldsymbol{P}_2\\ \boldsymbol{I} & \boldsymbol{0}\end{bmatrix}, \begin{bmatrix}\boldsymbol{Q}\\ \boldsymbol{0}\end{bmatrix}\right) \subseteq \operatorname{colsp}\left(\begin{bmatrix}\boldsymbol{Z}_{\mathrm{u}} & \boldsymbol{0}\\ \boldsymbol{0} & \boldsymbol{Z}_{\mathrm{u}}\end{bmatrix}\right) = \operatorname{colsp}\left(\hat{\boldsymbol{Z}}\right). \quad (5.38)$$

A consequence of that expression is that projecting the linearized form of a second-order system with $\hat{\boldsymbol{Z}}$ is equal to projecting the matrices of the second-order system directly by $\boldsymbol{Z}_{\mathrm{u}}$ (see Lehner [147], for example).

The above expressions were derived assuming an expansion point at zero, $\kappa = 0$. These expressions can be adapted straightforwardly for arbitrary expansion points, as a moment matching around κ is equal to a moment matching of the shifted problem $\hat{s} = s - \kappa_k$ at zero (Salimbahrami et al. [214]). The transfer function matrix, Equation (2.11), of the shifted second-order system is

$$\boldsymbol{H} = \boldsymbol{C}\left(\boldsymbol{A}_k + \hat{s}\hat{\boldsymbol{D}}_k + \hat{s}^2\boldsymbol{M}\right)^{-1}\boldsymbol{B},$$

while

$$\boldsymbol{A}_k = \kappa_k^2\boldsymbol{M} + \kappa_k\boldsymbol{D} + \boldsymbol{K} + i\operatorname{sgni}\left(\kappa_k\right)\boldsymbol{S}$$
$$\hat{\boldsymbol{D}}_k = 2\kappa_k\boldsymbol{M} + \boldsymbol{D}.$$

The formula of the input Krylov subspace for an interpolation at several expansion points is then found as

$$\bigcup_k \mathcal{G}_{o_{\mathrm{b}}(k)}\left(-\boldsymbol{A}_k^{-1}\hat{\boldsymbol{D}}_k, -\boldsymbol{A}_k^{-1}\boldsymbol{M}; -\boldsymbol{A}_k^{-1}\boldsymbol{B}\right) \subseteq \operatorname{colsp}(\boldsymbol{V}). \quad (5.39)$$

In the case of Petrov-Galerkin projection the two-stage output Krylov subspace is obtained by

$$\bigcup_k \mathcal{G}_{o_{\mathrm{c}}(k)}\left(-\boldsymbol{A}_k^{-H}\hat{\boldsymbol{D}}_k^H, -\boldsymbol{A}_k^{-H}\boldsymbol{M}^H; -\boldsymbol{A}_k^{-H}\boldsymbol{C}^H\right) \subseteq \operatorname{colsp}(\boldsymbol{W}). \quad (5.40)$$

At each expansion point, $o_\mathrm{b}(k)+o_\mathrm{c}(k)$ moments of the second-order system are matched when a Petrov-Galerkin projection is applied with the input and output Krylov subspace.

For the assumptions of the thesis for FOM subsystems, interface symmetry $\boldsymbol{C}=\boldsymbol{B}^H$ and real-valued symmetric system matrices ($\boldsymbol{K}$, $\boldsymbol{M}$, $\boldsymbol{D}$, $\boldsymbol{S}$), a valuable relationship between input and output Krylov subspace can be stated. For such subsystems,

$$\begin{aligned}\tilde{\boldsymbol{A}}_k &= \kappa_k^{*2}\boldsymbol{M}+\kappa_k^{*}\boldsymbol{D}+\boldsymbol{K}+i\,\mathrm{sgni}\left(\kappa_k^{*}\right)\boldsymbol{S}=\boldsymbol{A}_k^{*}=\boldsymbol{A}_k^{H}\\ \tilde{\boldsymbol{D}}_k &= 2\kappa_k^{*}\boldsymbol{M}+\boldsymbol{D}=\hat{\boldsymbol{D}}_k^{*}=\hat{\boldsymbol{D}}_k^{H}\end{aligned} \tag{5.41}$$

holds and the output space, Equation (5.40), can be rewritten as

$$\bigcup_k \mathcal{G}_{o_\mathrm{b}(k)}\left(-\tilde{\boldsymbol{A}}_k^{-1}\tilde{\boldsymbol{D}}_k,-\tilde{\boldsymbol{A}}_k^{-1}\boldsymbol{M};-\tilde{\boldsymbol{A}}_k^{-1}\boldsymbol{B}\right)\subseteq \mathrm{colsp}(\boldsymbol{W}). \tag{5.42}$$

As a result, the output space is the input space at the conjugate complex expansion point. In the case of purely real-valued expansion points, $\Im(\kappa_k)=0$, it follows that the output and input Krylov subspaces are equal. Due to that, $2\cdot o_\mathrm{b}(k)$ moments are matched per expansion point κ_k, although solely the input Krylov subspace is calculated and a Bubnov-Galerkin projection is performed, not Petrov-Galerkin. The subspaces are not equal in the case of complex-valued expansion points, $\Im(\kappa_k)\neq 0$. $o_\mathrm{b}(k)$ moments are matched at κ_k, and $o_\mathrm{b}(k)$ moments at the complex conjugate expansion points κ_k^* implicitly when applying Galerkin projection. Anyhow, the concept of a (Bubnov) Galerkin projection is employed in the following. The latter provides several advantages, the preservation of subsystem passivity and computational speedup, in particular, compensating the merely implicit match of output moments.

Note that Equation (5.42) does not hold for subsystems with non-symmetric interface $\boldsymbol{C}\neq\boldsymbol{B}^H$. A Galerkin projection is also possible in this case with an extended $\boldsymbol{V}$ but leads to larger ROMs in most cases. For a short discussion, see Lehner [147] and the references therein. Although not shown here, the same considerations regarding moment matching by Galerkin projection are valid for first-order systems.

5.4.3 Krylov-based MOR in the Context of Damping Modeling

The formulation for Krylov subspaces of second-order systems, Equation (5.39), respectively Equation (5.40) reveals one of the central ad-

vantages of Krylov-based MOR. The damping matrices $\boldsymbol{D}$ and $\boldsymbol{S}$ are used explicitly to calculate the projection matrices. Consequently, damping information is included in the Krylov subspace without further restrictions on $\boldsymbol{D}$ and $\boldsymbol{S}$. Even damping models with arbitrary frequency-dependency could be considered in a Krylov-based MOR. In this case, the parametric model order reduction framework of Chapter 6 provides the basis with the frequency of excitation as a variable input parameter. As a result, using Krylov-based MOR can potentially result in accurate ROMs for any damping from a methodical point of view. This exact damping modeling provides a basis for accurate energetic network evaluations.

An algorithm can be developed to construct two-stage Krylov subspaces as a projection basis of second-order systems. Following the basic algorithms for one-stage Krylov subspaces in Section 5.4.1, similar procedures can be developed for two-stage approaches. However, it is unnecessary to use two-stage Krylov subspaces for any second-order subsystem to obtain moment-matching. One can show that for many cases of damping modeling, moment matching can be achieved by a one-stage Krylov subspace of the form of Equation (5.27).

A one-stage Krylov subspace can be used instead of a two-stage one for systems with Rayleigh-damping $\boldsymbol{D} = \alpha \boldsymbol{M} + \beta \boldsymbol{K}$ or no damping, while ensuring the same moment-matching

$$\mathcal{G}_r\left(-\boldsymbol{A}_k^{-1}\hat{\boldsymbol{D}}_k, -\boldsymbol{A}_k^{-1}\boldsymbol{M}; -\boldsymbol{A}_k^{-1}\boldsymbol{B}\right) = \mathcal{K}_r(-\boldsymbol{A}_k^{-1}\boldsymbol{M}, -\boldsymbol{A}_k^{-1}\boldsymbol{B}). \tag{5.43}$$

Derivations can be found in Lehner et al. [148] starting from one-stage Krylov subspaces, or in Beattie et al. [26] and Eid et al. [73] starting from two-stage Krylov subspaces. There are special cases in which no damping information must be considered in the subspace, and a one-stage algorithm matches even the double number of moments compared to a two-stage one with the same ROM size. This holds for systems with no damping or solely stiffness proportional Rayleigh damping, which are expanded at $\kappa = 0$ (Eid et al. [73] and Salimbahrami et al. [214]).

None of the above studies consider structural damping in the case considerations. Explicit consideration of structural damping is presented in the following. As the basis, the proof of Equation (5.43) for Rayleigh damping is repeated from Eid et al. [73] in a refined notation.

In the original formulation, zero structural damping $\boldsymbol{S} = 0$ is assumed, which results in

$$\boldsymbol{A}_k = \left(\kappa_k^2 + \kappa_k \alpha\right)\boldsymbol{M} + \left(1 + \kappa_k \beta\right)\boldsymbol{K}$$
$$\hat{\boldsymbol{D}}_k = \left(2\kappa_k + \alpha\right)\boldsymbol{M} + \beta\,\boldsymbol{K}.$$

Reformulating $\hat{\boldsymbol{D}}_k$ in terms of $\boldsymbol{A}_k$ and $\boldsymbol{M}$ provides

$$\hat{\boldsymbol{D}}_k = \frac{\beta}{1+\kappa_k\beta}\boldsymbol{A}_k + \left(2\kappa_k + \alpha - \beta\,\frac{\kappa_k^2 + \kappa_k\alpha}{1+\kappa_k\beta}\right)\boldsymbol{M} = \tilde{\alpha}\boldsymbol{A}_k + \tilde{\beta}\boldsymbol{M}. \quad (5.44)$$

A proof by induction is possible with this reformulated $\hat{\boldsymbol{D}}_k$. Therefore, the sequence blocks $\boldsymbol{R}_j$ of the two-stage Krylov subspace, as defined by Equation (5.35), are compared to the blocks of the one-stage algorithm

$$\tilde{\boldsymbol{R}}_j = \boldsymbol{P}^{j-1}\boldsymbol{Q} = -\left(-\boldsymbol{A}_k^{-1}\boldsymbol{M}\right)^{j-1}\boldsymbol{A}_k^{-1}\boldsymbol{B},$$

where the starting and continuation matrices are inserted as defined in Equation (5.43). The starting matrix $\boldsymbol{Q}$ is the same for both sequences, thus the first two moments are related as

$$\boldsymbol{R}_0 = \boldsymbol{A}_k^{-1}\boldsymbol{B} = \tilde{\boldsymbol{R}}_0$$
$$\boldsymbol{R}_1 = -\boldsymbol{A}_k^{-1}\hat{\boldsymbol{D}}_k\boldsymbol{R}_0 = -\boldsymbol{A}_k^{-1}\left(\tilde{\alpha}\boldsymbol{A} + \tilde{\beta}\boldsymbol{M}\right)\tilde{\boldsymbol{R}}_0 = -\tilde{\alpha}\tilde{\boldsymbol{R}}_0 + \tilde{\beta}\,\tilde{\boldsymbol{R}}_1 = \sum_{m=0}^{1} w_m \tilde{\boldsymbol{R}}_m.$$

One can show for all subsequent two-stage blocks in the form of $\boldsymbol{R}_j = \sum_{m=0}^{j} w_m \tilde{\boldsymbol{R}}_m$, that the next block is again a weighted sum of one-stage blocks

$$\begin{aligned}\boldsymbol{R}_{j+1} &= -\boldsymbol{A}_k^{-1}\hat{\boldsymbol{D}}_k\boldsymbol{R}_j - \boldsymbol{A}_k^{-1}\boldsymbol{M}\,\boldsymbol{R}_{j-1} \\ &= \left(-\tilde{\alpha} - \tilde{\beta}\,\boldsymbol{A}_k^{-1}\boldsymbol{M}\right)\sum_{m=0}^{j} w_m\tilde{\boldsymbol{R}}_m - \boldsymbol{A}_k^{-1}\boldsymbol{M}\sum_{m=0}^{j-1} w_m\tilde{\boldsymbol{R}}_m \\ &= -\tilde{\alpha}\sum_{m=0}^{j} w_m\tilde{\boldsymbol{R}}_m + \tilde{\beta}\sum_{m=1}^{j+1} w_m\tilde{\boldsymbol{R}}_m + \sum_{m=1}^{j} w_m\tilde{\boldsymbol{R}}_m.\end{aligned} \quad (5.45)$$

Thus, every block in the two-stage sequence is a linear combination of the block one-stage sequences for Rayleigh-damping. Following

Section 5.2.2, the invariance property states that both projection matrices, which are constructed from the two sequences, span the same subspace. Thus, the same number of moments is matched, and the proof is completed for Rayleigh damping. Note, the proof for systems with no damping is also covered as a special case of Rayleigh damping with $\alpha = 0$ and $\beta = 0$.

If one now extends the above formulations for structural damping, one obtains

$$\begin{aligned}\boldsymbol{A}_k &= \left(\kappa_k^2 + \kappa_k \alpha\right)\boldsymbol{M} + \left(1 + \kappa_k \beta\right)\boldsymbol{K} + i\,\mathrm{sgni}\left(\kappa_k\right)\boldsymbol{S} \\ \hat{\boldsymbol{D}}_k &= \left(2\kappa_k + \alpha\right)\boldsymbol{M} + \beta\,\boldsymbol{K}.\end{aligned}$$

A reformulation of $\hat{\boldsymbol{D}}_k$ in terms of $\boldsymbol{A}_k$ and $\boldsymbol{M}$ includes the structural damping matrix

$$\begin{aligned}\hat{\boldsymbol{D}}_k &= \frac{\beta}{1+\kappa_k\beta}\boldsymbol{A}_k + \left(2\kappa_k + \alpha - \beta\frac{\kappa_k^2 + \kappa_k\alpha}{1+\kappa_k\beta}\right)\boldsymbol{M} + \beta\frac{i\,\mathrm{sgni}\left(\kappa_k\right)}{1+\kappa_k\beta}\boldsymbol{S} \\ &= \tilde{\alpha}\boldsymbol{A}_k + \tilde{\beta}\boldsymbol{M} + \gamma\boldsymbol{S}.\end{aligned} \tag{5.46}$$

As a result, the blocks of the two-stage sequence are not a linear combination of the one-stage sequence blocks anymore

$$\begin{aligned}\boldsymbol{R}_0 &= \tilde{\boldsymbol{R}}_0 \\ \boldsymbol{R}_1 &= -\boldsymbol{A}_k^{-1}\hat{\boldsymbol{D}}_k\boldsymbol{R}_0 = -\boldsymbol{A}_k^{-1}\left(\tilde{\alpha}\boldsymbol{A} + \tilde{\beta}\boldsymbol{M} + \gamma\boldsymbol{S}\right)\tilde{\boldsymbol{R}}_0 = \left(\gamma\boldsymbol{S} - \tilde{\alpha}\right)\tilde{\boldsymbol{R}}_0 + \tilde{\beta}\tilde{\boldsymbol{R}}_1.\end{aligned}$$

Therefore, a two-stage algorithm has to be used for moment matching if both general Rayleigh and structural damping are included in a subsystem. However, there are several important cases in which one-stage algorithms can also be used in the presence of structural damping: The proof of Eid et al. [73] can be conducted solely in cases in which $\hat{\boldsymbol{D}}_k$ can be expressed exclusively by a weighted sum of the two matrices $\boldsymbol{A}_k$ and $\boldsymbol{M}$. If the structural damping matrix is a linear combination of the stiffness and mass matrix $\boldsymbol{S} = \vartheta\boldsymbol{K} + \zeta\boldsymbol{M}$, $\hat{\boldsymbol{D}}_k$ can be expressed in terms of $\boldsymbol{A}_k$ and $\boldsymbol{M}$

$$\begin{aligned}\hat{\boldsymbol{D}}_k = &\frac{\beta}{1+\kappa_k\beta + i\,\mathrm{sgni}\left(\kappa_k\right)\vartheta}\boldsymbol{A}_k \\ &+ \left(2\kappa_k + \alpha - \beta\frac{\kappa_k^2 + \kappa_k\alpha + i\,\mathrm{sgni}\left(\kappa_k\right)\zeta}{1+\kappa_k\beta + i\,\mathrm{sgni}\left(\kappa_k\right)\vartheta}\right)\boldsymbol{M} = \tilde{\alpha}\boldsymbol{A}_k + \tilde{\beta}\boldsymbol{M},\end{aligned}$$

and the proof of Eid et al. [73] can be conducted as shown above. The other, more relevant case is structural damping of general form, while the Rayleigh coefficients take the form $\beta = 0$ and $\alpha \geq 0$. For this case, $\hat{\boldsymbol{D}}_k$ is represented by $\boldsymbol{M}$ only

$$\hat{\boldsymbol{D}}_k = \left(2\kappa_k + \alpha\right)\boldsymbol{M} = \tilde{\beta}\,\boldsymbol{M}. \tag{5.47}$$

As a result, an expression similar to Equation (5.45) can be found

$$\begin{aligned}
\boldsymbol{R}_{j+1} &= -\boldsymbol{A}_k^{-1}\hat{\boldsymbol{D}}_k\boldsymbol{R}_j - \boldsymbol{A}_k^{-1}\boldsymbol{M}\boldsymbol{R}_{j-1} \\
&= \left(-\tilde{\beta}\,\boldsymbol{A}_k^{-1}\boldsymbol{M}\right)\sum_{m=0}^{j} w_m\tilde{\boldsymbol{R}}_m - \boldsymbol{A}_k^{-1}\boldsymbol{M}\sum_{m=0}^{j-1} w_m\tilde{\boldsymbol{R}}_m \\
&= \tilde{\beta}\sum_{m=1}^{j+1} w_m\tilde{\boldsymbol{R}}_m + \sum_{m=1}^{j} w_m\tilde{\boldsymbol{R}}_m,
\end{aligned} \tag{5.48}$$

and one-stage algorithms provide the same moment matching properties as their two-stage counterpart. The above results are summarized in Table 5.3.

$\boldsymbol{S}$	$\boldsymbol{D}$	Required Krylov sequence
Arbitrary	Arbitrary	Two-stage
$\mathbf{0}$	$\mathbf{0}$	One-stage
Arbitrary	$\mathbf{0}$ or $\alpha\boldsymbol{M}$	One-stage
$\mathbf{0}$	$\alpha\boldsymbol{M} + \beta\boldsymbol{K}$	One-stage
$\zeta\boldsymbol{M} + \vartheta\boldsymbol{K}$	$\alpha\boldsymbol{M} + \beta\boldsymbol{K}$	One-stage

Table 5.3: The required Krylov sequence for correct moment matching in dependence of the subsystem damping modeling for expansion points $|\kappa_k| > 0$.

In any case, structural damping incorporates some additional challenges from an algorithmic point of view. As discussed above, the dynamic stiffness $\boldsymbol{A}_k$ necessarily becomes a complex-valued matrix, despite the choice of κ_k in the Laplace domain. The projection matrix $\boldsymbol{V}$ is complex valued per definition in such a damping setting. Classically, however, mainly real-valued projection matrices are assumed for the notation of projection-based MOR. Motivated by this, one can

replace the complex-valued projection matrix at an expansion point $\boldsymbol{V}_\kappa$ by a real-valued one using

$$\hat{\boldsymbol{V}}_\kappa = \left[\Re\left(\boldsymbol{V}_\kappa\right) \Im\left(\boldsymbol{V}_\kappa\right)\right]. \tag{5.49}$$

It is obvious that Equation (5.49) contains the subspace which is spanned by $\boldsymbol{V}_\kappa$

$$\operatorname{colsp}\left(\boldsymbol{V}_\kappa\right) \subset \operatorname{colsp}\left(\hat{\boldsymbol{V}}_\kappa\right). \tag{5.50}$$

As Equation (5.41) holds, the complex-valued projection matrix at the conjugate complex expansion point κ^* is equal to the conjugate complex projection matrix at κ

$$\boldsymbol{V}_{\kappa^*} = \boldsymbol{V}_\kappa^*. \tag{5.51}$$

Thus, also $\boldsymbol{V}_{\kappa^*}$ is contained in $\hat{\boldsymbol{V}}_\kappa$

$$\operatorname{colsp}\left(\boldsymbol{V}_{\kappa^*}\right) \subset \operatorname{colsp}\left(\hat{\boldsymbol{V}}_\kappa\right). \tag{5.52}$$

For the first time, the concept was used in Ruhe [212] for eigenvalue computations with complex-valued shifts and was applied to model order reduction of first-order systems in Grimme [105], for example. An approach for converting the basis vectors already during moment calculation is found in Lee et al. [145]. Lehner [147] discussed the approach in the context of second-order systems. For matching moments at κ and its conjugate κ^* concurrently, z complex-valued basis vectors can be replaced by z real ones (if no deflation is assumed, which is discussed in Section 5.5.2). Computational savings are achieved by the conversion to a real-valued basis from that perspective, as calculations in complex arithmetic can be replaced in many stages of MOR. Nevertheless, moments *have* to be matched explicitly at the two expansion points concurrently, regardless of the question if matching additional moments at the conjugate expansion points adds valuable information to the subspace or not. Potentially, it is more effective to match moments at another expansion point than at the conjugate complex of the current one. In practice, this leads to larger real-valued projection matrices, and therefore larger ROMs, to achieve some required accuracy compared to complex-valued ones.

No conversion to real-valued projection matrices is performed in the proposed method due to that reason, but the whole system

definition, as well as the projection-based MOR, is formulated for complex-valued quantities in the thesis.

Large-scale models of individual subsystems in vehicle networks usually are pure metal parts and contain solely structural damping, thus do not require two-stage algorithms (see Table 6.1). This is an attractive result, one-stage Arnoldi algorithms are more well-established and consolidated than corresponding two-stage procedures. Nevertheless, reformulations in complex arithmetic are required, as pointed out. In addition, numerical and practical issues also arise for one-stage Arnoldi-type methods, when the FOM has a high number of states and inputs and outputs. Motivated by this, the thesis focuses on one-stage algorithms in the following. Concepts are presented to handle industrial FOMs. The presented concepts can be straightforwardly transferred to two-stage algorithms in future research.

5.5 Block-Arnoldi one-stage Algorithm for MIMO Large-scale Second-Order Models

Common block-versions of the Arnoldi algorithm, as introduced in its basic formulation by Algorithm 5.1 can be used for the construction of one-stage Krylov subspaces; however, not without adjustments for large-scale industrial models. The final implementation, which is proposed in this thesis, is presented in Algorithm 5.2. It has two significant modifications: the orthogonalization and the deflation procedure, which are discussed below.

Algorithm 5.2 provides a generic formulation of a block-Arnoldi procedure for incremental construction of a projection matrix. Therefore, the above algorithm is called from an outer loop per sampling point, at which additional moments should be matched by adding basis vectors to the projection matrix $\boldsymbol{V}$. For a second-order system with structural and, respectively, or Rayleigh-damping, a continuation matrix of

$$\boldsymbol{P} = -\boldsymbol{A}_k^{-1}\boldsymbol{M} \tag{5.53}$$

and a starting matrix of

$$\boldsymbol{Q} = -\boldsymbol{A}_k^{-1}\boldsymbol{B} \tag{5.54}$$

evaluated at the corresponding sampling point are provided to the algorithm; respectively, the factorization for $\boldsymbol{P}$ in a practical imple-

Algorithm 5.2: Modified Block-Arnoldi algorithm with references to Algorithm 5.3 on page 123 and Algorithm 5.4 on page 125.

Input : Transformation matrix $\boldsymbol{V}$, Krylov matrix $\boldsymbol{P}$, starting matrix $\boldsymbol{Q}$, expansion order o, deflation vector length l_{tol}

Output : Augmented transformation matrix $\boldsymbol{V}$

1 **Function** `oneStageBlockArnoldi(`$\boldsymbol{V}, \boldsymbol{P}, \boldsymbol{Q}, o, l_{\text{tol}}$`)`**:**

`//  orthogonalize starting matrix against V`

2 $^1\boldsymbol{V} = \text{reorthoGramSchmidt}(\boldsymbol{V}, \boldsymbol{Q})$

`//  orthonormalize columns of starting matrix against each other and perform deflation`

3 $^1\boldsymbol{V} = \text{QRdeflation}(^1\boldsymbol{V}, l_{\text{tol}})$

`//  add starting matrix to basis`

4 $\boldsymbol{V} = [\boldsymbol{V}, {}^1\boldsymbol{V}]$

`//  loop over orders`

5 **for** *j = 1,2,...o-1* **do**

6 $\quad {}^{j+1}\boldsymbol{V} = \boldsymbol{P}\,{}^j\boldsymbol{V}$

$\quad$ `//  orthogonalize candidate vectors against V`

7 $\quad {}^{j+1}\boldsymbol{V} = \text{reorthoGramSchmidt}(\boldsymbol{V}, {}^{j+1}\boldsymbol{V})$

$\quad$ `//  orthonormalize candidate vectors against each other and perform deflation`

8 $\quad {}^{j+1}\boldsymbol{V} = \text{QRdeflation}({}^{j+1}\boldsymbol{V}, l_{\text{tol}})$

$\quad$ `//  add candidate vectors to basis`

9 $\quad \boldsymbol{V} = [\boldsymbol{V}, {}^{j+1}\boldsymbol{V}]$

10 **return** $\boldsymbol{V}$

mentation. This finally provides a multi-point moment matching (Equation (5.28)) by a restarting scheme. Depending on the concept for expansion point placement, the outer loop takes a different form (see Section 5.7); thus, it is not provided here as pseudo-code.

5.5.1 Orthogonalization Procedures for Large-Scale Models

A simple Gram-Schmidt orthogonalization as used in Algorithm 5.1 on page 110 may not be sufficient for ensuring orthogonality of the basis vectors in the Arnoldi procedure. While this may not play a significant role in the basis construction for small-scale models, practical experience shows that it is an issue for industrial large-scale FOMs.

Loss of orthogonality is very likely for such models, which is not just an issue for the algorithm's numerical stability but also for the deflation strategy, which is presented below.

The classical Gram-Schmidt procedure (CGS) of Algorithm 5.1 on page 110 can be replaced by a Modified Gram-Schmidt approach (MGS) to prevent such loss of orthogonality. Both approaches are equivalent in exact numerics. In the presence of round-off errors, however, the MGS method shows better numerical stability (Golub et al. [101]). Against CGS, in which all H_{ij}, are calculated once and independent of each other (see Algorithm 5.1 line 5), they are calculated subsequently in MGS while iterating through the orthogonalization of the new candidate vector against the single previous basis vectors. Consequently, in MGS, errors introduced during these iterations are not summed up as in CGS, as the vectors are orthogonalized against the errors made before.

However, even MGS procedures can be insufficient to ensure orthogonality (Saad [213]). Braconnier et al. [43] illustrated that issue for the calculation of eigenvalues for a Toeplitz matrix of size 100 through the Arnoldi algorithm. They showed that insufficient orthogonalization using CGS or MGS severely impacted their results. Giraud et al. [97] did not use Arnoldi procedures but orthogonalize a square matrix of size 183. They observed a loss of orthogonality using MGS and more significant for CGS. Re-orthogonalization is a remedy to that, in which CGS or MGS is repeated in an iterative procedure (rCGS, respectively rMGS). In the following, rCGS is preferred over rMGS as it allows for more efficient implementations: a straightforward parallelization is possible, as well as matrix-versions of the algorithms. MGS algorithms require strictly sequential calculations in contrast. Implementations are reported for a parallel version of CGS, for which two iterations of CGS are faster than one iteration of MGS (refer to Giraud et al. [97] and references herein). This can compensate for the additional numerical efforts introduced by the iterative approach. Two iterations of rCGS (or rMGS) are, in fact, already sufficient for orthogonalization of a non-singular set of initial vectors (Giraud et al. [98]). The corresponding implementation is short and presented in Algorithm 5.3. In accordance with the block version of the Arnoldi algorithm, the rCGS is implemented in a matrix version, too.

Note that there are other orthogonalization schemes besides Gram-Schmidt. For example, a version of the Arnoldi algorithm is found in Walker [270], which employs a Householder orthogonalization.

Algorithm 5.3: Iterative Gram-Schmidt algorithm.

Input : Orthogonal basis $\boldsymbol{V}$, candidates $\boldsymbol{W}$
Output : Orthogonalized candidates $\boldsymbol{W}$

Function `reorthoGramSchmidt(`$\boldsymbol{V},\boldsymbol{W}$`):`
  `//  initialize`
  $k = 0$
  `//  iteratively orthogonalize`
  while $k < 2$ **do**
    $\boldsymbol{Q} = \boldsymbol{W}$
    $\boldsymbol{H} = \boldsymbol{V}^H \boldsymbol{Q}$
    $\boldsymbol{W} = \boldsymbol{Q} - \boldsymbol{V}\boldsymbol{H}$
    $k += 1$
  return $\boldsymbol{W}$

5.5.2 Deflation

Linear dependencies of basis vectors, hence a rank-deficiency, is another possible numerical issue. This issue is particularly relevant for a moment matching of subsystems with many in- and outputs. Linear dependencies are possibly introduced at two stages in the block Arnoldi algorithm. The starting matrix $\boldsymbol{Q}$ can already contain linear dependencies, or the latter are introduced during the Arnoldi iterations over the single orders. These linear dependencies have to be detected and removed from the vector candidate set $\boldsymbol{V}_j$ by deflation. In the case of deflation, the Arnoldi algorithm cannot be continued for SISO systems. For a MIMO setting, the corresponding columns containing linear dependent vectors are removed, and the Arnoldi algorithm continues.

In exact arithmetic, a candidate vector has to be deflated if its length is zero after the orthogonalization against the existing basis

$$\left\| \boldsymbol{W}_j \right\|_2 = 0, \tag{5.55}$$

where $\|\square\|_2$ indicates the Euclidean norm for a vector. Thus, the candidate vector is linearly dependent on the columns of the existing projection matrix. The case of an exactly zero vector length is unlikely in finite-precision arithmetic. However, vectors with a small vector length in the range of machine precision would also lead to numeri-

cally unstable divisions in the algorithm. Vectors with an Euclidean norm smaller than a given tolerance l_{tol}

$$\left\| \boldsymbol{W}_j \right\|_2 \leq l_{\text{tol}} \tag{5.56}$$

have to be removed to prevent that, leading to *inexact* deflation. Vectors, which are *almost* linear dependent are removed as result. As vectors with a small but nonzero length are removed from the basis, exact moment matching is no longer ensured, and an error is introduced. In fact, the block Krylov sequence of Equation (5.27) changes to

$$\text{colsp}(\boldsymbol{V}) = \text{span}\left\{ {}_0\boldsymbol{R}, \boldsymbol{P} \cdot {}_1\boldsymbol{R}, ..., \boldsymbol{P}^{r-1} \cdot {}_r\boldsymbol{R} \right\} \tag{5.57}$$

which is has a modified starting matrix, which changes per sequence step, thus is no strict Krylov sequence anymore. In the case that no deflation occurred in step j, the starting matrix does not change and ${}_j\boldsymbol{R} = {}_{j-1}\boldsymbol{R}$ holds. Otherwise, ${}_j\boldsymbol{R}$ is a subset of the vectors of ${}_{j-1}\boldsymbol{R}$. Bounds for the error in the computed moments due to inexact deflation are found in Gugercin [108] for first-order systems.

A standard QR factorization (Golub et al. [101]) is used for the final orthogonalization of the candidate vectors of one iteration ${}^{j+1}\boldsymbol{V}$ against each other in Algorithm 5.2 on page 121 line 8. The QR factorization enables an efficient procedure for determining the lengths of the orthogonalized vectors before the normalization. Two matrices are provided by a QR factorization, a set of orthonormal column vectors $\boldsymbol{Z}$ and corresponding participation factors $\boldsymbol{\Gamma}$, from which ${}^{j+1}\boldsymbol{V}$ can be reconstructed as ${}^{j+1}\boldsymbol{V} = \boldsymbol{Z}\boldsymbol{\Gamma}$. For corresponding implementations of the QR factorization (Anderson [13]), $\boldsymbol{\Gamma}$ is upper tridiagonal; the absolute values on its diagonal determine the vector lengths of the column vectors of $\boldsymbol{Z}$ before normalization as required for deflation according to Equation (5.56). An implementation is found in Algorithm 5.4 on the facing page. The same procedure is used in order to determine (almost) linear dependencies in the starting vector $\boldsymbol{Q}$ in Algorithm 5.2 line 2.

Another common approach, which is followed in literature, is determining the rank of ${}^{j+1}\boldsymbol{V}$ by a rank-revealing QR (Hong et al. [123], for example). Arnoldi algorithms, which utilize such a rank-revealing QR can be found exemplary in Bonin et al. [38] and Gugercin [108].

Algorithm 5.4: Deflation algorithm.

Input : Candidate vectors $\boldsymbol{W}$, deflation length l_{tol}
Output : Orthonormal and deflated transformation matrix $\boldsymbol{W}$

Function `QRdeflation(`$\boldsymbol{W}$`):`
  `//  get QR factorization`
  $[\boldsymbol{Z}, \boldsymbol{\Gamma}] = \text{qr}(\boldsymbol{W})$
  `//  get initial vectors lengths`
  $\boldsymbol{L} = \text{diag}(\boldsymbol{\Gamma})$
  `//  find vectors not to deflate`
  $\boldsymbol{I}_{\text{incl}} = \text{find}(\text{abs}(\boldsymbol{L}) > l_{\text{tol}})$
  $\boldsymbol{W} = \boldsymbol{Z}(:, \boldsymbol{I}_{\text{incl}})$
  return $\boldsymbol{W}$

5.5.3 Efficiency Enhancements for MIMO Systems

Apart from the numerical challenges that arise with large-scale industry FOMs, there is a conceptual challenge in Krylov-based MOR for such systems. When matching o moments at n_{s} non-conjugate expansion points, the ROM size is

$$m = o\, n_{\text{s}} n_{\text{U}}.$$

A Bubnov-Galerkin projection by the complex-valued input Krylov subspace without deflation is assumed for this. Obviously, the ROM size depends linearly on the number of inputs n_{U} of the FOM. Dealing with subsystems of large-scale industrial assemblies, this linear dependency constitutes a bottleneck of Krylov subspace methods: such models have many inputs in the range of a few dozen to hundreds for vehicle models. As several expansion points are usually needed, the size of ROMs can grow prohibitively large. Thus, the dependency of the ROM size m on the number of inputs n_{U} has to be reduced by appropriate methods to obtain efficient ROMs. For this purpose, common methods are found in the literature.

Overview over Different Approaches

There are *a-priori methods* for breaking the linear dependency. The term a-priori refers here to a reduction of the starting or continuation matrix *before* the subsequent Krylov sequence vectors are calculated.

SVDMOR is such an a-priori method, which was introduced by Feldmann [78]; an illustrative description is found in Tan et al. [240]. The basic idea is to find a lower rank representation of the subsystem interface (called terminals in SVDMOR literature), thus a condensed form of the maps $\boldsymbol{B} = \tilde{\boldsymbol{B}}\tilde{\boldsymbol{V}}^H$ and $\boldsymbol{C} = \tilde{\boldsymbol{C}}\tilde{\boldsymbol{Z}}^H$. The transfer function then takes the form of

$$\boldsymbol{H} = \tilde{\boldsymbol{Z}}\tilde{\boldsymbol{C}}\boldsymbol{A}^{-1}\tilde{\boldsymbol{B}}\tilde{\boldsymbol{V}}^H = \tilde{\boldsymbol{Z}}\tilde{\boldsymbol{H}}\tilde{\boldsymbol{V}}^H,$$

in which a smaller $\tilde{n}_\mathrm{U} \times \tilde{n}_\mathrm{U}$ transfer function $\tilde{\boldsymbol{H}}$ is nested. The latter can be reduced in a second step by applying the standard Krylov method or any other model order reduction technique. In the original formulation, the required interface projection matrices $\tilde{\boldsymbol{V}}$ and $\tilde{\boldsymbol{Z}}$ are determined from an SVD of the 0^{th} order block moments at $\kappa = 0$ for a first-order system (Equation (5.26))

$$\boldsymbol{m}_0 = \tilde{\boldsymbol{Z}}\boldsymbol{\Theta}\tilde{\boldsymbol{V}}^H.$$

Liu et al. [154] introduced the extended SVDMOR (ESVDMOR) method. It follows the idea of SVDMOR, but the low-rank approximation is obtained from different enriched moment matrices. Higher-order moments are considered in addition, and the SVD is applied to separate moment matrices associated with the inputs, respectively outputs.

Tangential interpolation is another approach for a reduced dependency of the ROM size on the number of inputs. It is directly linked with Krylov-based MOR and was introduced by Gallivan et al. [87, 90]. The concept is not to match the transfer function at the expansion points κ_k (and possibly higher-order moments of it) in total but just in tangential right directions $\boldsymbol{t}_{\mathrm{r},k}$ when constructing the input Krylov subspace

$$\boldsymbol{H}_\mathrm{R}(\kappa_k)\boldsymbol{t}_{\mathrm{r},k} = \boldsymbol{H}(\kappa_k)\boldsymbol{t}_{\mathrm{r},k}. \tag{5.58}$$

As a result, the starting matrix for the Krylov sequence reduces to $\boldsymbol{Q} = -\boldsymbol{A}_{\kappa_k}^{-1}\boldsymbol{B}\boldsymbol{t}_{r,k}$. For the construction of the output Krylov subspace, corresponding left directions are determined, which are multiplied to Equation (5.58) on the left-hand side. The calculation of appropriate tangential directions $\boldsymbol{t}_{r,k}$ is closely related to the determination of expansion points. In a greedy basis construction, tangential directions can be determined along with expansion points from residuals for the next moments to be matched (Druskin et al. [70]). For $\mathcal{H}_2$-optimal

MOR, tangential directions are an enabler for MOR of MIMO systems and can be determined in several ways (Bunse-Gerstner et al. [49]). The concepts of $\mathcal{H}_2$-optimal MOR and greedy search are introduced more detailed in Section 5.7.

The projection matrix generation through the Arnoldi algorithm occurs in the offline phase, decoupled from later online assembly evaluations. The offline phase is less time-critical than the execution times in the online phase. Consequently, it may be a good compromise to choose a computationally more demanding approach of an *a-posteriori* approach for ROM size reduction. The benefit of these extra efforts is that as much information (moments) as possible can be used, as the significant directions are chosen *a-posteriori* after the calculation of each full $\boldsymbol{V}_\kappa$ at expansion point κ. This potentially leads to more accurate models for a given ROM size than a-priori approaches. For example, van Ophem [262] compares corresponding a-priori and a-posteriori methods. Identifying principal directions is closely linked to data-driven approaches for MOR (compare Section 5.2.3). In line with that, van Ophem [262] uses an SVD for determining the most significant directions in the Krylov sequence vectors a-posteriori. Compared with an a-priori method employing an SVDMOR-like approach but using a moment around $\kappa \neq 0$, a better approximation is observed in the vicinity of the expansion points.

A-posteriori Approach of the Thesis

In the method introduced in the following, no SVD on the whole projection matrix is performed. The Arnoldi procedure, as presented in Algorithm 5.2 on page 121, calculates orthogonal basis vectors and consequently provides already information about the linear dependency without any extra calculations. Based on that, a more geometrical approach is possible using vector lengths to identify the significant directions in a set of candidate vectors for a currently calculated moment matrix of the MIMO transfer function. Each of the candidate vectors is the component of the considered moment for a specific column, respectively row in the transfer function matrix, while the considered moment may not be equally important for all columns and rows. The concept can be illustrated by the situation in Figure 5.1: Two orthonormal vectors, $\boldsymbol{V}_1$ and $\boldsymbol{V}_2$, span the current subspace, to which a third direction should be added by the candidate vector $\boldsymbol{W}_3$. $\boldsymbol{W}_3$ is calculated in line 6 of Algorithm 5.2 on page 121 or is given by

the starting matrix. Prior to orthogonalization, $\boldsymbol{W}_3$ has some angle φ to the already existing subspace and an initial vector length $\left\|\boldsymbol{W}_3\right\|_2$. The non-normalized vector $\tilde{\boldsymbol{V}}_3$ is obtained by orthogonalization of $\boldsymbol{W}_3$. The vector length $l_3 = \left\|\tilde{\boldsymbol{V}}_3\right\|_2$ is obtained depending on the initial angle α and the initial vector length $\left\|\boldsymbol{W}_3\right\|_2$ when no normalization is performed

$$l_3 = \left\|\tilde{\boldsymbol{V}}_3\right\|_2 = \left\|\boldsymbol{W}_3\right\|_2 \sin(\varphi).$$

In Krylov subspace methods, a small vector length l_3 thus can have two reasons. Firstly, the initial angle φ may be small as the candidate vector, the component of the calculated moment for a specific column, respectively row, is almost linearly dependent on the already spanned subspace. Thus, it may be a reasonable approximation to represent the moment for this part of the transfer function by the existing basis. Secondly, the initial candidate vector length $\left\|\boldsymbol{W}_3\right\|_2$ may be small; thus, the considered moment is small for the correlated column/row of the transfer functions. As a result, the moment contribution is small, and the vector may also be omitted for the basis.

Having the block of candidate vectors for an expansion point, the idea is to include these with vector lengths $\left\|\tilde{\boldsymbol{V}}_j\right\| > l_{\text{tol}}$ in the projection matrix, as they add the important information to the basis. The selected vectors are normalized afterward. The concept of using vector lengths as selection criteria is already found in Salimbahrami [217], from which also Figure 5.1 was adapted. However, it is the first time that it is reported for use in an industry-scale model to the authors' knowledge. Salimbahrami [217] also proposes selection criteria based on the initial angles α. The vector length $\tilde{\boldsymbol{V}}$ is here preferred as it combines both, initial vector length *and* angle.

The approach described above is nothing else than the inexact deflation procedure of Section 5.5.2 but for a larger l_{tol}. No additional implementations are necessary. No computationally more demanding SVD on the whole projection matrix needs to be performed, but the results of the cheaper QR factorization of the candidate vectors at the current iteration are used. This is called *augmented deflation* in the following. Conceptually the same as inexact deflation, moment matching is not fulfilled exactly anymore as a result (see Section 5.5.2).

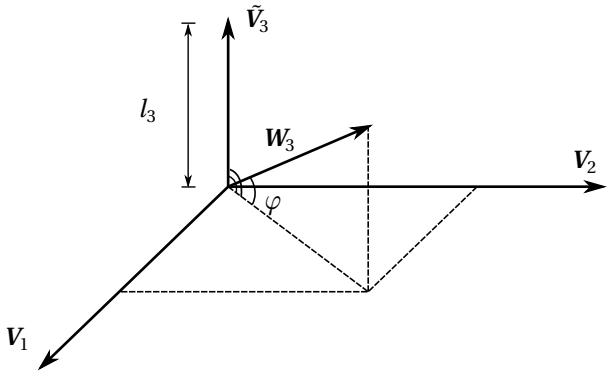

Figure 5.1: Visualization of the orthogonalization procedure during basis generation, adapted from Salimbahrami et al. [214].

5.6 Error Analysis for Reduced Subsystems

A Krylov-based MOR allows for a local fit in the band-limited (Laplace) domain of interest, thus for efficient ROMs. As one major drawback, it is challenging to find reliable and efficient error bounds for that band-limited domains, but heuristics are utilized in practice to estimate the error (Antoulas [15] and Grimme [105]).

The starting point for developing heuristics is the frequency-dependent error in the matrix of transfer functions

$$\varepsilon_{\mathrm{H}} = \boldsymbol{H} - \boldsymbol{H}_{\mathrm{R}}, \tag{5.59}$$

respectively some norm of that error matrix. In signal and system theory, there are many norms associated with specific properties of the signal or system. Such norms are the two norm $\mathcal{H}_2$ or the infinity norm $\mathcal{H}_\infty$. Refer to Soppa [234] for some overview over corresponding norms and to Panzer et al. [190] for an exemplary use in the context of Krylov-based MOR. These kinds of norms have in common that they provide information in a global manner, as they are evaluated over the whole (semi-) infinite time or frequency domain. In contrast, the error quantities in a limited frequency band are of interest when performing harmonic network analysis. Consequently, local errors need to be analyzed at distinct frequencies, and $\|\square\|$ is some norm for the evaluation at a frequency point.

It was pointed out in Section 2.3.4 that a sufficient phase accuracy of the transfer function matrix is required to enable accurate power quantities. This requirement is not sufficiently represented by a norm of $\boldsymbol{\varepsilon}_{\mathrm{H}}$ when developing an error measure to account for a later power evaluation in the coupled network. As a practical remedy, norms of the relative error can be evaluated instead

$$\left\|\boldsymbol{\varepsilon}_{\mathrm{H,rel}}\right\| = \frac{\left\|\boldsymbol{H}-\boldsymbol{H}_{\mathrm{R}}\right\|}{\|\boldsymbol{H}\|} = \frac{\left\|\boldsymbol{\varepsilon}_{\mathrm{H}}\right\|}{\|\boldsymbol{H}\|}, \tag{5.60}$$

where $\boldsymbol{\varepsilon}_{\mathrm{H,rel}}$ is again a matrix. This is an attractive approach for an energetic analysis; by assessing the relative error, an upper bound for the phase error $\varphi_{\varepsilon_{\mathrm{H}}}$ is obtained

$$\tan\varphi_{\varepsilon_{\mathrm{H}}} = \frac{\left\|\boldsymbol{\varepsilon}_{\mathrm{H}}\right\|}{\|\boldsymbol{H}\|}\sqrt{1-\frac{\boldsymbol{\varepsilon}_{\mathrm{H}}^{T}\boldsymbol{H}}{\|\boldsymbol{H}\|\left\|\boldsymbol{\varepsilon}_{\mathrm{H}}\right\|}} < \frac{\left\|\boldsymbol{\varepsilon}_{\mathrm{H}}\right\|}{\|\boldsymbol{H}\|}. \tag{5.61}$$

Thus, the relative error provides phase and amplitude errors concurrently and can account for the sensitivity of power quantities for phase errors. A geometric interpretation of Equation (5.61) is found in Figure 5.6 for the case of a SISO system.

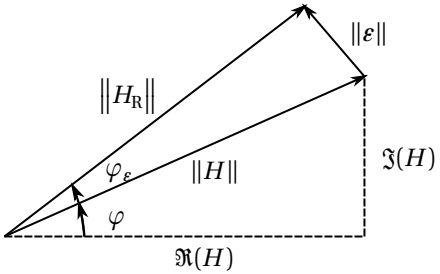

Figure 5.2: The relationship between the different components of the relative ROM error for SISO systems.

Equation (5.59) provides the error of the 0^{th} order moment of a transfer function. Corresponding errors can be calculated for any higher-order moment, too. Expressions, which allow for an efficient evaluation during the Arnoldi algorithm, are found in Lee et al. [145].

All the above expressions have in common that the FOM must be solved at each considered frequency point. This need foils the idea

of model order reduction, which should avoid the evaluation of the FOM. As a remedy, heuristics are used for error evaluation.

Two categories for approximations to the reduction error can be distinguished: extrapolatory and residual expressions. In extrapolatory error expressions, the reference solution is approximated by a second ROM. The error is then approximated by

$$\left\|\boldsymbol{\varepsilon}_{\mathrm{H}}\right\| = \left\|\boldsymbol{H} - \boldsymbol{H}_{\mathrm{R}}\right\| \approx \left\|\boldsymbol{H}_{\mathrm{R},2} - \boldsymbol{H}_{\mathrm{R}}\right\|, \tag{5.62}$$

respectively

$$\left\|\boldsymbol{\varepsilon}_{\mathrm{H,rel}}\right\| = \frac{\left\|\boldsymbol{H} - \boldsymbol{H}_{\mathrm{R}}\right\|}{\|\boldsymbol{H}\|} \approx \frac{\left\|\boldsymbol{H}_{\mathrm{R},2} - \boldsymbol{H}_{\mathrm{R}}\right\|}{\left\|\boldsymbol{H}_{\mathrm{R},2}\right\|}. \tag{5.63}$$

$\boldsymbol{H}_{\mathrm{R},2}$ may result from a reference ROM with interlaced expansion points. Grimme [105] initially suggested that approach, who called this kind of approximation *complementary*. Other choices for $\boldsymbol{H}_{\mathrm{R},2}$ are available in the literature. A ROM with increased moment order at the expansion points of the basis can be used (Bechtold et al. [29] and van de Walle [259]). In Grimme et al. [104] a weighted form of Equation (5.63) is proposed, in which a weighted sum of the differences between the current model with reduced models from several preceding iterations is calculated.

Such complementary error formulas are cheap to evaluate, but they require an additional reduced model. In addition, the quality of the approximation depends on the rate of convergence of the reference ROM to the solution of the FOM. Around the expansion points of the reference ROM, the approximation is supposed to give locally reasonable results, but this may not be the case for frequencies with a large distance to the expansion points. Both models, the ROM and reference ROM, may have the same (significant) error compared with the full system solution in such regions. Consequently, the error estimate may indicate a minimal error but hide the true one. Soppa [234] reports oscillating errors in such regions. However, a good approximation quality of complementary errors is reported for many applications (Grimme [105] and van de Walle [259]).

The second class of error estimators is based on residual expressions. For a subsystem, which is excited by the inputs $\boldsymbol{U}$, the residual in Laplace domain is

$$\begin{aligned}\boldsymbol{r}_{\mathrm{U}} &= \boldsymbol{B}\boldsymbol{U} - \boldsymbol{A}\boldsymbol{V}\boldsymbol{X}_{\mathrm{R}} = \boldsymbol{B}\boldsymbol{U} - \boldsymbol{A}\boldsymbol{V}\boldsymbol{A}_{\mathrm{R}}^{-1}\boldsymbol{V}^{H}\boldsymbol{B}\boldsymbol{U} \\ &= \boldsymbol{A}\underbrace{\left(\boldsymbol{A}^{-1}\boldsymbol{B}\boldsymbol{U} - \boldsymbol{V}\boldsymbol{A}_{\mathrm{R}}^{-1}\boldsymbol{V}^{H}\boldsymbol{B}\boldsymbol{U}\right)}_{\boldsymbol{\varepsilon}_{\mathrm{X}}} = \boldsymbol{A}\boldsymbol{\varepsilon}_{\mathrm{X}}.\end{aligned} \tag{5.64}$$

This allows to calculate the error of a subsystem's state vector introduced in the full order model by the reduced order model's solution from the residual as

$$\boldsymbol{\varepsilon}_{\mathrm{X}} = \boldsymbol{A}^{-1}\boldsymbol{r}_{\mathrm{U}}. \tag{5.65}$$

In order to calculate the error of the transfer function, the following input residual can be evaluated

$$\boldsymbol{r}_{\mathrm{B}} = \boldsymbol{B} - \boldsymbol{A}\boldsymbol{V}\boldsymbol{A}_{\mathrm{R}}^{-1}\boldsymbol{V}^{H}\boldsymbol{B} = \boldsymbol{A}\underbrace{\left(\boldsymbol{A}_{s}^{-1}\boldsymbol{B} - \boldsymbol{V}\boldsymbol{A}_{\mathrm{R}}^{-1}\boldsymbol{V}^{H}\boldsymbol{B}\right)}_{\boldsymbol{\varepsilon}_{\mathrm{B}}} = \boldsymbol{A}\boldsymbol{\varepsilon}_{\mathrm{B}}. \tag{5.66}$$

The error in the transfer function is obtained from

$$\boldsymbol{\varepsilon}_{\mathrm{H}} = \boldsymbol{C}\boldsymbol{\varepsilon}_{\mathrm{B}} = \boldsymbol{C}\boldsymbol{A}^{-1}\boldsymbol{r}_{\mathrm{B}}. \tag{5.67}$$

When $\boldsymbol{X}_{\mathrm{C}}$ is introduced as the solution of the dual (adjoint) problem,

$$\boldsymbol{A}^{T}\boldsymbol{X}_{\mathrm{C}} = \boldsymbol{C}^{T}, \tag{5.68}$$

and is inserted in Equation (5.67), one obtains a formula which is equal to the dual weighted residual method (DWR)

$$\boldsymbol{\varepsilon}_{\mathrm{H}} = \boldsymbol{C}\boldsymbol{A}^{-1}\boldsymbol{r}_{\mathrm{B}} = \boldsymbol{X}_{\mathrm{C}}^{T}\boldsymbol{r}_{\mathrm{B}}. \tag{5.69}$$

Applications of the DWR in model order reduction are found in Meyer et al. [175] and Voormeeren [269].

Taking a submultiplicative matrix norm of Equation (5.67), the following inequality holds

$$\left\|\boldsymbol{\varepsilon}_{\mathrm{H}}\right\| = \left\|\boldsymbol{C}\boldsymbol{A}^{-1}\boldsymbol{r}_{\mathrm{B}}\right\| < \left\|\boldsymbol{C}\boldsymbol{A}^{-1}\right\|\left\|\boldsymbol{r}_{\mathrm{B}}\right\| < \|\boldsymbol{C}\|\left\|\boldsymbol{A}^{-1}\right\|\left\|\boldsymbol{r}_{\mathrm{B}}\right\|. \tag{5.70}$$

The inverse of the dynamic stiffness matrix $\boldsymbol{A}$ must be calculated to evaluate Equation (5.70). This gives no computational savings against

calculating the true error directly from Equation (5.59). Nevertheless, Equation (5.70) can be used to calculate various approximations to the error norm $\left\|\varepsilon_{\mathrm{H}}\right\|$. The first and most basic approach is to omit the first part $\left\|\boldsymbol{C}\boldsymbol{A}^{-1}\right\|$ and just to assume a correlation between

$$\left\|\varepsilon_{\mathrm{H}}\right\| \sim \left\|\boldsymbol{r}_{\mathrm{B}}\right\|. \tag{5.71}$$

It is impossible to determine the quantitative error from this expression. However, Equation (5.71) potentially provides the qualitative trend of the true error ε_{H}. The qualitative trend may allow for determining the locations of maxima in the error in regions of the considered domain, in which the amplification by $\left\|\boldsymbol{A}^{-1}\right\|$ is not too high. Equation (5.71) consequently fails at system resonances with a low modal damping coefficient.

Another option is to approximate the adjoint solution by replacing the state of the full order system by the one of the ROM, either by the current one (Bodendiek et al. [37]) or by an extrapolated one as in complementary error estimates (Voormeeren [269]),

$$\left\|\varepsilon_{\mathrm{H}}\right\| < \left\|\boldsymbol{C}\boldsymbol{A}^{-1}\right\|\left\|\boldsymbol{r}_{\mathrm{B}}\right\| \approx \left\|\boldsymbol{C}_{\mathrm{R}}\boldsymbol{A}_{\mathrm{R}}^{-1}\right\|\left\|\boldsymbol{r}_{\mathrm{B}}\right\|. \tag{5.72}$$

Here, the same discussion holds as for complementary error approximations. The (extended) ROM needs to show sufficient convergence against the FOM solution for giving valuable results.

The third approach is to calculate some upper bound on $\left\|\boldsymbol{A}^{-1}\right\|$ and therefore a bound on the error $\left\|\varepsilon_{\mathrm{H}}\right\|$. Feng et al. [80] discuss several approaches for that. Corresponding methods, however, need an eigenvalue extraction from problems of FOM system size so that additional approximations need to be introduced for cost-efficient calculations.

Note, in the error expressions of Feng et al. [80], the residual $\boldsymbol{r}_{\mathrm{C}}$ of the dual problem Equation (5.68) is employed in addition. In fact, Equation (5.69) can be reformulated as (see Grimme [105])

$$\varepsilon_{\mathrm{H}} = \boldsymbol{r}_{\mathrm{C}}^{H}\boldsymbol{A}^{-1}\boldsymbol{r}_{\mathrm{B}}. \tag{5.73}$$

Involving dual systems, several other reformulations of Equation (5.69), respectively Equation (5.73) exist. Feng et al. [81] recently proposed a promising error estimate based on such reformulation, which, however, requires the construction of additional subspaces.

Although inversions of the FOM dynamic stiffness matrix may be avoided, any error estimate based on residuals needs matrix-vector,

respectively matrix-matrix multiplications of the full system size complexity. These costs can still form a severe computational bottleneck in a workflow if the latter requires the error estimate to be evaluated extensively many times. Methods thus should be limited to a reasonably low number of error estimator evaluations. As an alternative, the residue can be calculated cheaply as a side product for certain algorithms (see for example Gallivan et al. [89] and Skoogh [232]).

Corresponding to the idea of energetic analysis, which is followed throughout the thesis, a logical consequence would be to extend the (force-based) residual expressions to some energetic error measure. However, any extension of residuals leads to zero-valued expressions for a Galerkin projection as the residual does not exist in both the test and search spaces. The consequence is to monitor the error in the transfer function in both magnitude and phase, as discussed above.

5.7 Selection of Expansion Points in Laplace Domain

The Krylov-based MOR method, as presented above, answers *how* to match moments in a reduced model, but not on *where* in the Laplace domain and on to *what order*. In fact, one can generate very efficient and very poor ROMs with Krylov subspaces, depending on the choice of the expansion points and the expansion orders.

A limit for the maximum order at an expansion point is implicitly provided by the extended deflation of Section 5.5.3, although it may not be very efficient: If all candidate vectors in the iteration of an expansion order are deflated because they are below the minimum vector length, the expansion is naturally stopped at this iteration step. However, the question of the expansion point placement in the Laplace domain remains completely open in the above algorithms.

In principle, any complex-valued Laplace variable can be chosen as an expansion point κ. However, as follows from Equation (5.39) and Equation (5.40) moment matching at $\kappa = 0$ is not possible for a floating second-order subsystem, thus without Dirichlet boundary conditions applied. In such a setting, $\boldsymbol{K}$ is singular and $\boldsymbol{A} = \boldsymbol{K}$ as a result, too, which allows for no direct calculation of the required inverse.

Grimme [105] analyzed the effect of purely real and imaginary expansion points through the approximation of eigenvalues. He made the basic observation that purely imaginary expansion points $\kappa = i\omega$ lead to a better local approximation on the imaginary axis of

the Laplace domain around ω. Real-valued expansion points $\kappa = \sigma$, in contrast, provide a better global approximation over the whole frequency domain, but with lower local accuracy, especially around lightly damped eigenvalues. Nevertheless, an acceptable approximation is often also obtained around $\kappa = i\sigma$. In general, the choice of purely imaginary expansion points is more intuitive from a structural dynamics point of view, as the harmonic system analysis is performed along the imaginary axis of the Laplace domain. This choice allows controlling the error locally in the limited frequency band of interest. Therefore, expansion points on the imaginary axis of the Laplace domain are chosen in the following.

On the imaginary axis, expansion points could be placed manually by a try and error principle or in a fixed spacing. However, this is unlikely to result in a (pseudo-) optimal expansion point placement and, therefore, efficient ROMs. As a remedy, automated procedures exist. In such procedures, a training is performed, in which more optimal locations for expansion points are determined. Two major strategies are available: $\mathcal{H}_2$-optimal methods and greedy search strategies.

The first class is formed by $\mathcal{H}_2$-optimal methods. The $\mathcal{H}_2$-norm of the transfer function is defined as

$$\|\boldsymbol{H}\|_{\mathcal{H}_2} = \sqrt{\frac{1}{2\pi}\int_{-\infty}^{\infty} \operatorname{tr}\left(\boldsymbol{H}^H(i\omega)\boldsymbol{H}(i\omega)\right) d\omega}. \tag{5.74}$$

In the context of $\mathcal{H}_2$-optimality, methods seek to construct (pseudo-) optimal ROMs for which $\left\|\varepsilon_{\mathrm{H}}\right\|_{\mathcal{H}_2}$ is minimized, at least locally. Gugercin et al. [106, 107] introduced the iteratively corrected rational Krylov algorithm (IRKA), approaching that optimality for a prescribed number of expansion points, thus model size. Therefore, solely 0^{th} and 1^{st} order moments are calculated at these expansion points, which are shifted iteratively to the optimal locations for a first-order SISO system. The expansion points for the next iteration are the eigenvalues of the ROM in the current step, mirrored at the imaginary axis. In the general case, therefore, the expansion points are complex valued with both real and imaginary parts. The iteration is continued as long as the change in the eigenvalues is above a prescribed error threshold. The concept can be extended to MIMO systems with tangential interpolation (compare Section 5.5.3 and see Bunse-Gerstner et al. [49], Gugercin et al. [107], and Van Dooren et al. [261]). In the original form, IRKA is a fixed-point iteration. Other versions, which provide

monotonic decay in contrast to classic IRKA, employ Newton iterations (Beattie et al. [28]) or trust-region methods (Beattie et al. [27]), but need still further development (Panzer [189]). A formulation of IRKA for second-order systems can be found in Wyatt [275] or Soppa [234].

IRKA is a powerful method; however, it is not without drawbacks. There are challenges, especially concerning practical applications for large-scale models. IRKA considers the error in the transfer function globally over the whole frequency range as $\mathcal{H}_2$-optimal method, but not locally limited in the frequency band of interest. ROMs from IRKA, therefore, may be larger as required for that application. In addition, no error control on the transfer function is included in the original formulation, as solely the shift of eigenvalues is monitored. Moreover, the computations for the projection matrix generation are expensive as a repetitive factorization of $\boldsymbol{A}$ is required for all expansion points, which are shifted in each iteration.

The other class of training methods employs greedy search strategies to determine the placement of expansion points or the necessity for additional orders. In a greedy search, information is added one after the other to the basis. The best location for the next imaginary expansion point or additional orders is determined per step, based on an error measure evaluated over candidate samples. The latter form the training set, from which the location for adding information is chosen as the sample with the maximum error measure. Many different greedy approaches can be found in literature, differing among others in the used error measure or the training set. One may take the true error of higher-order moments on a fixed training set into account to iteratively add orders at expansion points (Lee et al. [145], or Soppa [234]). As determining the true error is not feasible for large-scale industrial FOMs, error estimates can be used as a proxy according to Section 5.6. Different residual expressions may be used, refer to Bodendiek et al. [37], Druskin et al. [69], and Grimme et al. [104] for examples. van de Walle [259] utilizes an extrapolatory error estimate.

Greedy approaches are attractive for practical algorithms for large-scale industrial models. Having the flexibility of error control, greedy approaches are suited for a targeted fitting of models for a frequency range of interest, as corresponding error expressions can be evaluated. The training phase can be computationally efficient when using approximations for the error. However, the selection of the training set and the quality of the error estimate are crucial for the final ROM

accuracy. The frequency range in which the model should be valid must be screened sufficiently during training. If the greedy search concept should be extended to parametric subsystems, this imposes a particular challenge. In principle, the flexibility of a greedy search allows for a straightforward extension to such a setting. Nevertheless, an additional dimension is added for each parameter, for which the ROM should be valid.

5.8 Chapter Summary

The concept of projection-based model order reduction was introduced to apply subsystem coupling approaches. For subsystems with a large number of states, an approximate subsystem model can be obtained by projecting the inner representation on a smaller subspace. In the offline phase, appropriate projection matrices are found for the single subsystems, decoupled from the assembly and preserving the interface structure. In the online phase, the resulting ROMs are used to evaluate the assembly in significantly less time.

After several MOR methods were discussed to calculate such projection matrices, the Krylov subspace method was chosen. The attraction of this approach for the energetic network analysis of vehicle structures was discussed. It is promising for subsystem coupling applications as it implicitly provides moment matching, respectively interpolation, of the input-to-output behavior of the subsystems, the relevant quantity for coupling. The interpolation is achieved locally controlled, thus allowing for the targeted fit of the ROM in band-limited domains of interest. Arbitrary damping information can be included in the projection matrix, which is essential for accurate damping modeling in the ROM and, therefore, accurate energy flows. The basic concepts of Krylov subspaces for second-order systems were discussed, with emphasis on the inclusion of structural damping. The latter, which is usually not included in corresponding formulations of the method, leads to complex-valued projection matrices and, thus, subsystem matrices. As a consequence, a complex notation was followed for the projection framework. It was shown that a complex-valued Bubnov-Galerkin projection preserves passivity following the novel formulation of Section 2.3.4. Therefore, a Bubnov-Galerkin projection was chosen using input Krylov subspaces concatenated from bases at several purely imaginary shifts of the Laplace variable.

A newly modified one-stage Arnoldi algorithm was introduced with particular emphasis on the application to large-scale industrial models. It was derived that this algorithm provides moment matching for second-order systems with Rayleigh damping and arbitrary structural damping. A modified orthogonalization procedure and a novel QR-based deflation procedure achieved applicability to large-scale industrial models. In addition, it includes a geometric approach for augmented deflation, allowing a reduction of the size of ROMs with many in- and outputs.

General error measures for ROMs were discussed. Based on those error considerations, two basic classes of adaptive training methods were discussed for an adaptive selection of expansion points in the Laplace domain. It was pointed out that a greedy training approach is conceptually promising for industrial models and allows for targeted model refinement in the Laplace domain.

CHAPTER 6

KRYLOV-SUBSPACE LEARNING FOR FE SUBSYSTEMS: PARAMETRIC SYSTEMS

The Krylov-based MOR approach needs to be extended for massive multi-query applications in the online phase, in which subsystem design parameters like the shell thickness or mass loading are varied. A method must be developed to preserve the explicit parametric dependency in the reduced model within pre-defined value bounds, thus without the need to repeat the whole process of Krylov-based MOR each time the parameters are varied.

Vehicle networks usually contain several hundreds of variable design parameters. Here, the subsystem coupling approach is the first enabler, as it allows for mapping the global parameters to the single subsystems. Reduced subsystem models do not have to cover this very high-dimensional parameter space as a result, but still high orders up to $d \leq 15$. At the same time, full-order vehicle subsystems have large-scale state vectors, as discussed above, and the basis generation may be computationally costly. The design of corresponding algorithms is challenging in light of this combination. In the following, a method is proposed to cope with this combination; many paragraphs follow closely Ullmann et al. [254] for this. For method development, it is

assumed throughout the chapter that the subsystem dynamics are highly parameter dependent but limited at a distinct parameter sample. In other words, the number of resonant modes of the subsystems is moderate ($n_{\mathrm{res}} < 20$) in the frequency ranges of interest.

6.1 From Non-Parametric to Parametric Model Order Reduction (pMOR)

6.1.1 A Classification Scheme for pMOR

In the context of the offline-online separation principle of the thesis, methods for parametric model order reduction (pMOR) can be classified according to the approaches chosen for the three necessary steps:

1. parameter sampling for identifying samples at which information should be included in the ROM subspace, thus the training strategy in the offline phase.
2. the projection matrix construction itself at the selected parameter values in the offline phase.
3. the ROM generation at a requested parameter set in the online phase.

This scheme is also followed by Benner et al. [32], who provide an extensive overview of pMOR methods. The first two steps were already discussed in Chapter 5 for non-parametric MOR and can be adapted for pMOR. For the second step of projection matrix generation, the approach of Krylov subspaces according to the preceding chapter is used. Several advantages of Krylov subspace methods were already discussed above, the direct approximation of the input-to-output behavior or the correct damping modeling, for example. Furthermore, Krylov subspace methods are also attractive for pMOR in particular, as the ability to add information locally targeted to the reduced model can be extended to the multi-dimensional parameter domain. Thus, it provides more control over the ROM training in high-dimensional but bounded domains as it would be possible with modal methods, for example. For Krylov subspace methods, the initial training step to determine parameter sampling points for expansion is closely linked

to the discussion of expansion point placement in the Laplace domain as provided in Section 5.7. However, it is more challenging for parametric problems: corresponding design parameter samples need to be determined in addition to the position of expansion points in the Laplace domain. The sampling strategy is extended in Section 6.2 with a new approach to meet that challenge.

The third step of ROM generation contains the basic concept of handling parameter variations in the ROM during the online phase. This step is not addressed yet and allows for a classification of pMOR methods in two basic schemes: local and global approaches. In global approaches, a projection basis is found, which covers the whole parameter space. Local approaches generate non-parametric ROMs at different parameter samples in the offline phase. These local ROMs are interpolated over the parameter space for any parameter sample at which the system should be evaluated in the online phase. Generically chosen interpolating basis functions are used for this. The basic concepts are visualized in Figure 6.1.

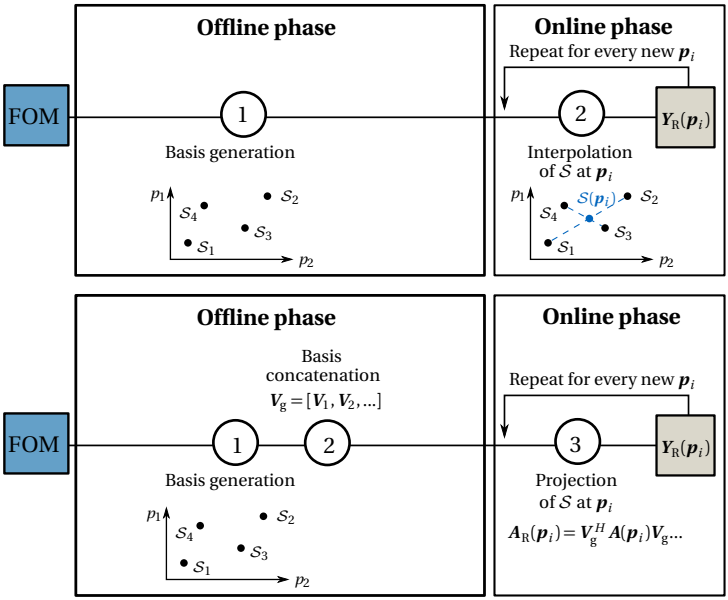

Figure 6.1: Visualization of the local versus global concatenation approach for parametric model order reduction.

Different concepts for interpolation exist in local methods: Amsallem et al. [11], Borggaard et al. [41], and Son [233] interpolate the local projection matrices. Amsallem et al. [10], Degroote et al. [67], and Panzer et al. [188] perform an interpolation of the reduced system matrices. Baur et al. [23] and Baur et al. [25] use an interpolated reduced transfer functions. In the context of the latter, an interpolation in the pole-residue form recently received attention (Yue et al. [277, 278]).

Local pMOR methods are attractive as no information about the parametric dependency is necessary. The basis functions for the interpolation are chosen generically, as polynomials, for example, which do not precisely reproduce the underlying parametric dependency of the interpolated quantity. This choice of basis functions enables pMOR approaches for parameter-black-box subsystems, which provide the outputs for any input and design parameters, but no knowledge about the output's analytic dependency on the design parameters. For interpolation of reduced system matrices or bases, the resulting ROMs are usually of small size and independent of the number of local ROMs in the parameter space. These advantages, however, come along with several drawbacks.

Analyzing the three necessary steps for pMOR, two stages can be challenging for systems with high-dimensional design parameter space. The latter needs to be sufficiently covered in both the first step of model training and the third step of ROM generation. The required coverage can potentially result in the *curse of dimensionality* arising from these two steps - depending on the pMOR method. Local approaches suffer from that *curse of dimensionality* at least for the third step of ROM generation for varying parameter values. The required number of local ROMs grows exponentially with the number of parameters for regular interpolation grids; thus, the computational costs to construct the ROMs in the offline phase and perform the interpolation in the online phase. As a result, higher-dimensional parameter spaces up to an order of $d = 15$ cannot be covered with classic formulations. Remedies are available, the application of sparse grids according to Baur et al. [23] and Geuss et al. [95], for example. However, hundreds to thousands of FOM evaluations are still needed in the offline phase, which is infeasible for industrial FOMs due to their large-scale nature. There is a second class of methods to remedy that, which is discussed in the following section.

6.1.2 The Global Basis Approach

A global basis method is a promising approach for such subsystems, as it appeared to be suitable for ROM generation in higher-dimensional parameter spaces (Benner et al. [32]). If an efficient training strategy is utilized, potentially fewer FOM system solutions are needed compared to local approaches, thus also considering the high computational costs of solving large-scale FOM systems.

In global approaches, one projection matrix $\boldsymbol{V}_\mathrm{g}$ is found, thus one ROM which is valid over the whole parameter space at any parameter. $\boldsymbol{V}_\mathrm{g}$ can be obtained by assembling local bases at different parameter points

$$\boldsymbol{V}_\mathrm{g} = \left[\boldsymbol{V}_1\ \boldsymbol{V}_2\ \ldots\ \boldsymbol{V}_z\right], \tag{6.1}$$

with $\boldsymbol{V}_i$ being the local basis for a design parameter sample $\boldsymbol{p}_i$. By selecting a sufficiently high number of local bases and appropriate locations in the parameter space for their generation, $\boldsymbol{V}_\mathrm{g}$ is valid for the whole bound d-dimensional parameter space of interest $\boldsymbol{p}_z \in \left[\boldsymbol{p}_\mathrm{l}, \boldsymbol{p}_\mathrm{u}\right]$, where d is the number of dimensions.

The single $\boldsymbol{V}_i$ are computed using the Krylov subspace methods of Chapter 5 in the following. Thus, one matches transfer function moments in one dimension along the Laplace variable s, as defined by Equation (5.25). Some methods extend the concept of moment matching to additional parameter dimensions for pMOR. Refer to Benner et al. [31] and Daniel et al. [64] for one approach. Such a method reformulates the transfer function's moments, thus its derivatives, for additional parameter dimensions. Although conceptually promising, established algorithms like Arnoldi-type approaches need to be at least modified, and generality for arbitrary parameter dependencies is an open topic as discussed by Baur et al. [24]. Therefore, such extension is not followed in the thesis, but moments solely with respect to the Laplace variable are calculated at samples in the multi-dimensional parameter space.

The global basis approach avoids most of the drawbacks of local approaches. A potential pitfall of global bases is a larger ROM size compared to local pMOR. Nevertheless, when the number of resonant modes n_res of the subsystems is moderate in the frequency range of interest, the size of each local basis is limited. Such setting is assumed in the thesis ($n_\mathrm{res} < 20$) as indicated above. An additional disadvantage arises when the global approach is used in its basic formulation as

visualized in Figure 6.1. The system matrices of the FOM change each time a parameter is changed. This change requires the projection of the system matrices according to Equation (5.8) after each parameter change during the online phase. The repetitive projection forms a computational bottleneck, as the right-hand side projection has a time complexity of $\mathcal{O}(n^2 m)$, where n is the size of the FOM.

An affine matrix decomposition of the FOM system matrices can be introduced for the global method to avoid these repetitive projections of the system matrices. The affine matrix decomposition of the parameter-dependent matrix $\boldsymbol{A}(\boldsymbol{p})$ is given by

$$\boldsymbol{A}(\boldsymbol{p}) = \sum_{j=1}^{h} f_j(\boldsymbol{p})\, \boldsymbol{A}_j, \tag{6.2}$$

while $f_j(\boldsymbol{p})$ are scalar functions of the parameter vector $\boldsymbol{p}$ and the affine matrices $\boldsymbol{A}_j \in \mathbb{C}^{n\times n}$ are parameter independent. Affine matrix decompositions may be accessible directly in a parameter-white-box approach, indirectly in parameter-gray-box settings, or just approximated in a parameter-black-box constraint. These cases are discussed in the section below. The knowledge of the affine decomposition of a matrix allows computing its projection by

$$\boldsymbol{A}_{\mathrm{R}}(\boldsymbol{p}) = \boldsymbol{V}_{\mathrm{g}}^H \boldsymbol{A}(\boldsymbol{p}) \boldsymbol{V}_{\mathrm{g}} = \sum_{j=1}^{h} f_j(\boldsymbol{p})\, \boldsymbol{V}_{\mathrm{g}}^H \boldsymbol{A}_j \boldsymbol{V}_{\mathrm{g}} = \sum_{j=1}^{h} f_j(\boldsymbol{p}) \boldsymbol{A}_{\mathrm{R},j}. \tag{6.3}$$

Consequently, it is possible to precompute the projections $\boldsymbol{A}_{\mathrm{R},j}$ once the projection basis is found. Afterward, $\boldsymbol{A}_{\mathrm{R}}(\boldsymbol{p})$ can be evaluated in the online phase for any parameter value by a weighted superposition of the single $\boldsymbol{A}_{\mathrm{R},j}$, without the need of projections. Combining the global basis method with an affine matrix decomposition, as illustrated in Figure 6.2, an efficient pMOR procedure is available for many large-scale FOMs. This combination is already well established, in particular in a class of techniques under the name of reduced basis methods (Patera et al. [193]). In these methods, the parameter sampling is performed using a greedy search strategy, and a global basis is constructed, mainly using Proper Orthogonal Decomposition (POD), refer to Sirovich [230].

If such a combined global basis method is used instead of a local pMOR approach, the challenge of interpolation is shifted to an earlier

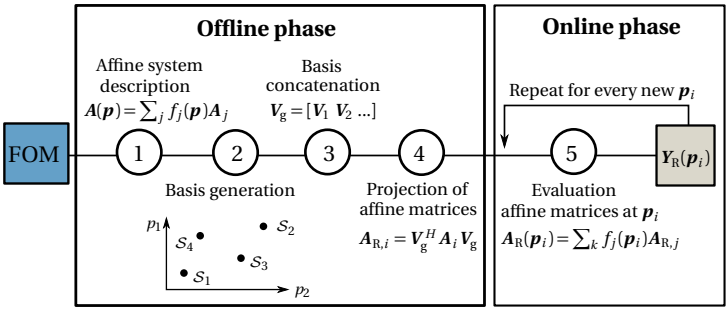

Figure 6.2: Workflow visualization of the global basis approach in combination with an affine matrix decomposition.

stage of the pMOR process. The interpolation rules for the FOM system matrices need to be constructed at the beginning of the offline phase. This shifted interpolation contrasts local methods, in which an interpolation scheme between different ROMs needs to be evaluated in the online phase. This shift leads to a significant advantage of global basis methods: there is a known low-rank dependency of the FOM system matrices with respect to many commonly used design parameters, which thus can be derived analytically. In contrast, the analytic relationship between the reduced systems in a local pMOR is usually unknown but generically approximated. Thus, additional knowledge is potentially available in global basis approaches to meet the curse of dimensionality in the step of ROM generation, as the system immanent interpolating basis functions are known. No generic interpolation scheme must be found on a possibly dense sample grid.

Following the global basis framework, two fundamental challenges remain open for the moment: Firstly, how corresponding affine matrix decompositions can be found. This is addressed in Section 6.1.3. Secondly, how an efficient global basis can be found to obtain a minimized ROM size for the desired accuracy. The latter question results in how a training phase can be designed, which provides a pseudo optimal sampling point placement in the high-dimensional parameter space and utilizes as little as possible FOM evaluations for the inclusion of large-scale industrial systems. Section 6.2 addresses such a training strategy.

Algorithm 6.1: Construction of system matrices by an affine description.

Input : System representation $\mathcal{S}$, parameter vector $\boldsymbol{p}$
Output : System matrices $\boldsymbol{A}$, $\boldsymbol{M}$

Function `evaluateSystemAt(`$\mathcal{S}$, $\boldsymbol{p}$`):`

```
// read affine description from system object
```

$\mathcal{S} \rightarrow f_{\mathrm{K},i}(\boldsymbol{p})$, $\boldsymbol{K}_i$, $f_{\mathrm{M},i}(\boldsymbol{p})$, $\boldsymbol{M}_i$, $f_{\mathrm{S},i}(\boldsymbol{p})$, $\boldsymbol{S}_i$, $f_{\mathrm{D},i}(\boldsymbol{p})$, $\boldsymbol{D}_i$

```
// evaluate system matrices of S at p
```

$\boldsymbol{K} = \sum_i f_{K,i}(\boldsymbol{p})\, \boldsymbol{K}_i$

$\boldsymbol{M} = \sum_i f_{M,i}(\boldsymbol{p})\, \boldsymbol{M}_i$

$\boldsymbol{S} = \sum_i f_{S,i}(\boldsymbol{p})\, \boldsymbol{S}_i$

$\boldsymbol{D} = \sum_i f_{D,i}(\boldsymbol{p})\, \boldsymbol{D}_i$

```
// get frequency of excitation
```

$\omega = \boldsymbol{p}(\mathrm{end})$

```
// calculate dynamic stiffness
```

$\boldsymbol{A} = \boldsymbol{K} + i\,\boldsymbol{S} + i\,\omega\boldsymbol{D} - \omega^2\boldsymbol{M}$

return $\boldsymbol{A}$, $\boldsymbol{M}$

6.1.3 Affine Decomposition for Second-Order System Matrices

To evaluate an affine matrix decomposition at a parameter sample numerically, Equation (6.2) can be reformulated as an interpolation problem

$$\boldsymbol{a}(\boldsymbol{p}) = \boldsymbol{\Omega}\hat{\boldsymbol{f}}(\boldsymbol{p}) \tag{6.4}$$

with the vectorized matrix $\boldsymbol{a}(\boldsymbol{p}) = \mathrm{vec}\big(\boldsymbol{A}(\boldsymbol{p})\big)$. $\hat{\boldsymbol{f}}(\boldsymbol{p}) \in \mathbb{C}^{h\times 1}$ contains the h basis functions for interpolation and $\boldsymbol{\Omega} \in \mathbb{C}^{n_\mathrm{a}\times h}$ the corresponding interpolation coefficients, respectively $\mathrm{vec}\big(\boldsymbol{A}_j\big)$ per column. n_a is the length of $\boldsymbol{a}(\boldsymbol{p})$.

An implementation for the evaluation and projection of affine second-order system matrices is presented in Algorithm 6.1, respectively Algorithm 6.2. Note that a representation of the system matrices in terms of an affine decomposition is not only valuable for avoiding repetitive projections in pMOR but also allows for analytic sensitivity calculations (see Algorithm 6.4 on page 160).

Although it is assumed in the following that such representation of the system matrices exists for the considered design parameters,

it is not guaranteed that the corresponding affine decomposition is accessible. As the presented work postulates the principle of non-intrusiveness, existing FE assembly routines are used as the basis for the pMOR of industrial models. However, commercial FE programs do not provide white-box access to their source code; thus, one cannot directly extract $\boldsymbol{\Omega}$ and $\hat{\boldsymbol{f}}(\boldsymbol{p})$ from the code. Instead, two non-intrusive approaches can be distinguished to reconstruct those quantities: parameter-black-box and parameter-gray-box approaches.

Algorithm 6.2: Projection of an affinely decomposed full-order system.

Input : System representation $\mathcal{S}$, projection matrix $\boldsymbol{V}$
Output : Reduced system representation $\mathcal{S}_\mathrm{R}$

Function `projectSystem(`$\mathcal{S}$`,`$\boldsymbol{V}$`):`

`//  read affine description from system object`
$\mathcal{S} \rightarrow f_{\mathrm{K},i}(\boldsymbol{p})$, $\boldsymbol{K}_i$, $f_{\mathrm{M},i}(\boldsymbol{p})$, $\boldsymbol{M}_i$, $f_{\mathrm{S},i}(\boldsymbol{p})$, $\boldsymbol{S}_i$, $f_{\mathrm{D},i}(\boldsymbol{p})$, $\boldsymbol{D}_i$
`//  project affine matrices`
for $i = 1$ *to* h_K **do**
  $\boldsymbol{K}_{\mathrm{R},i} = \boldsymbol{V}^H \boldsymbol{K}_i \boldsymbol{V}$
for $i = 1$ *to* h_M **do**
  $\boldsymbol{M}_{\mathrm{R},i} = \boldsymbol{V}^H \boldsymbol{M}_i \boldsymbol{V}$
for $i = 1$ *to* h_S **do**
  $\boldsymbol{S}_{\mathrm{R},i} = \boldsymbol{V}^H \boldsymbol{S}_i \boldsymbol{V}$
for $i = 1$ *to* h_D **do**
  $\boldsymbol{D}_{\mathrm{R},i} = \boldsymbol{V}^H \boldsymbol{D}_i \boldsymbol{V}$
`//  write affine description to reduced system object`
$\mathcal{S}_\mathrm{R} \leftarrow f_{\mathrm{K},i}(\boldsymbol{p})$, $\boldsymbol{K}_{\mathrm{R},i}$, $f_{\mathrm{M},i}(\boldsymbol{p})$, $\boldsymbol{M}_{\mathrm{R},i}$, $f_{\mathrm{S},i}(\boldsymbol{p})$, $\boldsymbol{S}_{\mathrm{R},i}$, $f_{\mathrm{D},i}(\boldsymbol{p})$, $\boldsymbol{D}_{\mathrm{R},i}$
return $\mathcal{S}_\mathrm{R}$

Parameter-Gray-box Approaches

In the case of a parameter-gray-box system, the program source code is not accessible for intrusive changes. However, additional knowledge is available on the parametric dependency of the FOM system matrices on $\boldsymbol{p}$. The basis functions for $\hat{\boldsymbol{f}}(\boldsymbol{p})$ are known analytically and are entirely determined. The knowledge of basis functions allows for an

exact interpolation: the interpolation coefficients $\boldsymbol{\Omega}$, respectively the affine matrices, can be obtained by

$$\boldsymbol{\Omega} = \boldsymbol{\chi}\, \boldsymbol{F}_{\mathrm{p}}^{-1}. \tag{6.5}$$

$\boldsymbol{\chi} = \left[\boldsymbol{a}(\boldsymbol{p}_1) \ldots \boldsymbol{a}(\boldsymbol{p}_h)\right]$ is a snapshot matrix and $\boldsymbol{F}_{\mathrm{p}} = \left[\hat{\boldsymbol{f}}(\boldsymbol{p}_1) \ldots \hat{\boldsymbol{f}}(\boldsymbol{p}_h)\right]$ the matrix of corresponding function values.

Basis functions are known for many parameters of vibroacoustic FE models in practice. There is a large class of parameters for which the whole system matrices or parts of it are linearly dependent. This linear dependency holds for material parameters of many finite element formulations: the dependency of the stiffness matrix on the modulus of elasticity E, of the mass matrix on the mass density ρ, of the damping matrices on the structural damping coefficient η or the Rayleigh damping coefficients α and β. Furthermore, discretized components in the model, like linear springs or viscous dampers, introduce linear dependencies on their characterizing parameters.

In the context of specific mechanical modeling, the basis functions are also known for many cases of geometric parametrization. For modeling shells by triangular plate elements, the system matrices depend on the thickness through a cubic polynomial. For the use of Euler-Bernoulli and Timoshenko beam elements, the parametrization for the element length and cross-section dimensions is known. If more general element formulations are used, solid elements, in particular, the derivation of Equation (6.4) is also possible for shape parameters characterizing variations like stretch or warping. Refer to Fröhlich et al. [86] for an exemplary parametrization, another one is found in Section 6.2.5.

Parameter-Black-box Approach

In contrast, neither the underlying FE code is accessible nor additional knowledge about the parameter dependency of the system matrices is available in a parameter-black-box approach. However, an approximated parametric dependency can be found by an inexact interpolation, again in the form of Equation (6.4). $\hat{\boldsymbol{f}}(\boldsymbol{p})$ are generically chosen basis functions in this case, typically polynomials. Alternatives are available, like regression methods, a Gaussian kernel regression (see Rasmussen et al. [205] for an illustrative explanation) or the method of moving least squares (Levin [151]).

Another conceptually different approach to Equation (6.4) is given by the Discrete Empirical Interpolation Method (DEIM). The DEIM combines interpolation with projection and was introduced by Chaturantabut et al. [52] for the approximation of non-linear problems. Later it was used for the approximation of nonaffinely parametrized linear operators, see Antil et al. [14] and Benner et al. [32]. In the DEIM, the interpolation coefficients $\boldsymbol{\Omega}$ are determined from an SVD of z parameter samples of $\boldsymbol{a}(\boldsymbol{p})$

$$\boldsymbol{\Omega}\boldsymbol{\Theta}\boldsymbol{N}^H = \left[\boldsymbol{a}(\boldsymbol{p}_1)...\boldsymbol{a}(\boldsymbol{p}_z)\right]. \tag{6.6}$$

Afterward, discrete values of $\hat{\boldsymbol{f}}(\boldsymbol{p})$ are obtained by enforcing Equation (6.4) not to approximate $\boldsymbol{a}(\boldsymbol{p})$ for its full parametric dependency, but to be exact for the requested parameter value $\boldsymbol{p}$. Ensuring the equivalence of the left and right-hand side of Equation (6.4) for any value in $\boldsymbol{a}(\boldsymbol{p})$ would result in a highly overdetermined system of equations, as $z \ll n_a$. As a remedy, the constraint is imposed only on some entries of $\boldsymbol{a}(\boldsymbol{p})$ and a permutation matrix $\boldsymbol{O}$ is introduced for the selection of the corresponding entries in $\boldsymbol{a}(\boldsymbol{p})$. Then, Equation (6.4) takes the form of

$$\boldsymbol{O}^T\boldsymbol{a}(\boldsymbol{p}) = \boldsymbol{O}^T\boldsymbol{\Omega}\hat{\boldsymbol{f}}(\boldsymbol{p}). \tag{6.7}$$

This results in the required interpolation coefficients for a parameter sample $\boldsymbol{p}$

$$\hat{\boldsymbol{f}}(\boldsymbol{p}) = \left(\boldsymbol{O}^T\boldsymbol{\Omega}\right)^{-1}\boldsymbol{O}^T\boldsymbol{a}(\boldsymbol{p}). \tag{6.8}$$

The DEIM determines $\boldsymbol{O}$ by a greedy approach, refer to Chaturantabut et al. [52] for details. Following the approach of POD and DEIM, an approximate affine matrix decomposition is finally obtained in the form of Equation (6.4). Apart from a black-box case, there are several other settings in which the DEIM method is useful: for obtaining an approximate decomposition when no affine decomposition theoretically exists for the FOM system matrices; for gray-box models, if the decomposition consists of many terms ($h \gg 1$) and should be reduced to a smaller h.

As a drawback of the approach, no analytic functions $\hat{\boldsymbol{f}}(\boldsymbol{p})$ are found, but discrete samples of the latter. The factor $\left(\boldsymbol{O}^T\boldsymbol{\Omega}\right)^{-1}\boldsymbol{O}^T$ can be pre-computed for efficiency improvements, however, $\boldsymbol{a}(\boldsymbol{p})$ must be evaluated at $\boldsymbol{p}$. For any change in the parameters, the evaluation

of $\boldsymbol{a}(\boldsymbol{p})$ requires the assembly of the FOM system matrices; thus, the external FE code is executed. The need to evaluate the FOM matrices and to exchange them between different programs foils the concept of a highly efficient pMOR code. The modification of the FE assembly code can be a remedy (see Negri et al. [181]), as only a few entries of $\boldsymbol{a}(\boldsymbol{p})$ are required in Equation (6.8). Such a modification, however, is intrusive and needs full access to the FE source code, which is not the case in a black-box setting.

In the following, the discussion focuses on parameter-gray-box systems, for which an exact affine matrix decomposition can be calculated. Only round-off errors are present as a consequence, and it is assumed that no errors are introduced for the generation of the affine matrix decomposition.

6.2 OGPA: Optimization-Based Greedy Parameter Sampling for Training

While the global basis approach faces the curse of dimensionality in the third step in pMOR methods, this is not necessarily the case for the first step of model training. For Krylov subspace methods, both proper sampling positions in the bounded high-dimensional parameter space of interest, as well as expansion points in the band-limited Laplace domain, have to be determined for the construction of each local basis $\boldsymbol{V}_{\mathrm{g}}$ in Equation (6.1), thus the training. This identification is achieved by a proper training strategy discussed in the following for an application to large-scale industrial models.

Note that the thesis postulates strict separation of the online and the offline phase. This separation implies that one trains the global basis for the whole admissible parameter space a-priori to the actual multi-query application in the online phase. No feedback of the multi-query application into the parametric reduced-order model (pROM) training is considered. Refer to Section 8.2.3 for a short discussion on potentially alternative concepts in the context of vehicle optimizations with pROMs.

6.2.1 Available Concepts for High-Dimensional Point Placement

The challenge of expansion point placement in the Laplace domain was discussed for non-parametric MOR in Section 5.7. As indicated above, finding appropriate samples in the parameter space is even more complex for pMOR methods, as not the one-dimensional frequency domain but higher-dimensional bound spaces must be covered. Therefore, the following overview is adapted from Ullmann et al. [254]. As in the non-parametric case, sampling-based greedy search strategies are attractive for such training. They are not globally optimal with respect to some norm, what IRKA-like concepts in the parameter domain can provide (see Baur et al. [24], Hund et al. [125], and Tomljanović et al. [246]). However, neither integrating the considered error measure over the high-dimensional parameter space nor the repetitive factorization of the system matrix $\boldsymbol{A}$ at all sampling points is necessary during a greedy search. Thus, greedy approaches are an attractive choice as an enabler for pMOR methods, which should be applied to large-scale industrial models.

To ensure that a greedy search determines efficient ROMs, it must provide sufficient coverage of the typically non-convex error measure. An appropriate training set usually is chosen for this, at which the error function is sampled and the ROM is trained. However, sufficient coverage by a training set is difficult for the d-dimensional parameter spaces of industrial FOMs, where the dimension d is high. Using regular sampling grids results in a time complexity of $\mathcal{O}(n_{\text{sam}}^d)$ for n_{sam} samples per parameter dimension d. Sampling a 15-dimensional parameter space just coarsely by three samples per parameter dimension already requires $14 \cdot 10^6$ grid points; this highlights the curse of dimensionality for the training phase of basis generation.

Several remedies are available for that. Non-regular sampling strategies can be used for the generation of a training set; refer to McKay et al. [170] for an example who used Latin Hypercube Sampling. Several adaptive greedy approaches were developed as an alternative to static training sets. Corresponding methods follow different refinement strategies, refer to Chellappa et al. [53], Haasdonk et al. [110], and Hesthaven et al. [122]. In that context, Sen [224] introduced a multi-stage procedure, Paul-Dubois-Taine et al. [194] used additional surrogate models to identify regions for sampling refinement. As in local methods, sparse grids are another alternative and provide

adaptive hierarchical greedy approaches, see Bungartz et al. [48] and Zenger [282]. This approach was already applied in global reduced basis methods, refer to Chen et al. [55] and Peherstorfer et al. [199].

As a further remedy, there are greedy methods that follow a grid-free sampling approach as introduced by Bui-Thanh et al. [46] and Bui-Thanh [47]. Again, the concept already found several applications in the context of reduced basis methods, refer to Iapichino et al. [128] and Urban et al. [258]. Opposed to the above-discussed greedy approaches, the maximization of the error measure is not performed on a fixed or adaptive grid. Instead, the constrained non-linear optimization problem

$$ {}^{j}\boldsymbol{p}_{\mathrm{opt}} = \underset{\boldsymbol{p}\in[\boldsymbol{p}_{\mathrm{l}},\boldsymbol{p}_{\mathrm{u}}]}{\operatorname{argmax}} \left\| \boldsymbol{\varepsilon}\left(\boldsymbol{p}\right) \right\| \tag{6.9} $$

is solved for the j-th expansion point position ${}^{j}\boldsymbol{p}_{\mathrm{opt}}$ to be added to the global basis at the j-th greedy iteration. The objective $\boldsymbol{\varepsilon}\left(\boldsymbol{p}\right)$ is an error function of the ROM, from which some norm is taken. At each iteration, an initial random guess of the parameter position ${}^{j}\boldsymbol{p}_{0}$ is provided as the starting point for optimization. Furthermore, an initial ROM with $\boldsymbol{V}_{\mathrm{g}} = \boldsymbol{V}_{0}$ is required for the initial error evaluations, thus starting the overall greedy procedure. Afterward, the original method of Bui-Thanh et al. [46] employed a gradient-based optimization for the solution of Equation (6.9) in each greedy iteration. Bui-Thanh et al. [46] developed the concept for systems both in a steady and unsteady configuration. For the latter, the error control was performed in the time domain for the state solution, and the error measure was integrated over the whole relevant time span for each parameter sample

$$ \boldsymbol{\varepsilon}\left(\boldsymbol{p}\right) = \int_{t} \boldsymbol{\varepsilon}\left(\boldsymbol{p}, t\right) \mathrm{d}t \tag{6.10} $$

to obtain the optimization objective. In each greedy iteration, optimization of this integrated error was performed to identify ${}^{j}\boldsymbol{p}_{\mathrm{opt}}$ in the first step. In the second step, a local basis was generated from the span of the state solutions over time at the parameter sample ${}^{j}\boldsymbol{p}_{\mathrm{opt}}$ by the POD method and was added to the global basis. In the case of a steady-state problem, naturally, calculations in the time dimension are unnecessary.

6.2.2 Novel Grid-Free Training Strategy for Harmonic Analyses

Problem Definition

The grid-free sampling approach provides the basic concept to meet the curse of dimensionality in the training phase of large-scale industrial models in the following. Therefore, a new training strategy is developed for band-limited frequency-domain analyses of mechanical networks and Krylov subspace methods. The method as proposed in Ullmann et al. [254] is called optimization-based greedy parameter sampling (OGPA) in the following. The error measure is evaluated in the frequency domain; it is developed goal-oriented for the MIMO subsystem transfer function matrix in subsystem coupling. Similar to the original method of Bui-Thanh et al. [46] a gradient-based approach to optimization is chosen. Therefore, gradients are derived efficiently in the framework of Chapter 4 for high-dimensional parameter spaces, thus based on an adjoint formulation.

Several algorithmic considerations are necessary for the application of large-scale industrial models. First, an error estimate is developed in Section 6.2.3 to limit the computationally expensive FOM solutions to a minimum. The use of an error estimate typically results in a trade-off between the ROM accuracy for a fixed ROM size, hence the efficiency, and the required computational efforts, which are necessary for an error evaluation in the subspace generation. Bui-Thanh et al. [46] showed this effect for their time-domain approach by comparing the true error function against a cheaper estimation by the residual, which is introduced in the FOM by the ROM solution. Utilizing the latter, more expansion points were necessary to obtain a prescribed error. This higher number of required expansion points illustrates that a point placement based on error estimates is potentially less optimal. Anyhow, the use of error estimates is mandatory for the application to large-scale industrial models as usually thousands of error evaluations are required.

Employing Krylov subspaces for the local bases, which should be valid over a band-limited frequency range, not only the optimal position in the parameter space has to be found as in the method of Bui-Thanh et al. [46]. However, appropriate sampling points in the Laplace domain are also required to determine the expansion points for each local basis. As the expansion points are placed on the imagi-

nary axis of the Laplace domain, the expansion points are completely described by a frequency-domain representation $\kappa = i\omega$ (compare Section 5.7). There are two basic approaches to include the frequency dependency of the system in the optimization process. Firstly, one can implement a separation principle according to the approach of Bui-Thanh et al. [46] for arbitrarily time-dependent problems. Such an approach utilizes an objective function for which the error is integrated over the relevant frequency band according to the time-domain equivalent in Equation (6.10). The optimization of Equation (6.9) is performed, and the parameter sample is identified at which the local ROM is constructed. Subsequently, the expansion point positions in the frequency domain are calculated for the Krylov subspace by another appropriate method. As the integration of an error expression similar to Equation (6.10) potentially requires an extensive sampling along the frequency axis and thus is computationally expensive, the separation strategy prohibits the application to large-scale industrial FOMs even for error estimates.

Secondly, there is another strategy in which the second-order system of Equation (2.11) is considered one steady-state problem with an additional parametric dependence on the circular frequency of excitation ω. The latter defines an additional parameter dimension and can be included in the enlarged parameter space represented by

$$\tilde{\boldsymbol{p}} = \left[\boldsymbol{p}^T, \omega\right]^T. \tag{6.11}$$

Furthermore, the following considers only one expansion point on the frequency axis per local basis. As a result, the definition of the parameter vector in Equation (6.11) enables the optimization problem solution in Equation (6.9) to provide both the position of the local basis in the parameter space as well as the frequency position of the expansion point. This approach avoids integration and is chosen to formulate the optimization problem for large-scale vehicle FOMs. For simplicity, the wording of expansion point position is considered to cover both the position of the local Krylov subspace in the parameter domain and the frequency position of the corresponding expansion points.

The error measure is potentially a highly non-convex and unknown function in the parameter space, especially as no frequency domain integration is considered. Globalized optimization approaches are required to find the global maximum of such an objective function

with a sufficiently high probability. As discussed in Appendix A.2, one may utilize a heuristic multi-start framework, incorporating several local gradient-based optimizations for starting points determined from a global randomized search phase. Such an approach results in considerably more computational efforts in each greedy iteration step, as it requires a significantly high number of objective evaluations. Globalized approaches become impractical in the case of the application to large-scale FOMs as a result, even for cheap error estimates chosen as objective. Thus, another more practical approach must be found as an enabler, incorporating only a single local gradient-based optimization per greedy iteration. The approach for local optimization is developed in Section 6.2.3 in detail.

Supplements for Relaxing Semi-Optimal Point Placement

Following a purely local optimization approach, the expansion point placement is likely to be semi-optimal with respect to a greedy approach, as one places the expansion point at the global maximum of the error estimate only with low probability. Consequently, the generated ROMs are less effective in their ratio of ROM size to accuracy. Although avoiding an actual globalized optimization by a multi-start framework but performing solely one gradient-based optimization, one may utilize the framework's concept of an additional phase of heuristic global search upfront to relax that semi-optimal placement. Several approaches are available for such a global phase to pre-select the starting point ${}^{j}\tilde{\boldsymbol{p}}_0$ at each j^{th} iteration of the greedy search algorithm; refer to Urban et al. [258] for applications in the context of ROM training. A computationally cheap approach is followed in OGPA, and a simple search for the maximum error measure on an initial candidate parameter set, sampled uniformly random, precedes the local optimization in each greedy step

$$ {}^{j}\tilde{\boldsymbol{p}}_0 = \underset{\tilde{\boldsymbol{p}}_k, k=1..n_{\text{pre}}}{\operatorname{argmax}} \left\| \boldsymbol{\varepsilon}\left(\tilde{\boldsymbol{p}}_k\right) \right\|. \tag{6.12} $$

$\boldsymbol{\varepsilon}\left(\tilde{\boldsymbol{p}}_k\right)$ is the same error measure as used as objective function in the local optimization. The initial sampling set is typically chosen to be small, $n_{\text{pre}} \leq 150$, to enable the application to industrial models. As a small sampling provides only a coarse sampling of the parameter domain, it is re-selected at each greedy iteration.

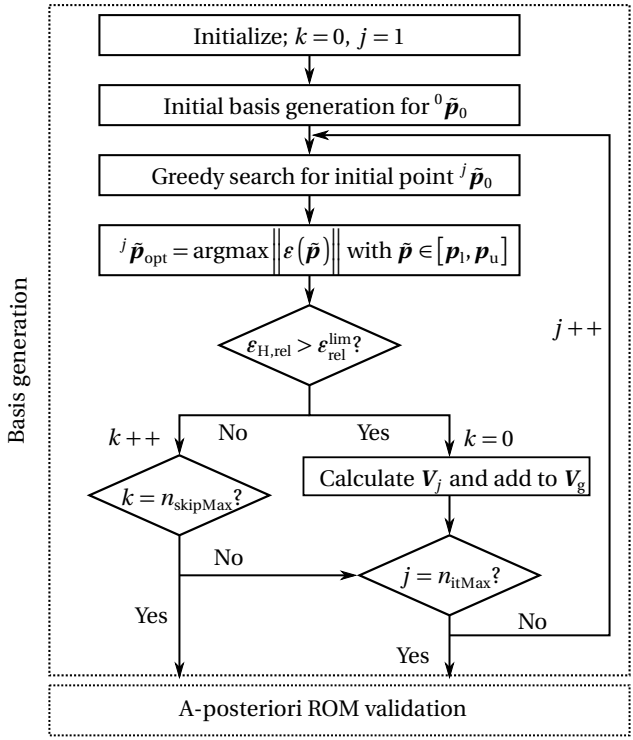

Figure 6.3: Flow diagram for the pMOR training and validation as adapted from Ullmann et al. [254].

From the initial problem definition perspective, the semi-optimal placement of expansion points in the parameter domain also results from using an error estimate instead of the true error. As a result, expansion points may not necessarily be placed at the local maxima of the true error, and the latter is unknown in its absolute magnitude. To address that, a baseline validation procedure for ${}^j\tilde{\boldsymbol{p}}_{\text{opt}}$ is introduced by a two-step approach: in an additional step after each optimization, the maximum norm of the true relative error at this candidate parameter sample point is evaluated in-situ. In the most conservative approach, the error must fulfill the following inequality

$$ {}^j\varepsilon_{\text{H,rel}}^{\text{max}} = \max_{k,l} \frac{|{}^jH_{kl} - {}^jH_{\text{R},kl}|}{|{}^jH_{kl}|} > \varepsilon_{\text{rel}}^{\text{lim}}, \tag{6.13} $$

where ${}^{j}H_{kl}$ is a transfer function matrix' entry in the k^{th} row and l^{th} column. Thus, the maximum error at the candidate position ${}^{j}\tilde{\boldsymbol{p}}_{\text{opt}}$ must be large enough justifying to add a new local basis at this position to $\boldsymbol{V}_{\text{g}}$. $\varepsilon_{\text{rel}}^{\text{lim}}$ is the user-defined error threshold, the targeted maximum relative error of the ROM transfer function after the training. As the same relative error threshold is considered for all entries of the transfer function $\boldsymbol{H}$, the approach of Equation (6.13) is conservative. In alternative formulations of Equation (6.13), another relaxed error threshold may be introduced for the relative error of transfer function entries with a small magnitude. Refer to Section 8.2.2 for an example.

Error Control

The necessarily chosen approach for the greedy search does not allow for a robust quantitative evaluation of the ROM accuracy at any stage of the ROM generation process. This lacking robustness implies two questions that remain open so far. Firstly, an approach is required to determine the ROM accuracy once the greedy training has ended. No training set is available from basis generation due to the grid-free approach, which would allow estimating the error bound directly from the sampling or some interpolation in between. An additional validation set is introduced for this purpose. The true error in the transfer functions is evaluated on this set after basis generation but still in the offline phase. Again, this leads to the curse of dimensionality trying to assess the error over the holistic high-dimensional parameter domain. Only statistical measures are employed as a remedy, and the distinct maximum error remains unknown. This is discussed in Section 6.2.4 in detail.

Secondly, a method must be found to determine when to terminate the greedy training. A practical approach is to employ the two-step procedure for the expansion point selection to define a stopping criterion for the greedy procedure. The basic idea is to consider the fact that n_{skipMax} successive iterations result in local maxima with $\varepsilon_{\text{H,rel}}^{\text{max}} < \varepsilon_{\text{rel}}^{\text{lim}}$ as an indicator for an accurate ROM over the whole parameter domain; thus with errors below the prescribed tolerance. Consequently, the ROM training is ended after n_{skipMax} iterations without an expansion point added. As the termination of the training was due to the desired result of an accurate ROM, this is considered a lucky breakdown. Afterward, the ROM accuracy can be re-evaluated in the a-posteriori ROM evaluation, see Section 6.2.4. In addition, the number of maximum

greedy iterations n_{itMax} is defined as a fallback, after which the training is ended in any case. Thus, if n_{itMax} iterations were performed, but no lucky breakdown occurred, there is a bad breakdown. The latter indicates that it was not possible to find a ROM in $n_{\mathrm{itMax}}-1$ iterations, which covers the parameter domain with the targeted accuracy. In this case, the basis generation can be restarted with different settings, which are chosen manually: most prominently, the deflation tolerance l_{tol} may be lowered, the maximum number of iterations n_{itMax} may be increased as well as the Krylov order o. The parameter space $[\boldsymbol{p}_{\mathrm{l}}, \boldsymbol{p}_{\mathrm{u}}]$ may be narrowed or the training error tolerance $\varepsilon_{\mathrm{rel}}^{\mathrm{lim}}$ may be increased. Alternatively, no restart is performed, but the ROM is evaluated for its qualification for the desired application in the a-posteriori ROM evaluation.

The stopping criterion finally defines the overall workflow of OGPA. The procedure for the training of the basis is summarized in Figure 6.3 on page 156. The latter already includes the residual-based error estimate r introduced below.

Implementation Aspects

A pseudo code for OGPA is provided in Algorithm 6.3 on the next page. The one-stage Krylov subspace in the implementation of Algorithm 5.2 on page 121 is employed for the expansion of the projection matrix $\boldsymbol{V}_{\mathrm{g}}$ in each step of the greedy algorithm, as described in Section 5.5. The algorithm allows for the moment matching of second-order systems, which include viscous Rayleigh or structural damping (see Table 5.3 on page 118). A two-stage procedure can replace it for correct moment matching of second-order systems with general damping modeling. Full use of the affine matrix decomposition concept is made to obtain an efficient code for the expansion point search. After each update of the global projection basis $\boldsymbol{V}_{\mathrm{g}}$, the single affine matrices are projected once in Algorithm 6.3 lines 4, respectively 15, which call Algorithm 6.2 on page 147. Then, during the greedy iteration, the FOM and ROM system matrices are evaluated efficiently for changing parameter combinations employing Algorithm 6.1 on page 146. After the calculation of an initial ROM for ${}^{0}\tilde{\boldsymbol{p}}_{0}$, the local optimization is performed in line 10 of Algorithm 6.3. It is described in Section 6.2.3 below, that this employs a minimization of the negative residual, for which the implementation is provided along with its gradient in Algorithm 6.5 on page 167. Line 9 of Algorithm 6.3 includes the

Algorithm 6.3: Main greedy search pMOR algorithm.

// define

parameter space $[\boldsymbol{p}_\mathrm{l}, \boldsymbol{p}_\mathrm{u}]$, Krylov order o, deflation tolerance l_tol, maximum number of iterations n_itMax, number of iterations for lucky breakdown n_skipMax, initial parameter point ${}^0\tilde{\boldsymbol{p}}_0$, training error tolerance $\varepsilon_\mathrm{rel}^\mathrm{lim}$

// provide

full-order model $\mathcal{S}$

// initialize

$\boldsymbol{V}_\mathrm{g} = [\,]$, $k = 0$, $j = 0$, $\mathcal{S} \rightarrow \boldsymbol{B}$

// update system representations at ${}^0\tilde{\boldsymbol{p}}_0$

$[\boldsymbol{A}, \boldsymbol{M}]$ =evaluateSystemAt($\mathcal{S}$, ${}^0\tilde{\boldsymbol{p}}_0$)

// get initial basis and ROM for ${}^0\tilde{\boldsymbol{p}}_0$

$\boldsymbol{V}_\mathrm{g}$ = oneStageBlockArnoldi ($\boldsymbol{V}_\mathrm{g}$, $-\boldsymbol{A}^{-1}\boldsymbol{M}$, $-\boldsymbol{A}^{-1}\boldsymbol{B}$, o, l_tol)

$\mathcal{S}_\mathrm{R}$ = projectSystem($\mathcal{S}, \boldsymbol{V}_\mathrm{g}$)

//

// greedy search loop over parameter space

while $j < n_\mathrm{itMax}$ *and* $k < n_\mathrm{skipMax}$ **do**

  $j{+}{+}$

  // get random starting point

  ${}^j\tilde{\boldsymbol{p}}_0$ = getNextStartPoint(j)

  // obtain new canditate for Sampling ${}^i\boldsymbol{p}_\mathrm{opt}$

  ${}^j\tilde{\boldsymbol{p}}_\mathrm{opt}$ = minimize(negativeResidual($\boldsymbol{p}$),${}^j\tilde{\boldsymbol{p}}_0, \boldsymbol{p}_\mathrm{l}, \boldsymbol{p}_\mathrm{u}$)

  // update system representations at ${}^j\tilde{\boldsymbol{p}}_\mathrm{opt}$

  $[\boldsymbol{A}, \boldsymbol{M}]$ = evaluateSystemAt($\mathcal{S}$, ${}^j\tilde{\boldsymbol{p}}_\mathrm{opt}$)

  $\boldsymbol{A}_\mathrm{R}$ = evaluateSystemAt($\mathcal{S}_\mathrm{R}$, ${}^j\tilde{\boldsymbol{p}}_\mathrm{opt}$)

  // calculate the transfer function error

  $\varepsilon_\mathrm{H,rel}^\mathrm{max} = \max \frac{\left\| \boldsymbol{C}\boldsymbol{A}^{-1}\boldsymbol{B} - \boldsymbol{C}_\mathrm{R}\boldsymbol{A}_\mathrm{R}^{-1}\boldsymbol{B}_\mathrm{R} \right\|}{\left\| \boldsymbol{C}\boldsymbol{A}^{-1}\boldsymbol{B} \right\|}$

  // for sufficiently large error expand basis

  if $\varepsilon_\mathrm{H,rel}^\mathrm{max} > \varepsilon_\mathrm{rel}^\mathrm{lim}$ **then**

    $\boldsymbol{V}_\mathrm{g}$ = oneStageBlockArnoldi ($\boldsymbol{V}_\mathrm{g}$, $-\boldsymbol{A}^{-1}\boldsymbol{M}$, $-\boldsymbol{A}^{-1}\boldsymbol{B}$, o, l_defl)

    $\mathcal{S}_\mathrm{R}$ = projectSystem($\mathcal{S}, \boldsymbol{V}_\mathrm{g}$)

    $k = 0$

  else

    $k{+}{+}$

greedy search-based determination of the following starting point for optimization according to Equation (6.12). As this involves a straightforward evaluation of the error estimate on a parameter set chosen from a uniformly random distribution, no pseudocode is provided for this.

Several implementation details, which are required for a high-performative code, are omitted in the above algorithms for readability: the reuse of the matrix factorization of $\boldsymbol{A}_\kappa$ is not noted explicitly, as well as the possible parallelization of the code, Algorithm 6.5 in particular. Furthermore, depending on the available computer memory and the sparsity of the FOM matrices, it can be beneficial to precompute matrix-vector products and hold them in memory, which are used several times in one iteration.

Algorithm 6.4: Derivative calculation of the system matrix utilizing its affine description.

Input : System $\mathcal{S}$, parameter vector $\boldsymbol{p}$, parameter index k
Output : Gradient of system matrix $\frac{\partial \boldsymbol{A}}{\partial p_k}$

Function `evaluateSystemGradientsAt(`$\mathcal{S}$, $\boldsymbol{p}$, k`):`
  `//  read affine description from system container`
  $\mathcal{S} \rightarrow f_{\mathrm{K},j}(\boldsymbol{p})$, $\boldsymbol{K}_j$, $f_{\mathrm{M},j}(\boldsymbol{p})$, $\boldsymbol{M}_j$, $f_{\mathrm{S},j}(\boldsymbol{p})$, $\boldsymbol{S}_j$, $f_{\mathrm{D},j}(\boldsymbol{p})$, $\boldsymbol{D}_j$
  `//  evaluate system matrices of` $\mathcal{S}$ `at` p_k
  $\frac{\partial \boldsymbol{K}}{\partial p_k} = \sum_j^{h_\mathrm{K}} \frac{\partial f_{\mathrm{K},j}}{\partial p_k}(\boldsymbol{p})\,\boldsymbol{K}_j$
  $\frac{\partial \boldsymbol{M}}{\partial p_k} = \sum_j^{h_\mathrm{M}} \frac{\partial f_{\mathrm{M},j}}{\partial p_k}(\boldsymbol{p})\,\boldsymbol{M}_j$
  $\frac{\partial \boldsymbol{S}}{\partial p_k} = \sum_j^{h_\mathrm{S}} \frac{\partial f_{\mathrm{S},j}}{\partial p_k}(\boldsymbol{p})\,\boldsymbol{S}_j$
  $\frac{\partial \boldsymbol{D}}{\partial p_k} = \sum_j^{h_\mathrm{D}} \frac{\partial f_{\mathrm{D},j}}{\partial p_k}(\boldsymbol{p})\,\boldsymbol{D}_j$
  `//  get frequency of excitation`
  $\omega = \boldsymbol{p}(\mathrm{end})$
  `//  calculate gradient of dynamic stiffness`
  $\frac{\partial \boldsymbol{A}}{\partial p_k} = \frac{\partial \boldsymbol{K}}{\partial p_k} + i\frac{\partial \boldsymbol{S}}{\partial p_k} + i\omega\frac{\partial \boldsymbol{D}}{\partial p_k} - \omega^2\frac{\partial \boldsymbol{M}}{\partial p_k}$
  if p_k *is* ω **then**
    $\frac{\partial \boldsymbol{A}}{\partial p_k} \mathrel{+}= i\boldsymbol{D} - 2\omega\boldsymbol{M}$
  return $\frac{\partial \boldsymbol{A}}{\partial p_k}$

6.2.3 Formulation of the Local Optimization Problem

A suitable error estimate needs to be developed as an objective function to formulate the local optimization problem. The workflow of Section 6.2.2 aims at a practical approach to minimize the necessary error evaluations during greedy training. Nevertheless, dozens of greedy iterations may be necessary, each involving hundreds of objective function evaluations. As a result, a suitable error measure must be primarily cheap for the application to large-scale vehicle FOMs.

This requirement motivates the use of residual expressions as discussed in Section 5.6. Residuals are an attractive choice as they use the FOM matrices without the necessity of factorizations of the latter. Among residual-based error estimates, the evaluation of the input residual as defined by Equation (5.71) is the cheapest approach. Neither it requires the construction of additional subspaces for error calculation, nor the estimation of $\left\|\boldsymbol{A}^{-1}\right\|$. Consequently, it is chosen as the objective function for the pMOR framework in the present work. Rewriting Equation (5.66), the residual associated with the ROM error in the subsystem transfer functions is

$$\boldsymbol{r}_{\mathrm{B}} = \boldsymbol{B} - \boldsymbol{A}\boldsymbol{V}_{\mathrm{g}}\boldsymbol{X}_{\mathrm{R,B}} \tag{6.14}$$

with the ROM solution

$$\boldsymbol{X}_{\mathrm{R,B}} = \boldsymbol{A}_{\mathrm{R}}^{-1}\boldsymbol{V}_{\mathrm{g}}^{H}\boldsymbol{B}. \tag{6.15}$$

Equation (6.14) provides a matrix expression per parameter point with $\boldsymbol{r}_{\mathrm{B}} \in \mathbb{C}^{n\times n_{\mathrm{U}}}$. To obtain the scalar objective function for optimization r, a norm has to be chosen for Equation (6.14), which must be submultiplicative to fulfill Equation (5.70). Following a conservative approach, the Frobenius norm is evaluated, as it is submultiplicative and gradients can be calculated for it

$$r = -\log_{10}\left(\left\|\boldsymbol{r}_{\mathrm{B}}\right\|_{\mathrm{F}}\right). \tag{6.16}$$

In the case that $\boldsymbol{r}_{\mathrm{B}}$ is a vector quantity, the Frobenius norm is equal to the vector length. The multiplication by -1 is introduced to enable optimization algorithms that usually aim to minimize expressions. Thus, the maximization of the error results in a minimization of the objective in Equation (6.16). The logarithm in Equation (6.16) accounts for the fact that the norm of the residual usually varies by orders of

magnitude in the parameter space. As a result, convergence criteria would be hard to determine without taking the logarithm.

The framework of Section 4.1.1 is followed to provide derivatives of r for the gradient-based optimization algorithm. There are usually multiple design parameters, but precisely one objective r, so the adjoint approach for gradient calculation is an efficient choice. Consider the case of a single input single output (SISO) system with $\boldsymbol{H} = \boldsymbol{c}\boldsymbol{A}^{-1}\boldsymbol{b}$ in a first step to derive the gradients for the general case of a MIMO system in the adjoint framework. As $\boldsymbol{c}^H = \boldsymbol{C}^H$ and $\boldsymbol{b} = \boldsymbol{B}$ are column vectors, the residual $\boldsymbol{r}_\mathrm{b}$ of Equation (6.14) is a column vector, too. With the auxiliary expression

$$\frac{\mathrm{d}\left\|\boldsymbol{r}_\mathrm{b}\right\|_\mathrm{F}^2}{\mathrm{d}p_j} = 2\Re\left(\boldsymbol{r}_\mathrm{b}^H \frac{\mathrm{d}\boldsymbol{r}_\mathrm{b}}{\mathrm{d}p_j}\right), \tag{6.17}$$

the adjoint approach of Equation (4.7) provides the gradient as

$$\begin{aligned}\frac{\mathrm{d}r}{\mathrm{d}p_j} &= k\left(\frac{\partial\left\|\boldsymbol{r}_\mathrm{b}\right\|_\mathrm{F}^2}{\partial p_j} + \boldsymbol{\Psi}^T\frac{\partial \boldsymbol{r}_\mathrm{R}}{\partial p_j}\right)\\ &= k\,\Re\left(2\boldsymbol{r}_\mathrm{b}^H\frac{\partial \boldsymbol{A}}{\partial p_j}\tilde{\boldsymbol{X}} + \boldsymbol{\Psi}^T\frac{\partial \boldsymbol{A}_\mathrm{R}}{\partial p_j}\boldsymbol{X}_\mathrm{R,b}\right).\end{aligned} \tag{6.18}$$

$k = {}^1\!/\!\left(2\|\boldsymbol{r}_\mathrm{b}\|_\mathrm{F}^2\log(10)\right)$ is obtained from applying the chain rule to the square root and the logarithm of $\left\|\boldsymbol{r}_\mathrm{b}\right\|_\mathrm{F}^2$. $\tilde{\boldsymbol{X}} = \boldsymbol{V}_\mathrm{g}\boldsymbol{X}_\mathrm{R,b}$ is introduced for brevity. Two different residual expressions are contained in Equation (6.18). One residual is $\boldsymbol{r}_\mathrm{b}$, which is used as the error estimator and is introduced when the ROM solution is substituted in the FOM residual according to Equation (6.14). The other residual $\boldsymbol{r}_\mathrm{R}$ is the residual of the governing equations, the residual of the solution of the ROM itself. In contrast to $\boldsymbol{r}_\mathrm{b}$, $\boldsymbol{r}_\mathrm{R}$ is zero by construction (see Equation (4.3))

$$\boldsymbol{r}_\mathrm{R} = \boldsymbol{b}_\mathrm{R} - \boldsymbol{A}_\mathrm{R}\boldsymbol{X}_\mathrm{R,b} = 0. \tag{6.19}$$

This is in line with the projection theory of Section 5.2.1, where the constraint space is chosen for a zero residual. Following Equation (4.8), the adjoint $\boldsymbol{\Psi}$ is obtained from the solution of

$$\left(\frac{\partial \boldsymbol{r}_\mathrm{R}}{\partial \boldsymbol{X}_\mathrm{R,b}}\right)^T\boldsymbol{\Psi} = -\left(\frac{\partial\left\|\boldsymbol{r}_\mathrm{b}\right\|_\mathrm{F}^2}{\partial \boldsymbol{X}_\mathrm{R,b}}\right)^T. \tag{6.20}$$

The left hand side of the equation is provided by the partial derivative of Equation (6.19) as $\partial r_\mathrm{R}/\partial x_\mathrm{R,b} = \boldsymbol{A}_\mathrm{R}$. The right hand side by deriving the SISO version of Equation (6.14) while utilizing Equation (6.17) as $\partial \|r_\mathrm{b}\|_\mathrm{F}^2/\partial x_\mathrm{R,b} = -2\boldsymbol{r}_\mathrm{b}^H \boldsymbol{A}\boldsymbol{V}_\mathrm{g}$. Thus, Equation (6.20) results in

$$\boldsymbol{\Psi} = \left(\boldsymbol{A}_\mathrm{R}^T\right)^{-1}\left(-2\boldsymbol{r}_\mathrm{b}^H \boldsymbol{A}\boldsymbol{V}_\mathrm{g}\right)^T. \tag{6.21}$$

Following the adjoint approach, the Hessian matrix $\boldsymbol{h} \in \mathbb{C}^{d\times d}$, which contains the second derivatives, can be provided to corresponding optimization algorithms, in addition. Papadimitriou et al. [191] discussed different approaches for the calculation of Hessian matrices. In the following, an adjoint-adjoint method is demonstrated. Therefore, the original Hessian is augmented by adding two adjoint matrices

$$h_{ij} = \frac{\mathrm{d}^2\tilde{r}}{\mathrm{d}p_i \mathrm{d}p_j} = \frac{\mathrm{d}^2 r}{\mathrm{d}p_i \mathrm{d}p_j} + \boldsymbol{\mu}_i \frac{\mathrm{d}\boldsymbol{r}_\mathrm{R}}{\mathrm{d}p_j} + \boldsymbol{\nu}_i \frac{\mathrm{d}\boldsymbol{r}_\Psi}{\mathrm{d}p_j}. \tag{6.22}$$

where $\boldsymbol{r}_\Psi$ is the residual of the adjoint equation (Equation (6.20)), which is zero by definition

$$\boldsymbol{r}_\Psi = \frac{\partial \boldsymbol{r}_\mathrm{R}}{\partial \boldsymbol{X}_\mathrm{R,b}}\boldsymbol{\Psi} + \frac{\partial r}{\partial \boldsymbol{X}_\mathrm{R,b}} = 0. \tag{6.23}$$

Calculating the derivatives in Equation (6.22) and choosing the two adjoints $\boldsymbol{\mu}_i$ and $\boldsymbol{\nu}_i$ such, that all required total derivatives vanish, one arrives at a formulation of one entry in the Hessian matrix as

$$\begin{aligned} h_{i,j} = \frac{\partial^2 r}{\partial p_i \partial p_j} + \boldsymbol{\Psi}\frac{\partial^2 \boldsymbol{r}_\mathrm{R}}{\partial p_i \partial p_j} + \boldsymbol{\mu}_i \frac{\partial \boldsymbol{r}_\mathrm{R}}{\partial p_j} + \boldsymbol{\nu}_i \frac{\partial^2 r}{\partial \boldsymbol{X}_\mathrm{R,b}\partial p_j} \\ + \boldsymbol{\nu}_i \boldsymbol{\Psi}\frac{\partial^2 \boldsymbol{r}_\mathrm{R}}{\partial \boldsymbol{X}_\mathrm{R,b}\partial p_j}. \end{aligned} \tag{6.24}$$

Two additional adjoint variables need to be determined as

$$\left(\frac{\partial \boldsymbol{r}_\mathrm{R}}{\partial \boldsymbol{X}_\mathrm{R,b}}\right)^T \boldsymbol{\nu}_i^T = -\left(\frac{\partial \boldsymbol{r}_\mathrm{R}}{\partial p_j}\right)^T \tag{6.25}$$

and

$$\left(\frac{\partial \boldsymbol{r}_\mathrm{R}}{\partial \boldsymbol{X}_\mathrm{R,b}}\right)^T \boldsymbol{\mu}_i^T = -\left(\frac{\partial^2 r}{\partial p_i \partial \boldsymbol{X}_\mathrm{R,b}} + \boldsymbol{\Psi}\frac{\partial^2 \boldsymbol{r}_\mathrm{R}}{\partial p_i \partial \boldsymbol{X}_\mathrm{R,b}} + \boldsymbol{p}_j \frac{\partial^2 r}{\partial \boldsymbol{X}_\mathrm{R,b}\partial \boldsymbol{X}_\mathrm{R,b}}\right)^T.$$

(6.26)

For the objective of the SISO system residual, one obtains

$$\begin{aligned}\frac{\mathrm{d}^2 r}{\mathrm{d}p_i \mathrm{d}p_j} = k\Re\Bigg[& 2\left(\left(\frac{\partial \boldsymbol{A}}{\partial p_j}\tilde{\boldsymbol{X}}\right)^H \frac{\partial \boldsymbol{A}}{\partial p_i} + 2\boldsymbol{r}_\mathrm{b}^H \frac{\partial^2 \boldsymbol{A}}{\partial p_i \partial p_j}\right)\tilde{\boldsymbol{X}} \\ & + \boldsymbol{\Psi}\frac{\partial^2 \boldsymbol{A}_\mathrm{R}}{\partial p_i \partial p_j} + \boldsymbol{\mu}_j \frac{\partial \boldsymbol{A}_\mathrm{R}}{\partial p_j}\boldsymbol{X}_\mathrm{R,b} \\ & + 2\boldsymbol{\nu}_i \boldsymbol{V}_\mathrm{g}^T \left(\boldsymbol{r}_\mathrm{b}\frac{\partial \boldsymbol{A}}{\partial p_j} + \left(\frac{\partial \boldsymbol{A}}{\partial p_j}\tilde{\boldsymbol{X}}\right)^H \boldsymbol{A}\right)^T + \boldsymbol{\nu}_i \frac{\partial \boldsymbol{A}_\mathrm{R}^T}{\partial p_j}\boldsymbol{\Psi}^T\Bigg].\end{aligned} \tag{6.27}$$

The adjoints are obtained from the solution of

$$\boldsymbol{A}_\mathrm{R}^T \boldsymbol{\nu}_i^T = -\left(\frac{\partial \boldsymbol{A}_\mathrm{R}}{\partial p_j}\boldsymbol{X}_\mathrm{R,b}\right)^T \tag{6.28}$$

respectively

$$\begin{aligned}\boldsymbol{A}_\mathrm{R}^T \boldsymbol{\mu}_i^T = -\Bigg(& 2\boldsymbol{r}_\mathrm{b}^H \frac{\partial \boldsymbol{A}}{\partial p_i}\boldsymbol{V}_\mathrm{g} + 2\left(\left(\boldsymbol{A}\boldsymbol{V}_\mathrm{g}\right)^H \frac{\partial \boldsymbol{A}}{\partial p_i}\tilde{\boldsymbol{X}}\right)^T + \boldsymbol{\Psi}\frac{\partial \boldsymbol{A}_\mathrm{R}}{\partial p_i} \\ & - 2\boldsymbol{\nu}_i\left(\boldsymbol{A}\boldsymbol{V}_\mathrm{g}\right)\boldsymbol{A}\boldsymbol{V}_\mathrm{g}\Bigg)^T.\end{aligned} \tag{6.29}$$

The gradient formulation for SISO systems provides the starting point for deriving the gradients and the Hessian for the general multiple-input multiple-output (MIMO) case. For the latter, the residual $\boldsymbol{r}_\mathrm{B}$ of Equation (6.14) is not a vector but a matrix with as many columns as the number of inputs. In order to extend the above framework for gradient calculation for MIMO systems, the squared Frobenius norm is considered as the sum of the squared column vector lengths of the residual $\left\|\boldsymbol{r}_{\mathrm{B},i}\right\|_\mathrm{F}^2$

$$\left\|\boldsymbol{r}_\mathrm{B}\right\|_\mathrm{F}^2 = \sum_{i=1}^{n_\mathrm{U}} \left\|\boldsymbol{r}_{\mathrm{B},i}\right\|_\mathrm{F}^2 = \mathrm{tr}\left(\boldsymbol{r}_\mathrm{B}^H \boldsymbol{r}_\mathrm{B}\right), \tag{6.30}$$

where $\mathrm{tr}(\square)$ is the trace of a matrix, thus the sum of its diagonal entries. The adjoint $\boldsymbol{\Psi}$ is calculated for the n_U objectives of the squared column lengths $\left\|\boldsymbol{r}_{\mathrm{B},i}\right\|_\mathrm{F}^2$ as a result. $\boldsymbol{\Psi}$ becomes a matrix, which is obtained from n_U right-hand sides according to Equation (6.21) as

$$\boldsymbol{\Psi} = \left(\boldsymbol{A}_\mathrm{R}^T\right)^{-1}\left(-\boldsymbol{r}_\mathrm{B}^H \boldsymbol{A}\boldsymbol{V}_\mathrm{g}\right)^T. \tag{6.31}$$

With that, Equation (6.18) is extended for MIMO systems to

$$\frac{\mathrm{d}r}{\mathrm{d}p_j} = k\,\Re\left(\mathrm{tr}\left(\boldsymbol{r}_\mathrm{B}^H \frac{\partial \boldsymbol{A}}{\partial p_j}\tilde{\boldsymbol{X}} + \boldsymbol{\Psi}^T \frac{\partial \boldsymbol{A}_\mathrm{R}}{\partial p_j}\boldsymbol{X}_\mathrm{R,B}\right)\right) \tag{6.32}$$

with $k = {}^1\!/\!\left(\left\|\boldsymbol{r}_\mathrm{B}\right\|_\mathrm{F}^2 \log(10)\right)$ and $\tilde{\boldsymbol{X}} = \boldsymbol{V}_\mathrm{g}\boldsymbol{X}_\mathrm{R,B}$. Equation (6.28) to Equation (6.33) are adapted correspondingly to calculate the Hessian for MIMO systems:

$$\begin{aligned}\frac{\mathrm{d}^2 r}{\mathrm{d}p_i \mathrm{d}p_j} = k\,\Re\Bigg[\mathrm{tr}\Bigg(2\left(\left(\frac{\partial \boldsymbol{A}}{\partial p_j}\tilde{\boldsymbol{X}}\right)^H \frac{\partial \boldsymbol{A}}{\partial p_i} + 2\boldsymbol{r}_\mathrm{B}^H \frac{\partial^2 \boldsymbol{A}}{\partial p_i \partial p_j}\right)\tilde{\boldsymbol{X}} \\ + \boldsymbol{\Psi}\frac{\partial^2 \boldsymbol{A}_\mathrm{R}}{\partial p_i \partial p_j} + \boldsymbol{\mu}_j \frac{\partial \boldsymbol{A}_\mathrm{R}}{\partial p_j}\boldsymbol{X}_\mathrm{R,B} \\ + 2\boldsymbol{\nu}_i \boldsymbol{V}^T\left(\boldsymbol{r}_\mathrm{B}\frac{\partial \boldsymbol{A}}{\partial p_j} + \left(\frac{\partial \boldsymbol{A}}{\partial p_j}\tilde{\boldsymbol{X}}\right)^H \boldsymbol{A}\right)^T + \boldsymbol{\nu}_i \frac{\partial \boldsymbol{A}_\mathrm{R}^T}{\partial p_j}\boldsymbol{\Psi}^T\Bigg)\Bigg]\end{aligned} \tag{6.33}$$

The additional adjoints become matrices, too,

$$\boldsymbol{A}_\mathrm{R}^T \boldsymbol{\nu}_i^T = -\left(\frac{\partial \boldsymbol{A}_\mathrm{R}}{\partial p_j}\boldsymbol{X}_\mathrm{R,B}\right)^T \tag{6.34}$$

and

$$\begin{aligned}\boldsymbol{A}_\mathrm{R}^T \boldsymbol{\mu}_i^T = -\Bigg(2\boldsymbol{r}_\mathrm{B}^H \frac{\partial \boldsymbol{A}}{\partial p_i}\boldsymbol{V}_\mathrm{g} + 2\left(\left(\boldsymbol{A}\boldsymbol{V}_\mathrm{g}\right)^H \frac{\partial \boldsymbol{A}}{\partial p_i}\tilde{\boldsymbol{X}}\right)^T + \boldsymbol{\Psi}\frac{\partial \boldsymbol{A}_\mathrm{R}}{\partial p_i} \\ - 2\boldsymbol{\nu}_i\left(\boldsymbol{A}\boldsymbol{V}_\mathrm{g}\right)\boldsymbol{A}\boldsymbol{V}_\mathrm{g}\Bigg)^T.\end{aligned} \tag{6.35}$$

To calculate the gradients of the objective function r, the solution of the adjoint system in Equation (6.31) is needed, along with the derivatives of the system matrices $\partial \boldsymbol{A}/\partial p_j$ and $\partial \boldsymbol{A}_\mathrm{R}/\partial p_j$. As the affine matrix decomposition is known for the dynamic stiffness, derivatives of $\boldsymbol{A}$ and $\boldsymbol{A}_\mathrm{R}$ can be obtained analytically. A pseudo code for such derivative calculation is provided in Algorithm 6.4 on page 160. The calculation of the adjoints is computationally cheap, as it is obtained from the ROM. In addition, the factorization of $\boldsymbol{A}_\mathrm{R}$ can be reused for real-valued projection matrices as the matrix is self-adjoint. For the general case of a complex-valued $\boldsymbol{V}_\mathrm{g}$, $\boldsymbol{A}_\mathrm{R}$ is not self-adjoint, and an additional factorization is required.

The sum of the required matrix-matrix and matrix-vector multiplications of FOM size complexity is computationally more demanding than the solution of the ROM for the adjoint variables for many large-scale systems. This is especially the case for the calculation of the Hessian matrix. For d parameters, $2d$ adjoints have to be calculated in addition. Equation (6.34) has to be solved d times, which solely incorporates inexpensive operations of ROM size complexity. Equation (6.35), which also needs to be solved d times, involves eight additional matrix-matrix multiplications of FOM size for one of the required d right-hand sides. Equation (6.33) has to be evaluated $(d+1)d/2$ times when the symmetry of the Hessian is exploited, ten matrix-matrix multiplications of FOM size are required for each evaluation. The last step requires 550 multiplications of FOM size complexity for one Hessian matrix evaluation already for a ten-parameter setting. There are alternatives to the adjoint-adjoint approach for Hessian calculation, which reduce the required (ROM) system solves of the reduced system, but not significantly the required number of FOM matrix multiplications, see Papadimitriou et al. [191]. For large-scale industrial FOMs, the Hessian evaluation is thus computationally expensive, although several matrix-matrix products may be pre-calculated and stored in memory.

As a result, an optimization algorithm is chosen in the following, which avoids the explicit evaluation of the Hessian matrix for the above objective function. Specifically, the method of Sequential Quadratic Programming (SQP) is used. This algorithm incorporates an estimation of the Hessian matrix via the Broyden-Fletcher–Goldfarb-Shanno approach, see Appendix A.1, for a further explanation of the algorithm.

Algorithm 6.5: Error indicator function for pMOR training.

Input : Parameter vector $\boldsymbol{p}$, reduced-order system $\mathcal{S}_\mathrm{R}$, full-order system $\mathcal{S}$

Output : Objective value r, gradient of the objective $\frac{\partial r}{\partial \boldsymbol{p}}$

Function `negativeResidual(`$\boldsymbol{p}, \mathcal{S}_\mathrm{R}, \mathcal{S}$`)`**:**

`//`

`// residual`

$\boldsymbol{A} = \text{evaluateSystemAt}(\mathcal{S}, \boldsymbol{p})$

$\boldsymbol{A}_\mathrm{R} = \text{evaluateSystemAt}(\mathcal{S}_\mathrm{R}, \boldsymbol{p})$

$\boldsymbol{X}_\mathrm{R} = \boldsymbol{A}_\mathrm{R}^{-1} \boldsymbol{B}_\mathrm{R}$

$\boldsymbol{r}_\mathrm{B} = \boldsymbol{B} - \boldsymbol{A}\boldsymbol{V}_\mathrm{g}\boldsymbol{X}_\mathrm{R}$

$r = -\log_{10}(\left\|\boldsymbol{r}_\mathrm{B}\right\|_\mathrm{F})$

`//`

`// sensitivites`

`// adjoint variable`

$\boldsymbol{\Psi} = \left(\boldsymbol{A}_\mathrm{R}^T\right)^{-1}\left(-\boldsymbol{r}_\mathrm{B}^H \boldsymbol{A}\boldsymbol{V}_\mathrm{g}\right)^T$

`// loop over parameters`

for $j = 1$ *to* d **do**

$\frac{\partial \boldsymbol{A}}{\partial p_j} = \text{evaluateSystemGradientsAt}(\mathcal{S}, \boldsymbol{p}, j)$

$\frac{\partial \boldsymbol{A}_\mathrm{R}}{\partial p_j} = \text{evaluateSystemGradientsAt}(\mathcal{S}_\mathrm{R}, \boldsymbol{p}, j)$

$\frac{\partial r}{\partial p_j} = \frac{1}{\left\|\boldsymbol{r}_\mathrm{B}\right\|_\mathrm{F}^2 \log(10)} \Re\left(\mathrm{tr}\left(\boldsymbol{r}_\mathrm{B}^H \frac{\partial \boldsymbol{A}}{\partial p_k} \boldsymbol{V}_\mathrm{g}\boldsymbol{X}_\mathrm{R} + \boldsymbol{\Psi}^T \frac{\partial \boldsymbol{A}_\mathrm{R}}{\partial p_j} \boldsymbol{X}_\mathrm{R}\right)\right)$

return r, $\frac{\partial r}{\partial \boldsymbol{p}}$

6.2.4 A-Posteriori Model Quality Evaluation

The method proposed in Section 6.2.2 provides an implicit evaluation of the ROM error solely. As indicated above, this leads to the requirement of an additional workflow step to assess the quality of the ROM over the whole bound design parameter space robustly a-posteriori to the training. An additional sample set for validation is introduced for this, on which the true relative error $\varepsilon_\mathrm{H,rel}^\mathrm{max}$ is evaluated before the online phase. The true error is assessed as for the two-step validation scheme during training; in the conservative approach according to (the left-hand side of) Equation (6.13).

It is impossible to evaluate the maximum error magnitude in the whole admissible parameter space reliably during the training. Thus,

it is not possible for the a-posteriori error evaluation. Necessarily, the curse of dimensionality has to be also faced at this stage. This is achieved by the basic concept not to assess the magnitude of the maximum $\varepsilon_{\mathrm{H,rel}}$ quantitatively in the bound parameter space but to consider more robust statistical measures. Consequently, histograms are provided for the examples, which are discussed below. Such an approach demonstrates the potential of the proposed pMOR method descriptively. However, even providing such statistical measures as mean and variance may be challenging for large-scale industrial models. The convergence rates may be low in high-dimensional parameter spaces, and a rather large validation set may still be required, while the FOM needs to be solved for each validation set sample to evaluate $\varepsilon_{\mathrm{H,rel}}$. Furthermore, one can only estimate the confidence levels of the obtained statistic measures by additional computationally extensive sampling approaches.

A sufficiently small validation set can be used if the information in the statistical evaluation is reduced and a bi-nominal setting is followed. The latter implies that one does not consider the actual magnitude of the error except whether it is below the error threshold or not; thus, solely two events are considered, a good and a bad outcome. Success, respectively a good outcome is defined as an error which is lower than the error threshold, $\varepsilon_{\mathrm{H,rel}}^{\mathrm{max}} \leq \varepsilon_{\mathrm{rel}}^{\mathrm{lim}}$. Accordingly, an error of $\varepsilon_{\mathrm{H,rel}}^{\mathrm{max}} > \varepsilon_{\mathrm{rel}}^{\mathrm{lim}}$ is classified as a bad outcome for a parameter sample, respectively an overshoot. The drop in information leads to a relaxed requirement for the ROM quality. This is demonstrated in Section 6.2.5. Even high errors of the ROM are accepted if there are only a few overshoots, which can be a sufficient requirement for many multi-query methods.

The application of a binomial setting as a quality indicator for engineering simulation outputs was already proposed by Lehar et al. [146] and Zimmermann et al. [284]. The latter introduced the approach to estimating failure probabilities for vehicle crash simulations. Zimmermann et al. [284] determined solution spaces in complex engineering models on that basis. In the following, this concept is adapted to model order reduction while the remaining section closely follows the notation in Lehar et al. [146].

The framework of Bayesian inference is used to provide statistical measures on that bi-nominal setting; to determine a subjective probability of a good outcome, a, including the confidence level, re-

spectively the probability for that assumed subjective probability of success. The main advantage of these measures is the fact that the width of confidence intervals shows a fast convergence for prescribed values of the confidence level a, as pointed out by Lehar et al. [146]: in the case of an actual a close to one or zero, thus good or very poor ROM quality, only a small validation set is necessary to obtain high confidence levels for relatively narrow confidence intervals.

In the following, these statistical measures are further described. The starting point is the Bayes theorem, which is obtained in its most basic form by

$$P(\mathcal{A}|\mathcal{B}) = \frac{P(\mathcal{B}|\mathcal{A})\,P(\mathcal{A})}{P(\mathcal{B})}. \tag{6.36}$$

In a general context, $\mathcal{A}$ and $\mathcal{B}$ are events, $P(\mathcal{A})$ and $P(\mathcal{B})$ are the prior probabilities of that events without any further conditions assumed. $P(\mathcal{A}|\mathcal{B})$ is a conditional probability, alternatively posterior probability under the condition that the event $\mathcal{B}$ occurred; $P(\mathcal{B}|\mathcal{A})$ a corresponding conditional probability. In the context of MOR, the involved quantities describe the following: $\mathcal{B}$ is an observed result from an experiment in which the ROM error was assessed. It is defined as a result of e parameter samples with $\varepsilon_{\mathrm{H,rel}} \leq \varepsilon_{\mathrm{rel}}^{\mathrm{lim}}$ and therefore a good outcome within n_{sam} samples, which were calculated during the experiment in total. $\mathcal{A}$ is a probability itself, the probability of a good outcome specifically. $P(\mathcal{A}|\mathcal{B})$ the probability of that probability under the condition that the experimental result occurred as specified, thus the confidence level. For the bi-nominal setting, Equation (6.36) can be rewritten as

$$\begin{aligned} p\left(a|e,n_{\mathrm{sam}}\right) &= \frac{p\left(e,n_{\mathrm{sam}}|a\right)p(a)}{\int_0^1 p\left(e,n_{\mathrm{sam}}|g\right)p(g)\mathrm{d}g} \\ &= \frac{\binom{n_{\mathrm{sam}}}{e}a^e(1-a)^{n_{\mathrm{sam}}-e}\,p(a)}{\int_0^1 \binom{n_{\mathrm{sam}}}{e}g^e(1-g)^{n_{\mathrm{sam}}-e}\,p(g)\mathrm{d}g}, \end{aligned} \tag{6.37}$$

where g is used as sequence variable for integration and $p()$ is a probability density.

The basic concept is to assume prior distributions in a first step, which are uniform between zero and one, as no knowledge about these distributions is available prior to the experiment. In a second step, the results from the experiment are used to update that initial

guess utilizing Bayes theorem. Thus, the prior probabilities are constant, $p(a) = p(g) = \text{const.}$, and can be removed from Equation (6.37). Furthermore, as the probability of a good outcome a is unknown to the experiment upfront, it is not practical to specify a single value for it a-priori. Such a guess typically does not reflect the actual probability, leading to low confidence levels. Instead, the confidence level $p\left(a|e, n_{\text{sam}}\right)$ is determined for confidence intervals of a instead, $a_{\text{l}} < a < a_{\text{u}}$. Finally, Equation (6.37) can be reformulated for confidence intervals of a as (Lehar et al. [146])

$$P\left(a_{\text{l}} < a < a_{\text{u}}|e, n_{\text{sam}}\right) = \frac{\int_{a_{\text{l}}}^{a_{\text{u}}} z^e (1-z)^{n_{\text{sam}}-e}\,\mathrm{d}z}{\int_0^1 g^e (1-g)^{n_{\text{sam}}-e}\,\mathrm{d}g}. \tag{6.38}$$

z is used as another sequence variable for integration. Equation (6.38) finally allows to determine the confidence level, that the probability a for a sufficient ROM accuracy $\varepsilon_{\text{H,rel}}^{\max} \leq \varepsilon_{\text{rel}}^{\lim}$ at any requested parameter combination $\boldsymbol{p}$ is in the confidence interval $a_{\text{l}} < a < a_{\text{u}}$. In a practical approach, the user predetermines the latter upfront, and the confidence level is returned for the true error provided, which is calculated at n_{sam} uniformly distributed parameter values.

6.2.5 Cantilever Solid Beam Example

The Model Setting In order to demonstrate the approach of OGPA and benchmark it against some other methods, a MIMO beam subsystem is considered the first example. It is illustrated in Figure 6.4 and was already discussed in Ullmann et al. [254]. The beam has a high-dimensional parameter space, for which the system matrices are parameterized. The latter are available in their affine decomposition for reproduction in Ullmann [250]. An interface-symmetric MIMO setting is considered incorporating two interface nodes, each providing six DOFs, which results in twelve inputs and twelve outputs. The local coordinate system in which the inputs and outputs are formulated is rotated intrinsically by $\varphi_{\text{z}} = 30°$ and $\varphi_{\text{x}} = 20°$ for the first interface node, and by $\varphi_{\text{z}} = 15°$ and $\varphi_{\text{x}} = 25°$ for the second node. This rotation introduces additional coupling terms between the single inputs and outputs. The model's geometry is conceptually simple as a straight beam is considered. Nevertheless, the example has relevance for industrial applications: modeling techniques for standard industrial models are used, provided by the commercial FE software Simulia

	E_1 $\times 10^4$	ρ_1 $\times 10^{-10}$	η_1 $\times 10^{-3}$	E_2 $\times 10^4$	ρ_2 $\times 10^{-9}$	η_2 $\times 10^{-3}$	a	L_1	L_2	ω
$\boldsymbol{p}_\mathrm{l}$	2.5	7	5	0.85	1	5	20	200	200	0
$\boldsymbol{p}_\mathrm{u}$	7.5	10	50	3.5	5	50	24	300	400	3000

Table 6.1: Lower and upper bounds of the parameter values for the cantilever beam example. All units are omitted as they are in Newton, millimeter and ton.

ABAQUS 2017 Hotfix 2. The beam is discretized by elements of type C3D8I, which are linear hexagon 3D elements with eight nodes and additional DOFs for incompatible modes. A relatively coarse mesh of three elements in each cross-section dimension and 40 elements per section length is introduced; the additional two interface nodes are tied to the corresponding surfaces of the beam via kinematic couplings. This modeling results in 13164 DOFs, including several internal DOFs not directly linked to spatial DOFs but introduced by the element formulation.

Nine variable input parameters are chosen to be preserved in the reduced model: the cross-section width a, and per section, the material density ρ_i, the Elastic modulus E_i, the structural damping coefficient η_i as well as the section length L_i.

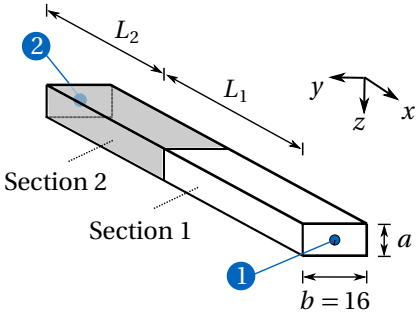

Figure 6.4: Schematic drawing of the cantilever beam example adapted from Ullmann et al. [254].

PMOR aims to extract the use-case-required information of the subsystem representation in the relevant frequency band and for the variable parameters in their range of validity. The latter must be specified already for the training of the pROM as a result. In the following, the parameter bounds are chosen according to Table 6.1. A ten-dimensional bounded parameter space has to be covered, while the frequency ω is included as an additional parameter dimension. The chosen parameter space leads to a significant variance in the subsystem's input-to-output behavior over the parameter range, which needs to be covered by the global basis. This is visualized for two entries of the transfer function in Figure 6.5: for a parameter set which is called *soft bound*, another called *hard bound*, and a third one with arbitrary parameter values called *base state* as a baseline. The upper bound values are chosen for ρ_i and L_i, the lower bound values for b, E_i, and η_i in the soft setting. In the hard setting, the values are defined oppositely.

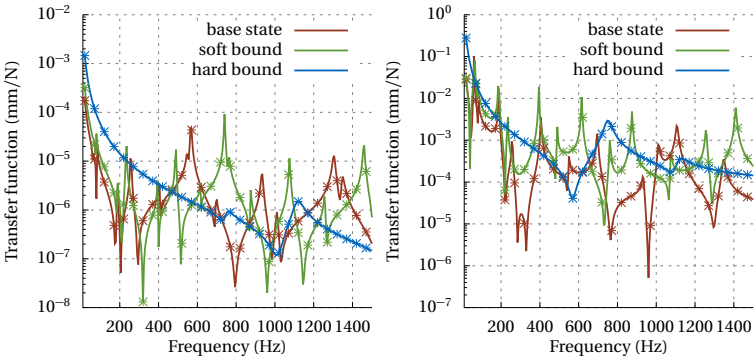

Figure 6.5: Magnitude of the transfer function matrix at (a) the diagonal element for node 1 DOF 5 (φ_y-rotation); (b) the off diagonal element, relating node 1 DOF 1 (x-direction) to node 2 DOF 2 (y-direction). Three parameter settings are considered, the soft and hard bound setting as well as a third one with arbitrary parameter values as baseline. Per setting, the solid line belongs to the transfer function of the FOM, the starred values to the one of the ROM.

Affine Matrix Decompositon As there is no ability to access the source code of the ABAQUS FE program, the affine matrix decomposition needs to be reconstructed from parameter samples of the FOM system matrices. An exact interpolation problem should be formulated for the beam example; thus, a parameter-gray-box approach is followed. For the latter, the required interpolation basis functions $f_j(\boldsymbol{p})$ need to be determined. The starting point is the brick element formulation in terms of the linear ansatz functions as found in Zienkiewicz et al. [283], for example. Basis functions can be derived from that formulation for the specific geometric parametrization. The exemplary procedure can be found in Fröhlich et al. [86], who derived a more complex geometric parametrization for shape optimization. In addition, reverse engineering is required for the affine representation of the internal DOFs of the specific C3D8I elements in ABAQUS, resulting in the element stiffness matrix

$$\boldsymbol{K}_\mathrm{e} = E\left(\boldsymbol{K}_{\mathrm{e},1} + b\,\boldsymbol{K}_{\mathrm{e},2} + L\,\boldsymbol{K}_{\mathrm{e},3} + b\,L\,\boldsymbol{K}_{\mathrm{e},4} + \frac{b}{L}\boldsymbol{K}_{\mathrm{e},5} + \frac{L}{b}\boldsymbol{K}_{\mathrm{e},6}\right),$$

where $\boldsymbol{K}_{\mathrm{e},i}$ are constant-valued parameter-independent matrices. The DOFs which are condensed in the kinematic coupling can be represented affinely by

$$\boldsymbol{K}_\mathrm{e} = E\left(\boldsymbol{K}_{\mathrm{e},7} + b^2\,\boldsymbol{K}_{\mathrm{e},8} + \frac{b}{L}\boldsymbol{K}_{\mathrm{e},9} + \frac{b^2}{L}\boldsymbol{K}_{\mathrm{e},10} + \frac{b^3}{L}\boldsymbol{K}_{\mathrm{e},11}\right),$$

which again was found by reverse engineering. This results in an affine representation of the overall beam stiffness matrix as

$$\begin{aligned}\boldsymbol{K} =& E_1\left(\boldsymbol{K}_1 + b\,\boldsymbol{K}_2 + L_1\,\boldsymbol{K}_3 + b\,L_1\boldsymbol{K}_4 + b^2\,\boldsymbol{K}_5 + \frac{b}{L_1}\boldsymbol{K}_6 + \frac{L_1}{b}\boldsymbol{K}_7\right.\\ &\left. + \frac{b^2}{L_1}\boldsymbol{K}_8 + \frac{b^3}{L_1}\boldsymbol{K}_9\right) + E_2\left(\boldsymbol{K}_{10} + b\,\boldsymbol{K}_{11} + L_1\,\boldsymbol{K}_{12} + b\,L_1\boldsymbol{K}_{13}\right.\\ &\left. + b^2\,\boldsymbol{K}_{14} + \frac{b}{L_1}\boldsymbol{K}_{15} + \frac{L_1}{b}\boldsymbol{K}_{16} + \frac{b^2}{L_1}\boldsymbol{K}_{17} + \frac{b^3}{L_1}\boldsymbol{K}_{18}\right).\end{aligned}$$

Correspondingly, the structural damping matrix takes the form of

$$\boldsymbol{S} = \eta_1\boldsymbol{K},$$

using the same affine matrices as the stiffness matrix and introducing solely an additional scaling by the structural damping coefficients.

Accordingly, the affine matrix decomposition of the mass matrix can be recovered, which is given for a single C3D8I elements as

$$\boldsymbol{M}_{\mathrm{e}} = \rho\, b\, L \boldsymbol{M}_{\mathrm{e},1},$$

and for the kinematic coupling as

$$\boldsymbol{M}_{\mathrm{e}} = \rho\, L \left(b\, \boldsymbol{M}_{\mathrm{e},2} + b^3 \boldsymbol{M}_{\mathrm{e},3} \right),$$

with the parameter-independent matrices $\boldsymbol{M}_{\mathrm{e},i}$. This results in a globally assembled mass matrix of

$$\boldsymbol{M} = \rho_1\, b\, L_1 \left(\boldsymbol{M}_1 + b^2 \boldsymbol{M}_2 \right) + \rho_2\, b\, L_2 \left(\boldsymbol{M}_3 + b^2 \boldsymbol{M}_4 \right).$$

Consequently, at least nine parameter samples of the system matrices per section are required to recalculate the affine matrices $\boldsymbol{K}_i$, $\boldsymbol{S}_i$ and $\boldsymbol{M}_i$ according to Equation (6.5). The corresponding samples were obtained by ABAQUS, and values smaller than the threshold $|K_{ij}| < 1 \cdot 10^{-7}$ and $|M_{ij}| < 1 \cdot 10^{-20}$ were not interpolated but set to zero. In addition, a scaling of the parameters was introduced while sampling to increase the accuracy by avoiding numerical cancellation.

Note that the affine matrix decomposition needs to be derived for the specifically chosen parametrization. If the other cross-section value a should be included as a variable parameter, for example, the above formula can be extended as found in Ullmann [250].

OGPA Training Results An OGPA training, according to Section 6.2.2, generates a parametric reduced order model for this setup. The meta parameters for the training are chosen according to Table 6.2. Furthermore, the center point in parameter space is chosen as the initial expansion point ${}^0\tilde{\boldsymbol{p}}_0$. The SQP algorithm in the MATLAB R2018b implementation is used for the local optimizations. The default settings are used for this algorithm, but the maximum number of residual evaluations per local optimization is limited to $n_{\mathrm{maxFun}} = 200$. Thus, non-converged parameter results may be accepted, for which the optimization algorithm could not find a minimum within n_{maxFun} objective evaluations.

Nineteen expansion points are added in 20 iterations of the greedy training for these settings. Afterward, $n_{\mathrm{skipMax}} = 12$ iterations provide an expansion point candidate, which has a true error smaller than $\varepsilon_{\mathrm{rel}}^{\mathrm{lim}}$, thus are discarded in the two-step validation. The greedy search

Description	Name	Value
Deflation length	l_{defl}	$1 \cdot 10^{-9}$
Krylov order	o	3
Max. no. of greedy iterations	n_{itMax}	50
Skipped iterations for lucky breakdown	n_{skipMax}	12
Sample set for pre-selection of ${}^{n}\tilde{\boldsymbol{p}}_0$	n_{pre}	50
Max. no. of residual calculations per iteration	n_{maxFun}	200
Error threshold	$\varepsilon_{\text{rel}}^{\text{lim}}$	$5 \cdot 10^{-3}$

Table 6.2: Meta parameters for pROM training of the beam example.

is ended after 32 iterations in a lucky breakdown, leading to a ROM size of $m = 235$.

The expansion point positions in parameter space are found in Table 6.3. In the latter, a general tendency of OGPA for problems in structural dynamics is visualized by a color scheme: the algorithm tends to place expansion points at the boundaries of specific parameter dimensions. If one concentrates on the original input parameter space without considering the additional frequency dimension, only 34 out of 171 parameter samples are no bound values. These findings confirm the observations by Maday et al. [163], which stated this general tendency for greedy approaches. This tendency is evident for the damping parameters η_1 and η_2 in particular, for which the lower bound values are obtained except for one iteration. Based on heuristic experience, this is a general tendency of OGPA, and mainly lower bound damping values are chosen for the basis construction of any structural model. This behavior can be utilized in practice, and the lower bound damping parameters can be directly used for basis construction if the parameter space dimension should be reduced for training.

As discussed in Section 5.5.3, the Krylov subspace depends linearly on the number of inputs if no deflation is considered. For the MIMO setting of the example, 20 expansion points with three orders and twelve inputs thus would result in a ROM size of $m = 720$. This illustrates that the ROM size reduction by inexact deflation is significant for this example, and 485 out of 720 candidates for basis vectors are omitted in the final basis.

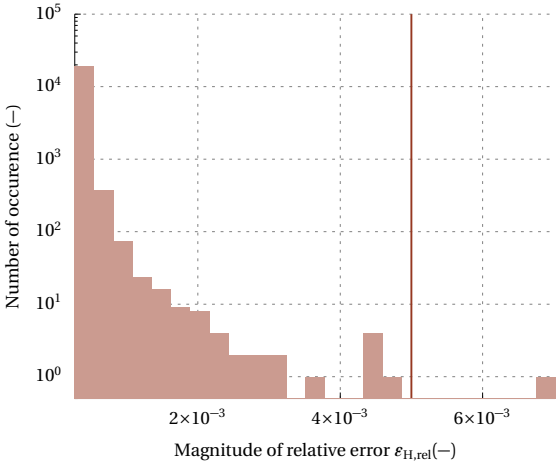

Figure 6.6: Histogram of the maximum relative error $\varepsilon_{\mathrm{H,rel}}^{\mathrm{max}}$ per parameter sample. $\varepsilon_{\mathrm{rel}}^{\mathrm{lim}}$, which was used as error threshold in the training phase is indicated by the red vertical line.

As evident from Figure 6.5, a good ROM quality is achieved for the three visualized parameter settings. The ROM quality is assessed more systematically in the following. According to Section 6.2.4 an a-posteriori validation set is introduced for this, on which the maximum relative error is assessed statistically. In an industrial setting, the validation set usually needs to be small, as evaluating the true error is computationally expensive for large-scale FOMs. However, as the FOM size $n = 13164$ is moderate for this first example, a large, randomly distributed validation set of size $n_{\mathrm{sam}} = 2 \cdot 10^4$ can be used, which allows for a more detailed error discussion in the following. The relative error distribution is calculated according to the left-hand side of Equation (6.13) and is visualized in Figure 6.6 for this large set. As visualized in the latter, solely one error overshoot with a value of $\varepsilon_{\mathrm{H,rel}}^{\mathrm{max}} = 6.5 \cdot 10^{-3}$ is observed, which is slightly larger than the error tolerance of $\varepsilon_{\mathrm{rel}}^{\mathrm{lim}} = 5 \cdot 10^{-3}$ for training. Consequently, one obtains a 100% confidence level for a probability of a good ROM outcome in between $99.9\% < a < 100\%$

$$P\,(99.9\% < a < 100\% | 19999, 20000) = 100\%,$$

when the Bayesian framework of Section 6.2.4 is employed. The Bayesian framework indicates this good ROM quality already with a small sample set; the latter is the standard scenario for large-scale industrial models. A validation set of 200 parameter points containing the overshoot already would have given $P(98.5\% < a < 100\%|199,200) = 80.5\%$, a set of 500 samples $P(98.5\% < a < 100\%|499,500) = 99.6\%$.

E_1	ρ_1 $\times 10^{-10}$	η_1	E_2	ρ_2 $\times 10^{-9}$	η_2	a	L_1	L_2	f_0
50000	8.5	0.0275	21750	3.0	0.0275	22	250	300	755.0
75000	7.0	0.005	8500	1.2	0.005	24	200	367	60.8
75000	7.0	0.005	8500	1.0	0.005	22.8	261	313	42.2
75000	7.0	0.005	32900	1.0	0.005	21.2	206	347	20
75000	7.0	0.005	35000	1.0	0.005	21.1	215	321	20
75000	7.0	0.05	35000	1.0	0.05	24	200	200	20
25000	7.0	0.005	35000	2.3	0.005	24	300	400	437.0
75000	7.0	0.005	8500	5.0	0.005	20	200	400	863.3
49567	7.0	0.005	21779	2.8	0.005	20	300	400	127.6
75000	7.0	0.005	8500	2.5	0.005	24	200	400	305.5
25000	7.0	0.005	35000	2.2	0.005	20	200	202	475.7
75000	7.0	0.005	8500	5.0	0.005	24	300	251	130.3
75000	9.1	0.005	8500	1.0	0.005	20	294	200	316.9
25000	10	0.005	8500	5.0	0.005	20	300	400	1500
75000	7.6	0.005	8500	5.0	0.005	20	300	306	1500
25000	7.0	0.005	35000	3.3	0.005	20	300	282	201.9
75000	7.0	0.005	8500	2.1	0.005	24	200	377	1335.6
25000	7.0	0.005	35000	5.0	0.005	20	261	400	140.3
71360	7.0	0.005	8500	5.0	0.005	23.6	300	230	1500
25000	10	0.005	35000	1.1	0.005	20	300	255	1500

Table 6.3: Overview of the optimized parameter samples for the greedy iterations in the beam example. All units are omitted. Green color-coded values belong to the lower bound, and blue color-coded values to the upper bound of the parameter range. The first line corresponds to the parameter values which were chosen generically for the initial Krylov subspace, thus are no result of the greedy search.

Performance of Alternative Training Strategies The comparably large validation set also allows discussing the performance of OGPA in

the context of more classic greedy search strategies with comparable costs as the OGPA setting. The following methods are compared:

- M-O50-50: OGPA with a lowered maximum number of residual evaluations per local optimization $n_{\mathrm{maxFun}} = 50$ for further efficiency enhancements. The remaining settings are chosen according to Table 6.2.
- M-RF400: greedy search strategy with a training set of 400 random parameter samples, which are fixed for all iterations.
- M-RC100: as M-RF400, but with a training set of 100 random parameter samples changing for each new iteration.

The same residual error indicator as for OGPA (Equation (6.16)) is used for all these greedy approaches to ensure comparability. The results from these methods are mapped to the performance of two baseline scenarios:

- M-WC: worst-case scenario in which the expansion points are placed arbitrarily in the parameter space without any training strategy at all.
- M-BC: quasi best-case scenario, in which an extensive greedy search is performed on the validation set by using the true relative error.

Each method which includes a random parameter sampling component exhibits some statistical variation in its results. Consequently, the following discussions are based on mean results for each approach, obtained from a linear average of five independent algorithm executions. An exception is M-BC utilizing a static validation set for training, thus does not require any averaging.

Many publications investigate the performance of pMOR methods by analyzing the maximum error and its decay rate for an increasing basis size, but not by a probabilistic framework as in Section 6.2.4. The maximum relative error is analyzed accordingly for the above methods in a first evaluation to align with these studies. The visualization of the results in Figure 6.7 provides two essential findings. Firstly, the obtained maximum error for the three analyzed methods M-O50-50, M-RC100, and M-RF400 are in between the worst and best-case point placement results. All these three methods involve a point placement

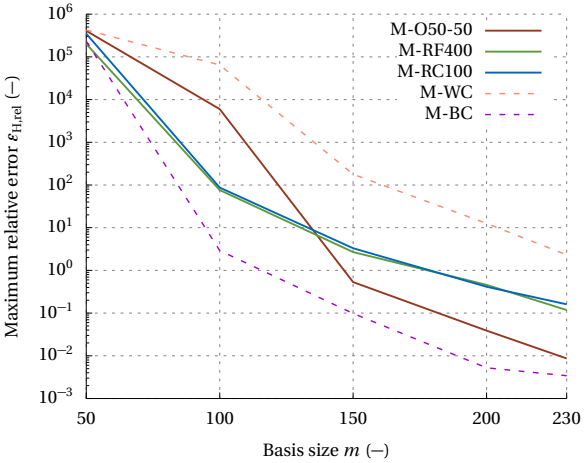

Figure 6.7: Comparison of the decrease of the maximum relative error $\varepsilon_{H,rel}^{max}$ on the validation set for an increasing basis size in the context of different methods for training. Averaged results are presented for five independent algorithm executions per method.

based on the error estimate of Section 6.2.3. This shows that this error indicator provides a valuable objective for training, although only the rough trend of the true error ε_H is provided. Secondly, OGPA outperforms more classic greedy search strategies for sufficiently large basis sizes when the same error indicator is used, and the meta parameters are set for all methods such that comparable numerical efforts are obtained (see Figure 6.7). At a basis size of $m = 230$, OGPA excels the other two methods by an error smaller by one order of magnitude. Thus, the approach of OGPA is valuable, especially for applications in which the maximum relative error is essential.

In a second analysis, the a-posteriori error evaluation is performed according to Section 6.2.4. Again, OGPA provides the best results around the converged basis size of $m = 230$: on average, there are five error overshoots within $n_{sam} = 2 \cdot 10^4$ samples for this approach. Anyhow, the proposed error analysis by Bayesian inference leads to another perspective on the ROM quality and thus often relaxed requirements. This is evident from the analysis of the alternative methods: the classic greedy search approach of M-RF400 also provides a small

number of 22 overshoots; even a purely random point placement by the method of M-WC produces a relatively small number of 203 overshoots on average. Evaluating the results of M-WC with Bayesian inference, still a confidence interval of $P(98.5\% < a < 100\%|19797, 20000) = 94.7\%$ can be obtained. In other words, the superiority of OGPA is less distinct for an error analysis with Bayesian inference. As a result, simpler training strategies than OGPA may be chosen for applications where the maximum error is not crucial, as long as there are not prohibitively many error overshoots.

6.3 Chapter Summary

An approach for model order reduction with the preservation of variable input parameters was developed, enabling large-scale FOMs with moderate modal density but a higher-dimensional input parameter space. A possible *curse of dimensionality* has to be faced for such high dimensional parameter spaces at two stages of the procedure: the training of the ROM in the offline phase and the evaluation of the ROM in the online phase. A global basis approach was chosen to address the latter, and local projection matrices for different parameter samples are concatenated in a global projection matrix, which is valid over the whole parameter space. Affine matrix decompositions are found as a parameter interpolation scheme for the system matrices. This approach avoids the *curse of dimensionality* in the online phase. It was briefly discussed how such a decomposition can be constructed non-intrusively to reuse standard commercial FE assemblers.

A high-dimensional input parameter space in the training phase is even more challenging as large-scale FOMs are considered. Only a few FOM system solutions are possible, but the model needs to be trained for the analytically unknown, non-convex error function in the high-dimensional parameter space. To enable the training for such models and thus to meet the *curse of dimensionality* in this phase, an optimization-based greedy search strategy was introduced (OGPA) for global basis generation. Motivated by the application of optimization-based strategies in reduced basis methods, the concept was transferred to a global basis construction through subspace algorithms and for the frequency-domain analysis of mechanical networks. The excitation frequency is considered an additional parameter dimen-

sion, and local bases, constructed at one expansion point, are added in each greedy iteration.

A goal-oriented error estimate was developed as an optimization objective for the application to subsystem coupling. This estimate is based on a residual expression as an indicator for the MIMO system's transfer function matrix error over the relevant parameter space. The gradient calculation of the objective was discussed. Based on the framework of Chapter 4, the gradients can be evaluated efficiently by an adjoint approach. Local optimizations are performed by using the gradients in the SQP optimization algorithm, providing local maxima of the error estimate. The global maximum of the error, however, remains unknown. As a remedy, firstly, a two-step selection procedure was introduced to account for the possibly non-optimal candidate expansion point placement. Secondly, an additional validation sampling set was introduced, on which the true error in the transfer function is evaluated after basis generation but before the online phase. Again, such evaluation is challenging for combining a large-scale FOM and high-dimensional input parameter space. Probability theory was employed to allow for a small validation set and simultaneously provide a reliable statement of ROM quality. A binomial setup was chosen, providing the probability of the transfer function matrix entries of the ROM below a given error tolerance. Confidence intervals are provided in addition. The efficiency of the pMOR approach was demonstrated based on a numerical example of a cantilever beam with a ten-dimensional parameter space.

CHAPTER 7

EXPERIMENTAL METHODS FOR THE ENERGETIC NETWORK ANALYSIS

For several purposes, experimental techniques for energetic network analysis are relevant during a virtual development process. The first application is the provision of reference measurements, either to validate numerical results or as a basis for a model updating like inverse parameter identification. Especially if damping parameters should be fitted, energetic quantities can be attractive as a reference. The second application is the inclusion of subsystems from a measurement-based identification in hybrid assemblies. However, such experimental methods can be challenging for energetic network analysis. As shown below, the lack of phase accuracy of measurement setups may require extra efforts for power evaluations, and systems may even lose their passivity. A method to correct systematic phase errors is introduced as a remedy. The focus is on SISO techniques for reference measurements, but with theoretical extensions to MIMO settings for an experimental subsystem identification.

For this, many paragraphs of Section 7.1 and Section 7.2 are reproduced from Ullmann et al. [256]. Assume a second-order system with

displacements as output $\boldsymbol{Y} : W$, and forces as input $\boldsymbol{U} : F$, as defined in Section 2.1.2 for the whole chapter.

7.1 Challenges for the Experimental Acquisition of Energetic Quantities

There are various challenges for measurements in structural dynamics, especially in the context of subsystem coupling. Continuous stress and displacement quantities need to be determined at the subsystem interfaces. Discretizing the latter, multi-axial force, moment, and displacement quantities must be evaluated concurrently at the same spatial locations. While this may be feasible for translational DOFs, the measurement of rotational DOFs requires extra effort. Furthermore, measurement points may not be directly accessible by measurement equipment. Additional error sources are present in standard experimental subsystem identification; an overview is provided in Allen et al. [6]. The remainder of this chapter does not focus on these general challenges of experimental methods. However, aspects that arise additionally from the direct measurement of energetic quantities and experimental subsystem identification for energetic network analysis are discussed.

7.1.1 Evaluation of Power Quantities

The measurement of power quantities in mechanical systems dates back to the 1970s. From then on, experimental approaches were developed to determine structure-borne sound power at arbitrary cutting sections inside basic mechanical (sub-)systems, such as trusses, beams, or plates. The displacement function is known from the analytical solution of such an idealized mechanical system and allows to calculate power from an acceleration sensor array. Corresponding methods are developed by Arruda et al. [17], Freschi et al. [82], Halkyard et al. [113], Linjama et al. [153], Mandal [164], Pavić [196], Szwerc et al. [237, 238], Troshin et al. [248], Verheij [265], and Williams et al. [272]. Mandal et al. [165] provide an overview. Such methods are inherently limited to analytical systems; complex geometric structures are excluded. Thus, only a few applications of such approaches may be found for industrial structures, but one must focus on the experimental acquisition of power quantities at the discrete inputs and outputs

of the assembled network or the decoupled subsystems. Technically, the evaluation of complex power at discrete points is straightforward for measurement systems, which provide the option to evaluate cross power spectra

$$P = \frac{i\omega}{2} \boldsymbol{U}^H \boldsymbol{Y} = \frac{i\omega}{2} S_{\mathrm{UY}}, \tag{7.1}$$

where S_{UY} is the cross power spectrum between the input and output signal. Practically, the challenging acquisition of power quantities for lightly damped systems was highlighted in Section 2.3.4, as the phase accuracy plays a key role. The required level of accuracy implies the presence of specific problems in experimental methods. It is known that each element in the measurement chain introduces a phase error. The sensors alone may have a systematic phase error that is considerably larger than the required accuracy. For example, impedance heads can have an absolute phase error that approaches $\varphi_{\mathrm{err}} = 5°$ (*PCB Model 288D01 Data Sheet* [197]).

Unfortunately, relative phase errors between force and acceleration channels are not documented in most cases. In addition, there is a dearth of systematic studies regarding the general phase accuracy of experimental methods and ways to improve them. Ganguly et al. [91] discusses the phase accuracy of frequency response function measurements; however, the study is limited to the particular case of capacitive sensors, and power quantities are not considered.

7.1.2 Determination of Energetic Measures

In addition to the analysis of mean power, the evaluation of the overall system energy might be of interest. The determination of energies may not only be valuable for network analysis but can also be used for damping characterization (see Ullmann et al. [256]). However, the measurement of energies is also not straightforward. Apart from the Lagrange energy, which can be calculated from the (sub)system input impedance by Equation (2.36), in general, one must integrate energy over the volume of the (sub)system (compare Equation (2.26)). Strains and stresses must be integrated over the system volume to obtain the potential energy, respectively, the velocities and mass distribution for kinetic energy. However, only the system input-to-output behavior can be directly measured. One computationally expensive remedy is fitting an inner system representation on the measurement data by

parametric system identification, from which energies can be calculated. Some aspects of such system identification are discussed briefly in Section 7.3. Another remedy to estimate energies from measured subsystems was discussed by Bobrovnitskii [35]. He showed for a SISO setting that the energies of a system in harmonic vibration could be estimated solely from its input-to-output behavior. For general MIMO systems of Section 2.1.2, the concept of Bobrovnitskii [35] is extended by:

$$\overline{E}_{\text{pot}} \approx \frac{\omega^2}{8} \boldsymbol{Y}^H \Re\left(\frac{\partial \frac{\partial \boldsymbol{U}}{\partial \boldsymbol{Y}\omega}}{\partial \omega} - \frac{\frac{\partial \boldsymbol{U}}{\partial \boldsymbol{Y}}}{\omega^2} \right) \boldsymbol{Y} = \frac{\omega^2}{8} \boldsymbol{Y}^H \Re\left(\frac{\partial \boldsymbol{H}^{-1}/\omega}{\partial \omega} - \frac{\boldsymbol{H}^{-1}}{\omega^2} \right) \boldsymbol{Y} \tag{7.2}$$

$$\overline{E}_{\text{kin}} \approx \frac{\omega^2}{8} \boldsymbol{Y}^H \Re\left(\frac{\partial \frac{\partial \boldsymbol{U}}{\partial \boldsymbol{Y}\omega}}{\partial \omega} + \frac{\frac{\partial \boldsymbol{U}}{\partial \boldsymbol{Y}}}{\omega^2} \right) \boldsymbol{Y} = \frac{\omega^2}{8} \boldsymbol{Y}^H \Re\left(\frac{\partial \boldsymbol{H}^{-1}/\omega}{\partial \omega} + \frac{\boldsymbol{H}^{-1}}{\omega^2} \right) \boldsymbol{Y}. \tag{7.3}$$

Corresponding formulas can be found for any other choice of inputs and outputs. Most publications use corresponding formulations, which are based on impedances $\boldsymbol{H}^{-1}/i\omega = \boldsymbol{F}/\boldsymbol{V}$, thus for velocities $\boldsymbol{V}$ as outputs. Reformulating Equation (7.2) and Equation (7.3) for impedances and assuming a SISO setting, one arrives at the formula of Bobrovnitskii [35]

$$\overline{E}_{\text{pot}} \approx -\frac{1}{8} |V|^2 \Im\left(\frac{\partial Z}{\partial \omega} - \frac{Z}{\omega} \right) \tag{7.4}$$

$$\overline{E}_{\text{kin}} \approx -\frac{1}{8} |V|^2 \Im\left(\frac{\partial Z}{\partial \omega} + \frac{Z}{\omega} \right), \tag{7.5}$$

where $Z = H^{-1}/i\omega$.

The above formulas allow for calculating the potential and kinetic energy from the inputs and outputs of any system. Nevertheless, Equation (7.2) to Equation (7.5) provide the correct energy quantities solely for undamped systems. It is only an approximation for damped structures, with an increasing error when damping increases. A discussion for the general MIMO case is found in Kim et al. [138], who use corresponding impedance formulations of Equation (7.2) and Equation (7.3).

Besides the approximation properties for damped systems, the sensitivity of the energy approximation to phase errors must be evaluated. The latter is discussed for the potential energy approximation

of SISO systems (Equation (7.4)), while generality for the MIMO case and the kinetic energy is preserved. The conditioning of the potential energy approximation becomes a more complex expression than that of mean power as provided in Equation (2.48). As an alternative, Equation (7.4) can be rewritten for the direct dependency on the relative phase as

$$\begin{aligned}\overline{E}_{\mathrm{pot}} \approx \frac{1}{8}\Bigg(& |F||V| \frac{\partial \Delta\varphi_{\mathrm{FV}}}{\partial \omega} \cos(\Delta\varphi_{\mathrm{FV}}) \\ & + \left(-\frac{\partial |V|}{\partial \omega}|F| + \frac{|F||V|}{\omega} - \frac{\partial |F|}{\partial \omega}|V| \right) \sin(\Delta\varphi_{\mathrm{FV}}) \Bigg).\end{aligned} \tag{7.6}$$

This reformulation already gives insight into the sensitivity of power with respect to the relative phase: Equation (7.6) potentially becomes sensitive to phase errors as soon as the cosine term grows sufficiently large. The latter is the case for frequencies in the vicinity of resonances. There, $\partial \Delta\varphi_{\mathrm{fv}}/\partial \omega$ takes high values for structures with light damping in particular and moderate phase errors thus are not expected to significantly distort the energy estimate of Equation (7.4).

Example 7.1 (Two-DOF system)

This assumption is validated in the following, and the calculation of the potential energy from interface quantities is exemplarily discussed for the two-DOF example of Section 2.3.4 as visualized in Figure 2.2 on page 37. A two-step error evaluation needs to be performed, as the potential energy is calculated through the approximation in Equation (7.4), but not the correct solution which is provided by

$$\overline{E}_{\mathrm{pot}}^{\mathrm{ex}} = \frac{1}{4}\left(k_1|X_1 - X_2|^2 + k_2|X_2|^2\right). \tag{7.7}$$

X_1 and X_2 are the two states of the two-DOF system, k_1 and k_2 the two stiffness values according to Table 2.1 on page 37.

In the first step, the approximation error is evaluated, thus the difference between Equation (7.4) and Equation (7.7). As no analytical function of the system's input-to-output behavior is generally available, the derivative of the input impedance must be calculated through finite differences. The use of finite differences implies introducing the step size as an additional variable in the discussion on the error. This discussion is not performed explicitly in the following, but a step size of $\Delta f = 0.3\,\mathrm{Hz}$ is chosen as a good compromise between numerical stability and accuracy for the example.

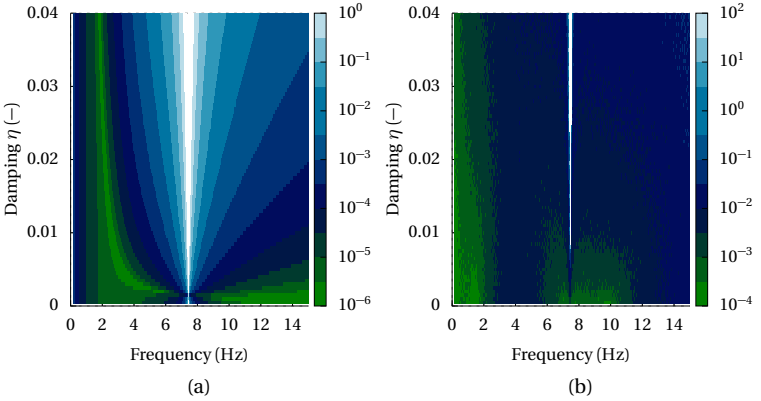

Figure 7.1: (a) Representation of the error of the energy estimate, Equation (7.4), compared with the correct solution of the potential energy of the two-DOF system, Equation (7.7); (b) Logarithmic representation of the coefficient of variation of the energy estimate, Equation (7.4), which is introduced by the uncertainty in the relative phase.

The error, which is introduced by the approximation in Equation (7.4) against the correct solution in Equation (7.7) is visualized in Figure 7.1(a). The latter illustrates that the error is negligible for most frequency ranges and small structural damping values, while it increases for increased damping. Furthermore, the error significantly increases in the proximity of the anti-resonance $f_\mathrm{A} = 7.71\,\mathrm{Hz}$ and results in negative energies, which is in line with the observations in Bobrovnitskii [35]. Consequently, as negative energies are nonphysical for passive systems, no error is calculated in such a case (Figure 7.1(a)).

In the second step, the sensitivity of the error approximation with respect to phase errors is evaluated. According to Section 2.3.4, a random relative phase error between $\Delta\varphi_{\mathrm{err}} \in [-1°, 1°]$ is introduced on $\Delta\varphi_{\mathrm{UY}}$ and the coefficient of variation for the potential energy is evaluated (compare Equation (2.49)). Furthermore, random noise is added to the frequency phase response to distort the calculation of finite differences, resulting in a standard deviation of $\sigma = 0.3$ over frequency. The results are provided in Figure 7.1(b), indicating that the potential energy estimate is less sensitive to phase errors. A coefficient of variation with respect to phase errors of $c < 10^{-3}$ is obtained for damping values $\eta < 0.01$.

■

As any industrial subsystem incorporates damping, the measurement-based energy determination is always incorrect. The two-DOF example illustrates that the energy estimate has a small error for low damping values, which increases with increasing damping. This is contrary to the dependency of the error in power on subsystem damping. Concurrent evaluations of energy and power in mechanical networks may be critical due to that reason.

7.2 The Concept of Phase Correction for Reference Measurements

As discussed in Section 7.1.1, the relative phase accuracy is crucial for correct power quantities of lightly damped systems. This requires additional efforts for a measurement-based acquisition of power, as each component of the measurement chain introduces a phase error, which can be significant. In the following, an approach is discussed to enable an experimental and direct determination of power quantities for lightly damped systems.

The basic concept is to analyze the measurement chain's overall systematic phase error and calculate an individual compensation per distinct channel pair and frequency point. These corrections should be test-specimen independent, thus independent of the system that is measured but purely determined by the measurement chain. The following approach is discussed for network reference measurements with a SISO setting. The basis for discussion is a benchmark problem with locally collocated assembly input and output. The measurement

at such collocated points allows for a measurement chain incorporating an impedance head and a two-channel data acquisition (DAQ) interface. It is discussed in Section 7.3 how one can extend the methodology to the measurement-based identification of lightly damped subsystems.

Several effects on the measurement of phases lead to systematic phase offsets and random errors (see ISO 16063 [1]). In the following, the focus is on systematic errors, and three sources of an erratic phase are considered:

1. leakage in signal processing.
2. phase lags in the DAQ interface.
3. phase offsets introduced by the impedance heads .

Leakage in the signal processing results in a distorted phase. It cannot be compensated by a general correction factor but must be reduced by appropriate excitation profiles and postprocessing strategies, which is discussed in Section 7.2.2.

In contrast, the other two sources of a systematic phase error are related to the measurement hardware. As it is assumed that these phase lags are test-specimen independent, test setups can be introduced for their identification per distinct channel pair in Section 7.2.3. As a result, a complex-valued phase correction factor

$$\boldsymbol{\Xi}_{\varphi} = \boldsymbol{\Xi}_{\mathrm{IH}} \circ \boldsymbol{\Xi}_{\mathrm{DAQ}} \tag{7.8}$$

can be introduced to the channel pairs to compensate for the phase lags in the measurement hardware during postprocessing. $\circ$ is the Hadamard product, $\boldsymbol{\Xi}_{\varphi}$ is the vector of complex-valued correction factors for the used combinations of input and output channels per frequency point. A corrected cross-power spectrum can be calculated from this correction factors by

$$S_{\mathrm{UY}}^{\mathrm{c}} = \boldsymbol{U}^{H}(\boldsymbol{\Xi}_{\varphi} \circ \boldsymbol{Y}). \tag{7.9}$$

The superscript $\square^{\mathrm{c}}$ indicates the correction for the phase lag of the measurement hardware in the following. Corrected power quantities, phase angles and input impedances can be calculated accordingly by introducing $\boldsymbol{\Xi}_{\varphi}$ in Equation (7.1), Equation (2.45) and Equation (7.4).

7.2.1 A Benchmark Problem for Validation

A benchmark problem is introduced, which provides the basis for discussing the phase correction method. The lightly damped benchmark problem, initially presented in Ullmann et al. [256], has a SISO setting with a unidirectional and collocated measurement of input and output. The benchmark allows discussing effects in power measurements of lightly damped systems. It is also the basis for evaluating the validity of a test-specimen independent phase correction approach.

The basic concept is a network of subsystems that correlate to basic analytical systems. A truss with a circular cross-section is suspended from a clamped beam with a rectangular cross-section (see Figure 7.2). Combined uniaxial sensors, the impedance heads IH:1 and IH:2, are placed at the truss interfaces to measure forces and accelerations concurrently. The mounting structures holding the clamp, truss, and beam are manufactured from the aluminum alloy EN AW-6060 to provide a lightly damped system and, thus, a challenging measurement benchmark.

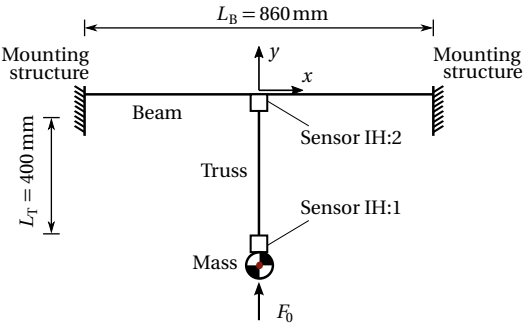

Figure 7.2: Basic concept of the benchmark structure for power measurements in uniaxial direction according to Ullmann et al. [256].

A two-dimensional FE model is employed without considering the sensors to find an initial design of the geometrical parameters.

A coarse discretization consists of 24 cubic beam elements and ten linear truss elements. The frequency range of interest is chosen as $f \in [1\,\text{Hz}, 800\,\text{Hz}]$, in which structure-borne power is analyzed at both, resonant and non-resonant frequencies. Three well-separated resonances should be presented that have symmetric mode shapes in the x-y plane of the system and with the truss vibrating along its longitudinal direction only (Table 7.3). The two sensors, IH:1 and IH:2, are only loaded on the longitudinal axis for these mode shapes. In order to tune the benchmark system for these resonances, the diameter of the truss cross section is chosen as $D = 0.016\,\text{m}$, the rectangular beam cross section dimensions as $b = 60\,\text{mm}$ and $t = 10\,\text{mm}$. Furthermore, an additional steel mass $m = 1.13 \cdot 10^3\,\text{t}$ is mounted between the lower end of the truss and excitation. For the aluminum material, the modulus of elasticity has a value of $E = 7 \cdot 10^4\,\text{N mm}^{-2}$, the mass density is $\rho = 2.85\,\text{t mm}^{-3}$ and a structural damping coefficient is specified as $\eta = 0.001$.

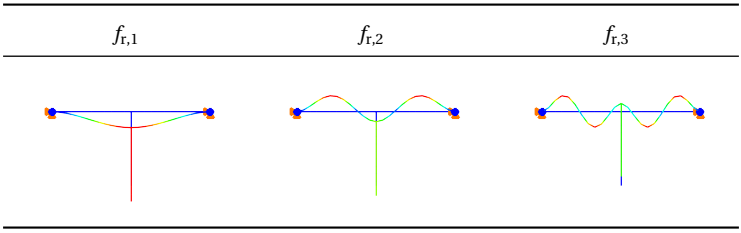

Figure 7.3: Mode shapes of the first resonances with the truss vibrating along its longitudinal direction only.

7.2.2 Phase Errors due to Leakage

Using the lightly damped benchmark structure, phase correction is discussed for three considered components of the measurement chain: impedance heads, DAQ, and signal processing. As indicated above, no correction factor can be found for the latter to compensate for leakage, but one must identify a combination of a suitable excitation profile and postprocessing strategy.

A numerical experiment is performed based on the simplified two-dimensional FE model of the benchmark structure introduced above and shown in Figure 7.2. Five excitation profiles are examined as listed

in Table 7.1. In order to calculate the time-domain response of the structure at IH:1 for these excitation profiles, a modal basis of the ten lowest mode shapes is considered for computational efficiency reasons. A preliminary modal refinement study showed convergence for that basis size. Each modal displacement is time-integrated by means of the Newmark-β time integration scheme (Belytschko et al. [30]) with a sampling rate of $f_s = 1/\Delta t = 102.8\,\mathrm{kHz}$. Afterward, the signals are transformed into the frequency domain using a short-time Fourier transformation (STFT) and Hanning windows. The settings for the transformation are contained in Table 7.1 per excitation profile. T_w is the window length of the STFT segments, θ their overlap. The first harmonic is extracted to identify the time-independent frequency response, except for signal profile p5, for which an averaging is performed.

		Parameters		STFT postprocessing	
No.	Profile	Speed	T_{tot}	T_w	θ
p1	Stepped sine	$T_f = 8\,\mathrm{s}$ resp. $1.5\,\mathrm{s}$	2640	1	-
p2	Linear chirp	$\Delta f = 1\,\mathrm{Hz\,s^{-1}}$	980	1	0.9
p3	Linear chirp	$\Delta f = 1\,\mathrm{Hz\,s^{-1}}$	980	10	0.99
p4	Logarithmic chirp	$\Delta f = 1\,\mathrm{Hz\,s^{-1}}$	1300	1	0.9
p5	Pseudo-random	$T_p = 1\,\mathrm{s}$	600	1	0.9

Table 7.1: Excitation profiles and corresponding postprocessing strategies, which are evaluated for the numerical study of the 2D benchmark system. T_p is the hold-off time period for a decaying homogenous solution, T_f the time a single frequency is kept. T_w is the window length of the STFT segments, θ their overlap.

Figure 7.4 visualizes the resulting phase errors of the transformed time signals from this numerical experiment against the direct harmonic solution of the system in the frequency domain. The phase error is generally below 1% except for some resonance shifts. Nevertheless, the error in the power quantities is significant for several excitation profiles, as shown in Figure 7.5. For the latter, the power values are normed by the square of the frequency-dependent load amplitude $|F|^2$ to limit the discussion on the influence of the identified phase angle.

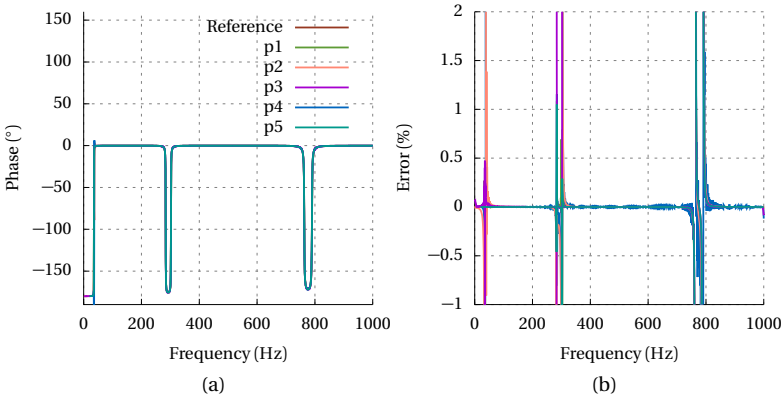

Figure 7.4: (a) Relative phase between input and output at the virtual sensor point IH:1 for the excitation profiles in the time domain and the harmonic solution in the frequency domain as reference; (b) Error of the relative phase at the different excitations with respect to the harmonic solution in the frequency domain.

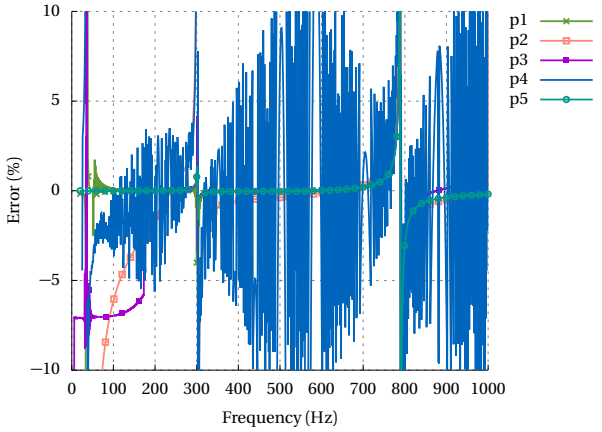

Figure 7.5: Numerical power spectra error at IH:1 for the different excitation profiles in the time domain with respect to the harmonic solution in the frequency domain.

Figure 7.6 illustrates the correspondingly normed power quantities and shows an erratic response around the lowest resonance frequency in particular. For such low resonant frequencies, systems with low damping possess a long-time homogeneous solution, which may still be present in measuring other excitation frequencies. Correspondingly, the stepped sine excitation p1 provides accurate power quantities. Each excitation frequency is held constant for a lengthy time period of T_p until the homogeneous solution decays. Using a transient chirp signal excitation (p2 to p4) can provide accurate power quantities, too. However, leakage necessarily is present; the amount depends on the selected parameters of the STFT, the window length T_w in particular. For a small window length of $T_\mathrm{w} = 1\,\mathrm{s}$, the frequency response of the power erratically indicates a non-passive system in the proximity of the first resonance as a result. Consequently, accurate power quantities may require larger window lengths for direct measurement by a chirp excitation for lightly damped systems. Alternatively, other transformation strategies are available for such an excitation. Such concepts are discussed by Orlando et al. [187] in the scope of the measurement of frequency response functions for modal analyses.

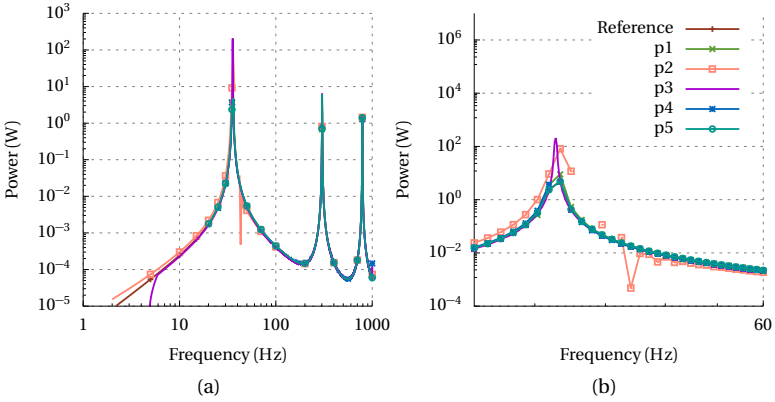

Figure 7.6: Numerical power spectra at IH:1 in the longitudinal direction of the truss for both, the different excitation profiles in the time domain and the reference harmonic solution in the frequency domain. All power spectra are normed by $|F|^2$.

Leakage can be avoided at all if a periodic multi-sine signal with a period length of T_p is used. Such periodic excitation is provided by the pseudo-random signal p5 as found in Phillips et al. [201]. Furthermore, several averages can be taken to reduce noise as the signal is periodic. It is evident from Figure 7.6 and Figure 7.5 that this excitation profile provides accurate power quantities for a direct measurement as a result.

7.2.3 Systematic Phase Errors in the Measurement Hardware

In contrast to leakage compensation, correction factors can be found for the phase lag of the measurement hardware, as discussed above. The DAQ interface and the impedance heads are considered for this, and test setups are introduced under the assumption of test-specimen independent phase lags. While the latter is reasonable for the DAQ interface, such an assumption requires additional elaboration for impedance heads.

Data Acquisition Interface

A SIEMENS SCADAS III system is used in the final experiments, and the systematic phase lag is evaluated for its two channel pairs to which the impedance heads IH:1 and IH:2 are later connected. Therefore, a test setup is introduced as follows: Each channel pair is connected to a one-channel signal generator by equal-length cables and a Y-branch adapter. The signal generator provides a chirp voltage signal (profile p3 listed in Table 7.1), which is recorded by the two channels concurrently. The resulting channel pair should have a zero relative phase $\Delta\varphi_\mathrm{DAQ} = 0$ assuming that the cables and adapters do not influence the phase. The correction factors $\boldsymbol{\Xi}_\mathrm{DAQ}$ are calculated for each of the two channel combinations $j = \{1,2\}$ directly from the Fourier spectra of channel voltage signals as a result,

$$\Xi_{\mathrm{DAQ},j} = \frac{\upsilon_{j1}\,\upsilon_{j2}^*}{|\upsilon_{j1}\,\upsilon_{j2}^*|}, \tag{7.10}$$

where υ is the complex-valued amplitude of the voltage signal.

For robustness, the measurement on the test setup is repeated six times for each of the two channel pairs. The resulting mean values, standard deviation, and extreme values of the relative phase are

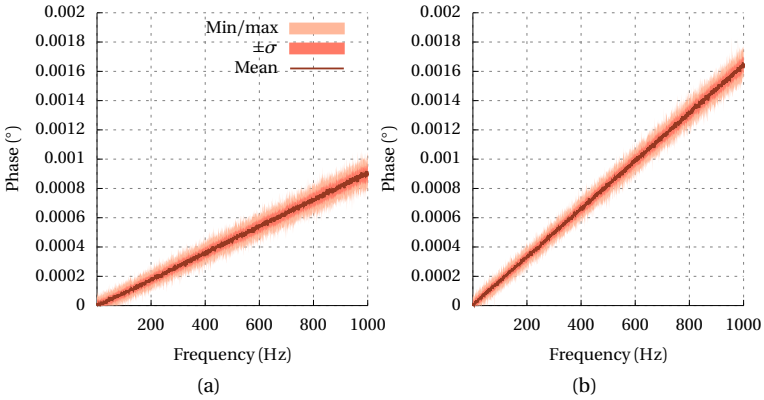

Figure 7.7: Measured relative phase of the SCADAS III DAQ channel pairs used for the power measurements ((a) channel pair used for IH:1 and (b) channel pair used for IH:2).

provided in Figure 7.7. The latter provides two essential findings on the phase lag of the DAQ interface: Firstly, all relative phase lags are small ($\Delta\varphi_{\text{err}} < 2 \cdot 10^{-3}$). Secondly, they are practically a linear function of the frequency in the considered frequency range. The linear frequency dependency is an indicator for a constant time shift, which is introduced into the measurement (Ganguly et al. [91]).

Impedance Heads

The systematic phase lags are classified into two groups for impedance heads: test-object-dependent and independent errors. Test-object-dependent errors originate from the mechanical interaction between the sensor spring-mass system and the attached test structure, which alters the frequency response of the coupled sensor-test-object system compared to the tested structure itself. This alteration is an issue for setups with force sensors in general and thus impedance heads: Force sensors need to be connected in series to the structure along the load path, leading to a mechanical mistuning of the test system. The latter mainly occurs around the additional resonances added by the sensor. The influence of such effects on the signal amplitudes was thoroughly investigated for several decades, refer to Brownjohn et al.

[45], Hakansson et al. [112], Haughton [120], Merkel et al. [174], and Rasmussen [206]. For the considered benchmark structure and used impedance heads, a study on the mechanical mistuning is available in Ullmann et al. [256], which focuses on the relative phases, not amplitudes. The study showed that the phase lags resulting from such mistuning are slight in the benchmark case. As a result, no compensation is provided for them in the following.

The situation is different for the second group of systematic phase errors, which are test-object independent. Consequently, these phase lags do not result from the mechanical interaction of the sensor and the test object. As demonstrated below in accordance with Ullmann et al. [256], these test-object-independent errors need to be considered for any sensor combination.

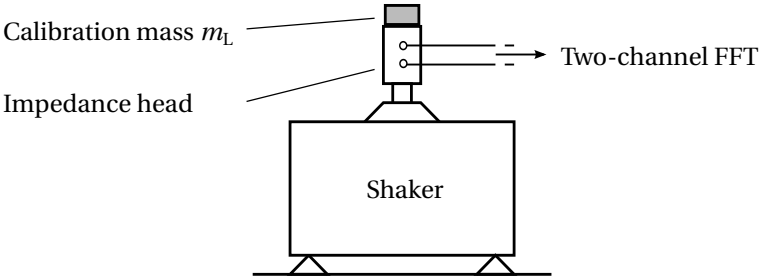

Figure 7.8: Schematic drawing of the top-mass setup for the impedance head phase measurements according to Ullmann et al. [256].

A test setup is created according to Figure 7.8 to identify these relative phase errors between force and acceleration signals of impedance heads. Such a setup is known from calibration experiments for impedance head signal amplitudes; refer to Scott et al. [223] for an example. The impedance head, for which the phase error should be determined, is mounted on a uniaxial shaker table. A mass as ideal as possible is placed on top of the impedance head. In the proposed test setup, three different masses are used, whose values are between $m = 76.3 \cdot 10^{-6}$ t and $m = 6.1 \cdot 10^{-4}$ t. Given that the masses are ideal, they have a purely imaginary impedance

$$Z = \mathrm{i}\,\omega\, m_\mathrm{L}. \tag{7.11}$$

A zero relative phase $\Delta\varphi_{\mathrm{IH}} = 0°$ should be measured for the acceleration signal A and force signal F at this imaginary impedance. As a result, the phase error is directly provided by the measured phase for each of the two impedance heads $j = \{1,2\}$,

$$\Xi_{\mathrm{IH},j} = \frac{F_j A_j^*}{|F_j A_j^*|}\,\Xi_{\mathrm{DAQ},j}^{-1}. \tag{7.12}$$

$\Xi_{\mathrm{DAQ},j}$ is the phase correction of the DAQ which is used for the test setup, F_j and A_j are the force and acceleration Fourier spectra.

The test-object-independent phase error of the impedance heads should be measured using the test setup. The setup, however, includes dependent phase errors itself, as they were discussed above. The latter result from the mechanical interaction of the sensor's mass-spring system with the mass loading. The phase response of the coupled system is measured and not the one of the mass alone. Such test-object-dependent phase errors should not hide the test-object-independent phase errors. Thus, the test-object-dependent error needs to be quantified first to determine the suitability of the test setup.

This is performed numerically using the model, which was provided by the sensor manufacturer DYTRAN and is shown in Figure 7.9 and Table 7.2.

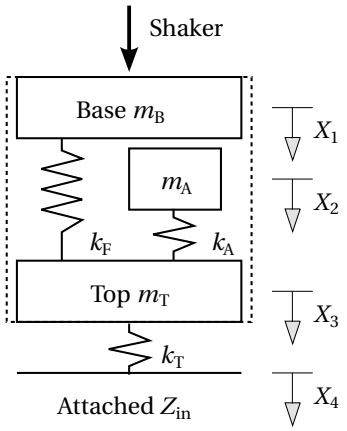

Figure 7.9: Impedance head model scheme.

Quantity	m_B	m_A	m_T	k_F	k_A	k_T	η
Value	$6.5 \cdot 10^{-9}$	$2.5 \cdot 10^{-8}$	$5.5 \cdot 10^{-10}$	1	0.25	0.25	0.01

Table 7.2: Impedance head model parameters scaled by k_F.

Uniform hysteretic damping is assumed with $\eta = 0.01$, which is a conservative estimate of the damping inside the sensor structure; therefore, also of the relative phase. The relative phase is evaluated at the top mass m_T for the cross correlation between the force in the force crystal spring, k_F, and the displacement of m_T,

$$S_{UY} = (1 - i\,\eta) k_F (X_1 - X_3)(X_3)^*. \tag{7.13}$$

As the input impedance Z_{in} is purely imaginary (compare Equation (7.11)), the test-object-dependent phase error in the test setup is equal to the phase of S_{UY} in Equation (7.13) deviating from $a\pi$ with $a \in \mathbb{Z}$. The corresponding phase error is evaluated for both the lowest and highest mass loading used in the top-mass setup of Figure 7.8 and is visualized in Figure 7.10. Figure 7.10(b) illustrates that the test-object-dependent phase error inside the impedance head model is small for the span of used mass loadings, $\Delta\varphi_{err} < 0.04°$. Accordingly, the above top-mass setup can provide an approximation of test-structure independent phase lags, which are significantly larger than $\Delta\varphi_{err} \gg 0.04°$.

With this known range of validity for the test setup, the test-object-independent phase error of the impedance heads is measured. Again, a chirp excitation (profile p3 of Table 7.1) is chosen, and the phase correction value is calculated based on twelve measurements as visualized in Figure 7.11; four for each mass.

Comparing the averaged phase results for the impedance head measurements of Figure 7.11 with the ones of the DAQ interface in Figure 7.7, they are similar in that they are again an almost linear function of frequency, indicating again a constant time shift as the reason for the phase lags. Nevertheless, the mean results differ as there are frequency ranges in which they deviate from the linear phase function; combined with this is a significant standard deviation σ. These frequency ranges are linked with test setup resonances, resulting from imperfections of the theoretically perfect uniaxial setup and distorting the phase function. For the different masses m_L, the resonant

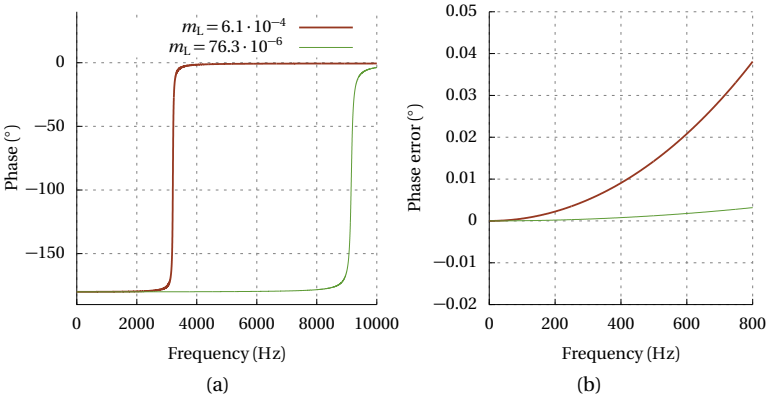

Figure 7.10: (a) Relative phase between force input and displacement output calculated at the top-mass, m_T, of the impedance head model. (b) The error of the relative phase due to mechanical interaction of the sensor system and the mass. Two mass loads, m_L, are evaluated: the lightest and heaviest masses used in the top-mass setup.

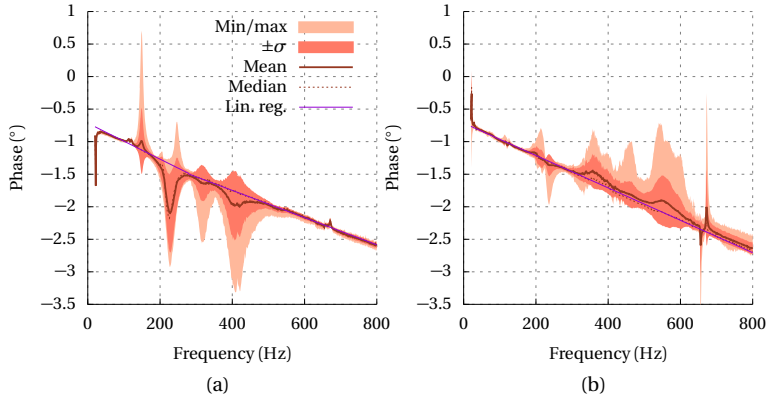

Figure 7.11: Relative phase of the two impedance heads used for the power measurement obtained by the top-mass setup ((a) IH:1, (b) IH:2). Three different masses are used, and four measurements are performed for each mass.

frequency ranges are shifted, which leads to a moderate effect on the median value of all measurements but a significant one on the mean and standard deviation. To compensate for these artifacts from imperfections of the test setup, not the mean value is directly employed, but the correction value is obtained from a (bi-)linear regression of the median value. The final phase correction from the regression approaches $\Delta\varphi_{\mathrm{IH}} = 3°$ at a frequency of $f = 800\,\mathrm{Hz}$ for the single impedance heads.

Note that for frequency ranges in which the test setup is not in resonance, the phase has a standard deviation of $\sigma \approx 0.1°$, which is small compared to the mean value. This slight standard deviation indicates that the influence of the mass loading is small for the evaluated masses; thus, it validates the test setup and confirms the numerical simulations above.

In comparing the magnitude of $\Delta\varphi_{\mathrm{IH}}$ with the one of $\Delta\varphi_{\mathrm{DAQ}}$, one observes that the latter is smaller both in terms of mean and standard deviation. The mean of $\Delta\varphi_{\mathrm{DAQ}}$ is smaller by three orders of magnitude compared to the mean of the impedance heads; it is even smaller than the expected distortion of phase results in the top-mass setup. Accordingly, the complex correction value of the overall measurement chain is simplified to the following:

$$\boldsymbol{\Xi}_{\varphi} \approx \boldsymbol{\Xi}_{\mathrm{IH}}. \tag{7.14}$$

7.2.4 Results for the Benchmark Problem

The potentials of the method for phase correction are demonstrated for the benchmark problem of Section 7.2.1 in the following. To validate measured power results, the hardware realization of the benchmark must correlate with a numerical model. In the first step, a FE model is found for this, which provides a reference for the power quantities. The hardware realization and the numerical model are presented in detail. Both are available online for reproduction in Ullmann [251]. In the second step, the measurement results for power are discussed using the correlated benchmark.

Correlation Hardware and Numerical Model

Hardware realization The hardware realization of the mechanical system in Section 7.2.1 should satisfy the idealized mechanical modeling assumptions as far as possible. Two identical pyramidal supports

are developed for this, as they provide a clamp condition for the beam and open space under the beam of $h = 720\,\text{mm}$ height, which allows suspending the truss vertically for avoiding bending loads. The pyramids are manufactured from 32 mm thick aluminum plates screwed together by 54 M10 screws per pyramid and to a foundation by 12 screws to ensure sufficient stiffness at the clamping. The beam is extended by 150 mm at each end to directly clamp the beam onto each of the pyramid supports by six M8 screws, resulting in an overall beam length of $\tilde{L}_\text{B} = 860\,\text{mm} + 2 \cdot 150\,\text{mm} = 1160\,\text{mm}$.

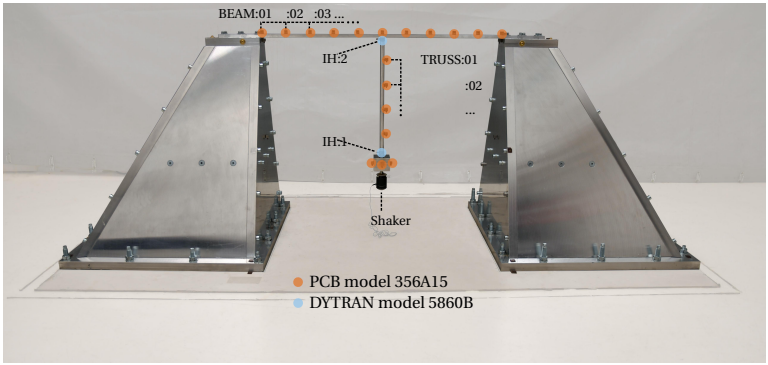

Figure 7.12: Hardware realization of the benchmark structure, including the sensor instrumentation for uniaxial phase and power measurements in the longitudinal direction of the truss.

Two impedance heads from DYTRAN, model 5860B, are installed at the positions IH:1 and IH:2; thus, between the beam and truss, and truss and mass, respectively. 10-32 UNF screws connect the impedance heads to the neighboring subsystems. As impedance heads are typically used to measure signals at the load point of a structure, they specify a side of the sensor that should be mounted to the test structure and another for the shaker attachment. The impedance heads are installed for the benchmark structure with the test-structure attachment site oriented toward the global y axis as defined in Figure 7.2. Furthermore, 19 triaxial accelerometers from PCB, model 356A15, are mounted to identify mode shapes as indicated in Figure 7.12. An LMS Qsources integral shaker is suspended below the mass. As this shaker is self-aligning, it minimizes the out-of-plane excitation.

The numerical model A more detailed three-dimensional linear FE model is introduced, which is found based on preliminary mesh convergence studies to prevent shear locking in the modeling of the pyramids. The resulting discretization is found in Table 7.3 and visualized in Figure 7.13. The FE program Simulia ABAQUS 2017 Hotfix 2 is used for the assembly and all evaluations of the benchmark model in the following.

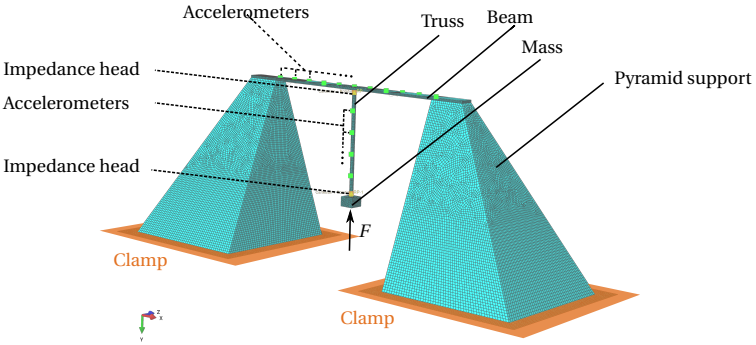

Figure 7.13: FE model of the benchmark structure.

Although the mesh is rather fine, the model implies several simplifications: tie contacts model all screw connections. Discrete spring elements with a stiffness value of k_{T} and k_{R} for the translational and rotational DOFs, respectively, are introduced to represent the impedance heads as well as point masses. The chosen values for the DYTRAN impedance heads are listed in Table 7.3. Kinematic couplings tie the spring reference points to each subsystem interface connected to the impedance heads.

The system is loaded in the global y-direction by a distributed load on the lower mass surface to avoid singularities. The net load amplitude equals the frequency response of the excitation force, which is obtained from the experiment below. This setting allows comparing the resulting frequency responses of the power and other energetic quantities from simulation and experiment. Anyhow, neither is there a perfect uniaxial excitation in the hardware realization nor a perfect response along the y-axis due to manufacturing tolerances or inexact

Part	Modeling	Material/ properties
Beam	39 925 tetrahedron/brick elements	Aluminum
Truss	4288 tetrahedron/brick elements	Aluminum
Mass	5600 tetrahedron/brick elements	Steel
Pyramid	19 144 quadrilateral shell elements	Aluminum
Impedance head	Spring element	$k_T = 1.1 \cdot 10^6\,\mathrm{N\,mm^{-1}}$
		$k_R = 1.0 \cdot 10^7\,\mathrm{N\,mm^{-1}}$
	Concentrated mass	$m = 3.7 \cdot 10^{-5}\,\mathrm{t}$
Accelerometer	Concentrated mass	$m = 1.2 \cdot 10^{-5}\,\mathrm{t}$

Table 7.3: Modeling of the different FE parts for the benchmark structure. All elements have linear element ansatz functions.

sensor positioning. An additional 1% of the net uniaxial excitation in y-direction is added to the remaining system coordinate directions to account for the effect of such geometrical imperfections qualitatively but not quantitatively.

The chosen material parameters are listed in Table 7.4. A uniform structural damping value of $\eta = 0.0025$ is introduced for the elements of the entire structure. The assumption of structural damping is a common engineering approach for metal parts and is validated below.

Material	E	ν	ρ	η
Aluminum	$7.05 \cdot 10^4\,\mathrm{N\,mm^{-2}}$	0.3	$2.65 \cdot 10^{-9}\,\mathrm{t\,mm^{-3}}$	0.0025
Steel	$2.1 \cdot 10^5\,\mathrm{N\,mm^{-2}}$	0.3	$7.86 \cdot 10^{-9}\,\mathrm{t\,mm^{-3}}$	0.0025

Table 7.4: Material properties of the FE model for the benchmark structure. ν is the Poisson value.

Correlation The simulation model is validated against the actual hardware representation through modal analysis. An eigenvalue analysis of the undamped numerical model is performed, and an experi-

mental modal analysis with a hammer excitation of the upper beam. Fourteen numerical and eleven experimental resonances are identified up to a frequency of $f = 800\,\mathrm{Hz}$. The numerical mode shapes are provided in Figure 7.14. The natural frequencies, mode shapes, and damping modeling are correlated for the experimental and numerical analysis in the following.

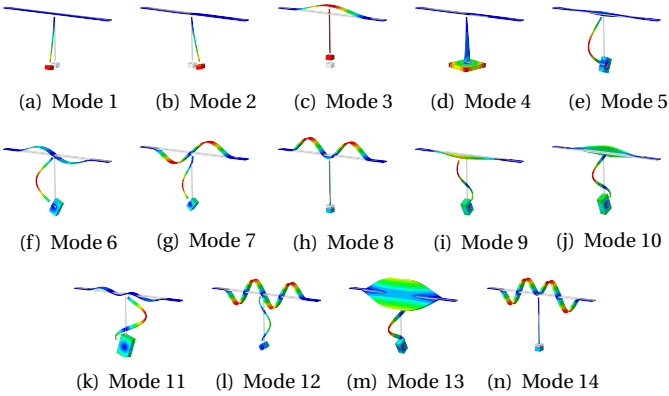

Figure 7.14: Normal mode shapes for the FE model's resonances up to $f = 800\,\mathrm{Hz}$.

Usually, normal modes are obtained from the eigenvalue problem of the undamped simulation model. However, the experimental modal analysis provides damped mode shapes; they contain relative phase information for the vibration of the single spatial points and are generally complex valued. A common approach is to transform the measured complex mode shapes to corresponding undamped normal modes to enable direct comparability to the simulation model; refer to Alvin et al. [8]. Such transformation omits the mode shape's phase information, thus dropping information. Pappa et al. [192] proposed the modal phase collinearity (MPC), which can be written as (Alvin et al. [8])

$$\mathrm{MPC} = \frac{\left(\Im(\boldsymbol{\Upsilon}_j)^T \Im(\boldsymbol{\Upsilon}_j) - \Re(\boldsymbol{\Upsilon}_j)^T \Re(\boldsymbol{\Upsilon}_j)\right)^2 + 4\left(\Re(\boldsymbol{\Upsilon}_j)^T \Im(\boldsymbol{\Upsilon}_j)\right)^2}{\left(\Im(\boldsymbol{\Upsilon}_j)^T \Im(\boldsymbol{\Upsilon}_j) + \Re(\boldsymbol{\Upsilon}_j)^T \Re(\boldsymbol{\Upsilon}_j)\right)^2} \tag{7.15}$$

to evaluate the amount of phase information, thus complexity, before the transformation. $\boldsymbol{\Upsilon}_j$ is a damped mode shape obtained from an experimental modal analysis. If the phase is correlated, all points vibrate within the same phase for a mode shape, and the MPC is equal to one; for an uncorrelated phase, the MPC equals zero. For a mode shape with a fully correlated phase, the transformation does not omit information on the mode itself. Consequently, Alvin et al. [8] state that a corresponding unambiguous normal mode $\tilde{\boldsymbol{\Upsilon}}_j$ can be found for a $\boldsymbol{\Upsilon}_j$ with MPC > 0.9.

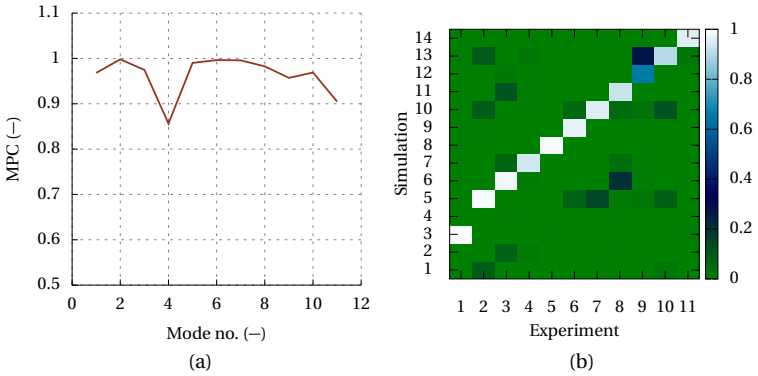

Figure 7.15: (a) Complexity of the experimentally determined mode shapes evaluated by means of the MPC; (b) MAC evaluation between the simulation model and experiment.

The MPC is evaluated for the experimental modal analysis of the benchmark structure in Figure 7.15(a). All mode shapes have an MPC > 0.95 apart from modes 4 and 11; therefore, they are almost correlated in phase and are transformed into approximate real-valued mode shapes. In the next step, these normal modes are compared to the ones of the undamped simulation model using the modal assurance criterion (MAC, Allemang [5])

$$\mathrm{MAC} = \frac{|\boldsymbol{\Phi}_i^H \tilde{\boldsymbol{\Upsilon}}_j|^2}{\boldsymbol{\Phi}_i^H \boldsymbol{\Phi}_i \tilde{\boldsymbol{\Upsilon}}_j^H \tilde{\boldsymbol{\Upsilon}}_j}, \tag{7.16}$$

where $\boldsymbol{\Phi}_i$ is a mode shape obtained from simulation. The resulting MAC matrix is shown in Figure 7.15(b). The latter indicates a good

correlation between the experimental and numerical mode shapes in the lower-frequent modes in particular. Although the MAC value decreases for mode shapes with increasing resonant frequency due to a more significant influence of geometrical imperfections, mode 14 still has a MAC value of 0.86. The MAC of mode 13 is an exception as it indicates a poorer correlation with a MAC = 0.65. Nevertheless, one can explain this by a lack of observability caused by the experimental setup rather than by an actual poor correlation. The sensor instrumentation of the beam is on its longitudinal axis; thus, it is unable to capture all beam rotations around this axis as indicated by the corresponding mode shape of the simulation model (see Figure 7.14).

Furthermore, the frequency values of the experimental and numerical resonances mapped through the MAC analysis are compared in Table 7.5. The latter shows that the frequency values differ only by a maximum of 6.7%.

No.	f_r			ξ	
	EMA (Hz)	FEM (Hz)	Error (%)	EMA (%)	FEM (%)
1		8.5			0.125
2		9.6			0.125
3	33.6	35.5	-5.4	0.18	0.125
4		111.7			0.125
5	136.2	141.8	-3.9	0.54	0.125
6	143.2	147.7	-3.0	0.20	0.125
7	201.8	205.3	-1.7	0.04	0.125
8	281.0	284.6	-1.3	0.15	0.125
9	319.0	339.1	-5.9	1.1	0.125
10	378.0	405.4	-6.8	0.93	0.125
11	393.0	413.2	-4.9	0.35	0.125
12	606.6	607.3	-0.1	0.1	0.125
13	669.3	688.4	-2.7	0.42	0.125
14	730.0	741.7	-1.6	0.1	0.125

Table 7.5: Natural frequencies f_r and modal damping values ξ of the benchmark structure for both the experimental and numerical model.

The correct damping representation in the numerical model is essential for a meaningful power evaluation and can be evaluated qualitatively and quantitatively for the FE model by the modal correlation. Qualitatively, one can state that the constant damping distribution over the entire spatial simulation model domain is admissible based on the high MPC values of the mode shapes from the experiment. In the case of highly localized damping, the phase of the mode shape would be uncorrelated. For a quantitative assessment, the frequency dependency of the damping is evaluated based on the modal damping ratios. Because the overall FE model includes a frequency-independent structural damping factor, the latter can be directly transformed into equivalent modal damping ratios using

$$\xi = \frac{\eta}{2} \cdot 100\%, \tag{7.17}$$

which results in a constant modal damping ratio of $\xi = 0.125$ for the simulation model. Table 7.5 shows that, on average, the experimentally determined values coincide well with this value for the mode shapes 3, 8, and 14. These mode shapes are similar to the one of Table 7.3 and include a vibration of the truss almost uniaxially along its longitudinal axis; The corresponding resonant frequencies are called longitudinal resonances in the following. As these mode shapes are mainly excited in the following experiments, the damping modeling of the simulation model is validated for this experimental setup.

Results

The experimental results for the power quantities and relative phases are analyzed at the impedance heads based on the validated benchmark structure. In the following, the mean value μ from 12 measurement runs is calculated, and the standard deviation σ is evaluated while a normal probability distribution of all measured quantities is assumed.

The experimental results at IH:1 and IH:2 are analyzed for post-processing without phase correction in the first step. Figure 7.16 compares the relative phase at IH:1 for the experimental results against the numerical ones and shows that the relative phase diverges the more the frequency increases, resulting in a maximum difference of almost 3°. Due to that mismatch, the experimentally determined relative phase is partly in the wrong quadrant of the imaginary plane

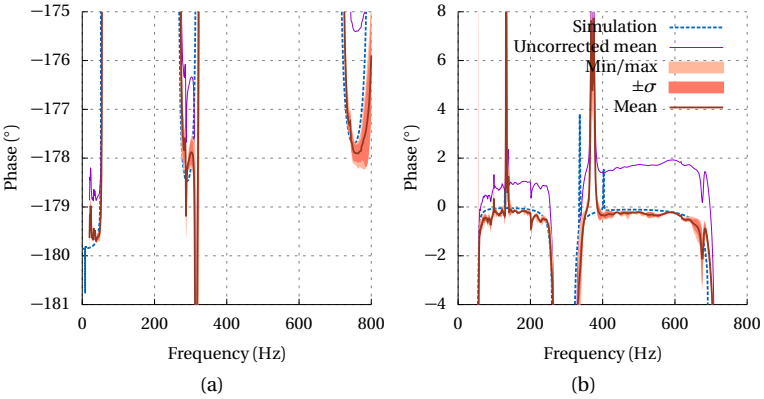

Figure 7.16: Relative phases between input and output, $\Delta\varphi_{UY}$, at IH:1, evaluated statistically for the experiment and compared with the simulation; (a) detail for a range between $\Delta\varphi_{UY} = -181°$ and $\Delta\varphi_{UY} = -175°$; (b) between $\Delta\varphi_{UY} = -5°$ and $\Delta\varphi_{UY} = 6°$.

(see Figure 7.16(b) and compare Equation (2.53)). The corresponding power quantities in Figure 7.17 wrongly indicate a non-passive system behavior as a result, except in frequency ranges close to resonances. This result visualizes the challenge of correctly determining power quantities for non-resonant frequencies and lightly damped systems.

The phase correction of Equation (7.9) provides a remedy. As a result, the relative phases differ from the ones of the simulation by a maximum value of 0.2° (see Figure 7.16). This value is equal to the span of the scatter band, which is obtained from the phase correction of the impedance heads; refer to Section 7.2.3. The corrected phases enable experimentally determined power quantities that match the ones of the simulation qualitatively and quantitatively, as shown in Figure 7.18. On a qualitative scale, the mean power is mainly positive and indicates a passive system for most frequencies when the phase correction is applied. This matches the results of the FE model and is discussed in more detail below. Furthermore, the experimentally determined power quantities reasonably match the ones of the simulation also qualitatively with a maximum mismatch of the mean by $5 \cdot 10^{-7}$ W; apart from the lowest resonance frequency. The latter is due to the experimental design, in which the auto-power spectrum

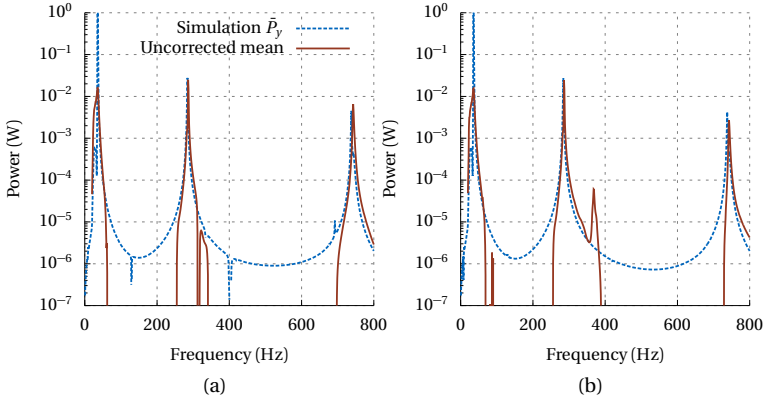

Figure 7.17: Mean power results at the impedance heads from simulation and measurement; the latter has no phase correction for the measurement chain ((a) IH:1 and (b) IH:2).

of the experimental shaker excitation is used for the FE calculations. At the lowest resonant frequency of the experimental setup, the force level drops significantly in a very narrow frequency band due to the light damping of the corresponding mode. As the numerical and experimental mode differs by two hertz (see Table 7.5), a significantly higher force is applied to the simulation in the first resonance than in the experimental setup.

It is evident from Figure 7.18 that there are frequency ranges in which negative power values are still obtained at IH:1 for the experimental phase-corrected results, but also the simulation model. For the simulation model, this is the case around the resonances at $f_{\mathrm{r},9} = 339.1\,\mathrm{Hz}$ and $f_{\mathrm{r},10} = 405.4\,\mathrm{Hz}$, which are linked to the experimental resonances at $f_{\mathrm{r},9} = 319.0\,\mathrm{Hz}$ and $f_{\mathrm{r},10} = 378.0\,\mathrm{Hz}$ by the MAC (see Table 7.5). The corresponding frequency range is provided more in detail in Figure 7.19, which illustrates the lack of observability using the impedance heads: Geometrical imperfections of the benchmark and inexact excitation result in an energy flow not only via the measured translational DOF at IH:1, but also via the remaining DOFs, the rotational ones in particular. The power of the remaining DOFs has a larger magnitude than the one of the negative power in the translational y-direction $\overline{P}_{\mathrm{y}}$ in the vicinity of the two resonance frequencies.

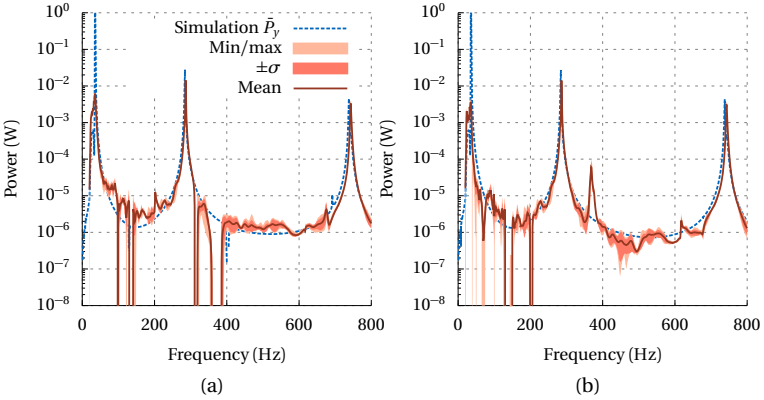

Figure 7.18: Mean power results at the impedance heads from simulation and measurement; the latter has a phase correction for the measurement chain ((a) IH:1 and (b) IH:2).

Thus, the overall power is positive, and passive system behavior is obtained, although $\overline{P}_{\mathrm{y}}$ is negative. In summary, the negative power values are not an issue of insufficient phase correction in these frequency ranges but are an artifact of the experimental setup causing a lack of observability. Note that, in general, moment-loading due to imperfections can affect the accuracy of the impedance head force sensor. The results from impedance heads can be erratic for setups not vibrating in the uniaxial direction, potentially providing another reason for apparent non-passive system behavior.

For the lightly damped benchmark, accurate energy estimates can be obtained from measurement in addition. This is demonstrated for the potential energy using the approximation of Equation (7.4). The potential energy is insensitive to the phase error (Figure 7.20), as discussed in Section 7.1.2. The values coincide well with those obtained from the simulation. In combination with the physically meaningful power quantities measured, it is possible to estimate structural damping, which is demonstrated in Ullmann et al. [256] for the benchmark structure.

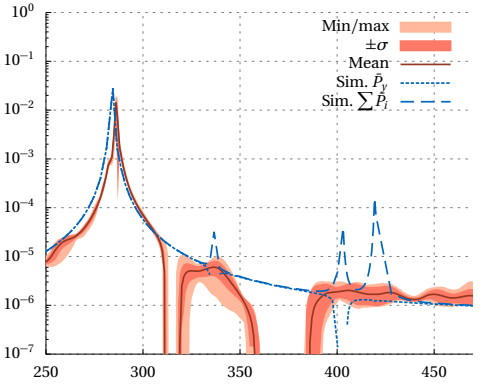

Figure 7.19: Mean power results at IH:1 for the frequency range of resonances that load the impedance head with a moment. For the simulation, power is evaluated for the translational DOF in y-direction (sim. $\overline{P}_y$) and for the sum of all DOFs (sim. $\sum P_i$).

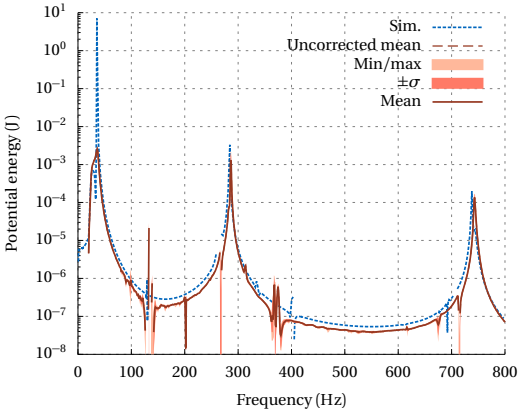

Figure 7.20: Potential energy obtained for the FE simulation by means of approximation of Equation (7.4) at IH:1. The approximation is also used to calculate the energy in the experimental setup.

7.3 Consequences for the Experimental Identification of Subsystems

The results for phase-corrected SISO reference measurements of energetic quantities can be transferred to the measurement-based identification of MIMO subsystems. The input-to-output behavior of the latter is required for coupling with a network and, thus, must be identified. The following briefly introduces the basic concepts of corresponding methods before the phase correction is discussed. Refer to Tangirala [242] for a recent and more complete overview of experimental subsystem identification.

For a measurement-based characterization of subsystems, one approach is to model the subsystem by the directly measured input-to-output behavior sampled at distinct frequency points. No underlying subsystem realization is determined, respectively inner representation. This is a classic approach for experimental substructuring in structural dynamics, with many applications in the automotive industry; see De Klerk [65], for example. The direct determination of the input-to-output behavior is also called non-parametric system identification (Tangirala [242]). Different techniques are available for a non-parametric characterization. In the most basic approach, the input-to-output behavior of subsystem k is determined directly from the division of the Fourier spectra of the measured inputs and outputs according to Equation (7.18)

$$H_{k,jl} = \frac{Y_{jl}}{U_l}. \tag{7.18}$$

In theory, this approach provides an accurate system description for a harmonic excitation. In practice, averaging, respectively smoothing techniques are required in combination with suitable excitation signals to account for measurement noise and the required short measurement times, refer to Phillips et al. [201] for some methods. In the presence of noise, the input-to-output behavior is commonly not estimated from the averaged Fourier transforms of the input and output signals but from averaged power spectra, as defined in Equation (2.30). Power spectra allow to filter out uncorrelated noise, which leads to zero cycle-averaged power, refer to Section 2.3.1. Depending on the noise modeling, different averaged cross- and auto-power spectra

can be used, leading to different estimators for the input-to-output behavior,

$$H_1 = \frac{\overline{S}_{\mathrm{YU}}}{\overline{S}_{\mathrm{UU}}} \qquad H_2 = \frac{\overline{S}_{\mathrm{YY}}}{\overline{S}_{\mathrm{YU}}},$$

for example, where $\overline{S}_{\mathrm{UU}}$ and $\overline{S}_{\mathrm{YY}}$ are the averaged auto-power of the input, respectively output and $\overline{S}_{\mathrm{YU}}$ is the averaged cross-power of the input and output. Different averaging techniques may be applied to the power spectra combined with different excitation signals. For example, the Welch estimator can perform averaging in the frequency domain. A time-domain averaging of power spectra is obtained by the method of Blackman-Tuckey. Refer to Brandt [44] for an explanation of these different averaging strategies. Alternative averaging methods are also discussed by Phillips et al. [201].

Conceptually simple, the entries of the input-to-output matrix are not based on one underlying model. Correspondingly, every matrix entry has individual errors, leading to inconsistencies between the different inputs and outputs. As one result, spurious peaks can be observed in the coupled response, as discussed by Rixen [208]. Inconsistencies are introduced again by both systematic and random errors. The propagation of random errors to the coupled response was investigated by Voormeeren et al. [267] using a first-order approximation and Meggitt [173]. In addition, the nature of non-parametric approaches without an underlying model does not guarantee that the measured input-to-output behavior is consistent with basic model assumptions of mechanical systems. Instead, additional postprocessing is required to ensure reciprocity or passivity, like averaging transfer functions and brute-force shifting of the phases to the right quadrant of the complex plane.

As an alternative to the above methods, parametric approaches are available for system identification. In such methods, usually, a first-order model is (iteratively) fitted on the observation of the subsystem outputs and, optionally, inputs. Approaches work either on time or frequency domain data. A fitted inner system representation is available as a result, from which the input-to-output behavior is calculated. Inconsistencies in the input-to-output behavior thus are avoided. Physical properties of the mechanical system, such as reciprocity, can be imposed as a constraint during the identification. In structural mechanics, parametric system identification is already well-established

for experimental modal analysis, see Alvin et al. [8]. Attractive from a mathematical point of view, corresponding methods are less common in subsystem coupling applications of mechanical networks. For some applications, refer to Sjövall et al. [231] in the context of airplanes or to Bylin et al. [50], who characterize an automotive body in white. Recently, Kammermeier et al. [134] performed a comparison between parametric and non-parametric approaches for structural dynamics.

It was observed for validation measurements in Section 7.2.4 that systematic phase errors can result in energetic quantities indicating non-passive systems. This issue is also present for system identification of lightly damped subsystems, which is demonstrated numerically in the following.

Example 7.2 (Three Subsystem Example)

Consider the three-subsystem example of Section 3.2, as visualized in Figure 3.1 on page 55 and with the values of Table 7.2. The 2×2 transfer function of subsystem $\mathcal{S}_3$ is assumed to be identified by a non-parametric experimental method. Further, it is assumed that two accelerometers, one at each output, are used, and one force sensor is relocated for the two necessary measurements.

Subsystem	k	m	η
$\mathcal{S}_1$	5000	$8 \cdot 10^{-4}$	0.01
$\mathcal{S}_2$	5000	$7 \cdot 10^{-4}$	0.01
$\mathcal{S}_3$	5000	$2 \cdot 10^{-3}$	0.01

Table 7.6: Parameter values for the three degree-of-freedom example.

The coupled system is evaluated twice, once for the analytic solution of $\mathcal{S}_3$ and once for a phase-distorted measured transfer function. To obtain the latter, a constant and frequency-independent time delay between acceleration and force signal of $\Delta t = 10^{-5}\,\mathrm{s}$ is added to the analytic solution for each combination of acceleration and force sensor. This is in the order of the phase errors introduced in the above validation measurements and results in a systematic phase shift of $\Delta\varphi_{\mathrm{FA}} = 3.6^\circ$ at $f = 1000\,\mathrm{Hz}$.

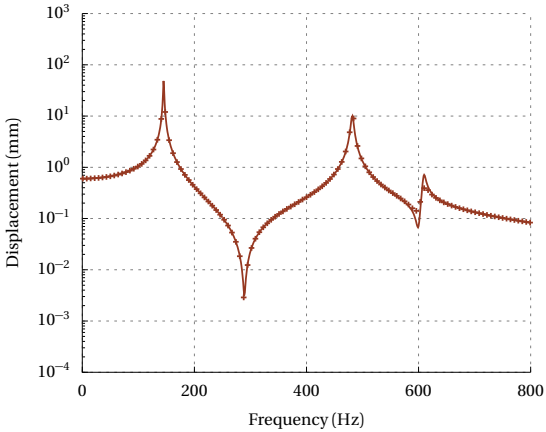

Figure 7.21: Absolute value of the displacement solution at the load point of $\mathcal{S}_2$ in the three degree-of-freedom example. The continuous line corresponds to the reference solution, the starred line to the phase distorted one.

While the systematic phase distortion in the input-to-output behavior of $\mathcal{S}_3$ visually has only a minor effect on the displacement response of the example (see Figure 7.21), this is not the case for the network input power in Figure 7.22. The phase distortion leads to a non-passive network in the non-resonant region between the two lower resonances. Negative results are obtained for the input power in this frequency range.

The effects of a systematic phase shift are observed correspondingly for analyzing the energy balance of subsystem $\mathcal{S}_3$ (see Figure 7.23). Between the two lower resonances, the power between subsystem $\mathcal{S}_2$ and $\mathcal{S}_3$ and the dissipated power are negative. $\mathcal{S}_3$ apparently generates energy, and a net flow is obtained from subsystem $\mathcal{S}_3$ to $\mathcal{S}_2$.

■

Passivity is no longer provided for the example on both subsystem and network levels due to phase distortion. Although it is an essential property of mechanical systems, passivity preservation is rarely discussed in the context of measurement-based subsystem identification. Some approaches are available for parametric identification based on

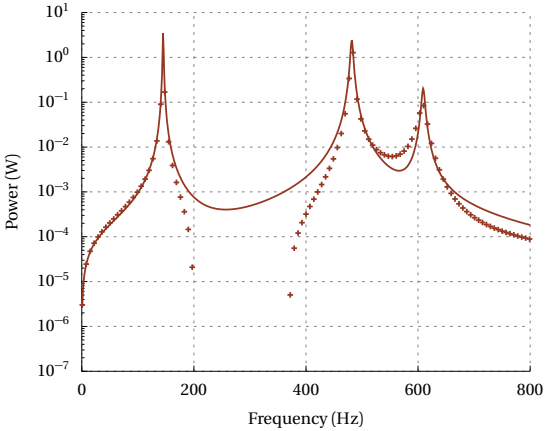

Figure 7.22: The input power at the load point of $\mathcal{S}_2$ in the three degree-of-freedom example. The continuous line corresponds to the reference solution, the starred line to the phase distorted one.

first-order systems. These methods modify the input and output map $\boldsymbol{B}_\mathrm{I}$, respectively $\boldsymbol{C}_\mathrm{I}$, to provide a passive subsystem input-to-output behavior. Liljerehn et al. [152] project the system on a modal basis and force each mode to be passive in the transfer function by calculating a minimal phase correction per mode to ensure that. McKelvey et al. [171] use an optimization procedure for $\boldsymbol{B}_\mathrm{I}$ and $\boldsymbol{C}_\mathrm{I}$ resulting in passive transfer functions. Such approaches ensure a passive system description but do not necessarily recover the true phase angles and, thus, the exact subsystem damping modeling.

Conceptually different, the phase errors can already be reduced in the input signals before system identification. The concept of phase correction, which was introduced in Section 7.2, therefore, can be extended to subsystem identification with sensors for setups in which the subsystem inputs and outputs are not obtained spatially collocated. Each non-collocated force and acceleration sensor combination must be measured to identify the relative phase error between the signals. The sensor test setup of Figure 7.8 can be modified for this purpose as illustrated in Figure 7.24.

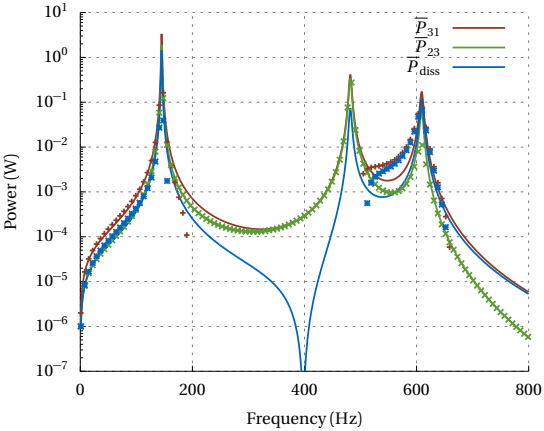

Figure 7.23: The power quantities of the energy equilibrium at subsystem $\mathcal{S}_3$ in the three degree-of-freedom example. $\overline{P}_{31}$ is the power in the interface between $\mathcal{S}_1$ and $\mathcal{S}_3$, $\overline{P}_{32}$ the one in the interface between $\mathcal{S}_2$ and $\mathcal{S}_3$, $\overline{P}_{\mathrm{diss}}$ is the power dissipated in $\mathcal{S}_3$. The continuous lines correspond to the reference solution, the starred lines to the phase distorted one.

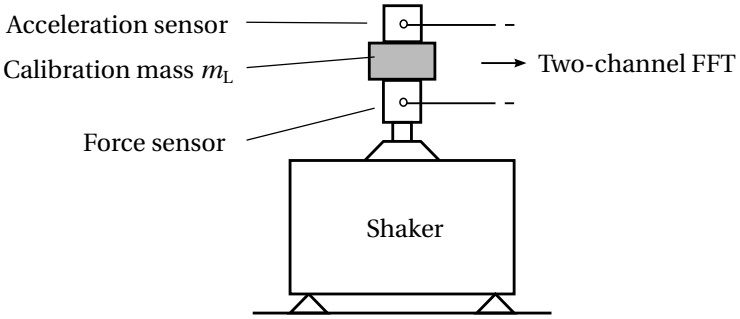

Figure 7.24: Schematic of an adapted top-mass setup for the relative phase measurements of single sensor combinations.

The relative phases are measured according to the assumptions of Section 7.2.3, and the complex correction factors are calculated using Equation (7.12). Each entry in the input-to-output behavior

is then multiplied by the complex-valued correction factor for the corresponding combination of acceleration and force signal. Systematic phase errors resulting from the measurement hardware can be reduced for subsystem identification using such a setup.

Note that model assumptions used in subsystem identification methods may introduce additional phase shifts. An example is the virtual point transformation, which utilizes the concept of local rigidities around interfaces. Haeussler et al. [111] investigate the resulting phase errors from that model assumption and possible remedies.

7.4 Chapter Summary

The measurement-based evaluation of energetic quantities was examined for validation measurements and subsystem identification. The measurement of discrete power quantities was discussed theoretically, and the possibility of estimating energies from the measured input-to-output behavior, which is more erratic, the higher the system damping is.

Practically, the unidirectional power measurement at driving points was discussed for network validation. A benchmark structure was introduced for this discussion, with a correlated numerical representation to analyze the experimental methods. All the required data to reproduce the benchmark are available online. Based on the benchmark structure, error sources for measuring system input power at driving points were identified, which are relevant for practical setups. Such errors can not only distort the magnitude of power but can result in a wrong sign of input power and, therefore, indicate spurious non-passive networks. It was shown that apparent non-passivity of networks could result from wrong model assumptions for calculating the energy balance for uniaxial measurements at driving points. There may be energy flow also over the remaining degrees of freedom at the driving point, caused by imperfections but not observed by the unidirectional sensor setup. Significant and systematic phase errors introduced by each element of the measurement chain are another source of spurious non-passivity.

To compensate for these systematic phase errors, the influence of the time-to-frequency transformation was discussed. Complex-valued phase corrections were introduced to reduce the systematic phase errors that arise from the sensors and the DAQ interface. The

phase errors are assumed to be test-specimen independent but solely determined by the measurement chain. Corresponding test setups could be thus introduced for identifying the phase errors of each measurement chain component. When the phase correction was applied, the power results were significantly improved for the benchmark structure's driving point measurements.

Phase errors do not only distort driving point measurements for network validation but also play a significant role in system identification. This role was discussed shortly in the context of energetic network analysis theoretically. After general concepts for system identification were summarized, it was shown that systematic phase errors potentially lead to spurious non-passive subsystems and, therefore, networks. As a remedy, it was discussed how the concept of phase correction could be extended to subsystem identification.

CHAPTER 8

APPLICATIONS OF ENERGETIC NETWORK SYNTHESIS

The performative numerical framework, combined with measurement-based validation methods, finally enables multi-query applications for complex industrial models in the online phase, while vibrational energy flows can be evaluated. As initially discussed, this opens up new possibilities for a robust end-to-end virtual vehicle development process, employing uncertainty quantification, inverse methods, global sensitivity analyses, and globalized synthesis. This chapter demonstrates the latter for a low-frequency setup in which global deflection shapes of the overall system dominate the response. Two numerical examples are introduced to show how the proposed approach allows maximizing the solution space for vibration minimization in frequency bands with arbitrarily complex constraints. The first example of a 2D radiating system provides the first basis for discussing the globalized synthesis of the mechanical network. The gains from subsystem coupling in the online phase are presented as well as a validation of the use of a power-based objective. The second component of the numerical framework, parametric model order reduction, is needed in the offline phase as another central aspect of the second

example: an industrial model of a vehicle consisting of a car body in white with an attached rear axle system, which can be finally synthesized.

This chapter focuses on highlighting the general potentials of the combination of subsystem coupling in the online phase and parametric model order reduction in the offline phase for an end-to-end virtual development process for vibroacoustic design. The in-depth and holistic discussion of all necessary concepts for a final application of globalized optimization, the necessary feedback loop into a distinct part design, for example, are out of scope for this chapter. The same also holds for validating the models to distinct hardware realizations, but the models are taken as they are.

8.1 Two-Dimensional Beam Assembly

8.1.1 The Model and Network Definition

A network of two-dimensional (2D) Euler-Bernoulli beams is first discussed, as illustrated in Figure 8.1, and for geometry details in Figure 8.2. It is conceptually simple but complex enough to discuss basic effects originating from real industrial systems. The model is derived from the example as published by Ullmann et al. [252] and discussed in Sicklinger et al. [226], but has different parameter settings and an additional beam replacing the initially used disc subsystem at the bottom.

Six beams, discretized by Euler-Bernoulli beam elements, are coupled via eight bushings. The bushings are modeled by springs in the translational and rotational directions without cross-coupling terms. The horizontal beam on top is coupled to an acoustic Helmholtz fluid. In the first setting, assume a free field setting; thus, an acoustic halfspace is modeled. Twenty-two outputs are provided for the evaluation of sound pressure levels in the fluid, which are placed at two half circles with radii $r_\mathrm{a} = 1800\,\mathrm{mm}$ and $r_\mathrm{i} = 800\,\mathrm{mm}$ as indicated in Figure 8.1.

All subsystem matrices were generated with the commercial FE software Simulia ABAQUS according to Table 8.1. An external harmonic load is applied at the center point of the bottom beam with $f_\mathrm{x} = 1 + 0.1\,i$ and $f_\mathrm{y} = 1$.

The coupling of the single subsystems is performed using the MRC framework of Chapter 3 according to the network representation in Figure 8.3. The beam subsystems should not contain variable de-

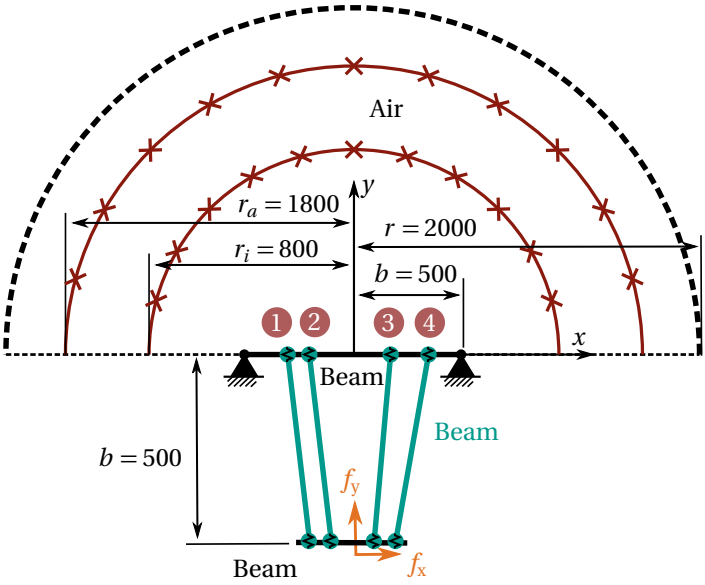

Figure 8.1: Sketch of the two-dimensional radiation example. The red crosses highlight the 22 points, in which the sound pressure level is evaluated. The circles in between the beams schematically indicate bushings. All units are in millimeters.

sign parameters and are provided as transfer function representation, calculated from the implicit ABAQUS subsystem models by Equation (2.11). The bushing subsystems with variable design parameters should allow for a zero mass, thus being singular if one chooses an implicit inner representation. To enable a systematic modular treatment of these subsystems, the MRC framework provides flexibility by choosing an explicit form with a partial input switching according to Section 3.2.2, and three inputs are switched per bushing subsystem. Each nodal interface of the subsystems has three DOFs. As a result, 24 constraint equations each of Dirichlet-Dirichlet and Neumann-Neumann, Dirichlet-Neumann, and Neumann-Dirichlet type are required for assembly definition. This leads to an interface problem of size $n_{\text{int}} = 96$ before introducing a mixed input vector and $n_{\text{int}} = 72$ afterward.

Part	Cross section parameters	Discretization by elements
Fluid	Thickness $d = 1000$	Finite domain: 32836 AC2D4
		Sommerfeld radiation conditon: 394 ACIN2D2
Beam-top	rect.: $a = 1$, $b = 1000$	100 B23
Beam-1	Box: $a = 50$, $b = 20$, $t = 2$	54 B23
Beam-2	Box: $a = 50$, $b = 20$, $t = 2$	54 B23
Beam-3	Box: $a = 50$, $b = 20$, $t = 2$	50 B23
Beam-4	Box: $a = 50$, $b = 20$, $t = 2$	52 B23
Beam-5	Rect.: $a = 20$, $b = 60$	22 B23
Each bushing		1 CONN3D2
		(stiffness + structural damping)

Table 8.1: The parts of the two-dimensional beam example. The beams have a rectangular cross section, respectively a box cross section with thickness t. All units are in millimeters.

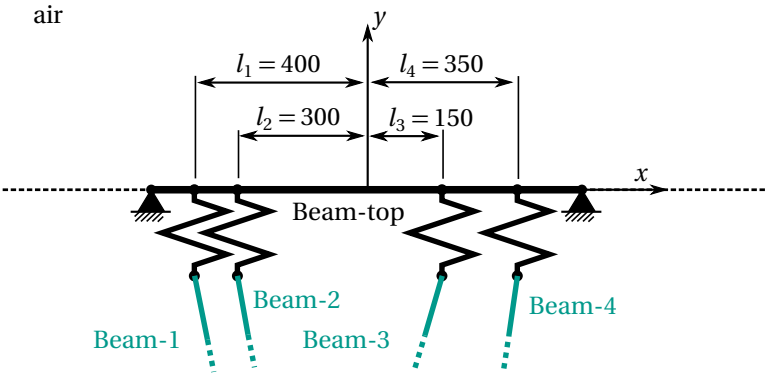

Figure 8.2: Detailed view on the positions of the four interface nodes of the radiating beam.

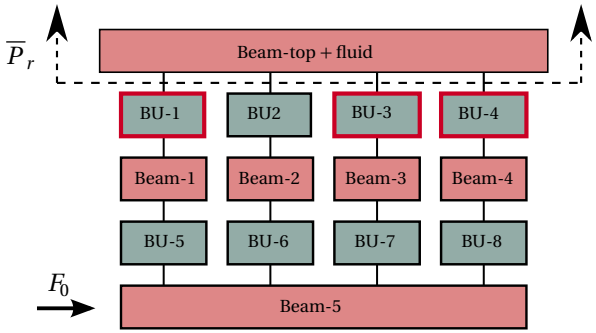

Figure 8.3: Network representation of the two-dimensional radiation example. Red colored subsystems are represented by a transfer function form, green colored by an explicit form with switched inputs and outputs.

8.1.2 Approach for Virtual Synthesis in Industrial Vibroacoustics

Optimization of Coupled Problems The optimization problem, Equation (A.1), is defined based on the subsystem coupling approach of MRC in Chapter 3. From a mathematical point of view, the optimization problem of sound transmission minimization can be formulated for the coupled problem as

$$\begin{aligned} &\min_{p_i \in \mathbb{R}} q\left(\boldsymbol{p}, \mathcal{S}_i\left(\boldsymbol{U}_i(\boldsymbol{p}), \boldsymbol{p}\right), \boldsymbol{U}_i(\boldsymbol{p}), i = 1 \ldots n_\mathrm{s}\right) \\ &\text{subject to} \quad \begin{cases} \boldsymbol{c}_\mathrm{i}\left(\boldsymbol{p}, \mathcal{S}_i\left(\boldsymbol{U}_i(\boldsymbol{p}), \boldsymbol{p}\right), \boldsymbol{U}_i(\boldsymbol{p}), i = 1 \ldots n_\mathrm{s}\right) \leq 0 \\ \boldsymbol{c}_\mathrm{e}\left(\boldsymbol{p}, \mathcal{S}_i\left(\boldsymbol{U}_i(\boldsymbol{p}), \boldsymbol{p}\right), \boldsymbol{U}_i(\boldsymbol{p}), i = 1 \ldots n_\mathrm{s}\right) = 0 \end{cases} \end{aligned} \tag{8.1}$$

while $q\left(\boldsymbol{p}, \mathcal{S}_i\left(\boldsymbol{U}_i(\boldsymbol{p}), \boldsymbol{p}\right), \boldsymbol{U}_i(\boldsymbol{p}), i = 1 \ldots n_\mathrm{s}\right)$ is an objective function describing the sound transmission problem and is a function of the design parameters $\boldsymbol{p}$ and the inputs and outputs of the n_s subsystems.

$$\boldsymbol{c}_\mathrm{i}\left(\boldsymbol{p}, \mathcal{S}_i\left(\boldsymbol{U}_i(\boldsymbol{p}), \boldsymbol{p}\right), \boldsymbol{U}_i(\boldsymbol{p}), i = 1 \ldots n_\mathrm{s}\right)$$

are inequality constraints,

$$\boldsymbol{c}_\mathrm{e}\left(\boldsymbol{p}, \mathcal{S}_i\left(\boldsymbol{U}_i(\boldsymbol{p}), \boldsymbol{p}\right), \boldsymbol{U}_i(\boldsymbol{p}), i = 1 \ldots n_\mathrm{s}\right)$$

equality constraints. These constraints can define lower and upper parameter bounds but may also include non-linear equations, like a minimum net stiffness of axle systems in vehicle acoustics or the maximum amount of added masses. Modular and thus efficient gradients of the objective and constraint equations can be provided to optimization algorithms by the approach of Section 4.1.2.

A significant reduction of computational complexity can be obtained by subsystem coupling if solely few and highly localized parameters are varied, like bushing parameters for the 2D example. Splitting the complex coupled problem in a network of subsystems allows for localized and modular re-calculations of only these small-scale bushing subsystems. The remaining subsystems need to be updated solely in the first optimization iteration.

Power-Based Objective for Optimization The sound pressure levels (SPLs) are the final relevant objective for acoustic design. However, single point-wise sound pressure levels may be highly sensitive to uncertainties in the considered network, particularly the radiating subsystem. Increased robustness is possible if more integral values are considered. Evaluating sound pressure levels at a very high number of points is one option, as it is possible for the 2D example.

An energetic approach is another remedy, which is followed in many studies on optimization, mainly for free field problems; refer to the references in Marburg [166] for examples. These studies use the overall radiated sound energy, mean power, respectively, as the objective; thus, the objective provides an integral quantity to determine the radiation into a fluid. No local measure is obtained, like SPLs at single points, but a global one, which accounts for the overall radiation.

Anyhow, evaluating the radiated sound power is impossible for general black-box subsystems, like experimentally determined ones. The latter do not expose their internal states, which need to resolve the pressure and velocities spatially over the whole radiating surface to calculate the radiated sound power. The potential inclusion of such a black-box subsystem as the radiator requires an alternative energetic approach: mean power is not evaluated at the radiating surface but spatially integrated at the subsystem's coupling interface. All required quantities, radiator subsystem inputs and outputs are available at the latter, and power can be calculated according to Equation (2.37) on page 32. The corresponding input power is provided

for the two-dimensional example in Figure 8.4. Thus, one has a de facto separation of the mechanical network into a passive side, the radiating receiver, and an active side, the source, which incorporates all remaining subsystems. Despite the attractiveness of power as a proxy inside the structure, it is not without drawbacks, like any other quantity, which is not directly evaluated at the radiator but at a larger distance. This is reflected critically in Section 8.1.3.

In line with the A-weighting of sound pressure levels, also power quantities are A-weighted for better correlation. An A-weighting is introduced by multiplying the non-square values by the frequency-dependent transfer function

$$H_\mathrm{a} = \frac{7.39705 \cdot 10^9 \omega^4}{(i\omega + 129.4)^2 (i\omega + 676.7)(i\omega + 4636)(i\omega + 76655)^2}. \tag{8.2}$$

To provide scalar optimization objectives q, the frequency-dependent power is calculated from the radiator subsystem input and output quantities and integrated numerically over the corresponding frequency band in which it should be minimized

$$q_\mathrm{P} = \int_{f_\mathrm{B}} \overline{P}_r H_\mathrm{a}^2 \mathrm{d}f \approx \mathcal{Z}\left({}^n\overline{P}_{r,\mathrm{a}}, \Delta f\right) \tag{8.3}$$

with the trapezoidal rule $\mathcal{Z}\left({}^n x, \Delta f\right)$

$$\mathcal{Z}\left({}^n x, \Delta f\right) = \Delta f \left(\frac{1}{2} {}^0 x + \sum_z^{n_\mathrm{F}-1} {}^z x + \frac{1}{2} {}^{n_\mathrm{F}} x \right).$$

n_F is the number of discrete frequency points. According to Equation (2.38) the A-weighted mean power at discrete frequency samples is given by

$${}^n\overline{P}_{r,\mathrm{a}} = -\pi \cdot {}^n f \, \Im\left({}^n \boldsymbol{U}_r^H \, {}^n \boldsymbol{Y}_r\right) {}^n H_\mathrm{a}^2.$$

Assume that subsystem $j = r$ is the radiator subsystem. As in the preceding part of the thesis, the inputs of the radiator are considered to be forces, the outputs displacements. For other subsystem definitions, Equation (8.3) can be adapted accordingly.

Following Equation (4.31) on page 89, the gradient for Equation (8.3) can be provided to gradient-based optimization approaches as

$$\begin{aligned}\frac{\mathrm{d}q_\mathrm{P}}{\mathrm{d}p_j} &= \int_{f_\mathrm{B}} \frac{\mathrm{d}\overline{P}_{r,\mathrm{a}}}{\mathrm{d}p_j}\mathrm{d}f = \pi \int_{f_\mathrm{B}} f\Re\left(\frac{\mathrm{d}\mathring{P}}{\mathrm{d}p}\right) H_\mathrm{a}^2 \mathrm{d}f \\ &= \pi \mathcal{Z}\left({}^n f\Re\left({}^n\frac{\mathrm{d}\mathring{P}}{\mathrm{d}p}\right){}^n H_\mathrm{a}^2, \Delta f\right)\end{aligned} \tag{8.4}$$

with the substitute quantity $\mathring{P}$ according to Section 4.2. For the 2D example, employing the adjoint approach to gradient calculation is efficient, as there is exactly one objective but multiple design parameters. Thus, the samples ${}^n\mathrm{d}\mathring{P}/\mathrm{d}p$ can be obtained in the adjoint framework according to Equation (4.34) to Equation (4.37) on page 89.

Setup and Design Parameter Selection

To benchmark the band-limited reduction of power in the interface between the active and passive side, three frequency ranges are selected for the 2D example based on the base state response in Figure 8.4: $f_{\mathrm{B}1} \in [75\,\mathrm{Hz}, 140\,\mathrm{Hz}]$, $f_{\mathrm{B}2} \in [340\,\mathrm{Hz}, 434\,\mathrm{Hz}]$, and $f_{\mathrm{B}3} \in [650\,\mathrm{Hz}, 770\,\mathrm{Hz}]$. In the base configuration, all spring stiffness values are chosen as $k_{i,0} = 1000\,\mathrm{N\,mm^{-1}}$, and $k_{i,0} = 1000\,\mathrm{N\,mm\,rad^{-1}}$, respectively. The aim is to reduce the global radiation by using the power objective, which is benchmarked against a direct optimization of the spatially averaged sound pressure level, evaluated over all 22 sound pressure level outputs of this example. The corresponding averaged sound pressure is visualized in Figure 8.5.

A classic parametric optimization is performed for the 2D example: The stiffness parameters of the three bushing subsystems at input nodes 1, 3, and 4 of the radiator (BU-1, BU-3, and BU-4) are chosen as design parameters. The same stiffness values are assumed for the two translational DOFs of each bushing, while the rotational stiffness is fixed to its nominal value. This setup results in a three-dimensional parameter space, in which the stiffness value of each bushing is varied within $k_i \in \left[50\,\mathrm{N\,mm^{-1}}, 10000\,\mathrm{N\,mm^{-1}}\right]$. As only design parameters of bushing subsystems are considered, the single iterations during optimization in the online phase are computationally cheap, as discussed above. Only three subsystems of size $n = 6$ need to be updated when MRC is used, along with the solution of the interface problem of size $n_\mathrm{int} = 72$.

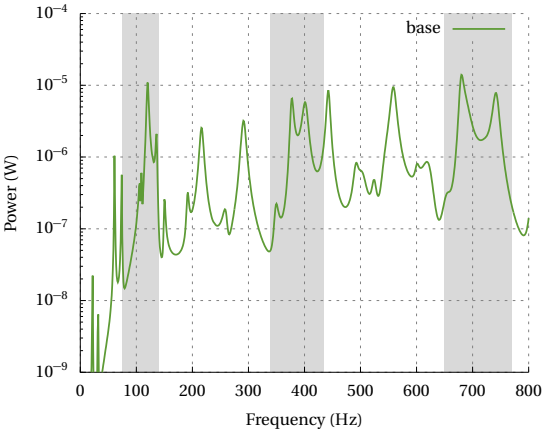

Figure 8.4: A-weighted structure-borne sound power for the initial parameter configuration with $k_{i,0} = 1000\,\mathrm{N\,mm^{-1}}$, evaluated at the four input nodes of the two-dimensional example's radiating beam.

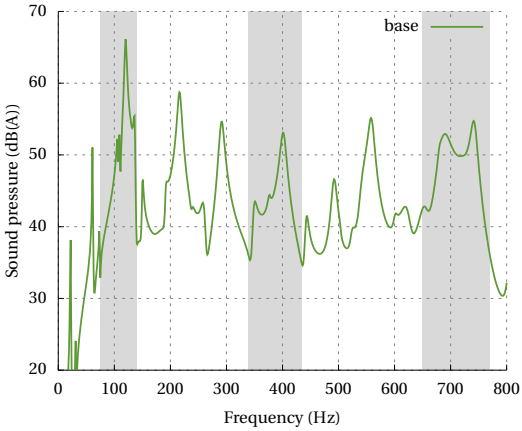

Figure 8.5: A-weighted sound pressure level for the initial parameter configuration with $k_{i,0} = 1000\,\mathrm{N\,mm^{-1}}$, averaged over the 22 observation points of the two-dimensional example.

Algorithmic Approach to Globalized Optimization Vibroacoustic design by numerical optimizations has already been discussed for

several decades; see Marburg [166] for an early overview. However, the application is still challenging for complex and large-scale industrial models: the objective functions are usually highly non-convex, and thus, a local gradient-based optimization does not result in the global optimum with a high probability. Refer to Hambric [114] for a vibroacoustic example. As a result, such an approach does not necessarily provide a high impact on the sound pressure levels.

This issue can be illustrated for the summed-up power in frequency range f_{B2} as a function of two bushing parameters of the 2D example in Figure 8.6. It is evident that if one optimizes for these two parameters, one arrives at the global minimum at $k_{BU2} = 7379\,\mathrm{N\,mm^{-1}}$ and $k_{BU3} = 50\,\mathrm{N\,mm^{-1}}$ only if the initial point is in a limited parameter range around these values. For other starting points, one obtains one of the three other local minima, which have an objective function value larger by a factor of four or more, resulting in a less effective optimization.

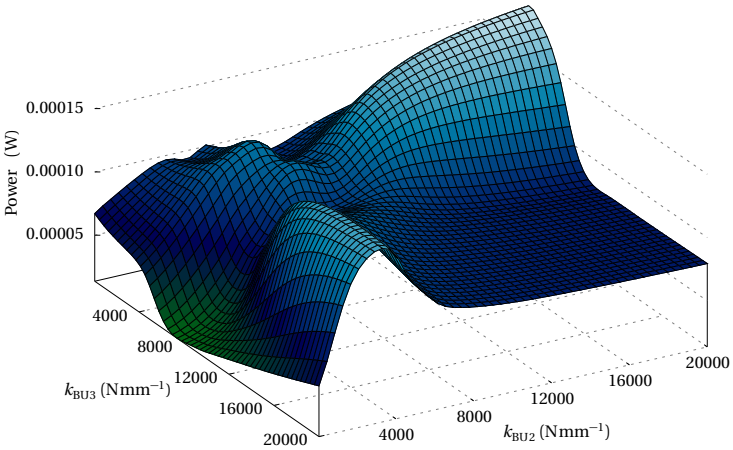

Figure 8.6: The power-based objective in frequency band f_{B1} in dependence of two design parameters k_{BU2} and k_{BU3}. The non-convex shape of the objective function highlights the need for globalized optimization.

Heuristic approaches are available to cope with such non-convex objective functions, as briefly discussed in Appendix A.2. These methods seek to find the global optimum in a heuristic way, thus without

a guarantee but computationally feasible. A multi-start scheme is utilized in the following, in which multiple local gradient-based optimizations are performed for starting points determined in a global phase. The latter incorporates a random search procedure. Network evaluations for an extensive number of parameter samples are necessary for such algorithms. For the problems which are discussed in this chapter, up to $n_{\mathrm{calc}} \approx 10^6$ evaluations of the objective in Equation (8.3) are necessary, while each objective evaluation incorporates several system solutions at distinct frequency points. The computation of gradients counts on top. This vast number of required system solutions and gradient calculations highlights the need for the efficient numerical framework introduced in the thesis.

In the following, the globalized multi-start optimization method of Ugray et al. [249] is used in the implementation provided by MATLAB R2018b and described in Appendix A.2. This method uses a scatter search procedure in the global phase, which is formulated for one initial parameter vector $\boldsymbol{p}_0$. Based on the results of the scatter search and filters, single gradient-based optimizations are performed again using the SQP algorithm as described in Appendix A.1. As an initial parameter vector $\boldsymbol{p}_0$ must be provided to the method of Ugray et al. [249], the result from the globalized optimization is dependent on $\boldsymbol{p}_0$. Several runs of globalized optimization are performed for this example due to this reason, and the results are averaged. In each run, another random parameter vector is chosen as $\boldsymbol{p}_0$ to enable a more robust discussion focused on power-based synthesis in vibroacoustics.

Results Ten runs of globalized optimization are performed for each considered frequency band and averaged results are presented for each in Figure 8.7. The scattering of results is provided by visualizing the standard deviation as metainformation. In addition, results from ten local optimizations per frequency band are provided, for which the starting points were selected as the first ten points of the 3D Sobol sequence.

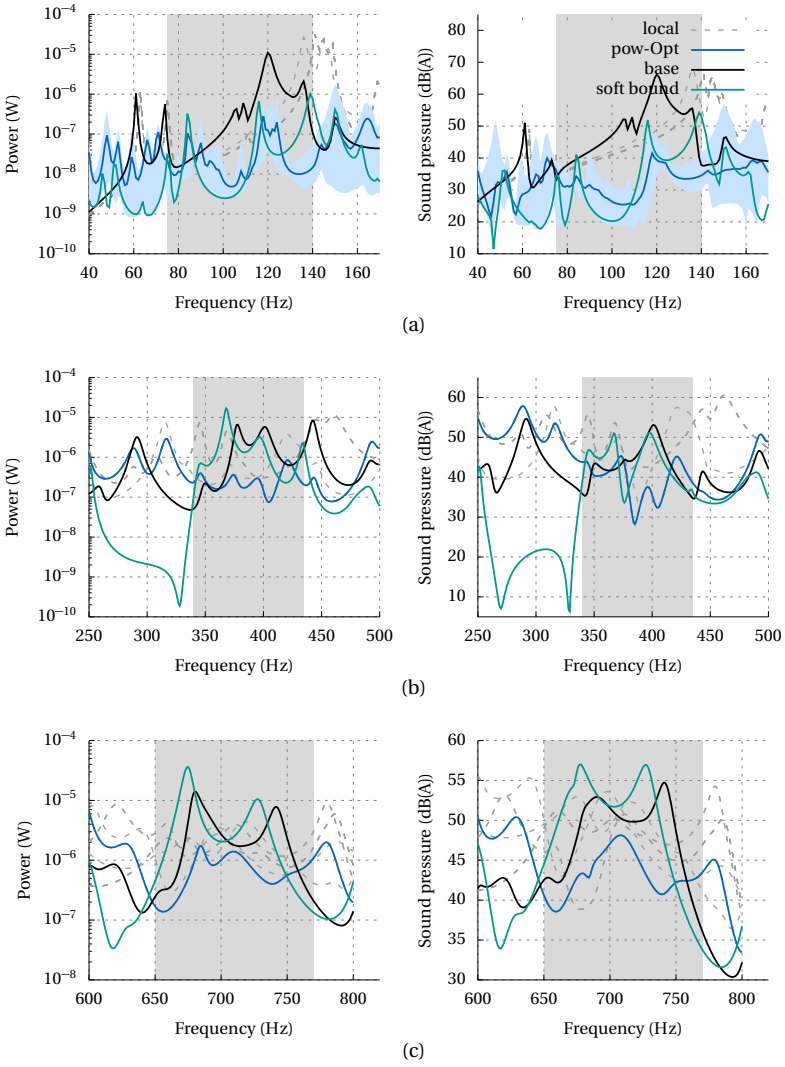

Figure 8.7: Globalized optimization results in the grayed frequency bands employing the power objective. Power quantities at the radiator inputs and SPLs are provided for the non-optimized base state and the optimized one. Averaged values, minima, and maxima are provided for the latter, which result from ten independent runs of globalized optimization. In addition, results from ten local optimizations are visualized.

A relatively high number of objective function evaluations is already required for this conceptually simple example with low dimensional design parameter space. On average, 2700 objective evaluations are needed, each incorporating the solution at 60 frequency points in 25 local optimizations per power-based optimization globalized optimization in frequency band three. The power-based globalized optimization significantly reduces both transmitted mean power and sound pressure levels over the whole acoustic domain.

The optimal values for the stiffness parameters of the rubber bearings are found for frequency band two as $k_{\mathrm{BU1}} = 1270$, $k_{\mathrm{BU2}} = 50$, $k_{\mathrm{BU3}} = 3715$, for frequency band three as $k_{\mathrm{BU1}} = 2557$, $k_{\mathrm{BU2}} = 2359$, $k_{\mathrm{BU3}} = 360$. Thus, compared to the nominal setting with $k_{\mathrm{BU}} = 1000$, two bushings are hardened for each frequency band, while one is softened. All ten globalized optimizations for the two frequency bands yield that stiffness values.

As visualized in Figure 8.7(b) and Figure 8.7(c), the results from the globalized approach outperform seven out of ten single local optimizations; for three local optimizations, the results are the same. The local optimizations result in - partly significantly - higher mean power and, therefore, sound pressure levels, which scatter depending on the selected initial points. This highlights the need for globalized optimization in structural dynamics. Globalized optimization even provides lower sound pressure levels than all ten local optimizations for frequency band f_{B1}, see Figure 8.7(a). Anyhow, the heuristic nature of the globalized approach of Ugray et al. [249] becomes evident in Figure 8.7(a): it is also dependent on a starting point and does not necessarily provide the *true* global optimum. Significant different stiffness values are obtained according to Table 8.2 and the optimized power and sound pressure levels from the single runs of globalized optimization scatter as visualized in Figure 8.7(a).

It is worth noting that the results permit overcoming simplifications like the design paradigm of *making bushings as soft as possible*. The latter is commonplace in vehicle acoustics but originates from local wave considerations in high-frequency regions. In such a setting, a very soft bushing and a stiff connection point of the car body lead to an increased impedance mismatch, thus increased reflection and less sound transmission to the car body. Clearly, these considerations can not be valid for low-frequency ranges in general, but soft bushings may amplify the overall system's global and strongly coupled deflection shape. Consequently, choosing solely lower bound values

No. of occurrence	Optimized parameters		
	k_{BU1}	k_{BU2}	k_{BU3}
3	308	50	142
2	9484	137	129
1	948	50	139
1	390	50	50
1	440	50	50
1	130	50	50
1	340	50	141

Table 8.2: Parameter values for globalized optimization in frequency band f_{B1}, which is repeated ten times.

for the bushings, the transmitted power and sound pressure levels are increased in each frequency band (see Figure 8.7).

8.1.3 Performance of Power as Objective Function

In the following, the performance of power should be discussed in more detail. Emphasis is on evaluating the correlation with sound pressure levels compared to other objectives. One has to leave the black-box approach to subsystems for this, as the internal states of the radiator need to be evaluated for a full assessment of radiation. Later in Section 8.2.4, an alternative approach to an analysis of the performance of power is performed on interface data only.

Free Field Problems

The use of mean power in the interface between the active and passive side of the network was motivated by the radiated sound power objective in many studies on optimization. The latter directly correlates with the sound radiation and thus with the spatially mean sound pressure levels for free field problems. When mean power is evaluated at the interface of the radiating subsystem, in turn, it provides an optimal proxy if the following proportionality holds

$$\overline{P}_r = \overline{P}_{r,\mathrm{diss}} + \overline{P}_{r,\mathrm{rad}} \overset{(a)}{\propto} \overline{P}_{r,\mathrm{rad}} \overset{(b)}{\propto} \varrho_{\mathrm{avg}}, \tag{8.5}$$

while ϱ_{avg} is the spatially averaged sound pressure inside the fluid, and $\propto$ indicates a direct proportionality. Proportionality (a) is only provided if the dissipated power in the radiator is zero, $\overline{P}_{r,\text{diss}} = 0$, or the radiation ratio

$$r\,r = \frac{\overline{P}_{r,\text{rad}}}{\overline{P}_{r,\text{diss}}} \tag{8.6}$$

is constant for the parameter variations during optimization. The latter implies that the operational deflection shape of the radiator does not change, except its magnitude. This is not exactly the case in any industrial system, which has a non-weakly coupling between the active and passive side, the source, and the radiator, respectively.

Proportionality (b) is not obtained if acoustic short circuits occur in the spatial vicinity of the radiator. At evaluation points very close to the radiator, thus there can be non-zero sound pressure levels due to near fields, although the net integral radiated energy is zero.

As a result, there is no proportionality as stated by Equation (8.5) in general. A proportionality, however, is not required for a valuable optimization objective, as long as the latter provides a correlation in a weaker sense, that it allows for a robust qualitative assessment and $\text{sgn}\left(\partial \overline{P}_r / \partial p\right) = \text{sgn}(\partial \varrho_{\text{avg}} / \partial p)$ holds for most of the design parameter space.

Potentially, power can be a robust indicator, as it provides a global view of the overall vibration of the damped radiator, although evaluated locally. At least this holds for radiating structures, which do not have zero or highly localized damping, which is dominant in the net energy equilibrium. From a data point of view, power combines primal and dual quantities and their phase correlation. There are no mismatched units when summing up translational and rotational degrees of freedom. Thus, all available information at the interface between the active and the passive side is considered and condensed in one quantity, and a maximum of information potentially provides a more robust insight into the system dynamics. Indeed, heuristic studies in the past indicated that structure-borne sound power inside the radiating structure can show proportionality to SPLs for geometrically simple structures, refer to Sicklinger et al. [226] and Singh et al. [229]. The latter also validated this in hardware experiments.

A heuristic study is performed based on the 2D example in the following to evaluate if a power objective provides such a correlation.

The above optimization showed that minimization of power results in a significant decrease of mean sound pressure levels for this example (see Figure 8.7(a) to Figure 8.7(c)). In the next step, the performance of the power objective should be assessed by comparing the results of globalized optimization to the ones with alternative local objectives at the radiator subsystem interface. A *reference* optimization provides a benchmark, using the average sound pressure level at all evaluation points in the fluid directly as objective

$$q_\mathrm{S} = \int_{f_\mathrm{B}} H_\mathrm{a}^2 \sum_{j=1}^{n_\mathrm{p}} \varrho_j^2 \mathrm{d}f = \mathcal{Z}\left({}^{n}H_\mathrm{a}^{2\,n}\boldsymbol{U}_r^{H\,n}\boldsymbol{H}_{r,\mathrm{p-U}}^{H}{}^{n}\boldsymbol{H}_{r,\mathrm{p-U}}{}^{n}\boldsymbol{U}_r, \Delta f\right). \tag{8.7}$$

$\boldsymbol{H}_{r,\mathrm{p-U}}$ is that part of the transfer function of subsystem r, which relates the subsystem inputs to the sound pressure outputs, and n_p is the number of evaluation points, which is $n_\mathrm{p} = 22$ for the 2D example. Gradients can be provided for real-valued design parameters p_j, which do not belong to the radiating system as

$$\frac{\mathrm{d}q_\mathrm{S}}{\mathrm{d}p_j} = \mathcal{Z}\left(\Re\left({}^{n}\boldsymbol{U}_r^{H\,n}\boldsymbol{H}_{r,\mathrm{p-U}}^{H}{}^{n}\boldsymbol{H}_{r,\mathrm{p-U}}{}^{n}\frac{\mathrm{d}\boldsymbol{U}_r}{\mathrm{d}p_j}\right){}^{n}H_\mathrm{a}^2, \Delta f\right). \tag{8.8}$$

${}^{\mathrm{d}\boldsymbol{U}_r}/_{\mathrm{d}p_j}$ is calculated in the modular, adjoint framework of MRC as

$$\frac{\mathrm{d}\boldsymbol{U}_r}{\mathrm{d}p_j} = \boldsymbol{\Psi}^T\left(\frac{\partial \boldsymbol{\mathcal{I}}}{\partial \boldsymbol{\mathcal{S}}}\frac{\partial \boldsymbol{\mathcal{S}}}{\partial p_j} + \frac{\partial \boldsymbol{\mathcal{I}}}{\partial p_j}\right), \tag{8.9}$$

while the adjoint is obtained from

$$\boldsymbol{J}^T\boldsymbol{\Psi} = -\left(\frac{\partial \boldsymbol{U}_r}{\partial \boldsymbol{U}}\right)^T \qquad \text{with} \qquad \frac{\mathrm{d}\boldsymbol{U}_r}{\mathrm{d}\boldsymbol{U}_j} = \begin{cases} \boldsymbol{I} & \text{for} \quad j = r \\ 0 & \text{else} \end{cases}. \tag{8.10}$$

Again, ten runs of globalized optimization are performed with random initial parameter points for each frequency band. The results are provided in Figure 8.8 for the three different frequency ranges. An optimization, which is directly based on the sound pressures in Equation (8.7), does not exactly provide the same results (mean and variance) as a power-based one since there is no one-by-one relation

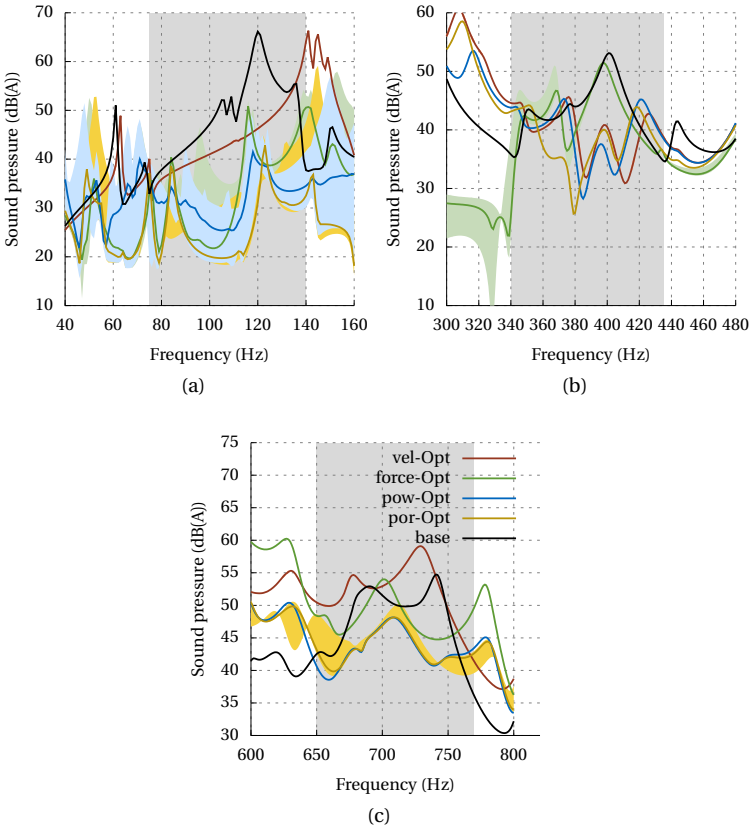

Figure 8.8: Optimization results utilizing the three different optimization objectives power, velocities, and forces in the grayed frequency bands. Power quantities at the interface of the radiating subsystem and mean SPLs are provided for the non-optimized base state and the optimized parameter values per objective function. Averaged values, minima, and maxima are provided for the latter, which result from ten independent runs of globalized optimization.

between power and SPLs. Anyhow, it can be stated that the results provide a comparable reduction of sound pressure level, as summarized in Table 8.3.

In addition, two other objectives in the interface between the active and passive side are considered for comparison, which are established in daily engineering work: Firstly, the sum of the squared translational velocities at the four interface nodes of the radiator

$$q_{\mathrm{V}} = \int_{f_{\mathrm{B}}} \sum_{j=1}^{n_{\mathrm{p}}} \left(V_x^2 + V_y^2 \right) \mathrm{d}f = 4\pi^2 \mathcal{Z} \left({}^{n}f^{2\,n} H_{\mathrm{a}}^{2\,n} \boldsymbol{Y}_{r,\mathrm{tr}}^{H\ n} \boldsymbol{Y}_{r,\mathrm{tr}}, \Delta f \right), \tag{8.11}$$

while $\boldsymbol{Y}_{k,\mathrm{tr}}$ are the displacement outputs of the radiating subsystem r corresponding to translational DOFs. Secondly the sum of the squared translational forces in this cutting section

$$q_{\mathrm{F}} = \int_{f_{\mathrm{B}}} \sum_{j=1}^{n_{\mathrm{p}}} \left(F_x^2 + F_y^2 \right) \mathrm{d}f = \mathcal{Z} \left({}^{n}H_{\mathrm{a}}^{2\,n} \boldsymbol{U}_{r,\mathrm{tr}}^{H\ n} \boldsymbol{U}_{r,\mathrm{tr}}, \Delta f \right), \tag{8.12}$$

with $\boldsymbol{U}_{r,\mathrm{tr}}$ as the inputs of the radiating subsystem r, which correspond to translational DOFs of the $n_{\mathrm{p}} = 4$ interface points. Gradients can be provided for Equation (8.11) and Equation (8.12) according to the derivation for Equation (8.7) for real-valued design parameters p_j. Rotations or moments are ignored in Equation (8.11) and Equation (8.12), as a summation of rotational and translational inputs or outputs is hindered due to different units.

The results are visualized in Figure 8.8 and summarized in Table 8.3, again averaged over ten globalized optimizations per frequency band and objective. The results for using Equation (8.11) and Equation (8.12) are of averaging quality. The use of the force-based objective, Equation (8.12), only leads to a slight improvement in Δf_{B2} and Δf_{B3}. The velocity objective, Equation (8.11), performs even worse, and the sound pressure levels are amplified but not reduced after optimization in Δf_{B3}. Thus, none of the two alternative objectives can provide a comparably robust reduction of sound pressure levels as power does for the 2D example. Structure-borne sound power at the interface of the radiator not only provides robust optimization results for sound pressure, but one can also anticipate the results from the optimizations based on forces and velocities on the sound pressure levels, see Figure 8.8(a) to Figure 8.8(c).

The (out)performance of the power objective always needs to be discussed for a specific system and design parameter setting, which

Objective	ΔL_{B1} (dB)	ΔL_{B2} (dB)	ΔL_{B3} (dB)
Power (Equation (8.3))	19.3	4.4	5.6
Force (Equation (8.12))	15.5	1.2	0.8
Velocity (Equation (8.11))	6.8	4.3	−4.0
Sound pressure (Equation (8.7))	23.2	5.7	5.5

Table 8.3: Reduction of the integrated average sound pressure level according to Equation (8.7) for the different optimization objectives and frequency bands. The results were averaged for the different runs of globalized optimization. Positive values correspond to a reduction.

is usually possible only after optimization. Section 8.2.4 presents an approach to anticipate when and why a power-based objective potentially provides different optimal parameters than more trivial objectives. However, no statement is possible about the performance concerning sound pressure levels.

For the 2D example, therefore, another discussion is presented, which approaches to assess the different quality of correlation of the objectives with SPLs in an illustrative way. The black-box setting of MRC is left for this, and the parameter setting is simplified to ensure mechanical interpretability: the initially three stiffness parameters are changed uniformly within $k \in \left[50\,\mathrm{N\,mm^{-1}}, 20000\,\mathrm{N\,mm^{-1}}\right]$, thus the design parameter space is reduced to 1D. No frequency band is considered to integrate the objective, but the correlation is analyzed for one single frequency point $f = 720\,\mathrm{Hz}$. The correlation of the different objectives in the interface between the passive and active side and the averaged sound pressure levels is visualized for 400 logarithmic spaced samples of k in Figure 8.9.

Figure 8.9 in combination with Figure 8.10 illustrates several fundamental findings for the different objectives. The latter provides the radiation ratio rr, the radiation efficiency σ_{rad} and the spatially averaged squared velocities $\overline{V_{\perp}^2}$, which are perpendicular to the radiating surface. The radiation efficiency is defined as

$$\sigma_{\mathrm{rad}} = \frac{\overline{P}_{\mathrm{rad}}}{\rho_{\mathrm{air}} c_{\mathrm{air}} S \overline{V_{\perp}^2}}, \tag{8.13}$$

while ρ_{air} is the density of air, c_{air} the speed of sound, S the area of the radiating surface. A radiation efficiency of one indicates that the radi-

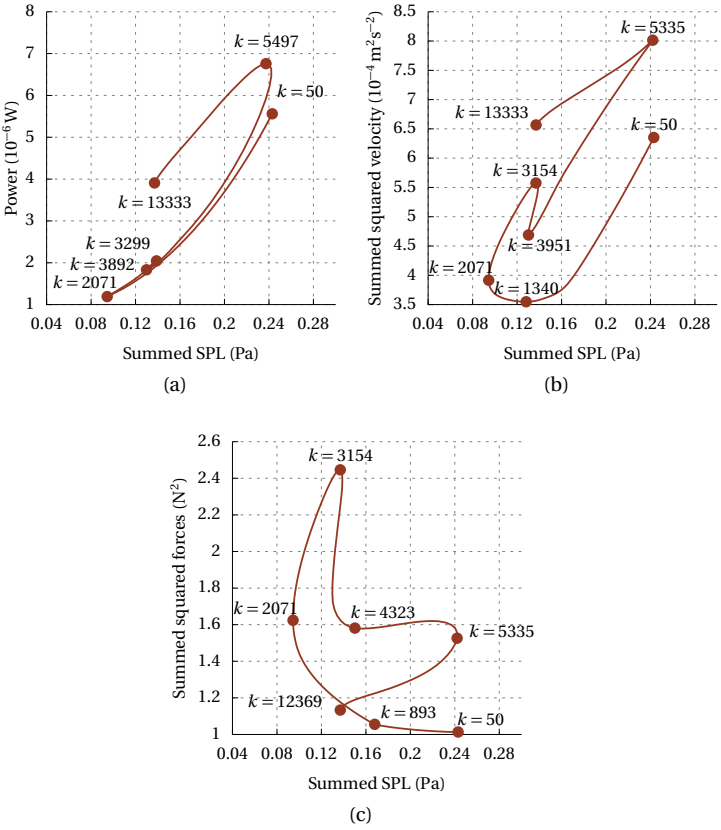

Figure 8.9: Correlation between the proxy (a) power, (b) squared translational velocities and (c) squared forces with sound pressure levels summed at the 22 evaluation points of the 2D example at $f = 720\,\text{Hz}$ for the 1D parameter space.

ator behaves like a piston radiator in a one-dimensional fluid. These quantities require spatial integrals at the radiator, which may not be possible for general black-box subsystems but can be performed for the 2D example.

When using the velocity-based objective of Equation (8.11), one aims to reduce the radiated sound pressure levels by reducing the

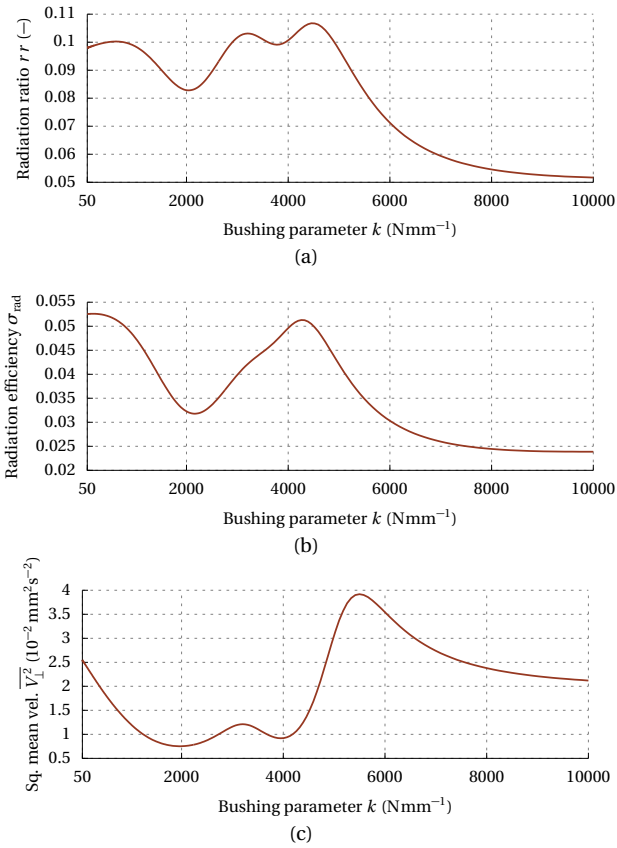

Figure 8.10: The (a) radiation ratio rr, (b) the radiation efficiency σ_{rad} and (c) the spatially averaged squared velocities $\overline{V_\perp^2}$ for the 2D example at $f = 720\,\mathrm{Hz}$ with 1D parameter space.

average velocity $\overline{V_\perp^2}$ of the radiator. However, as shown in Figure 8.9(b) and Figure 8.10(c), one may not necessarily reduce the average velocity, which is perpendicular to the radiator surface; even in the case of the 2D example, in which the radiating surface is directly attached to the radiator subsystem's inputs and outputs. Correspondingly, the velocity objective, Equation (8.11), has its minimum at $k = 1340\,\mathrm{Nmm^{-1}}$, which is not the minimum of the sound pressure level

at $k = 2071\,\mathrm{N\,mm^{-1}}$. $\overline{V_\perp^2}$, in contrast, is decreasing until a value of $k = 1950\,\mathrm{N\,mm^{-1}}$ is obtained. The mismatch results from the fact that the amplitudes of local quantities are observed at single points without any phases considered. This local information does not allow observing the radiator's global deflection shape. In addition, there is no direct correlation of $\overline{V_\perp^2}$ with the sound pressure levels. $\overline{V_\perp^2}$ may stay constant for varying k and thus changing deflection shapes of the radiator. Nevertheless, the radiation efficiency, Equation (8.13), may change and the radiated sound power as a consequence.

Contrary trends are possible, too: in between $k = 1950\,\mathrm{N\,mm^{-1}}$ and $k = 3520\,\mathrm{N\,mm^{-1}}$, $\overline{V_\perp^2}$ increases in line with the velocity objective. However, the radiation efficiency decreases, and so does the sound pressure level until it reaches its minimum at sample $k = 3154\,\mathrm{N\,mm^{-1}}$.

These deficiencies are not found in the power-based objective in the same way. The observation problem is relaxed, as the input power does not provide local information but a global one; it is related to the overall energy of the radiating subsystem. Also, the radiation efficiency has direct feedback on the energy balance and, therefore, the input power. As a result, only the minimum of power correlates with the minimum of sound pressure level at $f = 720\,\mathrm{Hz}$, but not the ones of the other proxy objectives.

Based on this, one can explain the optimization results for frequency band $\Delta f_{\mathrm{B3}} = [600\,\mathrm{Hz}, 770\,\mathrm{Hz}]$ in Figure 8.8(c), where power is the only valuable optimization objective. Solely the latter leads to a reduction of both, $\overline{V_\perp^2}$ and σ_{rad} over the whole frequency band. This is visualized in Figure 8.11.

Anyhow, Figure 8.9 also shows that power at the interface between the active and passive side is a more robust but not perfect proxy. As stated above, there is no one-to-one correlation with the mean sound pressure levels, which is linked to the changing deflection shape of the radiator in a strongly coupled system, when the stiffness k is varied. As a result, the radiation ratio rr changes, thus the ratio between input power and radiated one. The changing radiation efficiency is one reason for that change, although it is not the only influence, as evident in the slightly different functions of rr and σ_{rad} in Figure 8.9. Consequently, the exact minimum of SPL may be missed, and there is no unique sound pressure level for a power value in Figure 8.9. Anyhow, these observations also hold for the other objectives considered in Figure 8.9.

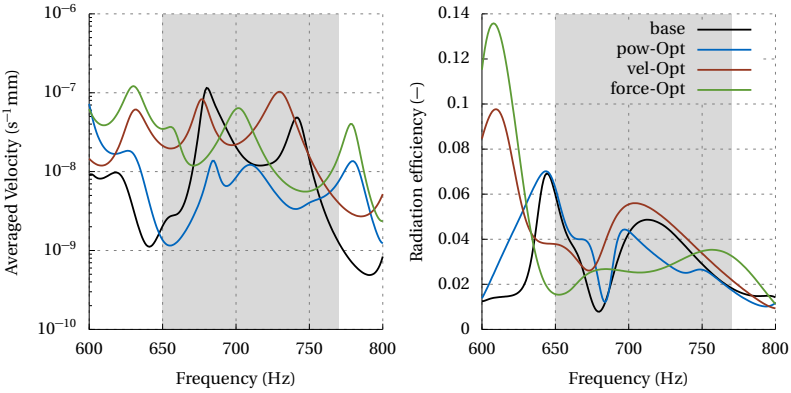

Figure 8.11: The perpendicular velocities of the beam surface, spatially averaged over the latter for frequency band $f_{B3}, \in [650\,\text{Hz}, 770\,\text{Hz}]$, as well as the radiation efficiency according to Equation (8.13). The spectra are provided for the optimization results of each of the three considered objectives and the base state.

Cavity Problems

Power-based objectives are mainly used for free field settings so far, which allow for a consistent discussion on the relationship between energy in the radiating subsystem and radiation into the fluid. However, when the acoustic vehicle quality should be improved finally for passengers of vehicles, the acoustic fluid forms a cavity in the vehicle but no free field. In preparation for such a vehicle setting, it can be validated heuristically in the following paragraphs that the above power-based objective is also valuable for a cavity setting of the 2D example.

The above 2D example is modified, and the radiating subsystem is changed according to Figure 8.12. The radiator now encloses the whole fluid, which is a half-circle with a radius of $r = 2000\,\text{mm}$. In addition, a non-radiating structure was added instead of the right-hand side support. This modification accounts for the fact that in a later vehicle assembly, the radiator, respectively the car body, has structural parts, which have no direct boundary to the fluid. All beams of the radiator have the same cross-section and a structural damping value of $\eta = 0.01$, and the non-radiating structure has an increased

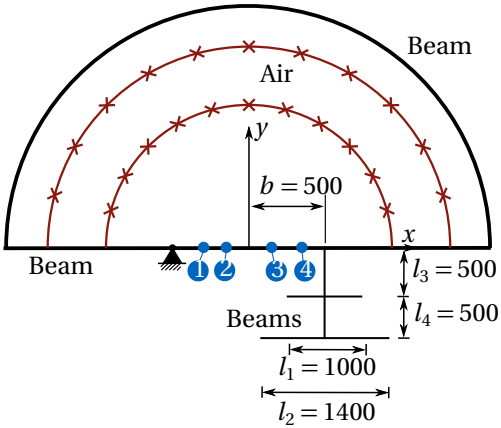

Figure 8.12: Modified radiating subsystem for the assessment of the cavity setting. The air cavity is fully enclosed by a beam structure. The four interface points are indicated by blue points. All units are in millimeters.

value of $\eta = 0.05$. A non-damped fluid with $\eta_A = 0$ is considered a limit case. The remaining network of the 2D example remains unchanged.

Again, a globalized optimization is performed using the four objectives above. Three slightly shifted frequency bands are considered for separate optimizations: $\Delta f_{B1} \in [105\,\text{Hz}, 145\,\text{Hz}]$, $\Delta f_{B2} \in [360\,\text{Hz}, 430\,\text{Hz}]$, and $\Delta f_{B3} \in [660\,\text{Hz}, 760\,\text{Hz}]$. The globalized optimization is repeated five times for the first points of the 3D Sobol sequence as initial parameter points, and the average reduction of sound pressure levels is presented in Table 8.4.

In cavity settings, the radiation ratio is significantly smaller, and in the above setting with $\eta_A = 0$, it is even zero. There is no proportionality according to Equation (8.5) anymore, and the discussion of Section 8.1.3 regarding the change of radiation ratio and radiation efficiency is not meaningful anymore. However, even in this limit case setting, the power objective still provides the most reasonable results of the three proxies at the interface between the active and passive side, as visualized in Table 8.4. Note, power provides even better results on average than a direct optimization of sound pressure levels in frequency range f_{B2}. Again, this is due to the heuristic nature of the globalized optimization approach.

Objective	ΔL_{B1} (dB)	ΔL_{B2} (dB)	ΔL_{B3} (dB)
Power (Equation (8.3))	14.5	3.6	4.1
Force (Equation (8.12))	5.9	1.5	0.4
Velocity (Equation (8.11))	9.3	3.3	−3.0
Sound pressure (Equation (8.7))	21.4	5.5	4.0

Table 8.4: Reduction of the integrated average sound pressure level according to Equation (8.7) for the different optimization objectives and frequency bands for the cavity setting of Figure 8.12 and $\eta_A = 0$. The results are averaged for the different runs of globalized optimization. Positive values correspond to a reduction.

What remains from the above discussion for the cavity setting is that mean power provides global information on the overall vibration of the damped radiator, although calculated from local interface data. Global information is not provided by the other proxies used in the interface. Apart from limit cases like zero or highly localized damping inside the radiator, heuristic experience confirms that power in the interface between the active and passive side provides a more robust measure for the overall vibration of the radiator and, thus, for the mean sound pressure inside the fluid. Thus, the power-based objective is used for the optimization of the following vehicle problem with an acoustic cavity.

Motivated by the fact that mean power at the interface provides a valuable objective even for zero radiated energy, one could even simplify the modeling for cavity settings. Assuming that the fluid loading has only a minor influence on the radiator itself, similar results as in Table 8.4 would have been obtained for the power-based objective with no fluid modeled. Authors like Schaal et al. [220] follow this idea. This approach can be relevant for daily engineering business, as inserting fluids in car body FE models is time-expensive. If one could leave this step, time savings during the virtual development process would be possible.

8.2 BMW 3series

The potentials of the numeric framework for a virtual end-to-end development process are presented finally for an energetic network synthesis of an industrial vehicle example. The 2019 BMW 3series is considered, for which structure-borne sound from road-induced noise should be reduced in the passenger cabin. The model consists of the rear axle attached to the car body, each modeled numerically by finite elements and visualized in Figure 8.13. Several components of the actual car are not modeled, like the wheels, the powertrain, and the interior. These components would be necessary to validate the numerical model against actual measurements of complete vehicles in hardware. Such validation, however, is not the aim of this example, but the gains from the numerical framework on industrial vehicle systems should be discussed. This discussion is enabled by the example, as the model has the complexity of a complete vehicle model.

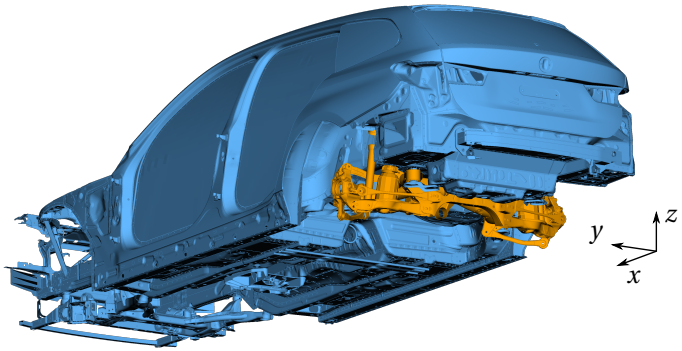

Figure 8.13: The BMW 3series rear axle example. The car body, thus the passive receiver, which is filled with an acoustic Helmholtz fluid, is colored blue. The rear axle system as the active source is colored orange.

As no wheel is modeled, an excitation is applied directly at the driver-side wheel carrier representing road-induced noise. For the synthetic setting, a translational harmonic force with amplitude $\boldsymbol{f} = \left[f_x, f_y, f_z\right] = [0.5, 0.2, 1.0]$ acts at the wheel hub, constant over the whole frequency range. Thus, the resulting frequency response functions can be considered a kind of unit transfer function that needs to be scaled over frequency for different road profiles. A frequency range of $f \in [10\,\text{Hz}, 300\,\text{Hz}]$ is defined for analysis and synthesis of road-induced noise.

Again the reduction of structure-borne sound should be obtained by a globalized optimization for mean power at the radiator subsystem interface. In contrast to the above 2D example, anyhow, not only stiffness parameters of bushings should be optimized, but also geometric parameters of other subsystems of the axle. Parametric model order reduction is required for this in addition to the modular subsystem coupling approach. Therefore, the step of parametric model order reduction is discussed for the BMW 3series after the model description below. Finally, a strategy is discussed to use these pROMs in optimization approaches, and the results are presented.

8.2.1 Model and Network Definition

The rear axle of the BMW 3series is a five-arm axle system. Five control arms define the kinematics on both sides of the axle. Each control arm has bushings at its two ends, connecting the wheel carrier with the rear axle carrier. The latter is mounted elastically to the car body by another four bushings. The vertical dynamics are delimited by a shock absorber, respectively damper, and a suspension spring on each side, which are supported by one of the control arms and the car body.

All subsystems of the vehicle model are discretized in the commercial FE software ABAQUS and illustrated in Figure 8.14. The five control arms (C1 to C5) are modeled by shell elements, as well as the rear axle carrier (RC). To each other (bushing) subsystem, these models have a single node as an interface with six degrees of freedom (DOFs), placed in the center of gravity of the neighboring bushing subsystems. The nodes are connected to the shell models by kinematic couplings. This interface modeling results in minimal interfaces and leads to a small interface problem, as discussed below. The wheel carrier (WC) is modeled from solid elements. The shock absorber (SA) and suspension spring (SP) are constructed from shell and beam ele-

ments, discrete frequency-dependent spring and damper elements. Also, these parts show the same interface modeling, except the interface of SA, which provides three points for the car body connection. The bushings are modeled as springs, dampers, and mass points with coincident points.

The subsystem of the vehicle body is considered a trimmed body model with fluid (TB). The bare-metal passenger cabin is entirely filled with a mesh of acoustic Helmholtz elements. The structural and acoustic domains are coupled via a tie contact; thus, a fully coupled structure-fluid interaction is considered. Ninety-seven evaluation points are distributed over the whole fluid, on which the sound pressure levels can be evaluated to assess the overall sound radiation into the car interior.

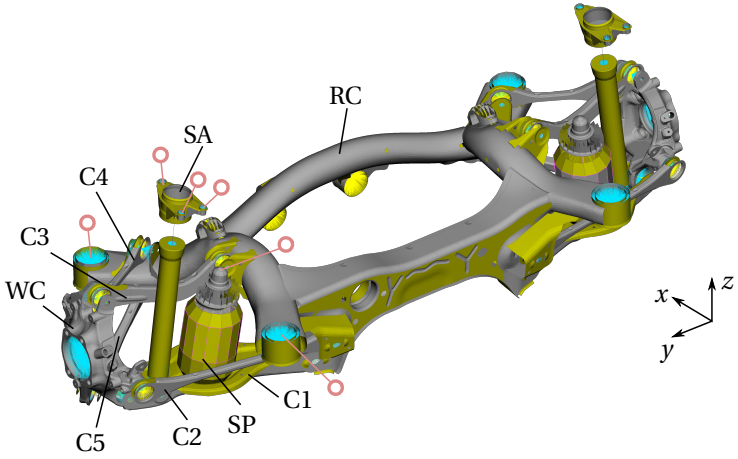

Figure 8.14: The FE model of the five-arm rear axle for the BMW 3series. On one side, the connection points to the car body are indicated by red circles, and the single subsystems are marked as follows. SA: shock absorber; SP: suspension spring; C1-C5: the five control arms; WC: wheel carrier; RC: rear axle carrier. The single colors of the model surfaces are introduced for visualization purposes without additional meaning.

The mechanical network is defined in the MRC framework of Chapter 3, thus in a distributed manner to enable a highly efficient localized parameter evaluation on the one hand. On the other hand, the idea

of a hybrid assembly with subsystems from different data sources should be illustrated by this example. Thus, the single subsystems are treated differently and coupled in different representations, although they exclusively result from an implicit FE system. The final assembly is visualized in Figure 8.15 for one side of the axle, including the number of internal states of the subsystems. The control arms (C1 to C5) on each axle side and the rear axle carrier (RC) are coupled in their inner representation, thus implicit form of Equation (2.6). For these subsystems, design parameters $\boldsymbol{p}_k$ should be preserved for later variations, like shell thicknesses, mass densities, point masses, or the modulus of elasticity. The trimmed body (TB), shock absorbers (SA), its connecting mount, suspension springs (SP), and the bushings, which connect the body and the rear axle carrier (RC-TB1 to RC-TB4), and the wheel carrier (WC) are provided each in transfer function representation of Equation (2.10). The latter is calculated from the FOM by Equation (2.11) for all subsystems, except for the trimmed body, for which it is calculated from a non-parametric projection-based ROM using component mode synthesis (CMS). The latter incorporates the modes shapes of the 600 lowest eigenvalues of the subsystem's undamped and unconstrained eigenvalue problem, as well as free interface modes following the Craig-Chang method (Craig et al. [59]). For none of these subsystems, design parameters are kept variable as a result.

The bushings between the wheel carriers and the control arms and between the latter and the rear axle carrier are considered in an early design phase. In this phase, rough estimates about the stiffness of bushings are available, but there is no mass information. Therefore, they are modeled as six-dimensional springs with structural damping. As they are massless, they can be considered as single subsystems by using an explicit subsystem formulation as introduced in Section 3.2.2. This allows for a consistent modular treatment also of these subsystems, thus the localized variation of the corresponding stiffness values.

In total, a network of 44 subsystems is obtained. The axle system is symmetric in its geometry and other subsystem parameters, which should be preserved during an optimization. Thus, when a bushing on the driver is changed, it is also changed on the co-driver's side. This symmetry can be exploited in the network definition. Only the driver-side subsystems of the network are calculated for a parameter variation. The outputs of the corresponding subsystems on the other

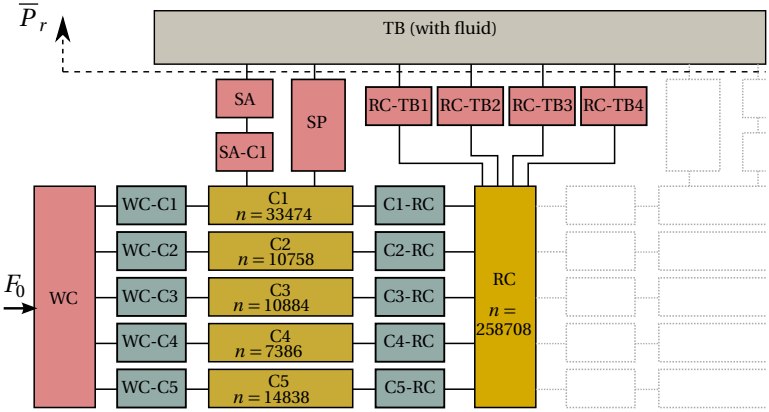

Figure 8.15: The BMW 3series rear axle assembly's network presentation incorporating the FOM subsystems. Only the axle's loaded left side is visualized, which is mirrored on the right side. Red-colored subsystems correspond to a transfer function representation, yellow-colored to an implicit finite element form, green-colored to explicit bushings with switched inputs and outputs. The light-brown colored subsystem is in a CMS representation. For subsystems in implicit representation, the number of internal states is provided by n.

side are subsequently recovered from the geometric manipulation of the driver-side outputs by mirroring on the longitudinal vehicle axis.

The 44 subsystems provide 62 nodal connections for the interconnections between the subsystems, each having six DOFs. As a partial switch of the interfaces quantities is performed for the massless subsystems according to Section 3.2.2, thus the network definition results in 20 nodal interfaces with Dirichlet-Neumann/Neumann-Dirichlet constraint pairs and 42 with Dirichlet-Dirichlet/Neumann-Neumann constraint pairs. The latter nodal interfaces can be reduced to half of the twelve required interface constraint equations using the mixed formulation according to Section 3.2.3. This network definition leads to an interface problem of size $n_{\text{int}} = 744$ without a mixed formulation, and finally $n_{\text{int}} = 492$ with the mixed input vector of the MRC framework.

8.2.2 Parametric Model Order Reduction of Large-scale Subsystems in the Offline Phase

Suppose design parameters inside large-scale FOM subsystems should be varied, like the rear axle carrier RC. In that case, the single parameter variations in the network become expensive, even for the application of MRC in Figure 8.15. As a consequence, the parameters of such subsystems can not be included in a globalized optimization without an additional parametric model order reduction. Using pMOR, any parameters of arbitrary subsystems may be extensively sampled during the online phase. As a result, one can maximize the solution space for optimization (performing a holistic network uncertainty quantification or inverse parameter estimation, respectively). In the following, the pMOR procedure is discussed exemplarily for two large-scale subsystems. Finally, the network representation of the BMW 3series rear axle incorporating pROM subsystems is introduced, as used for globalized optimization below.

Control Arm C1

Control arm 1 (C1) has four interface nodes for connections to four other subsystems. Each node has three translational and rotational DOFs, leading to an interface size of 24 inputs and outputs. The model was assembled using the ABAQUS STRI3 shell-like triangular plate elements, point masses, and multi-point constraints, resulting in an FE discretization with 33474 DOFs.

For the globalized parameter optimization below, a parametrization is introduced as follows: Three cross-sections are defined, as visualized in Figure 8.2.2. In each cross section, the shell thickness can be varied independently in the range of $t_i \in [1.5\,\text{mm}, 3.5\,\text{mm}]$. Two point masses m_1 and m_2 with range $m_i \in \left[0\,\text{t}, 10^{-4}\,\text{t}\right]$ are introduced as variable parameters, in addition. The frequency-range of interest is defined as $f \in [1\,\text{Hz}, 1000\,\text{Hz}]$, for the first. The parameter setting results in a 6D parameter space, in which the system dynamics must be represented by the global basis $\boldsymbol{V}_\text{g}$. Significantly different system dynamics need to be covered in the parameter space, which is visualized for two example transfer functions of $\boldsymbol{H} \in \mathbb{C}^{24\times 24}$ in Figure 8.17. Following the analytic beam example of Section 6.2.5, a soft setting with $m_i = 10^{-4}\,\text{t}$, $t_i = 1.5\,\text{mm}$, and a hard setting with $m_i = 0\,\text{t}$, $t_i = 3.5\,\text{mm}$ is defined for visualization.

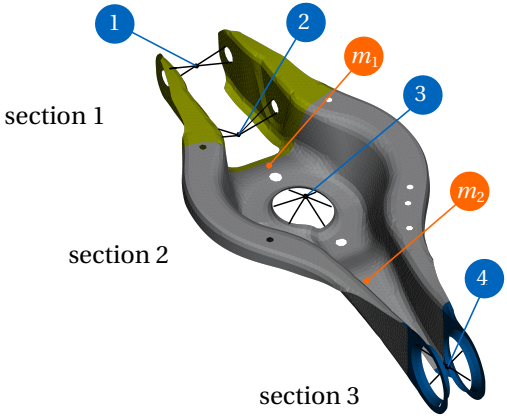

Figure 8.16: The control arm C1 of the BMW 3series rear axle and its sections and point masses for parametrization in pMOR training. The points marked with blue labels show the four connection points to other subsystems.

The commercial FE software ABAQUS is used, so no direct access to the required affine matrix decomposition is possible. Anyhow, additional knowledge is available on the affine functions $f_j(\boldsymbol{p})$, as one knows, that the dependency of the element matrices on the shell thickness can be reconstructed by cubic basis functions for the ABAQUS STRI3 elements. The dependency of the mass matrix on the point masses is linear. Thus, a parameter-gray-box approach can be followed to recover the affine decomposition from parameter samples of the system matrices (see Equation (6.5) on page 148), and the affine matrix decomposition of the CA1 results in

$$\boldsymbol{M} = m_1\boldsymbol{M}_1 + m_2\boldsymbol{M}_2 + \sum_{j=1}^{3}\left(t_j\boldsymbol{M}_{1,j} + t_j^3\boldsymbol{M}_{2,j}\right)$$

$$\boldsymbol{K} = \sum_{j=1}^{3}\left(t_j\boldsymbol{K}_{1,j} + t_j^3\boldsymbol{K}_{2,j}\right)$$

$$\boldsymbol{S} = \sum_{j=1}^{3}\left(t_j\boldsymbol{S}_{1,j} + t_j^3\boldsymbol{S}_{2,j}\right).$$

Description	Name	Value
Deflation length	l_{defl}	$1 \cdot 10^{-8}$
Krylov order	o	2
Max. no. of greedy iterations	n_{itMax}	50
Skipped iterations for lucky breakdown	n_{skipMax}	12
Sample set for pre-selection of ${}^{n}\tilde{\boldsymbol{p}}_0$	n_{pre}	50
Max. no. of residual calculations per iteration	n_{maxFun}	200
Error threshold	$\varepsilon_{\text{rel}}^{\text{lim}}$	$5 \cdot 10^{-3}$

Table 8.5: Metaparameters for pROM training of the control arm C1.

The OGPA training is performed as described for the analytic example in Section 6.2.5; the specific settings are provided in Table 8.5. As a result of the analytic beam example of Section 6.2.5, ${}^{0}\tilde{\boldsymbol{p}}_0$ for the initial basis to start the greedy search is defined as a combination of the parameter values of the soft setting ($t_j = 1.5\,\text{mm}$ and $m_j = 10^{-4}\,\text{t}$) along with the band middle frequency $f = 500\,\text{Hz}$.

Compared to the analytical example in Section 6.2.5, there is an adaption in the in-situ and a-posteriori error evaluation for industrial models. The range of values in the transfer function matrix is typically widespread for such models. Also, very small entries may be incorporated, for which it is not economical to ensure the above error threshold. The latter would result in unnecessarily large pROMs. Thus, the error control of Equation (6.13) on page 156 is slightly modified and a relaxed error limit $\varepsilon_{\text{rel}}^{\text{rlx}}$ is defined for these small entries

$$ {}^{j}\varepsilon_{\text{H,rel}}^{\max} \geq \begin{cases} \varepsilon_{\text{rel}}^{\text{lim}} & \text{for} \quad |H_{kl}| > H_{\text{sw}} \\ \varepsilon_{\text{rel}}^{\text{rlx}} & \text{for} \quad |H_{kl}| \leq H_{\text{sw}} \end{cases} , \tag{8.14} $$

where H_{sw} is a user-defined threshold to separate the magnitude of transfer function matrix entries into small and large values. For the control arm, $H_{\text{sw}} = 5 \cdot 10^{-9}$ and $\varepsilon_{\text{rel}}^{\text{rlx}} = 2 \cdot 10^{-1}$ is defined.

In summary, there are several meta-parameters to fine-tune the procedure of OGPA. In practice, however, most of the parameters can

be kept as described above for reasonable first results, but only l_{defl} and $\varepsilon_{\text{rel}}^{\text{lim}}$ (possibly along with H_{sw} and $\varepsilon_{\text{rel}}^{\text{rlx}}$) should be defined mandatory by the user.

OGPA identifies 25 additional parameter sample points in the first 29 iterations. Afterward, no more parameter samples are found which exceed $\varepsilon_{\text{rel}}^{\text{lim}} = 5 \cdot 10^{-3}$, respectively $\varepsilon_{\text{rel}}^{\text{rlx}} = 2 \cdot 10^{-1}$ in the in-situ error evaluation. The algorithm terminates in a lucky breakdown after 40 iterations, and a pROM of size $m = 424$ is obtained. Inexact deflation significantly increases the reduced model's efficiency for the large-scale MIMO setting. It allows including information on the system dynamics for more parameter sample points without resulting in inefficiently large pROMs. Without deflation, a global basis size of $m = 1248$ would have been obtained for local bases at 25 expansion points.

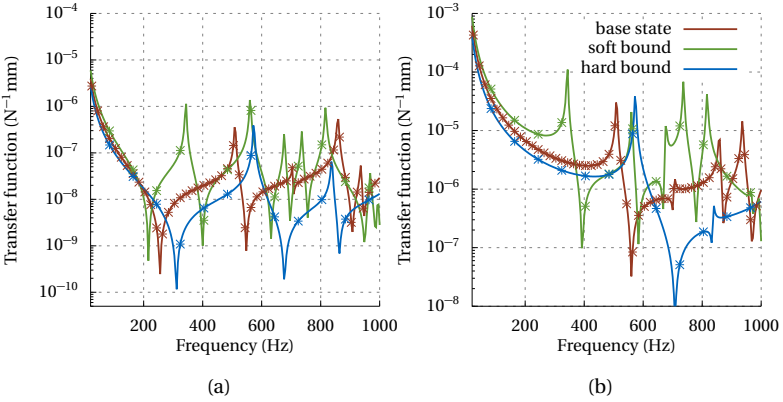

Figure 8.17: Absolute value of the transfer function at (a) the diagonal entry for node 1 DOF 4, (b) the entry for node 1 DOF 4 (rotation around x-axis) to node 4 DOF (rotation around y-axis). The solid line belongs to the transfer function of the FOM, the starred line to the one of the pROM.

In line with the cantilever beam example of Section 6.2.5, a general tendency in the parameter samples can be identified when the frequency dimension is excluded. The accepted parameter sampling points ${}^{n}\tilde{\boldsymbol{p}}_{\text{opt}}$ contain mostly values from the bounds of the variable parameter space, as 114 out of 150 sample values are bound values, either of the lower or upper parameter bounds.

After basis generation, an a-posteriori error evaluation is performed as described in Section 6.2.4. A validation set of size $n_{\text{sam}} = 2000$ is chosen, which is formed by the first elements of the corresponding Sobol sequence. More extensive sampling, as in the case of the analytic example in Section 6.2.5, is not efficient even for that mid-scale industrial FOM. To account for the training strategy, the error evaluation in the a-posteriori is adapted according to Equation (6.13) and Equation (8.14) and the maximum error

$$ {}^{j}\varepsilon_{\text{H,rel}}^{\max} = \begin{cases} \max\limits_{k,l} {}^{|{}^{j}H_{kl} - {}^{j}H_{\text{R},kl}|}/_{|{}^{j}H_{kl}|} & \text{for} \quad |H_{kl}| > H_{\text{sw}} \\ 0 & \text{for} \quad |H_{ij}| \leq H_{\text{sw}} \end{cases} \tag{8.15} $$

is determined per parameter sample j. Thus, the error is evaluated only for transfer function entries larger than $|H_{kl}| > H_{\text{sw}}$. The corresponding histogram of the maximum error distribution is found in Figure 8.18. On the sample grid, the largest error is $\varepsilon_{\text{H,rel}}^{\max} = 1.2 \cdot 10^{-2}$. Six error overshoots are counted out of 2000 samples; thus, an accurate pROM is obtained. The potentially high pROM transfer function accuracy is also reflected in the confidence interval provided by Bayesian inference, which provides

$$P(99\% < a < 100\% | 1994, 2000) = 99.9\%.$$

Rear Axle Carrier RC

As an additional example for pMOR, the 3series rear axle carrier (RC) is analyzed. Figure 8.19 illustrates the subsystem and its 14 6DOF connection points to 14 bushing subsystems, resulting in both, 84 inputs and outputs. Again a FE discretization by the FE software ABAQUS is used. Triangular plate-like shell elements STRI3 are considered along with several multi-point constraints, which connect single parts of the structure and the interface nodes to the shell. The discretized model has 258708 DOFs in total. Again, a parametrization similar to the control arm C1 is chosen for parameter optimization, but also with the mass density to identify regions for additional mass covers. The RC is partitioned into four segments, as visualized in Figure 8.20. The shell thickness is varied independently in each segment from $t_j \in [1.3\,\text{mm}, 2.3\,\text{mm}]$ and the material density $\rho_j \in \left[5.5 \cdot 10^{-9}\,\text{tmm}^{-3}, 13 \cdot 10^{-9}\,\text{tmm}^{-3}\right]$. A relevant frequency range of $f \in$

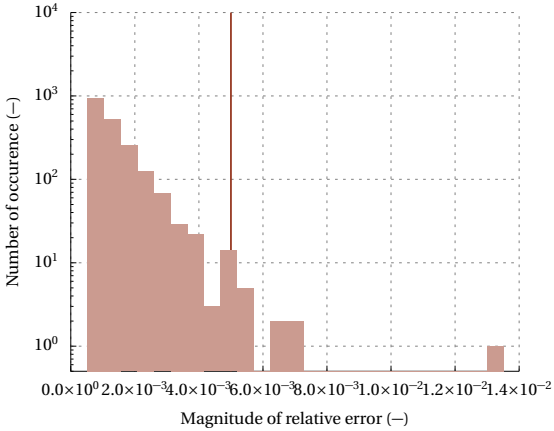

Figure 8.18: Histogram of the maximum relative transfer function error of Equation (8.15) in logarithmic representation for the a-posteriori error evaluation of the control arm C1 pROM on the validation set. $\varepsilon_{\text{rel}}^{\text{lim}}$ is indicated by the red vertical line.

[20 Hz, 500 Hz] is defined, in which the later optimization of the vehicle assembly is performed. This parametrization leads to a 9D parameter space that the global basis must cover in total.

As in the preceding control arm example, the affine decomposition of the system matrices, Equation (6.4), needs to be reconstructed in a gray-box approach from samples at fixed parameter values, resulting in the decomposition of

$$\boldsymbol{M} = \boldsymbol{M}_0 + \sum_{j=1}^{4} \left(t_j \boldsymbol{M}_{1,j} + t_j^3 \boldsymbol{M}_{2,j} \right)$$

$$\boldsymbol{K} = \boldsymbol{K}_0 + \sum_{j=1}^{4} \left(t_j \boldsymbol{K}_{1,j} + t_j^3 \boldsymbol{K}_{2,j} \right)$$

$$\boldsymbol{S} = \boldsymbol{S}_0 + \sum_{j=1}^{4} \left(t_j \boldsymbol{S}_{1,j} + t_j^3 \boldsymbol{S}_{2,j} \right).$$

Thus, nine affine terms are needed for both of the two matrices, $\boldsymbol{K}$ and $\boldsymbol{M}$, for their cubic dependency on the single t_i. The linear influence

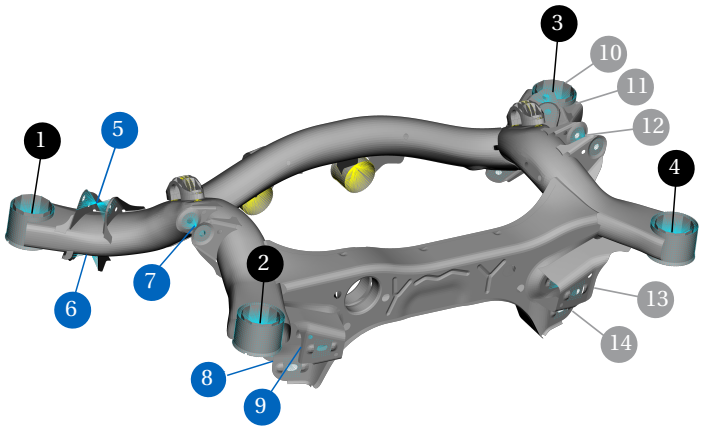

Figure 8.19: The BMW 3series rear axle carrier and its interface nodes. The nodes with black labels one to four are the connection points to the car body, and the ones with blue labels five to nine are the interface to the driver's side control arms. The gray labeled nodes ten to fourteen define the interface to the passenger's side control arms.

of ρ_j on $\boldsymbol{M}$, respectively η_j on $\boldsymbol{S}$, can be considered with the same decomposition.

The amplitudes of two exemplary transfer functions of $\boldsymbol{H} \in \mathbb{C}^{84\times84}$ are provided in Figure 8.21 for a visualization of the system dynamics, which need to be covered over the parameter space. For the latter, again, a soft setting with $\rho_j = 13\cdot10^{-9}\,\mathrm{tmm}^{-3}$, $t_j = 1.3\,\mathrm{mm}$, and a hard setting with $\rho_j = 5.5\cdot10^{-9}\,\mathrm{tmm}^{-3}$, $t_j = 2.3\,\mathrm{mm}$ is defined.

The training settings for OGPA are chosen according to Table 8.6. As in the training for C1, the parameter values of the soft setting along with $f = 250\,\mathrm{Hz}$ are chosen as initial point ${}^0\tilde{\boldsymbol{p}}_0$, which defines the initial local basis.

During 23 greedy iterations, the parameter sample ${}^j\tilde{\boldsymbol{p}}_{\mathrm{opt}}$ from the greedy optimization is omitted five times in the in-situ error evaluation according to Equation (8.14) until the last expansion point is found. Afterward, no local basis is added in twelve subsequent optimizations, and the OGPA finishes with a lucky breakdown after 35 greedy iterations in total. In summary, 18 local bases are sampled in

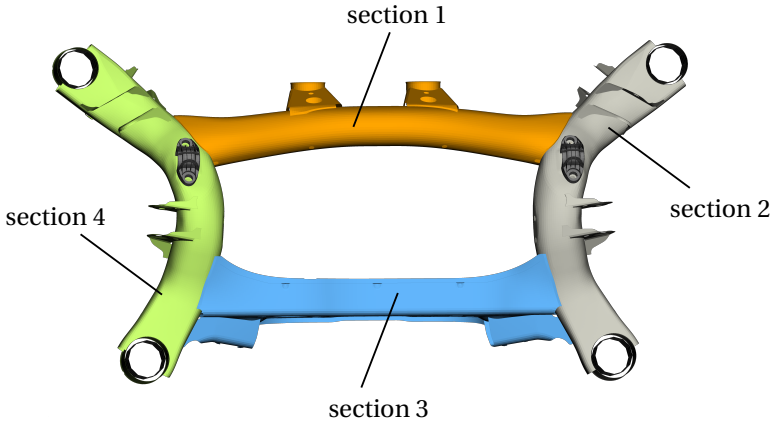

Figure 8.20: Partitioning of the rear axle carrier into different sections for parametrization in pROM training.

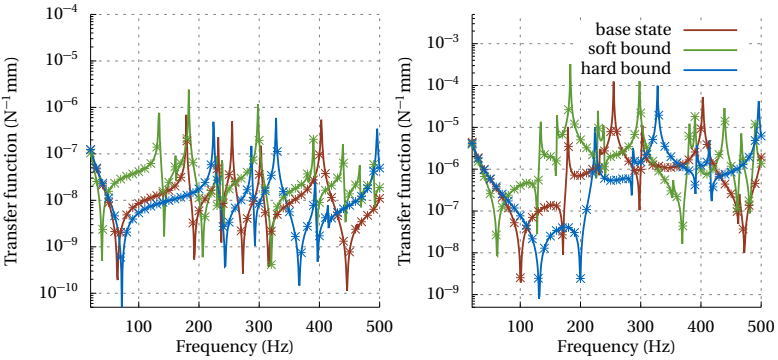

Figure 8.21: Absolute value of the transfer function at the (a) diagonal entry for node 3 DOF 5 (rotation around x-axis), (b) off diagonal entry relating node 3 DOF 5 and node 7 DOF 1 (translation in x-direction). The solid line belongs to the transfer function of the FOM, the starred line to the one of the pROM.

Description	Name	Value
Deflation length	l_{defl}	$1 \cdot 10^{-7}$
Krylov order	o	2
Max. no. of greedy iterations	n_{itMax}	50
Skipped iterations for lucky breakdown	n_{skipMax}	12
Sample set for pre-selection of ${}^{n}\tilde{\boldsymbol{p}}_0$	n_{pre}	150
Max. no. of residual calculations per iteration	n_{maxFun}	200
Error threshold	$\varepsilon_{\text{rel}}^{\text{lim}}$	$5 \cdot 10^{-3}$
Relaxed error threshold	$\varepsilon_{\text{rel}}^{\text{rlx}}$	$2 \cdot 10^{-1}$
Transfer function amplitude threshold for $\varepsilon_{\text{rel}}^{\text{rlx}}$	H_{sw}	$5 \cdot 10^{-9}$

Table 8.6: Metaparameters for pROM training of the rear axle carrier.

the parameter space in addition to the one of ${}^{0}\tilde{\boldsymbol{p}}_0$, and a basis size of $m = 798$ is obtained.

The discussion of the parameter sample positions can be repeated for the rear axle carrier. Again, the parameter sample points ${}^{j}\tilde{\boldsymbol{p}}_{\text{opt}}$ contain mostly values from the bounds of the parameter space when one does not consider the frequency dimension. Thus, only 39 of 144 sample values are no bound values. As for the preceding examples, inexact deflation plays a significant role in basis reduction. Nineteen expansion points would result in a model size of $m = 3192$ for no deflation. Compared to the actual size of $m = 798$, 75% of the candidate vectors for $\boldsymbol{V}_{\text{g}}$ are omitted during basis generation.

It is evident from Figure 8.21 that the resulting pROM visually replicates the transfer function for the base, soft, and hard bound in an accurate manner. For a more systematic analysis of the error, a validation set of size $n_{\text{sam}} = 1000$ is chosen, and the a-posteriori ROM error evaluation is performed. Evaluating the error according to Equation (8.15) in Figure 8.22 shows that the error ${}^{j}\varepsilon_{\text{H,rel}}^{\text{max}}$ is below $\varepsilon_{\text{rel}}^{\text{lim}}$ for 997 samples. Three error overshoots are obtained, which result in a statistical ROM quality according to Bayesian inference of

$$P(99\% < a < 100\% | 997, 1000) = 99.0\%.$$

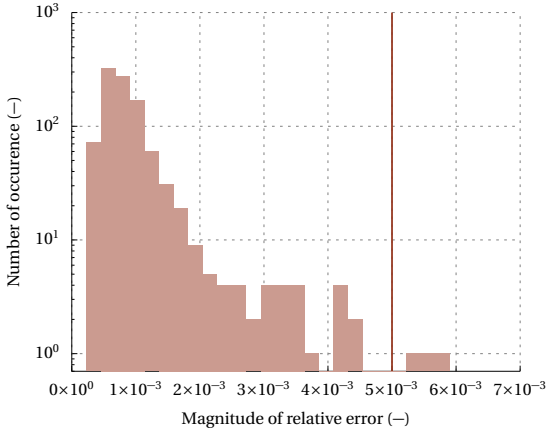

Figure 8.22: Histogram of the relative transfer function error of Equation (8.15) in logarithmic representation for the a-posteriori error evaluation of the rear axle carrier on the validation set. $\varepsilon_{\text{rel}}^{\text{lim}}$ is indicated by the red vertical line.

Reduced Network Definition

The pMOR training procedure is repeated for all subsystems, including variable (design) parameters for the later multi-query methods. In the globalized optimization of the assembly below, usually, only a limited number of subsystems should be changed, at least in later development stages. Consequently, one may include pROMs only for these single subsystems and consider the remaining ones by a transfer function representation. Anyhow, one may approach a more holistic optimization of the overall system in earlier phases and, thus, of all subsystems. Moreover, although one may want to change only a few subsystems, one needs to identify the most sensitive design parameters by screening in a step preceding assembly optimization. Such a screening maximizes the solution space with only a limited number of design parameters, which is discussed shortly below.

Consequently, all implicit FOM parts are replaced for the following by pROM subsystems. The system analysis and synthesis should be performed in a frequency range in between $f \in [1\,\text{Hz}, 500\,\text{Hz}]$. As a result, the pROM of C1 presented above is trained for an unnecessarily wide frequency range. As visualized in Figure 8.17(a) and

Figure 8.17(b), significantly less system dynamics of C1 have to be covered for $f \in [1\,\text{Hz}, 500\,\text{Hz}]$, enabling smaller pROMs. In Appendix B, the training of an alternative pROM of C1 in the reduced frequency range is presented, as well as for the other control arms. The corresponding reduced network representation is visualized in Figure 8.23 based on these pROMs.

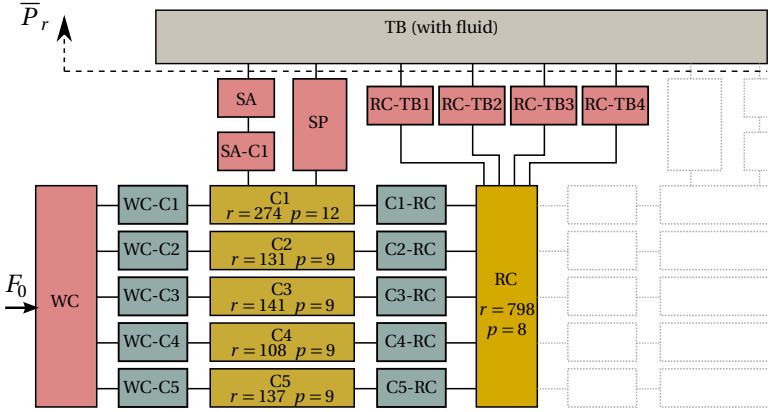

Figure 8.23: The BMW 3series rear axle assembly incorporating pROM subsystems (yellow-colored). The subsystem size and the number of preserved parameters are provided for these subsystems.

The computational efforts for single parameter evaluations are reduced drastically using the pROM network. There is no subsystem with more than $m = 798$ internal states; most are significantly smaller. On average, the subsystem size was reduced by 99.1%. Anyhow, 56 variable parameters in the pROMs and 60 in the bushing subsystems are still preserved for multi-query methods applied to the whole vehicle assembly of this section. Despite the drastic reduction of subsystem size, only small errors are introduced when power is evaluated in the pROM network instead of the FOM equivalent. On the frequency sample grid of Figure 8.24, the evaluation of the relative error of the mean power $\overline{P}_r$ at the radiator, thus the car body interface

$$\varepsilon_{\overline{P}} = \frac{|\overline{P}_r - \overline{P}_{\mathrm{R},r}|}{|\overline{P}_r|} \tag{8.16}$$

equals $\max_f \varepsilon_{\overline{P}} = 1.2 \cdot 10^{-3}$. This error is in the same range as the error threshold used for pROM training.

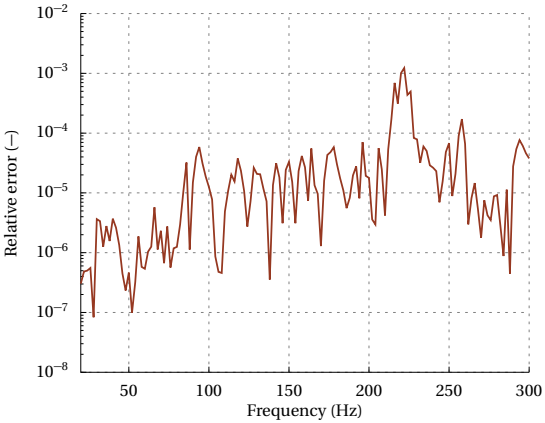

Figure 8.24: Relative error of the mean power $\overline{P}_r$ in the interface between axle system and car body, which is introduced by the evaluation of the pROM network instead of the FOM representation. The error is evaluated according to Equation (8.16) for the nominal parameters.

8.2.3 Synthesis With pMOR in the Online Phase

Methodology

Globalized network optimization of the BMW 3series rear axle assembly is performed according to Section 8.1.2 in the following. Again, the objective is the mean power evaluated at the interface between the active and passive side of the network, thus at the car body interface, and integrated over band-limited frequency ranges according to Equation (8.3). Again, the method of Ugray et al. [249] in the implementation of MATLAB R2018b is chosen for globalized optimization, which incorporates gradient-based local optimizations. For the latter, the same SQP algorithm is employed as for the 2D example, with analytical gradients provided by Equation (8.4) according to Section 4.2.

Thus, the basic setup is as for the 2D example, but with the additional need for error control in the online phase; thus, to manage the error, which is introduced in the objective using pROM subsystems instead of the FOM representations.

In a wider sense, there are two basic strategies for such error control in literature. The first is following a strict separation between the

offline and online phase, mainly in the context of reduced basis methods (Dihlmann et al. [68] and Oliveira et al. [186]). In these methods, one pROM is trained in the offline phase, which is used for calculating the objective during the whole online phase. Error estimates are introduced to validate the results from such an approach with pROMs against the FOM model. The optimization algorithm may use distinct paths through the possibly high-dimensional design parameter space. Thus, unnecessary information may be contained in the pROM for the latter's training on the whole admissible high-dimensional design parameter space; respectively, it may not be possible to find a practical training strategy to cover it robustly. This is the motivation for the second strategy to use adaptive pROMs, as found in Fröhlich et al. [86], Tomljanović et al. [246], Yue et al. [279], and Zahr et al. [281]. Starting with a very inaccurate pROM, the latter is refined iteratively along the optimization path in the design parameter space. Thus, the offline-online principle is levered as one performs the pROM training and optimization side-by-side. Many flavors of such adaptive approaches with different pROM updating strategies and thus with different model management strategies exist. Several adaptive methods are also found under the name of multi-fidelity approaches; refer to Peherstorfer et al. [198] for an overview. Prominently, one can mention model management strategies, which are based on classic trust-region algorithms, but use (p)ROM models; see Alexandrov et al. [2] for an early work.

Modularity is a key concept for the methods of this thesis. The concept of offline-online separation was postulated to ensure this for using pMOR. This separation excludes adaptive methods for error control during optimization, and the pROMs were trained independently of the actual optimization for the whole admissible parameter space in Section 6.2.

The omission of adaptive methods has not necessarily the proclaimed drawback of a significant decrease in efficiency and feasibility when one follows the thesis framework. With subsystem coupling, the training is performed on a subsystem-local level. The individual training needs to cover a significantly smaller design parameter space as it would be required for one monolithic pROM of the whole (vehicle) network. This subsystem-local training potentially relaxes the issue of prohibitively large parameter spaces that cannot be covered holistically by one training and enables efficient procedures in an offline-online scheme.

Modularity implies that the error control during pROM training in the offline phase is performed on a subsystem-local level, not considering the coupling operator and thus not explicitly the error in the final network. Despite this fact, the proposed model management strategy does not include continuous error control on the FOM network level in the online phase. This non-continuous error control is due to another essential requirement in the thesis: all approaches need to apply to large-scale industrial models. A globalized optimization of the latter in a high-dimensional parameter space requires an extensive amount of iterations; the continuous monitoring of the error, in turn, is computationally expensive. As a result, the optimization of such systems may become too expensive, although pROMs are used. This may also be the case when error estimates are evaluated instead of the true error; refer to Section 5.6. Instead, the error of the reduced objective $q_\mathrm{R}(\boldsymbol{p})$ with respect to the true one $q(\boldsymbol{p})$ is evaluated solely at the end of the optimization. In the following, the relative error is considered

$$\varepsilon_{\mathrm{q,rel}}(\boldsymbol{p}) = \frac{|q_\mathrm{R}(\boldsymbol{p}) - q(\boldsymbol{p})|}{q(\boldsymbol{p})}. \tag{8.17}$$

Note, in contrast to Equation (8.1), solely the objective's dependency on $\boldsymbol{p}$ is noted explicitly for brevity.

Multi-start algorithms like the one of Ugray et al. [249] provide several parameter candidates ${}^{j}\boldsymbol{p}_\mathrm{lopt}$ for the global minimum, from which usually the one with the smallest objective function value is considered as the heuristic global minimum. Two procedures are discussed for an error management strategy in the following. In method A, the true objective value $q({}^{j}\boldsymbol{p}_\mathrm{lopt})$ is evaluated in the FOM network for all parameter candidates, which were obtained from the globalized optimization of the pROM network. The one with the smallest value is selected as the heuristic global optimum. Anyhow, evaluating the objective in the FOM network at all parameter candidates is usually computationally costly, as the industrial FOM subsystems are large-scale. This motivates another method B, in which one assumes that the pROM network provides results that are accurate over the relevant parameter range on a qualitative scale; thus, the ranking of the parameter candidates concerning their objective function values is assumed to be the same in the FOM and pROM network. Then, one can start with that parameter sample which has the lowest

$q_R\left({}^j\boldsymbol{p}_{\text{lopt}}\right)$ and evaluate the error $\varepsilon_{\text{q,rel}}\left({}^j\boldsymbol{p}_{\text{lopt}}\right)$. In the case it is above the user-defined threshold $\varepsilon_{\text{rel}}^{\text{lim}}$, one can discard that parameter candidate and repeat the error evaluation with the next smallest $q_R\left({}^j\boldsymbol{p}_{\text{lopt}}\right)$. The corresponding procedures are illustrated in Figure 8.25.

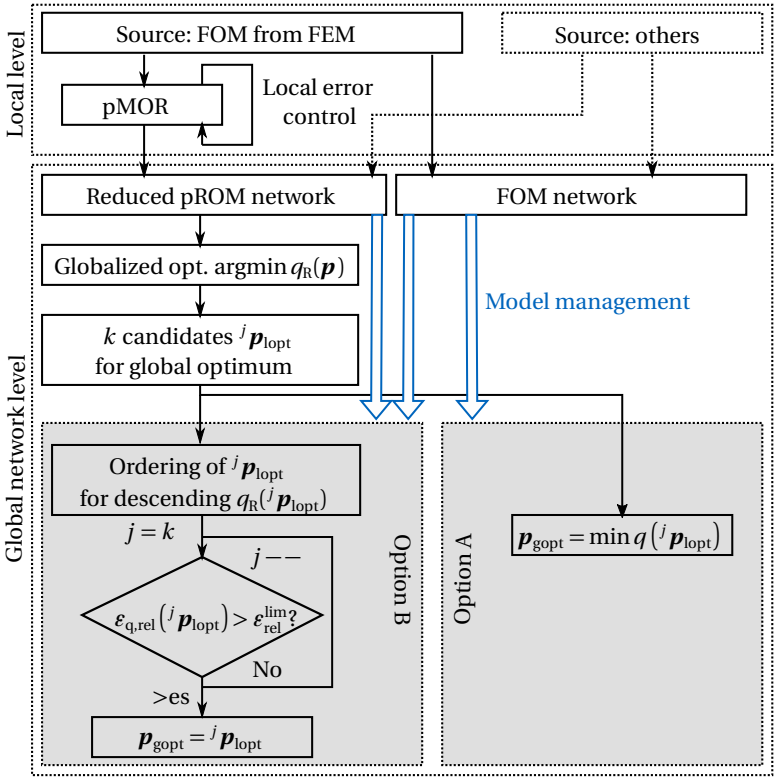

Figure 8.25: Flow diagram for the error control during globalized multi-start optimization on networks of pROMs. Two options are provided, differing in the final selection of the appropriate local minimum.

In summary, such an error control strategy ensures applicability to large-scale industrial models. No intrusive changes to the global

optimization algorithm are needed, but the latter can be used as a black box. Anyhow, there are drawbacks of such a strategy: the path to the true minima of the FOM network may be hidden for the single local gradient-based optimization, as only the obtained minima are error-controlled but not each iteration. Such a scenario cannot be detected during code execution, which augments the heuristic nature of globalized optimization. Gradients can be provided analytically for the affine pROMs, but are not error controlled against the FOM counterparts, neither in the online phase nor in training during the offline phase in the current implementation. As a result, the proposed approach requires pROM subsystems that are sufficiently accurate over the subsystem design parameter spaces. This required accuracy is the motivation to invest computational efforts into the training phase of the pROMs through OGPA.

Setup and Design Parameter Selection

The frequency band of $f_B \in [175\,\text{Hz}, 195\,\text{Hz}]$ is selected, in which the mean power in the interface to the car body should be minimized (see Figure 8.26). The frequency range mainly contains two dominant resonances, resulting in a transmitted energy peak.

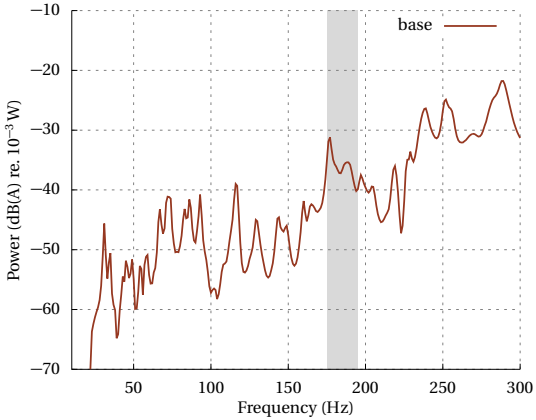

Figure 8.26: Mean power $\overline{P}_r$ in the interface between axle system and car body. The frequency band f_B, in which the power should be minimized is indicated by a gray box.

In total, the mechanical network of Figure 8.23 provides 117 variable design parameters for optimization. One may not change all of these parameters concurrently as neither can optimization algorithms efficiently cope with such high-dimensional parameter space, nor may it be feasible from a process point of view at later vehicle development stages at least. Thus, the most influential design parameters must be identified to maximize the solution space for a minimal set of parameters. In an end-to-end development process, this identification is performed necessarily prior to optimization. Several approaches of global sensitivity analysis methods are available for such identification; a prominent one is the variance-based sensitivity analysis found in Saltelli et al. [218]. As such approaches need to screen the high-dimensional parameter space with sufficient accuracy, they are multi-query applications on their own and potentially require extensive parameter evaluations. Here, the numerical framework of the thesis is the enabler, too.

In order to limit the discussion on optimization itself, another approach is taken in the following, which chooses a more high-level parametrization and is valuable for an early development stage in particular. At this stage, it is assumed that a first design of bushings and the rear axle carrier should be found. For nine control arm bushings (WC-C2 to WC-C5 and RC-Cx), all stiffness parameters vary proportionally per bushing. Thus, each of the bushings has one stiffness parameter, which can be varied between $k_j \in \left[500\,\mathrm{N\,mm^{-1}}, 100000\,\mathrm{N\,mm^{-1}}\right]$. This corresponds to the stiffness value along the longitudinal axis direction of the control arm. The other three stiffness parameters of each bushing are varied proportionally according to the stiffness ratio of the initial bushing geometry. Parameters of WC-C1 are not included in the design parameter space, as the bushing is a ball bearing. For the rear axle carrier, the shell thickness is varied independently in each segment for $t_j \in [1.3\,\mathrm{mm}, 2.3\,\mathrm{mm}]$ and the material density for $\rho_j \in \left[7.8 \cdot 10^{-9}\,\mathrm{t\,mm^{-3}}, 13 \cdot 10^{-9}\,\mathrm{t\,mm^{-3}}\right]$. The latter indicates where an additional mass loading is effective. This parametrization results in a 17D design parameter space linked to parameters in eleven subsystems.

Results

As initially discussed, optimal parameter choice is a non-linear, non-convex problem for strongly coupled systems in the low-frequency

domain. This is also the case for the BMW 3series example with its 17D design parameter space, as visualized in Figure 8.27. The latter provides the power objective at the interface of the car body (Equation (8.3)) for the frequency band f_B as a function of the bushing values in C1-RC and C2-RC. The function is highly non-convex with several local minima.

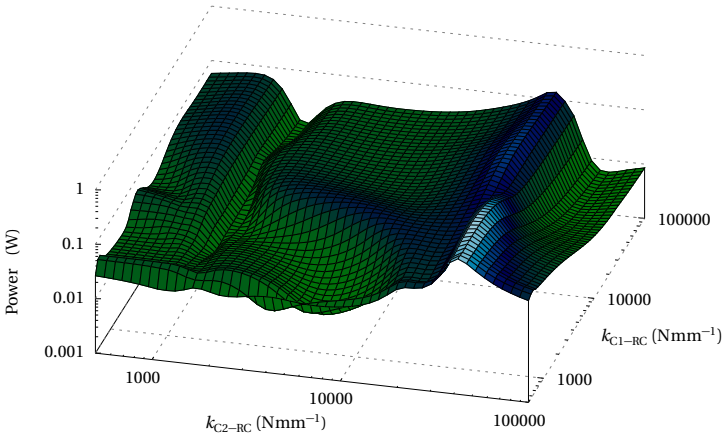

Figure 8.27: The power-based objective in the considered frequency band f_B in dependency of two design parameters k_{C1-RC} and k_{C2-RC} (bushing stiffnesses). The non-convex shape of the objective function highlights the need for globalized optimization.

In correspondence with the highly non-convex, parameter-high-dimensional objective function, a significant amount of objective evaluations are required for globalized optimization. The reduced network of Figure 8.23, anyhow, enables such an optimization approach. It was possible to perform the globalized optimization below on a consumer hardware laptop in less than a day (Intel Core i7-8850H, 32GB DDR4-RAM, Windows 10). Seventy-two local optimizations were performed with 18477 parameter evaluations at 21 frequency points each, which resulted in 388.017 system solutions, times two for the gradient calculation. Out of 72 local optimizations, 14 parameter combinations ${}^{j}\boldsymbol{p}_{\mathrm{lopt}}$ are provided as candidates for the global minimum of the reduced network. Method A is selected for error control according to Figure 8.25 and all parameter combinations ${}^{j}\boldsymbol{p}_{\mathrm{lopt}}$ are evaluated in

the non-reduced FOM network. The resulting power objective values are presented in Figure 8.28, along with the error the objective q_R introduces for these parameter values (Equation (8.17)).

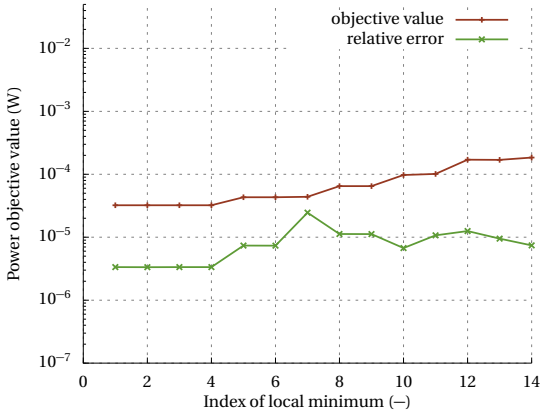

Figure 8.28: The power-based objective function values of Equation (8.3) evaluated in the FOM network for the different parameter candidates for the global minimum, ${}^{j}\boldsymbol{p}_{\mathrm{lopt}}$, as obtained during the globalized optimization of the pROM network. The local minima are sorted for increasing values of the objective value in the reduced network q_R. In addition, the relative errors which were introduced by the latter are provided according to Equation (8.17).

It is evident from Figure 8.28 that low relative errors in the range of 10^{-5} are introduced for all possible minima in the objective when the latter is evaluated in the pROM network instead of the FOM equivalent. Thus, the pROM network has a high fidelity in the analyzed parameter positions. With this in mind, one could follow a more effective strategy for error analysis and use strategy B of Figure 8.25.

Following Figure 8.28, the globalized minimum of the objective from the reduced network $q_R({}^{0}\boldsymbol{p}_{\mathrm{lopt}})$ is selected as final optimization results as the corresponding evaluation in the FOM network is the lowest, too. Note, the first four parameter candidates ${}^{0}\boldsymbol{p}_{\mathrm{lopt}}$ to ${}^{3}\boldsymbol{p}_{\mathrm{lopt}}$ providing a minimum objective value are equal except round-off errors. The resulting mean power in the interface between the rear axle and car body is visualized in Figure 8.29. A significant reduction by two orders of magnitude is achieved for the mean power in the consid-

ered frequency band. This significant improvement is also reflected in the results for the sound pressure levels (SPLs) averaged over all 97 evaluation points, ϱ_{avg}, and an average reduction of $\Delta\varrho_{\mathrm{avg}} = 28\,\mathrm{dB}$ is obtained for the SPLs (compare Figure 8.30). These results highlight the potential of globalized optimization for vehicle networks. Such improvement certainly is only possible in an early development stage when a significant number of parameters can be varied. Anyhow, possibly several of the 17 design parameters could have been omitted in the optimization setup without reducing the solution space, as no global sensitivity analysis for screening was performed prior to the optimization.

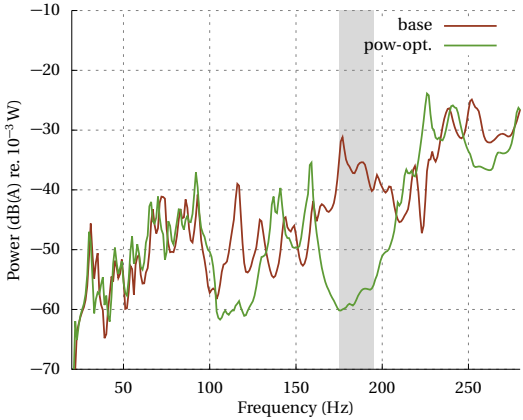

Figure 8.29: The mean power in the interface between the rear axle and the car body before and after globalized optimization utilizing the power-based objective in frequency band $f_{\mathrm{B}} \in [175\,\mathrm{Hz}, 195\,\mathrm{Hz}]$.

The resulting optimal parameter values $\boldsymbol{p}_{\mathrm{gopt}}$ for the globalized minimum of mean power are provided graphically in Figure 8.31. Again, the presence of globally coupled operational deflection shapes in the low-frequency domain leads to the fact that $\boldsymbol{p}_{\mathrm{gopt}}$ is not formed from basic commonplaces like lower bound values for bushing stiffness quantities and upper bounds values for mass loadings or shell thicknesses. Eight of nine bushings tend to be stiffer after optimization. For one bushing, the upper bound value is obtained. Only for three of the four thickness parameters of the rear axle carrier, the upper

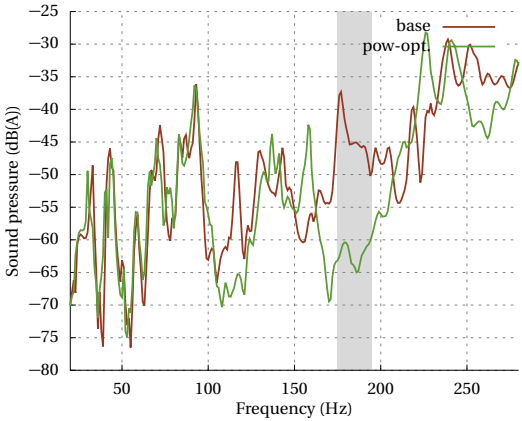

Figure 8.30: The mean sound pressure level, spatially averaged over 97 evaluation points in the car body cavity before and after globalized optimization utilizing the power-based objective in frequency band $f_B \in [175\,\text{Hz}, 195\,\text{Hz}]$.

bound value is chosen to stiffen the problem, but not for the fourth. Without any mass constraints provided, the upper bound for additional mass loading is obtained only for two sections of the rear axle carrier. In summary, using a numeric optimization approach based on a global search enlarges the solution space for optimal parameter combinations and provides new possibilities for structural design in vibroacoustics, which one may not have anticipated.

8.2.4 Performance of Power as Optimization Objective - continued

For the 2D example above, the power-based objective was advantageous for an optimization-based SPL reduction compared to other objectives in the interface between the active and passive sides of the network. This discussion is revisited for the BMW 3series example, and globalized optimization of the rear axle is repeated for the mean SPL as the direct objective function, as provided by Equation (8.7) for the $n_p = 97$ evaluation points in the fluid. Furthermore, additional runs of globalized optimization are performed for the objectives of

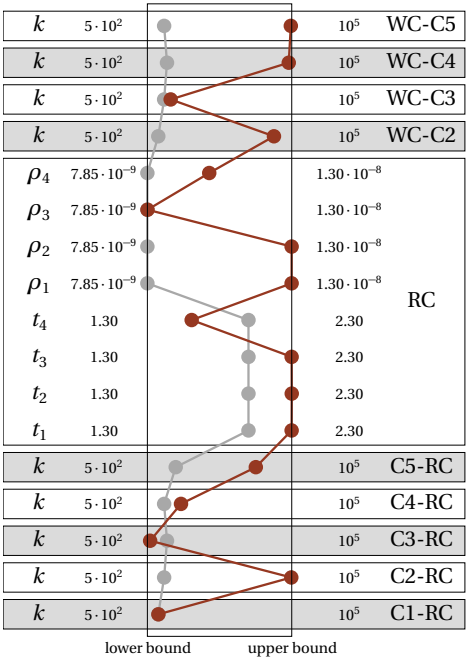

Figure 8.31: The obtained parameter combination $\boldsymbol{p}_{\text{gopt}}$ for the minimization of mean power in the frequency band $f_{\text{B}} \in [175\,\text{Hz}, 195\,\text{Hz}]$ for the BMW 3series, indicated by the red line. The initial parameter values are provided by the gray line in addition, as well as the lower and upper bound values. k indicates a stiffness, ρ a mass density, and t a shell thickness parameter.

Equation (8.11) and Equation (8.12), which solely rely on squared sums of either input or output amplitudes at the interface. Figure 8.32 and Figure 8.33 provide the corresponding results. They show that power-based and directly SPL-based optimization provide a similar SPL reduction, proofing mean power in the interface between the car body and the axle system as a valuable optimization criterion.

Anyhow, it is evident from the same figures that also the objectives solely relying on squared sums of either inputs or outputs provide similar SPL reductions in the vehicle example. This result is contrary to

the one of the 2D radiation example, in which a power-based objective introduced a significant gain in the optimization results. Reasons for the different behavior are discussed in the following; now based on interface data only, as this is the available data for general hybrid mechanical networks.

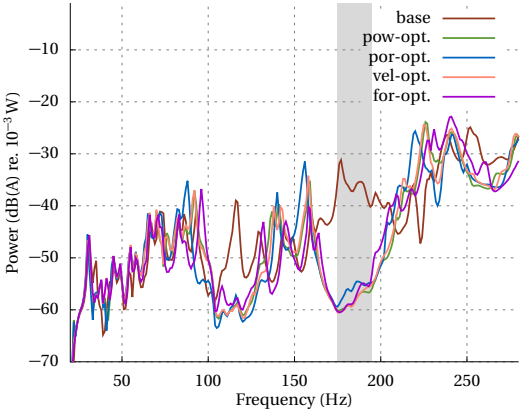

Figure 8.32: The mean power in the interface between the rear axle and the car body before and after globalized optimization in frequency band $f_B \in [175\,\text{Hz}, 195\,\text{Hz}]$ for the power-, velocity-, sound pressure-, and force-based optimization.

To anticipate, one can find the reasons for this behavior in the fact that the interface points of the BMW 3series car body are stiff at which the axle is mounted. Such stiff interface points are not a random result for vehicle systems but the consequence of a fundamental vehicle design paradigm. Following the latter, one aims to ensure an impedance mismatch between the car body and the bushing elements to which the rear axle is mounted. The impedance mismatch implies that the interface points of the car body need to be stiff without significant resonant effects present.

Two major deficiencies of squared amplitude-based objectives were discussed above for the 2D radiation example, differentiating a power-based objective from these proxies. Firstly, the latter objectives cannot include rotational DOFs, which thus need to be unobserved. This issue, however, is not relevant in the numerical vehicle example.

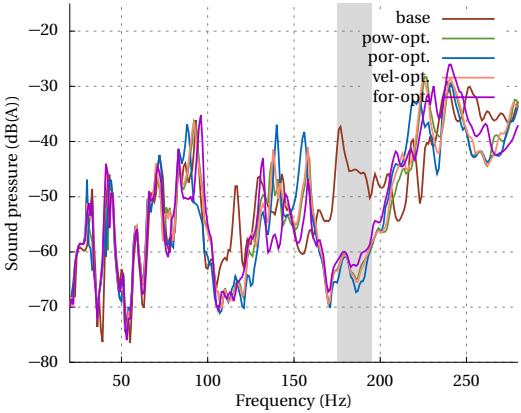

Figure 8.33: The spatially mean sound pressure levels before and after globalized optimization in frequency band $f_B \in [175\,\text{Hz}, 195\,\text{Hz}]$ for the power-, velocity-, sound pressure-, and force-based optimization.

Only 4% of the power-based objective value, thus the band-integrated mean power, result from moment contributions for the nominal parameter setting. This minor contribution is due to minimal angular velocities at the stiff interface points.

Secondly, the lack of phase information was highlighted for squared amplitude-based objectives. Except simply running the optimization, it is challenging to assess the significance of phase information for optimization, as the phase relations would need to be evaluated over the whole design parameter range of the coupled problem. However, there is an approach to provide first indications without running the optimization itself, given that the passive side, the receiver, is not changed during optimization. This setup of an unchanged receiver is followed for the thesis examples. In such a setup, one can identify reasons for the different objectives' performance in the receiver's transfer function properties based on a procedure as follows and without assessing the whole possible parameter space. Therefore, the relationship between the power-based and the velocity-output-based objective is exemplified; a corresponding discussion is possible for the force-input-based objective. Assume the velocities as $\boldsymbol{Y}_v = i\omega \boldsymbol{Y}_r$ and the transfer function relating force inputs and velocity outputs

$\boldsymbol{H}_{\mathrm{v}} = i\omega \boldsymbol{H}_r$, while the subscript $\square_r$ again is referring to the radiating subsystem. For the first, assume that there is no output and input of the receiver, which is related to rotational DOFs. Then the ratio of the power-based and velocity-based objective is expressed as

$$\Delta = \frac{\Re\left(\boldsymbol{Y}_{\mathrm{v}}^H \boldsymbol{H}_{\mathrm{v}}^{-1} \boldsymbol{Y}_{\mathrm{v}}\right)}{2\boldsymbol{Y}_{\mathrm{v}}^H \boldsymbol{Y}_{\mathrm{v}}} = \frac{\boldsymbol{Y}_{\mathrm{v}}^H \Re\left(\boldsymbol{H}_{\mathrm{v}}^{-1}\right) \boldsymbol{Y}_{\mathrm{v}}}{2\boldsymbol{Y}_{\mathrm{v}}^H \boldsymbol{Y}_{\mathrm{v}}}. \tag{8.18}$$

The analysis of the theoretical range of a system's ratio Δ indicates the relative performance of the two objectives. If the ratio changes only slightly during the parameter optimization, the performance is similar for the mean power objective and the sum of squared velocities. As a result, it is examined how large the potential span of Δ is in what follows.

An upper and lower bound for Δ can be calculated from the eigenvalue decomposition of the matrix $\boldsymbol{\Pi} = \Re\left(\boldsymbol{H}_{\mathrm{v}}^{-1}\right)$, which is obtained from

$$\left(\boldsymbol{\Pi} - \lambda_j \boldsymbol{I}\right) \boldsymbol{V}_j = 0, \tag{8.19}$$

with $\boldsymbol{V} = \left[\boldsymbol{V}_1 \ldots \boldsymbol{V}_p\right]$ providing the orthonormal eigenvectors and the corresponding eigenvalues $\boldsymbol{\Lambda} = \mathrm{diag}(\lambda_j)$. The eigenvalues do not correspond to resonant frequencies or any other frequency value but are a property of the matrix $\boldsymbol{\Pi}$ at one distinct frequency point. As the eigenvectors are orthonormal, $\boldsymbol{V}\boldsymbol{V}^H = \boldsymbol{I}$ holds and one can describe the energy flow at the radiating subsystem's interface in a modal basis through $\boldsymbol{V}$,

$$\overline{P} = \frac{1}{2}\boldsymbol{Y}_{\mathrm{v}}^H \boldsymbol{\Pi} \boldsymbol{Y}_{\mathrm{v}} = \frac{1}{2}\boldsymbol{Y}_{\mathrm{v}}^H \boldsymbol{V}\boldsymbol{V}^H \boldsymbol{\Pi} \boldsymbol{V}\boldsymbol{V}^H \boldsymbol{Y}_{\mathrm{v}} = \frac{1}{2}\boldsymbol{\Psi}^H \boldsymbol{\Lambda} \boldsymbol{\Psi} = \frac{1}{2}\sum_i |\Psi_i|^2 \lambda_i, \tag{8.20}$$

with

$$\boldsymbol{\Psi} = \boldsymbol{V}^H \boldsymbol{Y}_{\mathrm{v}}. \tag{8.21}$$

Thus, the eigenvectors of $\boldsymbol{V}$ provide the principal orthogonal directions in which energy can be transmitted in a subsystem interface. They are referred to as *power modes* and Equation (8.20) as power modal decomposition as a result.

On an abstract level, this is equal to the concept of power mode decomposition as introduced by Jianxin et al. [132] and used for receiver characterization by several others (Ji et al. [131] and Weisser et al. [271]). The latter use a decomposition of force inputs, not velocity outputs. However, using the abstract input/output concept of the thesis, any output can be considered an input and vice versa if the subsystem is reformulated. When $\boldsymbol{H}_{\mathrm{v}}^{-1}$ is assumed as the subsystem transfer function, the velocities are the subsystem's inputs for the latter, the forces its outputs. So, the concepts are the same if the method of Jianxin et al. [132] is interpreted for generic types of inputs. Anyhow, the notation is kept as above for clarity, and formulas are presented for output quantities.

Equation (8.21) provides the transformed velocity vector in power modal coordinates. As $\boldsymbol{V}^H \boldsymbol{V} = \boldsymbol{I}$ holds, the squared velocity sum in the denominator of Equation (8.18) can be calculated from the transformed components as

$$\boldsymbol{Y}_{\mathrm{v}}^H \boldsymbol{Y}_{\mathrm{v}} = \boldsymbol{\Psi}^H \boldsymbol{\Psi} = \sum_i |\Psi_i|^2. \tag{8.22}$$

As a result, Equation (8.18) can be rewritten as

$$\Delta = \frac{\sum_i |\Psi_i|^2 \lambda_i}{2 \sum_i |\Psi_i|^2} \tag{8.23}$$

and bounds can be finally provided by the minimum and maximum eigenvalue of $\boldsymbol{\Pi}$:

$$\frac{1}{2}\lambda_{\min} \leq \Delta \leq \frac{1}{2}\lambda_{\max}. \tag{8.24}$$

In the case that $\lambda_{\min}$ is in the same order of magnitude as $\lambda_{\max}$, the potential change of the ratio of the mean power and the sum of squared velocities in the radiating subsystem's interface is limited for parameter variations.

If $\boldsymbol{Y}_{\mathrm{v}}^H \boldsymbol{Y}_{\mathrm{v}}$ contains translational and rotational components, the transfer function entries are linked to different dimensions. Although mathematically still valid, the bounds of Equation (8.24) may be hard to interpret. This issue is addressed by Moorhouse [176], who introduced a scaling procedure for mobility matrices resulting in unit diagonal entries and dimensionless interface DOFs. This procedure can be adapted to a scaling of $\boldsymbol{\Pi}$ by $\boldsymbol{S} = \mathrm{diag}(\sqrt{\Pi_{ii}})$,

$$\tilde{\boldsymbol{\Pi}} = \boldsymbol{S}^{-1} \boldsymbol{\Pi} \boldsymbol{S}^{-1}. \tag{8.25}$$

Dimensionless velocities $\tilde{\boldsymbol{Y}}_\mathrm{v} = \boldsymbol{S}\,\boldsymbol{Y}_\mathrm{v}$ are defined correspondingly. A ratio adapted from Equation (8.18) is formulated using these scaled values as

$$\tilde{\Delta} = \frac{\tilde{\boldsymbol{Y}}_\mathrm{v}^H\,\tilde{\boldsymbol{\Pi}}\,\tilde{\boldsymbol{Y}}_\mathrm{v}}{2\,\tilde{\boldsymbol{Y}}_\mathrm{v}^H\,\tilde{\boldsymbol{Y}}_\mathrm{v}}, \tag{8.26}$$

for which lower and upper bounds can be provided again as

$$\frac{1}{2}\tilde{\lambda}_\mathrm{min} \leq \tilde{\Delta} \leq \frac{1}{2}\tilde{\lambda}_\mathrm{max}. \tag{8.27}$$

$\tilde{\lambda}_i$ are the eigenvalues of

$$\left(\tilde{\boldsymbol{\Pi}} - \tilde{\lambda}_i\,\boldsymbol{I}\right)\tilde{\boldsymbol{V}}_i = 0. \tag{8.28}$$

The mean power is calculated from these scaled values as

$$\overline{P} = \frac{1}{2}\,\tilde{\boldsymbol{Y}}_\mathrm{v}^H\,\tilde{\boldsymbol{\Pi}}\,\tilde{\boldsymbol{Y}}_\mathrm{v} = \frac{1}{2}\tilde{\boldsymbol{\Psi}}^H\,\tilde{\boldsymbol{\Lambda}}\tilde{\boldsymbol{\Psi}} = \frac{1}{2}\sum_i |\tilde{\Psi}_i|^2\,\tilde{\lambda}_i. \tag{8.29}$$

Again, Equation (8.27) does not provide bounds for the ratio of the two above-used objectives, mean power with rotational components, and the sum of velocities without. However, another insight is provided into the behavior of the receiver: $|\tilde{Y}_{\mathrm{v},i}|^2 = |Y_{\mathrm{v},i}|^2\,\Pi_{ii}$ is the point-wise power for a velocity input with amplitude $|Y_{\mathrm{v},i}|$ at input i of the receiver. Thus, the denominator of Equation (8.26) provides twice the sum of the point-wise power values; the energy one would transmit to the receiver if no coupling between the single interface DOFs but the same output amplitudes would be present. As a result, Equation (8.26) is a measure of the coupling between the interface quantities and the potential importance of phase relations between the velocity components. Indirectly, this gives insight into the potential gain of the power-based objective of Equation (8.3) as the phase relation is fully considered in this objective compared to the others, which solely use the amplitude information in the interface. In other words, if the ratio of Equation (8.26) changes significantly along the optimization path in the design parameter space, the power-based objective is likely to provide different optimization results than a velocity or force-based objective.

As the above-used optimization objectives do not include a frequency point, but a band f_B, a frequency-band integrated version of the ratio $\tilde{\Delta}$ can be introduced

$$\mathring{\Delta} = \frac{\int_{f_\mathrm{B}} \tilde{\boldsymbol{Y}}_\mathrm{v}^H \tilde{\boldsymbol{\Pi}} \tilde{\boldsymbol{Y}}_\mathrm{v} \mathrm{d}f}{2 \int_{f_\mathrm{B}} \tilde{\boldsymbol{Y}}_\mathrm{v}^H \tilde{\boldsymbol{Y}}_\mathrm{v} \mathrm{d}f}, \tag{8.30}$$

where the nominator contains the power objective, Equation (8.3), in terms of power modes

$$q_\mathrm{P} = \int_{f_\mathrm{B}} \overline{P}_r \mathrm{d}f = \frac{1}{2} \int_{f_\mathrm{B}} \tilde{\boldsymbol{\Psi}}^H \tilde{\boldsymbol{\Lambda}} \tilde{\boldsymbol{\Psi}} \mathrm{d}f \approx \mathcal{Z} \left(\sum_i |{}^n\tilde{\Psi}_i|^2 \, {}^n\tilde{\lambda}_i, \Delta f \right). \tag{8.31}$$

The A-weighting is omitted for brevity.

Equation (8.28) needs to be solved at every sampled frequency point in the frequency band. Although mathematically independent, the underlying mechanical properties of the subsystem change continuously over frequency. Thus, the power modes from the eigenvalue decomposition also change continuously when the frequency is changed, as noted by Weisser et al. [271], and distinct power modes can be tracked over the single frequencies by a MAC procedure.

The frequency band integration adds complexity to the analysis of eigenvalues for examining the potential span of the ratio $\mathring{\Delta}$. An appropriate approach to eigenvalue analysis is developed for this setting in the following, starting from the different mechanisms to minimize q_P during optimization. Therefore, a power-modal point of view is utilized. There is the trivial option, in which the excitation $|{}^n\tilde{\Psi}_i|^2$ of the different power modes is decreased uniformly for all components in the frequency band. This decrease does not lead to a change of $\mathring{\Delta}$ and may not be assessed by an eigenvalue analysis. In lower frequency ranges, the energy is transmitted to the receiver mainly over a couple of different power modes in the frequency band. Thus, there are two other possibilities, which lead to a reduction of $\mathring{\Delta}$:

- vertical shift at a frequency point: choosing other dominant power modes with smaller eigenvalues for the main excitation per frequency point. Thus, the excitation $|{}^n\tilde{\Psi}_i|^2$ of the single power modes, which are tracked over the frequency band, is changed in integral over the frequency band.

- horizontal shift across frequencies: keeping the excitation of a single tracked power mode constant in integral over the frequency band but shifting peaks of the excitation to a frequency point, at which the amplification by the eigenvalues is reduced. Such frequencies correspond to regions of resonances or anti-resonances of the receiver, in which the phase coupling plays a more significant role.

A vertical shift at a distinct frequency point requires two things:

1. a sufficiently large span of the eigenvalues of the receiver, and
2. a significant change of the shape of the (transformed) velocity vector at the considered frequency point during optimization.

A horizontal shift across several different frequencies also has two requirements:

1. a significantly changing function of the eigenvalues over frequency per tracked power mode, and
2. the ability of the optimization setup for the coupled problems to shift modal excitations to such region.

The second prerequisite for both shift types needs to be assessed over the whole relevant design parameter space of the entire coupled problem and cannot be evaluated just from the receiver subsystem data. However, the first prerequisite of both shifts can be examined from the isolated analysis of the eigenvalues of the receiver transfer function matrix. This examination is provided for the examples of this chapter in the following.

For this, the eigenvalues are provided for the car body (TB) of the BMW 3series numerical example, the latter with a similar performance of all objectives in Figure 8.34(a). As a comparison, the same is repeated in Figure 8.34(b) for the receiver of the 2D example, which showed a varying objective performance. Analyzing the properties of the car body in Figure 8.34(a) for the frequency band $f_B \in [175\,\text{Hz}, 195\,\text{Hz}]$, the eigenvalue distribution has a large span between the minimum and maximum value. Thus, the first requirement for a vertical shift is met. Examining the first prerequisite for a horizontal shift, the span of eigenvalues changes only slightly over f_B, as no explicit (anti-) resonant behavior is present. In fact, one can

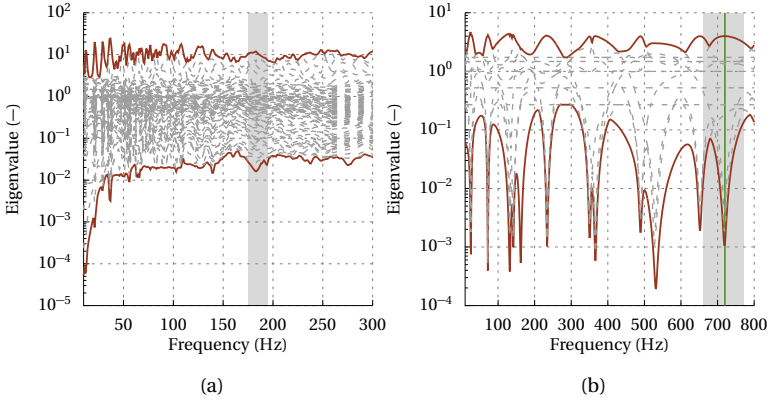

Figure 8.34: The eigenvalues of the transfer function matrix $\boldsymbol{\Pi}$ according to Equation (8.28) for (a) the BMW 3series body, (b) the 2D example's receiver. Equation (8.28) is solved per frequency point, and a MAC procedure reconstructs the continuous functions of eigenvalues. The lowest and highest eigenvalue are highlighted, while the remaining ones are grayed for clarity.

approximate band-integrated power with small relative errors around 1% for the car body as

$$q_\mathrm{P} = \int_{f_\mathrm{B}} \overline{P}_r \mathrm{d}f = \frac{1}{2} \int_{f_\mathrm{B}} \tilde{\boldsymbol{\Psi}}^H \tilde{\boldsymbol{\Lambda}} \tilde{\boldsymbol{\Psi}} \mathrm{d}f \approx \frac{1}{2} \int_{f_\mathrm{B}} \tilde{\boldsymbol{\Psi}}^H \mathrm{d}f \, \overline{\tilde{\boldsymbol{\Lambda}}} \int_{f_\mathrm{B}} \tilde{\boldsymbol{\Psi}} \mathrm{d}f. \tag{8.32}$$

Thus, the possibility of a horizontal shift is disqualified, as shifting the excitation of a tracked power mode to another frequency point inside f_B has no effect on the power objective q_P, thus on $\mathring{\Delta}$. The exclusion of a horizontal shift already indicates why the different objectives lead to a comparable SPL reduction.

The option of a vertical shift can be further assessed for its second requirement when the coupled problem is considered, and the power-modal decomposition is compared before and after the above power-based globalized optimization of the BMW 3series. The approximation of Equation (8.32) is considered, and integral values are evaluated for this. The integral excitation of power modes changes between single modes as visualized by the two graphics on the left of Figure 8.35. Thus, the globalized optimization changes each tracked

power mode's individual contribution to the frequency band's overall power, as shown on the right-hand side of Figure 8.35. Nevertheless, this interchange of modal excitation is limited mainly to neighboring modes, and the clusters of dominantly excited modes remain relatively constant. As the associated eigenvalues do not change in these clusters significantly, the band-integrated ratio $\mathring{\Delta}$ only slightly changes from $\mathring{\Delta} = 0.18$ before optimization to $\mathring{\Delta} = 0.17$ afterward for the BMW 3series example, which leads to an equivalent performance of mean power and other objectives for the vehicle example.

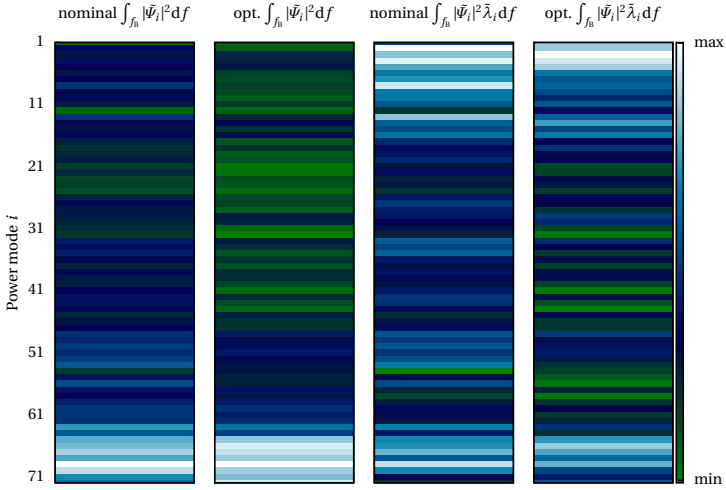

Figure 8.35: The power modal decomposition of the BMW 3series. The values are integrated over the frequency band $f_B \in [175\,\mathrm{Hz}, 195\,\mathrm{Hz}]$ for each power mode; thus, one scalar per mode is obtained. The two left-hand side plots represent the modal excitation before and after optimization, and the right-hand side ones the corresponding modal parts of the overall power. A scaling of the color scheme of each plot is performed for the minimum and maximum values.

In summary, although only complete with a consideration of the coupled problem, the analysis of the receiver eigenvalues in Figure 8.34(a) for the first prerequisite of both shift types already indicated equivalent objective performance. It showed the system's lack of a changing $\mathring{\Delta}$ due to horizontal shifting. The key point here is the non-resonant behavior of the stiff receiver interface, which leads to a limited change of the eigenvalues over frequency.

The limitations from constant eigenvalue functions over f_B are highlighted when the analysis is repeated for the free-field 2D example of Section 8.1. The latter showed large differences in the optimization results for the different objectives in $f_{\mathrm{B}3} \in [660\,\mathrm{Hz}, 770\,\mathrm{Hz}]$, in particular. Starting with the isolated analysis of the receiver, the comparison of Figure 8.34(b) with Figure 8.34(a) shows that the overall spread of eigenvalues is similar to the car body on average. However, the change of eigenvalues over frequency is more significant, leading to a maximum eigenvalue spread at $f = 720\,\mathrm{Hz}$. The latter is an anti-resonance of the receiver, at which several diagonal entries of the transfer function show a local maximum. Consequently, the first prerequisite for horizontal shifts is met, and the latter can lead to a significant change of $\mathring{\Delta}$.

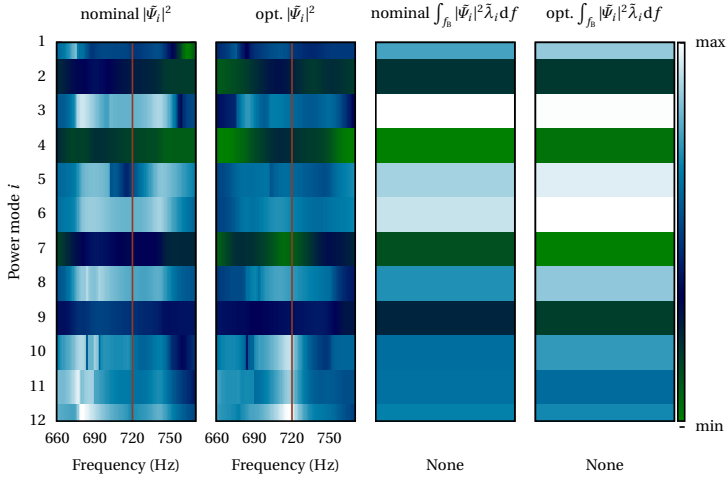

Figure 8.36: The power-modal decomposition of the free field 2D radiation example. The optimization results for power-based optimization in the frequency band $f_{\mathrm{B}3} \in [660\,\mathrm{Hz}, 770\,\mathrm{Hz}]$ are recapped. The two left-hand side plots represent the modal excitation over frequency before and after optimization, and the right-hand side ones the corresponding modal parts of the overall power integrated over frequency. The position of the anti-resonance at $f = 720\,\mathrm{Hz}$ is marked by a vertical line. A scaling of the color scheme of each plot is performed for the minimum and maximum values.

Taking the coupled problem of the 2D example into account, the modal excitation is indeed shifted horizontally to the receiver's anti-

resonance at $f = 720\,\mathrm{Hz}$ during optimization, especially for the power modes with lower eigenvalues. This shift is visualized on the left-hand side of Figure 8.36. In contrast to the vehicle example, the shift leads to a significant change of the band-integrated ratio $\mathring{\Delta}$ from $\mathring{\Delta} = 0.70$ before power-based global optimization to $\mathring{\Delta} = 0.14$ afterward. Although the frequency-band-integrated power in the interface is decreased from $5.1 \cdot 10^{-4}$ to $1.2 \cdot 10^{-4}$, the large change of the ratio $\tilde{\Delta}$ results in an increase of the denominator of the latter, the point-wise summed up powers from $7.4 \cdot 10^{-4}$ to $8.0 \cdot 10^{-4}$. Minimizing the overall power leads to the opposite effect in the point-wise powers, highlighting the changing importance of cross-coupling terms and, thus, phase information before and after optimization for the 2D example.

8.3 Chapter Summary

The potentials arising from the numerical framework and the use of energetic quantities were highlighted for the online phase. Therefore, the example of a globalized optimization for a band-limited, low-frequency sound pressure level (SPL) reduction was chosen, which forms an integral part of a virtual end-to-end development process. Based on a two-dimensional example, it was discussed how numerical optimization benefits from the modular approach of MRC. A power-based objective was utilized, which measures the frequency-band integrated energy flow into the passive network side, the receiver. The need for globalized optimization was stressed to maximize solution spaces, arising from the high non-convexity of the power objective function. A multi-start framework for globalized optimization employing the power-based objective provided a robust reduction of SPLs in each of the three chosen frequency bands, which was comparable to a direct optimization of SPLs. More significant SPL reductions were obtained compared to local optimization approaches or alternative objectives in the receiver's interface, which solely rely on amplitude information. The latter difference was mainly explained by the fact that power combines all available local information in the interface and provides a global view of the receiver's energy.

A BMW 3series assembly of a trimmed body and a five-arm rear axle was provided as an industrial example. Different types of subsystems were coupled by the MRC framework, which was combined with pMOR employing OGPA. The latter is necessary, as many FOM

subsystems are computationally too expensive for repetitive parameter evaluations during optimization. The effectiveness of OGPA was discussed in detail for two subsystems. On average, the size of subsystems was reduced by two orders of magnitude in the BMW 3series assembly, while several dozens of parameters were still available for optimization. For the latter, the introduction of pMOR required the development of a multi-fidelity model management strategy for error control. Two variants were provided for a strict separation between the offline and online phases. Again, globalized optimization was performed by a multi-start framework using the power-based objective for one frequency band, which resulted in an SPL reduction of several orders of magnitude for a 17D design parameter space. It turned out that the power objective in the interface of the receiver does not provide more significant SPL reductions than amplitude-based objectives for the vehicle example. An eigenvalue analysis approach based on a power mode decomposition was introduced for an explanation. It was shown that the stiff design of the car body - the receiver - interface limits the possible eigenvalue shifts in the power-modal space. Solely such a shift would change the ratio of power and amplitude-based objectives, thus resulting in different optimization results.

CHAPTER 9

SUMMARY AND OUTLOOK

An end-to-end virtual development process for vehicle vibroacoustics requires the application of many multi-query methods for robustness. Such methods imply thousands to millions of different parameter evaluations, which is impossible with state-of-the-art FE modeling. Therefore, a highly performative numerical framework was introduced for the frequency-domain analysis of structure-borne sound problems. The focus was on linear systems with separable modal behavior. The framework relies on distributed calculations employing subsystem coupling and parametric model order reduction for a significant reduction of subsystem size. The subsystem coupling was performed based on the MRC framework introduced in the thesis. MRC formulates the coupling problem based on residual equations for generic subsystem inputs and outputs on the level of algebraic equations. It is thus truly modular with a minimum set of requirements for the subsystems. Standard methods like Frequency Based Substructuring were shown to be subcases. Furthermore, MRC allows for hybridization to increase robustness; single subsystems with unknown modeling can be replaced by experimentally determined ones. Parametric model order reduction was introduced to reduce the subsystem size by orders of magnitude while preserving several parameters for later varia-

tion. A projection matrix was constructed based on Krylov subspaces, which are appealing for use in subsystem coupling applications as a Taylor-series-expansion-like moment matching of transfer functions is implicitly obtained. The method was formulated for subsystems with structural damping. An automated training was introduced to ensure the pROM model quality for the whole considered parameter space. A grid-free approach using local optimizations was chosen, which enables the reduction of complex industrial FE subsystems.

The potential of the numerical framework for multi-query methods was finally demonstrated on a globalized optimization of both an academic and an industrial vehicle example for structure-borne sound transmission. A corresponding algorithm that requires hundreds of thousands of parameter evaluations could be run on a consumer hardware laptop using the numerical framework within one day.

The robustness of a virtual development process is also increased by a proper postprocessing quantity, which is used as a more integral proxy for sound pressure levels. In the thesis, mean power was used, which was evaluated at the radiating subsystem's inputs. Therefore, one emphasis was on correct power evaluation throughout the numerical method development. Measurement-based methods were discussed for validation and as a first step for hybridization. It was worked out that phase accuracy plays a significant role, especially for the power-based analysis of lightly damped subsystems. It was shown heuristically for numerical optimization that a power-based objective can provide a benefit against alternative objectives, especially for academic examples. Anyhow, more simplified engineering measures may be used for many vehicle applications providing comparable performance. This comparable performance was explained using a power mode decomposition, showing the limited solution space for receiving structures without distinct modal behavior observable at its inputs.

In summary, the following novelties were introduced per chapter to enable an end-to-end virtual development process for vehicle vibroacoustics:
Chapter 2 (basics):

- extended passivity requirements for systems with structural damping and, thus, complex-valued system matrices.

Chapter 3 (subsystem coupling):

- newly formulated framework of MRC for the efficient coupling of linear systems with a maximum of flexibility.
- new approach for the systematic inclusion of pure Neumann subsystems.
- integration of common substructuring methods into the new formulation of MRC.

Chapter 4 (gradient calculation):

- modular approach to calculating gradients in subsystem coupling applications by means of MRC.

Chapter 5 (non-parametric model order reduction):

- consequent reformulation and discussion of Krylov-based model order reduction for structural damping. An extended proof for the use of one-stage Krylov subspaces was presented.
- adaptions of the Arnoldi algorithm for industrial applications with respect to efficient deflation and orthogonalization concepts.
- first rigorous application of existing deflation concept to large-scale industrial models.

Chapter 6 (parametric model order reduction)

- provision of an efficient reduced-order model training strategy extending grid-free approaches to frequency-domain analyses of industrial models.
- introduction of a goal-oriented and cheap error estimate for subsystem coupling applications.
- extension of an a-posteriori error evaluation concept based on Bayes theorem for the new context of model order reduction.

Chapter 7 (experimental methods):

- systematic discussion of necessity for phase-correct measurements in the context of energetic quantities.

- introduction of the phase correction concept for phase-correct measurements.
- provision of a benchmark system.

Chapter 8 (application):

- application of the new reduced-order model training strategy to industrial models.
- globalized optimization of a complete vehicle example on a consumer-hardware laptop.
- extensive discussion of the performance of a power-based optimization objective against others. The power mode decomposition was generalized for this.

The presented work motivates further research in virtual end-to-end low-frequency vibroacoustic vehicle development with an evaluation of energies. The numerical methods of the thesis could be further improved. For example, the training of parametric reduced models could be combined with parameter-local approaches, in which the subsystem parameter space would be split, and different pROMs would be trained for each region. A look-up table would manage the latter. Such an approach would enable pMOR for even higher subsystem parameter space dimensions. Global optimization of vibroacoustic systems could be further enabled for practical applications. This enabling would include the enrichment by the necessary step, in which the optimization results are transferred back into hardware. Different optimization algorithms could be benchmarked, like evolutionary ones. The numerical framework enables the application of many other elements of a virtual end-to-end development process involving multi-query approaches, which were not discussed yet by the thesis. Global sensitivity analysis to identify relevant parameter sets is a predecessor for numerical optimization and uncertainty quantification. Inverse parameter identification approaches may be used to validate and update numerical models against their corresponding hardware realization. Such methods are again boosted by the presented work, thus providing completely new possibilities in low-frequency industrial structure-borne sound problems.

Appendices

APPLIED OPTIMIZATION ALGORITHMS

An overview of the concepts and algorithms of constrained non-linear optimization is provided, which are utilized throughout the thesis. The following assumes deterministic problems with a continuous and bound parameter domain and continuously differentiable constraint and objective functions. The latter are considered to be scalar without loss of generality.

A.1 Local Gradient-Based Optimization Through SQP

Sequential Quadratic Programming (SQP) is a class of algorithms that share the same basic concept for constrained optimization of non-linear convex problems. This concept is illustrated in the following, while a line search method is described in an inequality formulation. Refer to Nocedal et al. [183] for both more detailed substeps and a more comprehensive overview.

Given the following non-linear optimization problem

$$\begin{aligned} &\min_{p_i \in \mathbb{R}} q\left(\boldsymbol{p}\right) \\ &\text{subject to} \quad \begin{cases} \boldsymbol{c}_{\mathrm{i}}\left(\boldsymbol{p}\right) \geq 0 \\ \boldsymbol{c}_{\mathrm{e}}\left(\boldsymbol{p}\right) = 0, \end{cases} \end{aligned} \tag{A.1}$$

one may define a corresponding Lagrange Function

$$L\left(\boldsymbol{p}, \tilde{\boldsymbol{\lambda}}\right) = q(\boldsymbol{p}) - \tilde{\boldsymbol{\lambda}} \begin{bmatrix} \boldsymbol{c}_{\mathrm{e}}\left(\boldsymbol{p}\right) \\ \boldsymbol{c}_{\mathrm{i}}\left(\boldsymbol{p}\right) \end{bmatrix} = q(\boldsymbol{p}) - \boldsymbol{\lambda} \boldsymbol{c}_{\mathrm{ei}}\left(\boldsymbol{p}\right), \tag{A.2}$$

where $\tilde{\boldsymbol{\lambda}}$ is the vector of Lagrange multipliers. The Karush-Kuhn-Tucker (KKT) conditions state the first-order necessary conditions, which are that a point $(\boldsymbol{p}_{\mathrm{opt}}, \tilde{\boldsymbol{\lambda}}_{\mathrm{opt}})$ minimizing $q(\boldsymbol{p})$ and fulfilling the constraints satisfies

$$\frac{\mathrm{d}L\left(\boldsymbol{p}_{\mathrm{opt}}, \tilde{\boldsymbol{\lambda}}_{\mathrm{opt}}\right)}{\mathrm{d}\boldsymbol{p}} = 0 \tag{A.3}$$

$$c_{\mathrm{e},j}\left(\boldsymbol{p}_{\mathrm{opt}}\right) = 0 \tag{A.4}$$

$$c_{\mathrm{i},j}\left(\boldsymbol{p}_{\mathrm{opt}}\right) \leq 0 \tag{A.5}$$

$$\tilde{\lambda}_j \geq 0 \tag{A.6}$$

$$\tilde{\lambda}_j \, c_{\mathrm{ei},j}\left(\boldsymbol{p}_{\mathrm{opt}}\right) = 0. \tag{A.7}$$

Equation (A.7) states that either the constraint $c_{\mathrm{ei},j}$ is zero or it's corresponding Lagrange multiplier, respectively both. As a consequence, one may rewrite the KKT condition of Equation (A.3) as

$$\begin{bmatrix} \frac{\mathrm{d}L\left(\boldsymbol{p}_{\mathrm{opt}}, \boldsymbol{\lambda}_{\mathrm{opt}}\right)}{\mathrm{d}\boldsymbol{p}} \\ \boldsymbol{g}(\boldsymbol{p}_{\mathrm{opt}}) \end{bmatrix} = \begin{bmatrix} \frac{\mathrm{d}q\left(\boldsymbol{p}_{\mathrm{opt}}\right)}{\mathrm{d}\boldsymbol{p}} - \boldsymbol{\lambda} \frac{\mathrm{d}\boldsymbol{g}(\boldsymbol{p}_{\mathrm{opt}})}{\mathrm{d}\boldsymbol{p}} \\ \boldsymbol{g}(\boldsymbol{p}_{\mathrm{opt}}) \end{bmatrix} = 0. \tag{A.8}$$

$\boldsymbol{g}(\boldsymbol{p})$ is the active set, including all equality constraints $\boldsymbol{c}_{\mathrm{e}}\left(\boldsymbol{p}\right)$ as well as the subset of inequality constrains $\boldsymbol{c}_{\mathrm{i}}\left(\boldsymbol{p}\right)$ which are active. Inequality constraints are active if they take the form of an equality constraint at the considered parameter point $\boldsymbol{p}$, thus are zero.

Given the case the active set would be known, a Newton iteration may be performed for convex problems to find an appropriate direction $\boldsymbol{d}$ for a given $\boldsymbol{p}$ to obtain $\boldsymbol{p}_{\mathrm{opt}}$ iteratively. If the active set would

remain constant for the parameter range of one Newton iteration, one may have fast convergence. An alternative approach to solve Equation (A.8) for $\boldsymbol{p}_{\text{opt}}$ is discussed in the following, which provides the Lagrange multipliers simultaneously. Using Newton's iteration on the KKT first-order optimality conditions is equal to solving the quadratic subproblem with linearized constraints in order to determine the step direction $\boldsymbol{d}$,

$$\begin{aligned} &\min_{d_i \in \mathbb{R}} q\left(\boldsymbol{p}\right) + \boldsymbol{d}^T \frac{\mathrm{d}q\left(\boldsymbol{p}\right)}{\mathrm{d}\boldsymbol{p}} + \frac{1}{2}\boldsymbol{d}^T \frac{\mathrm{d}^2 L\left(\boldsymbol{p},\boldsymbol{\lambda}\right)}{\mathrm{d}\boldsymbol{p}^2}\boldsymbol{d} \\ &\text{subject to} \qquad \frac{\mathrm{d}\boldsymbol{g}\left(\boldsymbol{p}\right)}{\mathrm{d}\boldsymbol{p}}\boldsymbol{d} + \boldsymbol{g}\left(\boldsymbol{p}\right) = 0. \end{aligned} \tag{A.9}$$

The active set is not known in advance; thus, the solution of Equation (A.9) needs to be determined iteratively in a nested iteration loop per main iteration of the solution of the actual problem in Equation (A.1). A line search approach can be utilized to solve the quadratic subproblem iteratively. One may again formulate a Lagrange function and use the KKT condition of Equation (A.3) for determining the step direction and Lagrange multipliers per nested iteration from a system of equations corresponding to the one of Equation (A.8). The latter may be solved directly using a null space method, conjugate-gradient approach, or similar; refer to Nocedal et al. [183] for an overview. The step length of a nested iteration is equal to one if there is no additional blocking constraint. The latter is an inequality constraint not contained in the active set $\boldsymbol{g}\left(\boldsymbol{p}\right)$ during one iteration to solve Equation (A.9) but limiting the allowed step size to a value smaller than one. In that case, the active set in the next nested iteration is enlarged by the corresponding blocking constraints. Thus, the iterative solution of the quadratic optimization problem, Equation (A.9), provides updates for the active set. Correspondingly, constraints may also be removed from the active set for a step direction of zero length in one nested iteration. In this case, the inequality constraint with the most negative Lagrange multiplier is removed from the active set as it violates the KKT condition of Equation (A.6).

Suppose there is no negative Lagrange multiplier for a zero step direction length. In that case, all KKT conditions are fulfilled for the quadratic subproblem, and the nested loop has identified its minimum, thus determined the step direction $\boldsymbol{d}$ for the main iteration. Then, one may determine a feasible step length for the main iteration,

ensuring a sufficiently smaller merit function value. Different choices are available for merit functions, like penalty functions combining the objective function value and some weighted sum of constraint violation measures. An example is found in Powell [203].

Formulating the quadratic subproblem for a Newton iteration approach to Equation (A.1), the Hessian matrix $\mathrm{d}^2 L / \mathrm{d}\boldsymbol{p}^2$ needs to be calculated explicitly, which may be expensive. Thus, one may replace the true Hessian by an estimate $\boldsymbol{N}$ in Equation (A.9), resulting in a quasi-Newton method. Such an estimate is based on the approximation of the change of the Hessian matrix during two subsequent iteration steps

$$\frac{\mathrm{d}^2 q\left({}^{j+1}\boldsymbol{p} - {}^{j}\boldsymbol{p}\right)}{\mathrm{d}\boldsymbol{p}^2} \approx \frac{\mathrm{d}q\left({}^{j+1}\boldsymbol{p}\right)}{\mathrm{d}\boldsymbol{p}} - \frac{\mathrm{d}q\left({}^{j}\boldsymbol{p}\right)}{\mathrm{d}\boldsymbol{p}} = {}^{j}\boldsymbol{y}, \tag{A.10}$$

which is valid for a region near $\boldsymbol{p}_{\mathrm{opt}}$ in which the Hessian is positive definite. As a result, the estimate $\boldsymbol{N}$ is chosen to fulfill the corresponding secant equation

$${}^{j+1}\boldsymbol{N} \cdot {}^{j}\boldsymbol{s} = {}^{j}\boldsymbol{y}, \tag{A.11}$$

where ${}^{j}\boldsymbol{s} = {}^{j+1}\boldsymbol{p} - {}^{j}\boldsymbol{p}$ is the j^{th} step. Utilizing the secant information with the additional conditions of symmetry and low-rank differences between the estimate in successive iteration steps, one can derive the Broyden-Fletcher-Goldfarb-Shanno (BFGS) formula

$${}^{j+1}\boldsymbol{N} = {}^{j}\boldsymbol{N} - \frac{{}^{j}\boldsymbol{N} \cdot {}^{j}\boldsymbol{s} \cdot {}^{j}\boldsymbol{s}^T \cdot {}^{j}\boldsymbol{N}}{{}^{j}\boldsymbol{s}^T \cdot {}^{j}\boldsymbol{N} \cdot {}^{j}\boldsymbol{s}} + \frac{{}^{j}\boldsymbol{y}\,{}^{j}\boldsymbol{y}^T}{{}^{j}\boldsymbol{y}^T\,{}^{j}\boldsymbol{s}}. \tag{A.12}$$

Refer to Nocedal et al. [183] for the explicit derivation.

Multiple distinct SQP algorithms exist, differing in the merit function used, additional step acceptance criteria, or the Hessian matrix approximation. Practical algorithms include correction mechanisms for the latter, which ensure the Hessian estimate to be positive definite, which is a requirement for the above derivations. Again, different approaches exist for this correction. Furthermore, algorithms may split the re-calculation of the active set from the solution of the quadratic subproblem, or the above line search approach may be replaced by a trust-region method. Throughout the thesis, the SQP implementation of MATLAB R2018b is used. This implementation uses a line search strategy as described above, a BFGS strategy for the approximation

of the Hessian according to Powell [203, 204]. The merit function in the main iteration loop is similar to the ones used by Han [116] and Powell [203, 204].

A.2 Globalized Optimization Using a Multi-Start Method

Gradient-based algorithms like SQP assume convex problems for determining the objective's minimum. Therefore, such an approach may not find the global objective's minimum for non-convex problems but identify a local one solely. Another method has to be determined for such problem classes, and one may choose a heuristic approach incorporating a random search as a compromise between computational feasibility and the probability of identifying the actual global minimum. An overview of appropriate random search approaches is found in Zabinsky [280].

Two-phase methods are a subclass of random search approaches, incorporating a global and a local phase. Again, different methods may be used for the phases. In the following, the essential motivation is to combine the advantages of heuristic global search approaches with the ones of local gradient-based optimization; thus, it is a natural extension of the above-described SQP algorithm for local optimization. The global search provides potential starting points ${}^{j}\boldsymbol{p}_0$ for the single local optimizations in such a two-phase method, leading to a multi-start scheme. The particular method, which is employed, is based on the Multistart Framework for Global Optimization by Ugray et al. [249].

The framework utilizes the idea of scatter search to generate trial points in the first phase of global screening. Scatter search is a general algorithmic framework, which can be defined according to Glover [99] and allows for a heuristic search on a problem domain. It is a population-based method, therefore linked with evolutionary programming as it utilizes an existing population, which is a set of n_{trial} trial points, to generate the next set iteratively. The first starting population is generated for an overall starting point $\boldsymbol{p}_0$, the parameter bounds, their center point, and a diversification approach. The latter is a greedy approach, and that point from a random set is chosen which is most distant from its nearest neighbor per iteration. Scatter search then uses a geometric approach to combine pairs of points

of the existing population to new candidates within the parameter bounds in the main iteration loop until a stopping criterion is met. Therefore, hyper-rectangles are defined along the line in the parameter space given by the considered point pair. Random sample points are placed in these rectangle domains afterward. The distinct method used for generating the trial points in the following is described in Ugray et al. [249].

Once the trial points ${}^{j}\boldsymbol{p}_0$ are found, the method of Ugray et al. [249] starts local gradient-based optimizations in the second phase, which is the local one. One may choose a simple multi-start approach in this phase, thus running local optimization for all trial points determined in the global phase. However, such an approach would be inefficient. One may approach the same local minimum from many trial points, resulting in an unnecessarily large amount of computationally expensive local optimizations. Ugray et al. [249] introduced a filtering approach as a remedy incorporating two filters in the local phase. The first is the distance filter, and the gradient-based optimization is started for a trial point ${}^{j}\boldsymbol{p}_0$ solely if

$$\left\| {}^{j}\boldsymbol{p}_0 - {}^{k}\boldsymbol{p}_{\text{lopt}} \right\|_2 > \tau_{\text{dist}} \cdot r_k \tag{A.13}$$

holds for all k local minima ${}^{k}\boldsymbol{p}_{\text{lopt}}$ which were already identified previously during the run. τ_{dist} is a user-defined distance threshold factor. r_k is the radius of the basin of attraction for the k^{th} local minimum. Thus, the idea is that spherical basins of attraction exist around the local minima, in which any starting point is likely to result in an optimization result of the corresponding local minimum.

The second filter is the merit filter, defining another condition for the start of a local optimization at ${}^{j}\boldsymbol{p}_0$,

$$u\left({}^{j}\boldsymbol{p}_0, \boldsymbol{w}\right) < u_{\text{lim}}. \tag{A.14}$$

u_{lim} is the local solver threshold, which is dynamically determined by the algorithm. $u(\boldsymbol{p}, \boldsymbol{w})$ is the score function, which is chosen as the penalty function for the violation of the optimization problem's non-linear constraints

$$u(\boldsymbol{p}, \boldsymbol{w}) = q(\boldsymbol{p}) + \boldsymbol{w}^T \text{viol}\left(\boldsymbol{c}(\boldsymbol{p})\right). \tag{A.15}$$

$\mathrm{viol}\big(\boldsymbol{c}(\boldsymbol{p})\big)$ is the vector of magnitudes of violation for the constraints of the problem definition in Equation (A.1). $\boldsymbol{w}$ are non-negative penalty weights and are determined by

$$w_j > |\lambda_{\mathrm{opt},j}|, \tag{A.16}$$

where λ_{opt} is the vector of Lagrange multipliers in Equation (A.2) for a local minimum of the objective. This vector is directly obtained from the algorithm performing a local optimization as described in Appendix A.1, and $\boldsymbol{w}$ is updated after each identification of a local minimum if necessary. Initially, a starting value can be assumed for the penalty weights, 1000, for example.

If both filter conditions are met, a local gradient-based optimization is performed for ${}^{j}\boldsymbol{p}_0$. In the case this optimization step successfully provides ${}^{j}\boldsymbol{p}_{\mathrm{lopt}}$, it is checked if ${}^{j}\boldsymbol{p}_{\mathrm{lopt}}$ was already detected and registered previously for another trial point. This check is performed numerically, evaluating if the differences $\left\|{}^{j}\boldsymbol{p}_{\mathrm{lopt}} - {}^{k}\boldsymbol{p}_{\mathrm{lopt}}\right\|_2 < \tau_{\mathrm{p}}\max\big(1, {}^{\mathrm{j}}\boldsymbol{p}_{\mathrm{lopt}}\big)$ and $|{}^{j}q_{\mathrm{lopt}} - {}^{k}q_{\mathrm{lopt}}| < \tau_{\mathrm{q}}\max\big(1, {}^{j}q_{\mathrm{lopt}}\big)$ are smaller than user-defined threshold values τ_{p}, respectively τ_{q}, for all k already available local minima. If not, ${}^{j}\boldsymbol{p}_{\mathrm{lopt}}$ is registered as an additional local minimum in the overall run of the optimization software.

In any case of a successful run of the local optimization, u_{lim} is replaced by the score $u\big({}^{j}\boldsymbol{p}_0, \boldsymbol{w}\big)$, and the radius r_k of the basin of attraction is updated to the maximum of the current value, if existing, and the distance $\left\|{}^{j}\boldsymbol{p}_0 - {}^{j}\boldsymbol{p}_{\mathrm{lopt}}\right\|_2$.

Counters are introduced to monitor the case of subsequent trial points, for which one of the filter conditions is not met; thus, no local optimization is performed. One counter counts the violation of the merit filter condition. Given the case the counter has a value larger than the user-defined n_{maxCyle}, the local solver threshold is updated as

$$u_{\mathrm{lim}} = u_{\mathrm{lim}} + \tau_{\mathrm{PT}}\big(1 + |u_{\mathrm{lim}}|\big), \tag{A.17}$$

where τ_{PT} is the user-specified penalty threshold factor. Furthermore, one counter per basin of attraction is introduced to monitor the distance filter for each registered local minimum. If a counter exceeds n_{maxCyle}, the corresponding basin radius r_k is updated as

$$r_k = r_k \cdot (1 - \tau_{\mathrm{BR}}), \tag{A.18}$$

where the basin radius factor τ_{BR} is again user-defined.

The algorithm finally terminates once all trial points are analyzed and assumes that registered local minimum as the global one, which has the lowest objective function value ${}^{k}q_{\text{lopt}}$.

Initial values are required for the local solver threshold u_{lim} and basins of attraction r_k at the start of the second phase to prevent the algorithm from running an optimization simply for the first trial point evaluated. Therefore, a local optimization is performed upfront to the second phase, while the trial point with the lowest score function value in the trial set, the most promising one, is chosen as starting point. If the local optimization was successful, the optimization result could be used to register a first local minimum with a radius of basin attraction, the penalty weights could be updated, and the local solver threshold.

The software MATLAB provides an implementation of the method, which is used in the version of R2018b throughout the thesis. The algorithmic approach implemented in MATLAB coincides with the above description. However, it uses another local optimization starting from $\boldsymbol{p}_0$ at the beginning of the overall algorithm. The resulting extra information is used to determine the initial u_{lim} as well as an additional initial basin of attraction. Furthermore, the algorithm uses only a subset of n_{phase1} trial points to select the starting point of the optimization at the end of phase one. This subset is then removed from the trial point set for the second phase. While different algorithms for gradient-based local optimization could be utilized, the SQP method according to Appendix A.1 is employed exclusively for the thesis setting. Furthermore, the settings of Table A.1 are considered if not explicitly specified differently.

Description	Name	Value
Size of trial point set	n_{trial}	1000
Size of trial point subset for optimization	n_{phase1}	200
Distance threshold factor	τ_{dist}	0.75
Penalty threshold factor	τ_{PT}	0.2
Basin radius factor	τ_{BR}	0.2
Number of wait cyles for the counters	n_{maxCyle}	20
Threshold values for equal minima	τ_{p}, τ_{p}	10^{-6}

Table A.1: Standard settings for the global search as applied in the thesis.

APPENDIX B

PROMs of the Control Arms for the BMW 3series

PROMs are calculated for the five different control arms in the BMW 3series rear axle to define the reduced network of Section 8.2.2, which finally enables the use of globalized optimization algorithms. All control arm subsystems are divided into different sections, in which the mass density ρ_i and the shell thickness t_i can be varied independently of each other. In addition, point masses m_i are placed on the control arms. The division into sections and the positions of the point masses are visualized for the single control arms C1 to C5 in Figure B.1 to Figure B.5. The corresponding settings result in a 12D parameter space for C1 and a 9D one for C2 to C5, while one dimension is the frequency of excitation $\omega \in [20\,\text{Hz}, 500\,\text{Hz}]$. The parameter bounds are given in Table B.3.

As for the remaining BMW 3series, the commercial FE software Simulia ABAQUS 2017 Hotfix 2 is used to define all subsystems, and STRI3 elements are utilized to model the shell structure of the control arms. This modeling allows for a parameter-gray-box approach to reconstruct the affine matrix decompositions required for the global

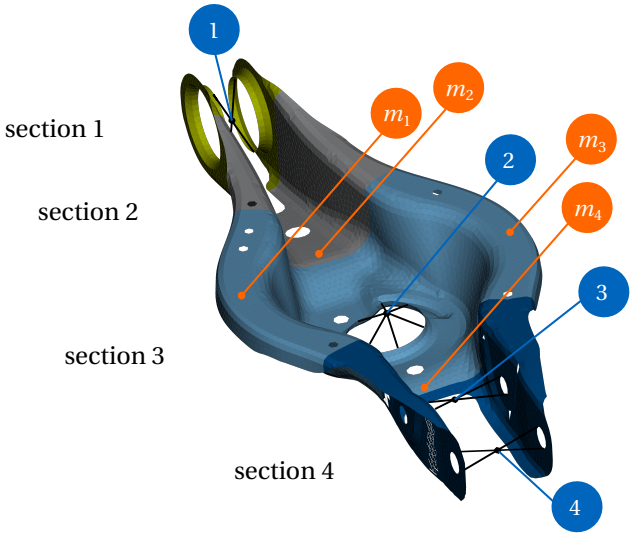

Figure B.1: The control arm C1 of the BMW 3series rear axle and its sections and point masses for parametrization in pMOR training performed for global optimization. The points marked with blue labels show the four connection points to other subsystems.

basis approach to pMOR. Refer to Section 8.2.2 for the explicit formulas.

The parameters of Table B.1 are chosen as meta settings for the reduction of the control arms through OGPA. Except for the diverging training settings of Table B.2 for the control arm C1, the meta parameters are not further tuned per control arm; thus, a lower ROM quality may be accepted for single control arms. The corresponding training results are summarized for the control arms in Table B.4. The latter also provides a-posteriori error evaluation results for a validation sample set of size $n_{\text{sam}} = 2000$.

Description	Name	Value
Deflation length	l_{defl}	$1 \cdot 10^{-7}$
Krylov order	o	2
Max. no. of greedy iterations	n_{itMax}	100
Skipped iterations for lucky breakdown	n_{skipMax}	12
Sample set for pre-selection of ${}^{n}\tilde{\boldsymbol{p}}_0$	n_{pre}	50
Max. no. of residual calculations per iteration	n_{maxFun}	200
Error threshold	$\varepsilon_{\text{rel}}^{\text{lim}}$	$5 \cdot 10^{-3}$
Relaxed error threshold	$\varepsilon_{\text{rel}}^{\text{rlx}}$	$2 \cdot 10^{-1}$
Transfer function amplitude threshold for $\varepsilon_{\text{rel}}^{\text{rlx}}$	H_{sw}	$5 \cdot 10^{-9}$

Table B.1: Metaparameters for the pROM training of the BMW 3series rear axle control arms.

Description	Name	Value
Deflation length	l_{defl}	$5 \cdot 10^{-8}$
Sample set for pre-selection of ${}^{n}\tilde{\boldsymbol{p}}_0$	n_{pre}	150

Table B.2: Metaparameters for pROM training of the control arm C1 deviating from the specification in Table B.1.

		C1	C2	C3	C4	C5
$m_i \left(\times 10^{-4}\right)$	$\boldsymbol{p}_\mathrm{l}$	0	0	0	0	0
	$\boldsymbol{p}_\mathrm{u}$	2.5	2.5	2.5	5	5
	$\boldsymbol{p}_0$	2.5	2.5	2.5	5	5
t_i	$\boldsymbol{p}_\mathrm{l}$	2.1	1.3	1.3	1.3	1.3
	$\boldsymbol{p}_\mathrm{u}$	3.1	2.7	2.7	2.8	2.7
	$\boldsymbol{p}_0$	2.1	1.3	1.3	1.3	1.3
$\rho_i \left(\times 10^{-9}\right)$	$\boldsymbol{p}_\mathrm{l}$	2.5	2.5	2.5	3	2.5
	$\boldsymbol{p}_\mathrm{u}$	11	12	12	12	12
	$\boldsymbol{p}_0$	11	12	12	12	12

Table B.3: The lower and upper bound values of the design parameters for the control arms C1 to C5 as well as the parameter sampling point ${}^0\boldsymbol{p}_0$ of the initial basis. All units are omitted as they are in Newton, millimeter and ton.

	d	n	m	n_it	n_exp	$n_\mathrm{overshoot}$	P
C1	12	33474	274	34	21	4	100.0%
C2	9	10758	131	33	15	20	96.6%
C3	9	10884	141	31	17	22	92.1%
C4	9	7386	108	26	14	24	84.5%
C5	9	14838	137	28	16	11	100.0%

Table B.4: The training results for each of the BMW 3series control arms. The FOM model size n, the ROM model size m, the greedy iterations per training n_it, the resulting number of expansion points n_exp are provided. In addition, the results from an a-posteriori error evaluation on a set of $n_\mathrm{sam} = 2000$ random samples are given by the number of error overshoots $n_\mathrm{overshoot}$ as well as conditional probability $P\left(98.5\% < a < 100\% | 2000 - n_\mathrm{overshoot}, 2000\right)$.

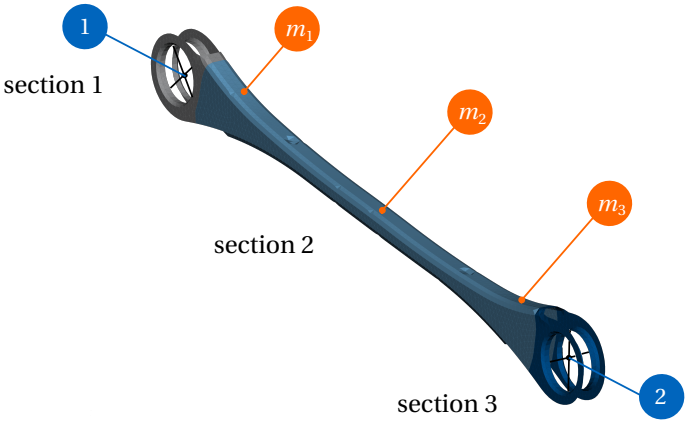

Figure B.2: The control arm C2 of the BMW 3series rear axle and its sections and point masses for parametrization in pMOR training performed for global optimization. The points marked with blue labels show the four connection points to other subsystems.

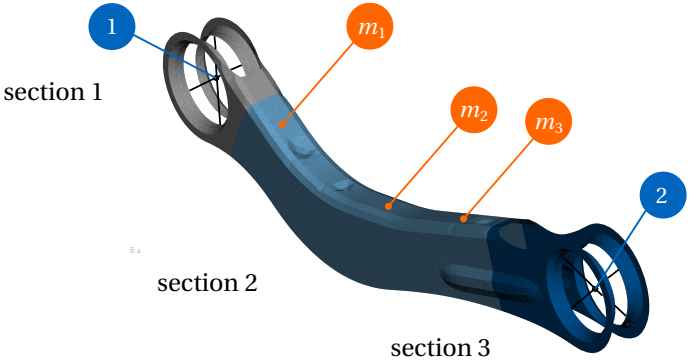

Figure B.3: The control arm C3 of the BMW 3series rear axle and its sections and point masses for parametrization in pMOR training performed for global optimization. The points marked with blue labels show the four connection points to other subsystems.

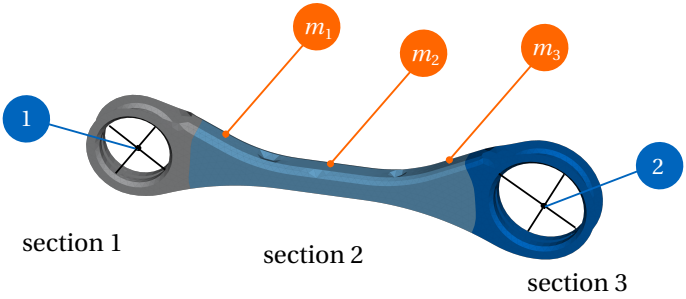

Figure B.4: The control arm C4 of the BMW 3series rear axle and its sections and point masses for parametrization in pMOR training performed for global optimization. The points marked with blue labels show the four connection points to other subsystems.

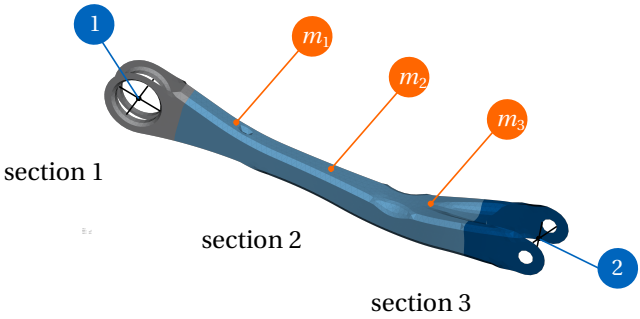

Figure B.5: The control arm C5 of the BMW 3series rear axle and its sections and point masses for parametrization in pMOR training performed for global optimization. The points marked with blue labels show the four connection points to other subsystems.

BIBLIOGRAPHY

[1] I. 16063. *ISO 16063-1:1998(E) Methods for the Calibration of Vibration and Shock Transducers - Part 1: Basic Concepts*. Vol. 1998. Geneva, Switzerland: International Organization for Standardization, Oct. 1998.

[2] N. M. Alexandrov, J. Dennis, R. M. Lewis, and V. Torczon. "A Trust-Region Framework for Managing the Use of Approximation Models in Optimization." In: *Structural optimization* 15.1 (1998), pp. 16–23. DOI: 10.1007/BF01197433.

[3] K. S. Alfredsson. "Active and Reactive Structural Energy Flow." In: *Journal of Vibration and Acoustics* 119.1 (1997), pp. 70–79. DOI: 10.1115/1.2889689.

[4] K. S. Alfredsson, B. Josefson, and M. Wilson. "Use of the Energy Flow Concept in Vibration Design." In: *AIAA Journal* 34.6 (1996), pp. 1250–1255. DOI: 10.2514/3.13220.

[5] R. J. Allemang. "The Modal Assurance Criterion–Twenty Years of Use and Abuse." In: *Sound & Vibration* 37.8 (2003), pp. 14–23.

[6] M. S. Allen, D. Rixen, M. van der Seijs, P. Tiso, T. Abrahamsson, and R. L. Mayes. *Substructuring in Engineering Dynamics: Emerging Numerical and Experimental Techniques*. Vol. 594. CISM International Centre for Mechanical Sciences. Cham: Springer, 2020. ISBN: 978-3-030-25532-9. DOI: 10.1007/978-3-030-25532-9.

[7] J. O. Almirón, F. Bianciardi, P. Corbeels, R. Ullmann, and W. Desmet. "Mount Characterization Analysis in the Context of FBS for Component-based TPA on a Wiper System." In: *Forum Acusticum*. Lyon, France, 2020, pp. 2011–2018. DOI: 10.48465/FA.2020.0251.

[8] K. F. Alvin, A. N. Robertson, G. W. Reich, and K. C. Park. "Structural System Identification: From Reality to Models." In: *Computers & Structures* 81.12 (2003), pp. 1149–1176. DOI: 10.1016/S0045-7949(03)00034-8.

[9] M. A. Aminpour, J. B. Ransom, and S. L. McCleary. "A Coupled Analysis Method for Structures with Independently Modelled Finite Element Subdomains." In: *International Journal for Numerical Methods in Engineering* 38.21 (1995), pp. 3695–3718. DOI: 10.1002/nme.1620382109.

[10] D. Amsallem and C. Farhat. "An Online Method for Interpolating Linear Parametric Reduced-Order Models." In: *SIAM Journal on Scientific Computing* 33.5 (2011), pp. 2169–2198. DOI: 10.1137/100813051.

[11] D. Amsallem and C. Farhat. “Interpolation Method for Adapting Reduced-Order Models and Application to Aeroelasticity.” In: *AIAA Journal* 46.7 (2008), pp. 1803–1813. DOI: 10.2514/1.35374.

[12] B. D. O. Anderson and S. Vongpanitlerd. *Network Analysis and Synthesis: A Modern Systems Theory Approach*. Mineola, NY: Dover Publications, 2006. ISBN: 978-0-486-45357-6.

[13] E. Anderson, ed. *LAPACK Users' Guide*. 3rd ed. Software, Environments, Tools. Philadelphia: Society for Industrial and Applied Mathematics, 1999. ISBN: 978-0-89871-447-0.

[14] H. Antil, M. Heinkenschloss, and D. C. Sorensen. “Application of the Discrete Empirical Interpolation Method to Reduced Order Modeling of Nonlinear and Parametric Systems.” In: *Reduced Order Methods for Modeling and Computational Reduction*. Ed. by A. Quarteroni and G. Rozza. MS&A - Modeling, Simulation and Applications 9. Cham: Springer, 2014, pp. 101–136. ISBN: 978-3-319-02090-7. DOI: 10.1007/978-3-319-02090-7_4.

[15] A. C. Antoulas. *Approximation of Large-Scale Dynamical Systems*. Advances in Design and Control. Society for Industrial and Applied Mathematics, 2005. ISBN: 978-0-89871-871-3. DOI: 10.1137/1.9780898718713.

[16] W. E. Arnoldi. “The Principle of Minimized Iterations in the Solution of the Matrix Eigenvalue Problem.” In: *Quarterly of Applied Mathematics* 9.1 (1951), pp. 17–29. DOI: 10.1090/qam/42792.

[17] J. R. F. Arruda, J. P. Campos, and J. I. Piva. “Experimental Determination of Flexural Power Flow in Beams Using a Modified Prony Method.” In: *Journal of Sound and Vibration* 197.3 (1996), pp. 309–328. DOI: 10.1006/jsvi.1996.0534.

[18] S. Badia, F. Nobile, and C. Vergara. “Robin–Robin Preconditioned Krylov Methods for Fluid–Structure Interaction Problems.” In: *Computer Methods in Applied Mechanics and Engineering* 198.33-36 (2009), pp. 2768–2784. DOI: 10.1016/j.cma.2009.04.004.

[19] Z. Bai and Y. Su. “Dimension Reduction of Large-Scale Second-Order Dynamical Systems via a Second-Order Arnoldi Method.” In: *SIAM Journal on Scientific Computing* 26.5 (2005), pp. 1692–1709. DOI: 10.1137/040605552.

[20] Z. Bai and Y. Su. “SOAR: A Second-order Arnoldi Method for the Solution of the Quadratic Eigenvalue Problem.” In: *SIAM Journal on Matrix Analysis and Applications* 26.3 (2005), pp. 640–659. DOI: 10.1137/S0895479803438523.

[21] G. A. J. Baker. *Essentials of Padé Approximants*. New York: Academic Press, 1975. ISBN: 978-0-323-15615-8.

[22] K.-J. Bathe. *Finite Element Procedures*. Second. Watertown, MA: Bathe, 2006. ISBN: 978-0-9790049-0-2.

[23] U. Baur, P. Benner, A. Greiner, J. Korvink, J. Lienemann, and C. Moosmann. “Parameter Preserving Model Order Reduction for MEMS Applications.” In: *Mathematical and Computer Modelling of Dynamical Systems* 17.4 (2011), pp. 297–317. DOI: 10.1080/13873954.2011.547658.

[24] U. Baur, C. Beattie, P. Benner, and S. Gugercin. “Interpolatory Projection Methods for Parameterized Model Reduction.” In: *SIAM Journal on Scientific Computing* 33.5 (2011), pp. 2489–2518. DOI: 10.1137/090776925.

[25] U. Baur and P. Benner. “Modellreduktion für parametrisierte Systeme durch balanciertes Abschneiden und InterpolationModel Reduction for Parametric Systems Using Balanced Truncation and Interpolation.” In: *at - Automatisierungstechnik* 57.8 (2009). DOI: 10.1524/auto.2009.0787.

[26] C. Beattie and S. Gugercin. “Krylov-Based Model Reduction of Second-Order Systems with Proportional Damping.” In: *Proceedings of the 44th IEEE Conference on Decision and Control, and the European Control Conference 2005*. Seville, Spain: IEEE, 2005, pp. 2278–2283. ISBN: 978-0-7803-9567-1. DOI: 10.1109/CDC.2005.1582501.

[27] C. A. Beattie and S. Gugercin. “A Trust Region Method for Optimal H2 Model Reduction.” In: *Proceedings of the 48h IEEE Conference on Decision and Control (CDC) Held Jointly with 2009 28th Chinese Control Conference*. Shanghai, China: IEEE, Dec. 2009, pp. 5370–5375. ISBN: 978-1-4244-3871-6. DOI: 10.1109/CDC.2009.5400605.

[28] C. A. Beattie and S. Gugercin. “Krylov-Based Minimization for Optimal H2 Model Reduction.” In: *2007 46th IEEE Conference on Decision and Control*. New Orleans, LA, USA: IEEE, 2007, pp. 4385–4390. ISBN: 978-1-4244-1497-0. DOI: 10.1109/CDC.2007.4434939.

[29] T. Bechtold, E. B. Rudnyi, and J. G. Korvink. “Error Estimation for Arnoldi-based Model Order Reduction of MEMS.” In: *TechConnect Briefs* 2 (2004), pp. 430–433.

[30] T. Belytschko and T. J. R. Hughes, eds. *Computational Methods for Transient Analysis*. Vol. Series 1, Computational methods in mechanics. Mechanics and Mathematical Methods. Amsterdam: North-Holland, 1983. ISBN: 978-0-444-86479-6.

[31] P. Benner and L. Feng. “A Robust Algorithm for Parametric Model Order Reduction Based on Implicit Moment Matching.” In: *Reduced Order Methods for Modeling and Computational Reduction*. Ed. by A. Quarteroni and G. Rozza. MS&A - Modeling, Simulation and Applications 9. Cham: Springer, 2014, pp. 159–185. ISBN: 978-3-319-02090-7. DOI: 10.1007/978-3-319-02090-7_6.

[32] P. Benner, S. Gugercin, and K. Willcox. “A Survey of Projection-Based Model Reduction Methods for Parametric Dynamical Systems.” In: *SIAM Review* 57.4 (2015), pp. 483–531. DOI: 10.1137/130932715.

[33] P. Benner, P. Kürschner, and J. Saak. “Frequency-Limited Balanced Truncation with Low-Rank Approximations.” In: *SIAM Journal on Scientific Computing* 38.1 (2016), A471–A499. DOI: 10.1137/15M1030911.

[34] G. Berkooz, P. Holmes, and J. L. Lumley. “The Proper Orthogonal Decomposition in the Analysis of Turbulent Flows.” In: *Annual Review of Fluid Mechanics* 25 (1993), pp. 539–575. DOI: 10.1146/annurev.fl.25.010193.002543.

[35] Y. I. Bobrovnitskii. “Estimating the Vibrational Energy Characteristics of an Elastic Structure via the Input Impedance and Mobility.” In: *Journal of Sound and Vibration* 217.2 (1998), pp. 351–386. DOI: 10.1006/jsvi.1998.1806.

[36] P. Bochev and R. B. Lehoucq. “On the Finite Element Solution of the Pure Neumann Problem.” In: *SIAM Review* 47.1 (2005), pp. 50–66. DOI: 10.1137/S0036144503426074.

[37] A. Bodendiek and M. Bollhöfer. “Adaptive-Order Rational Arnoldi-type Methods in Computational Electromagnetism.” In: *BIT Numerical Mathematics* 54.2 (2014), pp. 357–380. DOI: 10.1007/s10543-013-0458-9.

[38] T. Bonin, H. Faßbender, A. Soppa, and M. Zaeh. “A Fully Adaptive Rational Global Arnoldi Method for the Model-Order Reduction of Second-Order MIMO Systems with Proportional Damping.” In: *Mathematics and Computers in Simulation* 122 (2016), pp. 1–19. DOI: 10.1016/j.matcom.2015.08.017.

[39] T. Bonin, H. Faßbender, A. Soppa, and M. Zaeh. “A Global Arnoldi Method for the Model Reduction of Second-Order Structural Dynamical Systems.” 2010.

[40] E. Bonisoli and J. E. Mottershead. “Complex-Damped Dynamic Systems in the Time and Frequency Domains.” In: *Shock and Vibration* 11 (2004), pp. 209–225. DOI: 10.1155/2004/849417.

[41] J. Borggaard, K. R. Pond, and L. Zietsman. “Parametric Reduced Order Models Using Adaptive Sampling and Interpolation.” In: *IFAC Proceedings Volumes* 47.3 (2014), pp. 7773–7778. DOI: 10.3182/20140824-6-ZA-1003.02664.

[42] G. Bosse and A. Glaab. *Grundlagen der Elektrotechnik III*. VDI-Buch. Berlin, Heidelberg: Springer, 1996. ISBN: 978-3-642-48824-5.

[43] T. Braconnier, P. Langlois, and J. Rioual. “The Influence of Orthogonality on the Arnoldi Method.” In: *Linear Algebra and its Applications* 309.1-3 (2000), pp. 307–323. DOI: 10.1016/S0024-3795(99)00100-7.

[44] A. Brandt. *Noise and Vibration Analysis: Signal Analysis and Experimental Procedures*. Chichester: Wiley, 2011. ISBN: 978-0-470-97816-0.

[45] J. M. W. Brownjohn, G. H. Steele, P. Cawley, and R. D. Adams. “Errors in Mechanical Impedance Data Obtained with Impedance Heads.” In: *Journal of Sound and Vibration* 73.3 (1980), pp. 461–468. DOI: 10.1016/0022-460X(80)90527-1.

[46] T. Bui-Thanh, K. Willcox, and O. Ghattas. “Model Reduction for Large-Scale Systems with High-Dimensional Parametric Input Space.” In: *SIAM Journal on Scientific Computing* 30.6 (2008), pp. 3270–3288. DOI: 10.1137/070694855.

[47] T. Bui-Thanh. “Model-Constrained Optimization Methods for Reduction of Parameterized Large-Scale Systems.” PhD thesis. Cambridge, Massachusetts: Massachusetts Institute of Technology, 2007.

[48] H.-J. Bungartz and M. Griebel. “Sparse Grids.” In: *Acta Numerica* 13 (2004), pp. 147–269. DOI: 10.1017/S0962492904000182.

[49] A. Bunse-Gerstner, D. Kubalińska, G. Vossen, and D. Wilczek. “H2-Norm Optimal Model Reduction for Large Scale Discrete Dynamical MIMO Systems.” In: *Journal of Computational and Applied Mathematics* 233.5 (Jan. 2010), pp. 1202–1216. DOI: 10.1016/j.cam.2008.12.029.

[50] A. Bylin, M. Gibanica, and T. J. S. Abrahamsson. “Experimental-Analytical State-Space Synthesis of Passenger Car Components.” In: *Proceedings of ISMA2018 International Conference on Noise and Vibration Engineering and USD2018 International Conference on Uncertainty in Structural Dynamics*. Leuven, Belgium, 2018, pp. 4021–4035.

[51] T. K. Caughey and M. E. J. O’Kelly. “Classical Normal Modes in Damped Linear Dynamic Systems.” In: *Journal of Applied Mechanics* 32.3 (1965), pp. 583–588. DOI: 10.1115/1.3627262.

[52] S. Chaturantabut and D. C. Sorensen. “Nonlinear Model Reduction via Discrete Empirical Interpolation.” In: *SIAM Journal on Scientific Computing* 32.5 (2010), pp. 2737–2764. DOI: 10.1137/090766498.

[53] S. Chellappa, L. Feng, and P. Benner. “An Adaptive Sampling Approach for the Reduced Basis Method.” 2019. arXiv: 1910.00298.

[54] K.-F. Chen and S.-W. Zhang. “On the Impulse Response Precursor of an Ideal Linear Hysteretic Damper.” In: *Journal of Sound and Vibration* 312.4-5 (2008), pp. 576–583. DOI: 10.1016/j.jsv.2007.07.091.

[55] P. Chen and A. Quarteroni. “A New Algorithm for High-Dimensional Uncertainty Quantification Based on Dimension-Adaptive Sparse Grid Approximation and Reduced Basis Methods.” In: *Journal of Computational Physics* 298 (2015), pp. 176–193. DOI: 10.1016/j.jcp.2015.06.006.

[56] E. Chiprout and M. Nakhla. “Analysis of Interconnect Networks Using Complex Frequency Hopping (CFH).” In: *IEEE Transactions on Computer-Aided Design of Integrated Circuits and Systems* 14.2 (1995), pp. 186–200. DOI: 10.1109/43.370425.

[57] A. K. Chopra. *Dynamics of Structures: Theory and Applications to Earthquake Engineering*. 4. ed. Prentice Hall International Series in Civil Engineering and Engineering Mechanics. Harlow: Pearson Prentice Hall, 2014. ISBN: 978-0-273-77424-2.

[58] R. R. Craig and M. C. C. Bampton. “Coupling of Substructures for Dynamic Analyses.” In: *AIAA Journal* 6.7 (1968), pp. 1313–1319. DOI: 10.2514/3.4741.

[59] R. R. Craig and C.-J. Chang. “A Review of Substructure Coupling Methods for Dynamic Analysis.” In: *NASA. Langley Reserach Center Advances in Engineering Science* 2 (1976).

[60] R. R. Craig and A. Kurdila. *Fundamentals of Structural Dynamics*. 2nd ed. Hoboken, N.J: Wiley, 2006. ISBN: 978-0-471-43044-5.

[61] S. H. Crandall. “The Hysteretic Damping Model in Vibration Theory.” In: *Proceedings of the Institution of Mechanical Engineers, Part C: Mechanical Engineering Science* 205.1 (1991), pp. 23–28. DOI: 10.1243/PIME_PROC_1991_205_086_02.

[62] S. H. Crandall. “The Role of Damping in Vibration Theory.” In: *Journal of Sound and Vibration* 11.1 (1970), pp. 3–18. DOI: 10.1016/S0022-460X(70)80105-5.

[63] R. Curtain. “Old and New Perspectives on the Positive-Real Lemma in Systems and Control Theory.” In: *ZAMM - Journal of Applied Mathematics and Mechanics / Zeitschrift für Angewandte Mathematik und Mechanik* 79.9 (1999), pp. 579–590. DOI: 10.1002/(SICI)1521-4001(199909)79:9<579::AID-ZAMM579>3.0.CO;2-8.

[64] L. Daniel, O. Siong, L. Chay, K. Lee, and J. White. “A Multiparameter Moment-Matching Model-Reduction Approach for Generating Geometrically Parameterized Interconnect Performance Models.” In: *IEEE Transactions on Computer-Aided Design of Integrated Circuits and Systems* 23.5 (2004), pp. 678–693. DOI: 10.1109/TCAD.2004.826583.

[65] D. De Klerk. “Dynamic Response Characterization of Complex Systems through Operational Identification and Dynamic Substructuring: An Application to Gear Noise Propagation in the Automotive Industry.” PhD thesis. Delft, Netherlands: TU Delft, Delft University of Technology, 2009.

[66] D. de Klerk. “The Frequency Based Substructuring (FBS) Method Reformulated According to the Dual Domain Decomposition Method.” In: *Proceedings of the XXIV International Modal Analysis Conference*. St. Louis, Missouri, 2006.

[67] J. Degroote, J. Vierendeels, and K. Willcox. “Interpolation among Reduced-Order Matrices to Obtain Parameterized Models for Design, Optimization and Probabilistic Analysis.” In: *International Journal for Numerical Methods in Fluids* 63.2 (2009), pp. 207–230. DOI: 10.1002/fld.2089.

[68] M. A. Dihlmann and B. Haasdonk. “Certified PDE-constrained Parameter Optimization Using Reduced Basis Surrogate Models for Evolution Problems.” In: *Computational Optimization and Applications* 60.3 (2015), pp. 753–787. DOI: 10.1007/s10589-014-9697-1.

[69] V. Druskin and V. Simoncini. “Adaptive Rational Krylov Subspaces for Large-Scale Dynamical Systems.” In: *Systems & Control Letters* 60.8 (2011), pp. 546–560. DOI: 10.1016/j.sysconle.2011.04.013.

[70] V. Druskin, V. Simoncini, and M. Zaslavsky. “Adaptive Tangential Interpolation in Rational Krylov Subspaces for MIMO Dynamical Systems.” In: *SIAM Journal on Matrix Analysis and Applications* 35.2 (2014), pp. 476–498. DOI: 10.1137/120898784.

[71] J. Ebert, T. Stöwer, C. Schaal, J. Bös, and T. Melz. “Opportunities and Limitations on Vibro-Acoustic Design of Vehicle Structures by Means of Energy Flow-Based Numerical Simulation.” In: *NOVEM 2015, Noise and Vibration - Emerging Technologies. Proceedings*. Dubrovnik, Croatia, 2015.

[72] C. Eckart and G. Young. “The Approximation of One Matrix by Another of Lower Rank.” In: *Psychometrika* 1.3 (1936), pp. 211–218. DOI: 10.1007/BF02288367.

[73] R. Eid, B. Salimbahrami, B. Lohmann, E. B. Rudnyi, and J. G. Korvink. *Parametric Order Reduction of Proportionally Damped Second Order Systems*. Tech. rep. Vol. TRAC-1. Munich: Lehrstuhl für Regelungstechnik, TUM, 2006.

[74] D. Enns. "Model Reduction with Balanced Realizations: An Error Bound and a Frequency Weighted Generalization." In: *The 23rd IEEE Conference on Decision and Control*. Las Vegas, Nevada: IEEE, 1984, pp. 127–132. DOI: 10.1109/CDC.1984.272286.

[75] F. J. Fahy. *Sound Intensity*. London: E & FN Spon, an imprint of Chapman & Hall, 1995. ISBN: 978-0-419-19810-9.

[76] C. Farhat, M. Lesoinne, P. LeTallec, K. Pierson, and D. Rixen. "FETI-DP: A Dual–Primal Uniÿed FETI Method—Part I: A Faster Alternative to the Two-Level FETI Method." In: *international journal for numerical methods in engineering* 50.7 (2001), pp. 1523–1544. DOI: 10.1002/nme.76.

[77] C. Farhat and F.-X. Roux. "A Method of Finite Element Tearing and Interconnecting and Its Parallel Solution Algorithm." In: *International Journal for Numerical Methods in Engineering* 32.6 (1991), pp. 1205–1227. DOI: 10.1002/nme.1620320604.

[78] P. Feldmann. "Model Order Reduction Techniques for Linear Systems with Large Numbers of Terminals." In: *Proceedings Design, Automation and Test in Europe Conference and Exhibition*. Vol. 2. Paris, France: IEEE, 2004, pp. 944–947. ISBN: 978-0-7695-2085-8. DOI: 10.1109/DATE.2004.1269013.

[79] P. Feldmann and R. Freund. "Efficient Linear Circuit Analysis by Pade Approximation via the Lanczos Process." In: *IEEE Transactions on Computer-Aided Design of Integrated Circuits and Systems* 14.5 (1995), pp. 639–649. DOI: 10.1109/43.384428.

[80] L. Feng, A. C. Antoulas, and P. Benner. "Some a Posteriori Error Bounds for Reduced-Order Modelling of (Non-)Parametrized Linear Systems." In: *ESAIM: Mathematical Modelling and Numerical Analysis* 51.6 (2017), pp. 2127–2158. DOI: 10.1051/m2an/2017014.

[81] L. Feng and P. Benner. "A New Error Estimator for Reduced-Order Modeling of Linear Parametric Systems." In: *IEEE Transactions on Microwave Theory and Techniques* 67.12 (2019), pp. 4848–4859. DOI: 10.1109/TMTT.2019.2948858.

[82] A. A. Freschi, A. K. Pereira, K. M. Ahmida, J. Frejlich, and J. R. F. Arruda. "Analyzing the Total Structural Intensity in Beams Using a Homodyne Laser Doppler Vibrometer." In: *Shock and Vibration* 7 (2000), pp. 299–308. DOI: 10.1155/2000/952482.

[83] R. Freund. "SPRIM: Structure-Preserving Reduced-Order Interconnect Macromodeling." In: *IEEE/ACM International Conference on Computer Aided Design, 2004. ICCAD-2004.* San Jose, California: IEEE, 2004, pp. 80–87. ISBN: 978-0-7803-8702-7. DOI: 10.1109/ICCAD.2004.1382547.

[84] R. W. Freund. "Krylov-Subspace Methods for Reduced-Order Modeling in Circuit Simulation." In: *Journal of Computational and Applied Mathematics* 123.1-2 (2000), pp. 395–421. DOI: 10.1016/S0377-0427(00)00396-4.

[85] M. Friswell, S. Garvey, and J. Penny. “Model Reduction Using Dynamic and Iterated IRS Techniques.” In: *Journal of Sound and Vibration* 186.2 (1995), pp. 311–323. DOI: 10.1006/jsvi.1995.0451.

[86] B. Fröhlich, J. Gade, F. Geiger, M. Bischoff, and P. Eberhard. “Geometric Element Parameterization and Parametric Model Order Reduction in Finite Element Based Shape Optimization.” In: *Computational Mechanics* 63.5 (2019), pp. 853–868. DOI: 10.1007/s00466-018-1626-1.

[87] K. Gallivan, A. Vandendorpe, and P. V. Dooren. *Model Reduction via Tangential Interpolation*. 2002.

[88] K. Gallivan, E. Grimme, and P. Van Dooren. “Asymptotic Waveform Evaluation via a Lanczos Method.” In: *Applied Mathematics Letters* 7.5 (1994), pp. 75–80. DOI: 10.1016/0893-9659(94)90077-9.

[89] K. Gallivan, G. Grimme, and P. Van Dooren. “A Rational Lanczos Algorithm for Model Reduction.” In: *Numerical Algorithms* 12 (1996), pp. 33–63. DOI: 10.1007/BF02141740.

[90] K. Gallivan, A. Vandendorpe, and P. Van Dooren. “Model Reduction of MIMO Systems via Tangential Interpolation.” In: *SIAM Journal on Matrix Analysis and Applications* 26.2 (2004), pp. 328–349. DOI: 10.1137/S0895479803423925.

[91] V. Ganguly and T. L. Schmitz. “Phase Correction for Frequency Response Function Measurements.” In: *Precision Engineering* 38.2 (2014), pp. 409–413. DOI: 10.1016/j.precisioneng.2013.12.007.

[92] P. Gardonio. “Active Isolation of Structural Vibration on a Multiple-Degree-of-Freedom System, Part I: The Dynamics of the System.” In: *Journal of Sound and Vibration* 207.1 (1997), pp. 61–93. DOI: 10.1006/jsvi.1997.1152.

[93] P. Gardonio. “Active Isolation of Structural Vibration on a Multiple-Degree-of-Freedom System, Part II: Effectiveness of Active Control Strategies.” In: *Journal of Sound and Vibration* 207.1 (1997), pp. 95–121. DOI: 10.1006/jsvi.1997.1153.

[94] M. Géradin and D. Rixen. *Mechanical Vibrations: Theory and Application to Structural Dynamics*. 3rd ed. Chichester, United Kingdom: Wiley, 2015. ISBN: 978-1-118-90020-8.

[95] M. Geuss, D. Butnaru, B. Peherstorfer, H.-J. Bungartz, and B. Lohmann. “Parametric Model Order Reduction by Sparse-Grid-Based Interpolation on Matrix Manifolds for Multidimensional Parameter Spaces.” In: *2014 European Control Conference (ECC)*. Strasbourg: IEEE, June 2014, pp. 2727–2732. ISBN: 978-3-9524269-1-3. DOI: 10.1109/ECC.2014.6862414.

[96] R. Ghanem, D. Higdon, and H. Owhadi. *Handbook of Uncertainty Quantification*. New York: Springer, 2017. ISBN: 978-3-319-12384-4.

[97] L. Giraud, J. Langou, and M. Rozloznik. “The Loss of Orthogonality in the Gram-Schmidt Orthogonalization Process.” In: *Computers & Mathematics with Applications* 50.7 (2005), pp. 1069–1075. DOI: 10.1016/j.camwa.2005.08.009.

[98] L. Giraud, J. Langou, and M. Rozloznık. *On the Round-off Error Analysis of the Gram-Schmidt Algorithm with Reorthogonalization*. Tech. rep. Technical Report TR/PA/02/33. Toulouse: CERFACS, 2002.

[99] F. Glover. "A Template for Scatter Search and Path Relinking." In: *Artificial Evolution*. Ed. by G. Goos, J. Hartmanis, J. van Leeuwen, J.-K. Hao, E. Lutton, E. Ronald, M. Schoenauer, and D. Snyers. Vol. 1363. Lecture Notes in Computer Science. Berlin, Heidelberg: Springer, 1997, pp. 1–51. ISBN: 978-3-540-64169-8. DOI: 10.1007/BFb0026589.

[100] K. Glover. "All Optimal Hankel-norm Approximations of Linear Multivariable Systems and Their {L_∞} -Error Bounds." In: *International Journal of Control* 39.6 (1984), pp. 1115–1193. DOI: 10.1080/00207178408933239.

[101] G. H. Golub and C. F. Van Loan. *Matrix Computations*. 4th ed. Johns Hopkins Studies in the Mathematical Sciences. Baltimore: The Johns Hopkins University Press, 2013. ISBN: 978-1-4214-0794-4.

[102] P. Gosselet and C. Rey. "Non-Overlapping Domain Decomposition Methods in Structural Mechanics." In: *Archives of Computational Methods in Engineering* 13 (2006), pp. 515–572. DOI: 10.1007/BF02905857.

[103] H. Goyder and R. White. "Vibrational Power Flow from Machines into Built-up Structures, Part I: Introduction and Approximate Analyses of Beam and Plate-like Foundations." In: *Journal of Sound and Vibration* 68.1 (1980), pp. 59–75. DOI: 10.1016/0022-460X(80)90452-6.

[104] E. Grimme and K. Gallivan. *A Rational Lanczos Algorithm for Model Reduction II: Interpolation Point Selection*. 1998.

[105] E. J. Grimme. "Krylov Projection Methods for Model Reduction." PhD thesis. Urbana, Illinois: University of Illinois at Urbana-Champaign, 1997.

[106] S. Gugercin, A. C. Antoulas, and C. Beattie. *Rational Krylov Methods for Optimal {$\mathcal H_2$} Model Reduction*. 2006.

[107] S. Gugercin, A. C. Antoulas, and C. Beattie. "{$\mathcal{H}_2$} Model Reduction for Large-Scale Linear Dynamical Systems." In: *SIAM Journal on Matrix Analysis and Applications* 30.2 (2008), pp. 609–638. DOI: 10.1137/060666123.

[108] S. Gugercin. "Projection Methods for Model Reduction of Large-Scale Dynamical Systems." PhD thesis. Houston, Texas: Rice University, 2003.

[109] R. J. Guyan. "Reduction of Stiffness and Mass Matrices." In: *AIAA Journal* 3.2 (1965), pp. 380–380. DOI: 10.2514/3.2874.

[110] B. Haasdonk, M. Dihlmann, and M. Ohlberger. "A Training Set and Multiple Bases Generation Approach for Parameterized Model Reduction Based on Adaptive Grids in Parameter Space." In: *Mathematical and Computer Modelling of Dynamical Systems* 17.4 (2011), pp. 423–442. DOI: 10.1080/13873954.2011.547674.

[111] M. Haeussler, S. Klaassen, and D. Rixen. "Experimental Twelve Degree of Freedom Rubber Isolator Models for Use in Substructuring Assemblies." In: *Journal of Sound and Vibration* 474 (2020), p. 115253. DOI: 10.1016/j.jsv.2020.115253.

[112] B. Hakansson and P. Carlsson. “Bias Errors in Mechanical Impedance Data Obtained with Impedance Heads.” In: *Journal of Sound and Vibration* 113.2 (1987), pp. 173–183. DOI: 10.1016/S0022-460X(87)81349-4.

[113] C. R. Halkyard and B. R. Mace. “Structural Intensity in Beams—Waves, Transducer Systems and the Conditioning Problem.” In: *Journal of Sound and Vibration* 185.2 (1995), pp. 279–298. DOI: 10.1006/jsvi.1995.0380.

[114] S. A. Hambric. “Approximation Techniques for Broad-Band Acoustic Radiated Noise Design Optimization Problems.” In: *Journal of Vibration and Acoustics* 117.1 (1995), pp. 136–144. DOI: 10.1115/1.2873857.

[115] S. A. Hambric, S. H. Sung, and D. J. Nefske, eds. *Engineering Vibroacoustic Analysis: Methods and Applications*. Chichester: Wiley, 2016. ISBN: 978-1-119-95344-9.

[116] S. P. Han. “A Globally Convergent Method for Nonlinear Programming.” In: *Journal of Optimization Theory and Applications* 22.3 (1977), pp. 297–309. DOI: 10.1007/BF00932858.

[117] H. Harman. *Modern Factor Analysis*. Chicago: The University of Chicago Press, 1960.

[118] C. M. Harris and A. G. Piersol, eds. *Harris' Shock and Vibration Handbook*. 5th ed. McGraw-Hill Handbooks. New York: McGraw-Hill, 2002. ISBN: 978-0-07-137081-3.

[119] T. Hartmann, G. Tanner, G. Xie, D. Chappell, and J. Bajars. “Modelling of High-Frequency Structure-Borne Sound Transmission on FEM Grids Using the Discrete Flow Mapping Technique.” In: *Journal of Physics: Conference Series* 744 (Sept. 2016), p. 012237. DOI: 10.1088/1742-6596/744/1/012237.

[120] P. M. Haughton. “A Method for Checking the Calibration of the Bruel & Kjaer Type 8000 Mechanical Impedance Head.” In: *British Journal of Audiology* 19.1 (1985), pp. 53–56. DOI: 10.3109/03005368509078963.

[121] M. Häußler. “Modular Sound & Vibration Engineering by Substructuring.” PhD thesis. Munich: Technische Universität München, 2021.

[122] J. S. Hesthaven, B. Stamm, and S. Zhang. “Efficient Greedy Algorithms for High-Dimensional Parameter Spaces with Applications to Empirical Interpolation and Reduced Basis Methods.” In: *ESAIM: Mathematical Modelling and Numerical Analysis* 48.1 (2014), pp. 259–283. DOI: 10.1051/m2an/2013100.

[123] Y. P. Hong and C.-T. Pan. “Rank-Revealing QR Factorizations and the Singular Value Decomposition.” In: *Mathematics of Computation* 58.197 (1992), pp. 213–232. DOI: 10.2307/2153029.

[124] H. Hotelling. “Analysis of a Complex of Statistical Variables into Principal Components.” In: *Journal of Educational Psychology* 24.6 (1933), pp. 417–441. DOI: 10.1037/h0071325.

[125] M. Hund, P. Mlinarić, and J. Saak. “An $\mathscr{H}_2 \otimes \mathscr{L}_2$ -Optimal Model Order Reduction Approach for Parametric Linear Time-Invariant Systems.” In: *Proceedings in Applied Mathematics and Mechanics* 18.1 (2018). DOI: 10.1002/pamm.201800084.

[126] W. Hurty. “Vibrations of Structural Systems by Component Mode Synthesis.” In: *Journal of the Engineering Mechanics Division* 86.4 (1960), pp. 51–70. DOI: 10.1061/JMCEA3.0000162.

[127] C. Hwang and M.-Y. Chen. “A Multipoint Continued-Fraction Expansion for Linear System Reduction.” In: *IEEE Transactions on Automatic Control* 31.7 (1986), pp. 648–651. DOI: 10.1109/TAC.1986.1104357.

[128] L. Iapichino and S. Volkwein. “Optimization Strategy for Parameter Sampling in the Reduced Basis Method.” In: *IFAC-PapersOnLine* 48.1 (2015), pp. 707–712. DOI: 10.1016/j.ifacol.2015.05.020.

[129] J. A. Inaudi and N. Makris. “Time-Domain Analysis of Linear Hysteretic Damping.” In: *Earthquake Engineering & Structural Dynamics* 25.6 (1996), pp. 529–545. DOI: 10.1002/(SICI)1096-9845(199606)25:6<529::AID-EQE549>3.0.CO;2-P.

[130] F. Jacobsen. “Active and Reactive, Coherent and Incoherent Sound Fields.” In: *Journal of Sound and Vibration* 130.3 (1989), pp. 493–507. DOI: 10.1016/0022-460X(89)90072-2.

[131] L. Ji, B. Mace, and R. Pinnington. “A Power Mode Approach to Estimating Vibrational Power Transmitted by Multiple Sources.” In: *Journal of Sound and Vibration* 265.2 (2003), pp. 387–399. DOI: 10.1016/S0022-460X(02)01457-8.

[132] S. Jianxin, A. Moorhouse, and B. Gibbs. “Towards a Practical Characterization for Structure-Borne Sound Sources Based on Mobility Techniques.” In: *Journal of Sound and Vibration* 185.4 (1995), pp. 737–741. DOI: 10.1006/jsvi.1995.0415.

[133] A. Jund and L. Gagliardini. “Noise Control Using Input Power at Low and Mid-Frequencies: Sensitivity to Structural Design Changes.” In: *Proceedings of ISMA 2010 Including USD 2010*. Leuven, Belgium, 2010, pp. 4141–4148.

[134] B. Kammermeier, J. Mayet, and D. J. Rixen. “Hybrid Substructure Assembly Techniques for Efficient and Robust Optimization of Additional Structures in Late Phase NVH Design: A Comparison.” In: *Dynamic Substructures*. Ed. by A. Linderholt, M. S. Allen, R. L. Mayes, and D. Rixen. Vol. 4. Conference Proceedings of the Society for Experimental Mechanics Series. Cham: Springer, 2020, pp. 35–45. ISBN: 978-3-030-12183-9. DOI: 10.1007/978-3-030-12184-6_4.

[135] K. Karhunen. *Zur Spektraltheorie Stochastischer Prozesse*. Vol. 34. Annales Academiae Scientiarum Fennicae. 1946.

[136] M. C. Kennedy and A. O’Hagan. “Bayesian Calibration of Computer Models.” In: *Journal of the Royal Statistical Society: Series B (Statistical Methodology)* 63.3 (2001), pp. 425–464. DOI: 10.1111/1467-9868.00294.

[137] G. Kerschen, J.-c. Golinval, A. F. Vakakis, and L. A. Bergman. “The Method of Proper Orthogonal Decomposition for Dynamical Characterization and Order Reduction of Mechanical Systems: An Overview.” In: *Nonlinear dynamics* 41 (2005), pp. 147–169. DOI: 10.1007/s11071-005-2803-2.

[138] S. Kim and R. Singh. “Alternate Methods for Characterizing Spectral Energy Inputs Based Only on Driving Point Mobilities or Impedances.” In: *Journal of Sound and Vibration* 291.3-5 (2006), pp. 604–626. DOI: 10.1016/j.jsv.2005.06.026.

[139] T. Kim. “Frequency-Domain Karhunen-Loeve Method and Its Application to Linear Dynamic Systems.” In: *AIAA Journal* 36.11 (1998), pp. 2117–2123. DOI: 10.2514/2.315.

[140] G. Kirchhoff. *Vorlesungen Über Mathematische Physik*. Leipzig: Teubner, 1876.

[141] J. Korta, R. Raniolo, M. Danti, and T. Uhl. “Energy Flow Analysis in Car Structure Nvh Problems.” In: *Proceedings of ISMA2012 Including USD2012*. Leuven, Belgium, 2012.

[142] A. Krylov. “On the Numerical Solution of Equation by Which are Determined in Technical Problems the Frequencies of Small Vibrations of Material Systems.” In: *Izvestiia Akademii nauk SSSR* 7.4 (1931), pp. 491–539.

[143] C. Lanczos. “An Iteration Method for the Solution of the Eigenvalue Problem of Linear Differential and Integral Operators.” In: *Journal of Research of the National Bureau of Standards* 45.4 (1950), pp. 255–282. DOI: 10.6028/jres.045.026.

[144] A. Le Bot. *Foundation of Statistical Energy Analysis in Vibroacoustics*. 1st ed. Oxford, United Kingdom: Oxford University Press, 2015. ISBN: 978-0-19-872923-5.

[145] H.-J. Lee, C.-C. Chu, and W.-S. Feng. “An Adaptive-Order Rational Arnoldi Method for Model-Order Reductions of Linear Time-Invariant Systems.” In: *Linear Algebra and its Applications* 415.2-3 (2006), pp. 235–261. DOI: 10.1016/j.laa.2004.10.011.

[146] M. Lehar and M. Zimmermann. “An Inexpensive Estimate of Failure Probability for High-Dimensional Systems with Uncertainty.” In: *Structural Safety* 36–37 (2012), pp. 32–38. DOI: 10.1016/j.strusafe.2011.10.001.

[147] M. Lehner. “Modellreduktion in elastischen Mehrkörpersystemen.” PhD thesis. Stuttgart: Universität Stuttgart, 2007. ISBN: 978-3-8322-6783-4.

[148] M. Lehner and P. Eberhard. “On the Use of Moment-Matching to Build Reduced Order Models in Flexible Multibody Dynamics.” In: *Multibody System Dynamics* 16.2 (2006), pp. 191–211. DOI: 10.1007/s11044-006-9018-2.

[149] M. S. Lenzi, G. Stigliano, S. Donders, B. Pluymers, and W. Desmet. “New Insights of an Energy Flow Visualization into Vehicle Design.” In: *Proceedings of ISMA2010 Including USD2010*. Leuven, Belgium, 2010, pp. 2025–2038. ISBN: 978-90-73802-87-2.

[150] A. Y.-T. Leung. “An Accurate Method of Dynamic Condensation in Structural Analysis.” In: *International Journal for Numerical Methods in Engineering* 12.11 (1978), pp. 1705–1715. DOI: 10.1002/nme.1620121108.

[151] D. Levin. “The Approximation Power of Moving Least-Squares.” In: *Mathematics of Computation* 67.224 (1998), pp. 1517–1532. DOI: 10.1090/S0025-5718-98-00974-0.

[152] A. Liljerehn and T. J. S. Abrahamsson. “Dynamic Sub-Structuring with Passive State-Space Components.” In: *Proceedings of ISMA2014 Including USD2014*. Leuven, Belgium, 2014, pp. 3879–3890. ISBN: 978-90-73802-91-9.

[153] J. Linjama and T. Lahti. “Estimation of Bending Wave Intensity in Beams Using the Frequency Response Technique.” In: *Jourrnal of Sound and Vibration* 153.1 (1992), pp. 21–36. DOI: 10.1016/0022-460X(92)90624-7.

[154] P. Liu, S. Tan, B. Yan, and B. McGaughy. “An Extended SVD-based Terminal and Model Order Reduction Algorithm.” In: *2006 IEEE International Behavioral Modeling and Simulation Workshop*. San Jose, California, USA: IEEE, 2006, pp. 44–49. ISBN: 978-0-7803-9742-2. DOI: 10.1109/BMAS.2006.283468.

[155] M. Loève. *Probability Theory I*. Ed. by P. R. Halmos. 4th ed. Vol. 45. Graduate Texts in Mathematics. New York, USA: Springer, 1977. ISBN: 978-1-4684-9464-8. DOI: 10.1007/978-1-4684-9464-8.

[156] E. N. Lorenz. *Empirical Orthogonal Functions and Statistical Weather Prediction*. Technical Report 1. Cambridge, MA, USA: Massachusetts Institute of Technology, 1956.

[157] D. Lu, Y. Su, and Z. Bai. “Stability Analysis of the Two-level Orthogonal Arnoldi Procedure.” In: *SIAM Journal on Matrix Analysis and Applications* 37.1 (2016), pp. 195–214. DOI: 10.1137/151005142.

[158] R. H. Lyon and R. G. DeJong. *Theory and Application of Statistical Energy Analysis*. 2nd ed. Boston: Butterworth-Heinemann, 1995. ISBN: 978-0-7506-9111-6. DOI: 10.1016/C2009-0-26747-X.

[159] B. Mace and P. Shorter. “A Local Modal/Perturbational Method for Estimating Frequency Response Statistics of Built-up Structures with Uncertain Properties.” In: *Journal of Sound and Vibration* 242.5 (2001), pp. 793–811. DOI: 10.1006/jsvi.2000.3389.

[160] B. Mace and P. Shorter. “Energy Flow Models from Finite Element Analysis.” In: *Journal of Sound and Vibration* 233.3 (2000), pp. 369–389. DOI: 10.1006/jsvi.1999.2812.

[161] B. Mace, W. Desmet, and B. Pluymers. “Mid-Frequency Methods in Sound and Vibration—Part A.” In: *Journal of Sound and Vibration* 332.8 (2013), pp. 1895–1896. DOI: 10.1016/j.jsv.2012.12.012.

[162] R. H. MacNeal. “A Hybrid Method of Component Mode Synthesis.” In: *Computers & Structures* 1.4 (1971), pp. 581–601. DOI: 10.1016/0045-7949(71)90031-9.

[163] Y. Maday and B. Stamm. “Locally Adaptive Greedy Approximations for Anisotropic Parameter Reduced Basis Spaces.” In: *SIAM Journal on Scientific Computing* 35.6 (2013), A2417–A2441. DOI: 10.1137/120873868. arXiv: 1204.3846.

[164] N. K. Mandal. “One Transducer Method for Quantifying Vibration Power Flow in Orthotropic Plates for Both General and Far-field Conditions.” In: *Trends in Applied Sciences Research* 1.1 (2006), pp. 1–8. DOI: 10.3923/tasr.2006.1.8.

[165] N. K. Mandal and S. Biswas. “Vibration Power Flow: A Critical Review.” In: *The Shock and Vibration Digest* 37.1 (2005), pp. 3–11. DOI: 10.1177/0583102404049168.

[166] S. Marburg. “Developments in Structural-Acoustic Optimization for Passive Noise Control.” In: *Archives of Computational Methods in Engineering* 9.4 (2002), pp. 291–370. DOI: 10.1007/BF03041465.

[167] J. R. R. A. Martins and J. T. Hwang. “Review and Unification of Methods for Computing Derivatives of Multidisciplinary Computational Models.” In: *AIAA Journal* 51.11 (2013), pp. 2582–2599. DOI: 10.2514/1.J052184.

[168] T. P. A. Mathew. *Domain Decomposition Methods for the Numerical Solution of Partial Differential Equations*. Lecture Notes in Computational Science and Engineering 61. Berlin: Springer, 2008. ISBN: 978-3-540-77209-5. DOI: 10.1007/978-3-540-77209-5.

[169] W. Maysenhölder. *Körperschallenergie: Grundlagen Zur Berechnung von Energiedichten Und Intensitäten*. Stuttgart: Hirzel, 1994. ISBN: 978-3-7776-0607-1. DOI: 10.18419/opus-6738.

[170] M. D. McKay, R. J. Beckman, and W. J. Conover. “A Comparison of Three Methods for Selecting Values of Input Variables in the Analysis of Output from a Computer Code.” In: *Technometrics* 21.2 (1979), pp. 239–245. DOI: 10.2307/1268522.

[171] T. McKelvey and S. Reza Moheimani. “Estimation of Phase Constrained MIMO Transfer Functions with Application to Flexible Structures with Mixed Collocated and Non-Collocated Actuators and Sensors.” In: *IFAC Proceedings Volumes* 38.1 (2005), pp. 219–224. DOI: 10.3182/20050703-6-CZ-1902.00037.

[172] K. Meerbergen. “Fast Frequency Response Computation for Rayleigh Damping.” In: *International Journal for Numerical Methods in Engineering* 73.1 (2008), pp. 96–106. DOI: 10.1002/nme.2058.

[173] J. W. R. Meggitt. “On the Treatment of Uncertainty in Experimentally Measured Frequency Response Functions.” In: *Metrologia* 55.6 (2018), pp. 806–818. DOI: 10.1088/1681-7575/aadeeb.

[174] R. Merkel, K. Gatzwiller, and D. Brown. “Important Aspects of Precise Driving Point FRF Measurements Using a Mechanical Impedance Head Sensor.” In: *Proceedings of the Sixteenth International Modal Analysis Conference*. Santa Barbara, CA, USA, 1998, pp. 795–799.

[175] M. Meyer and H. G. Matthies. “Efficient Model Reduction in Non-Linear Dynamics Using the Karhunen-Loève Expansion and Dual-Weighted-Residual Methods.” In: *Computational Mechanics* 31.1-2 (2003), pp. 179–191. DOI: 10.1007/s00466-002-0404-1.

[176] A. T. Moorhouse. “A Dimensionless Mobility Formulation for Evaluation of Force and Moment Excitation of Structures.” In: *The Journal of the Acoustical Society of America* 112.3 (2002), pp. 972–980. DOI: 10.1121/1.1497622.

[177] A. T. Moorhouse. “On the Characteristic Power of Structure-Borne Sound Sources.” In: *Journal of Sound and Vibration* 248.3 (2001), pp. 441–459. DOI: 10.1006/jsvi.2001.3797.

[178] Z. P. Mourelatos, G. Zhang, M. P. Castanier, and C. Pierre. “Vibration and Power Flow Analysis of a Vehicle Structure Using Characteristic Constraint Modes.” In: *SAE 2003 Noise & Vibration Conference and Exhibition*. SAE International, 2003, pp. 2003-01–1602. DOI: 10.4271/2003-01-1602.

[179] G. Müller and M. Buchschmid. “Hybrid Approaches for Vibroacoustical Problems Based on the Finite Element Method and Statistical Energy Analysis.” In: *Wave Motion* 51.4 (2014), pp. 622–634. DOI: 10.1016/j.wavemoti.2013.11.003.

[180] D. J. Nefske and S. H. Sung. “Power Flow Finite Element Analysis of Dynamic Systems: Basic Theory and Application to Beams.” In: *Journal of Vibration Acoustics Stress and Reliability in Design* 111.1 (1989), pp. 94–100. DOI: 10.1115/1.3269830.

[181] F. Negri, A. Manzoni, and D. Amsallem. “Efficient Model Reduction of Parametrized Systems by Matrix Discrete Empirical Interpolation.” In: *Journal of Computational Physics* 303 (2015), pp. 431–454. DOI: 10.1016/j.jcp.2015.09.046.

[182] S. Neumark. *Concept of Complex Stiffness Applied to Problems of Oscillations with Viscous and Hysteretic Damping*. Tech. rep. 3269. London: Ministry of Aviation, 1957, p. 36.

[183] J. Nocedal and S. J. Wright. *Numerical Optimization*. 2nd ed. Springer Series in Operations Research and Financial Engineering. New York, USA: Springer, 2006. ISBN: 978-0-387-30303-1. DOI: 10.1007/978-0-387-40065-5.

[184] J. O’Callahan, P. Avitabile, and R. Riemer. “System Equivalent Reduction Expansion Process (SEREP).” In: *Proceedings of 7th International Modal Analysis Conference*. Las Vegas, NV, USA, 1989, pp. 29–37. ISBN: 978-99908-73-41-2.

[185] A. Odabasioglu, M. Celik, and L. Pileggi. “PRIMA: Passive Reduced-Order Interconnect Macromodeling Algorithm.” In: *IEEE Transactions on Computer-Aided Design of Integrated Circuits and Systems* 17.8 (1998), pp. 645–654. DOI: 10.1109/43.712097.

[186] I. B. Oliveira and A. T. Patera. “Reduced-Basis Techniques for Rapid Reliable Optimization of Systems Described by Affinely Parametrized Coercive Elliptic Partial Differential Equations.” In: *Optimization and Engineering* 8.1 (2007), pp. 43–65. DOI: 10.1007/s11081-007-9002-6.

[187] S. Orlando, B. Peeters, and G. Coppotelli. “Improved FRF Estimators for MIMO Sine Sweep Data.” In: *Proceedings of ISMA2008*. Leuven, Belgium, 2008, pp. 229–241.

[188] H. Panzer, J. Mohring, R. Eid, and B. Lohmann. “Parametric Model Order Reduction by Matrix Interpolation.” In: *at - Automatisierungstechnik* 58.8 (2010). DOI: 10.1524/auto.2010.0863.

[189] H. K. F. Panzer. “Model order reduction by Krylov subspace methods with global error bounds and automatic choice of parameters.” PhD thesis. Munich, Germany: Technische Universität München, Jan. 2015.

[190] H. K. F. Panzer, T. Wolf, and B. Lohmann. "$\mathcal{H}2$ and $\mathcal{H}\infty$ Error Bounds for Model Order Reduction of Second Order Systems by Krylov Subspace Methods." In: *2013 European Control Conference (ECC)*. Zurich: IEEE, 2013, pp. 4484–4489. ISBN: 978-3-033-03962-9. DOI: 10.23919/ECC.2013.6669657.

[191] D. I. Papadimitriou and K. C. Giannakoglou. "Direct, Adjoint and Mixed Approaches for the Computation of Hessian in Airfoil Design Problems." In: *International Journal for Numerical Methods in Fluids* 56.10 (2008), pp. 1929–1943. DOI: 10.1002/fld.1584.

[192] R. S. Pappa, K. B. Elliott, and A. Schenk. "Consistent-Mode Indicator for the Eigensystem Realization Algorithm." In: *Journal of Guidance, Control, and Dynamics* 16.5 (1993), pp. 852–858. DOI: 10.2514/3.21092.

[193] A. T. Patera and G. Rozza. *Reduced Basis Approximation and A Posteriori Error Estimation for Parametrized Partial Differential Equations*. 2007.

[194] A. Paul-Dubois-Taine and D. Amsallem. "An Adaptive and Efficient Greedy Procedure for the Optimal Training of Parametric Reduced-order Models." In: *International Journal for Numerical Methods in Engineering* 102.5 (2015), pp. 1262–1292. DOI: 10.1002/nme.4759.

[195] G. Pavic. "The Role of Damping on Energy and Power in Vibrating Systems." In: *Journal of Sound and Vibration* 281.1-2 (2005), pp. 45–71. DOI: 10.1016/j.jsv.2004.01.030.

[196] G. Pavić. "Measurement of Structure Borne Wave Intensity, Part I: Formulation of the Methods." In: *Journal of Sound and Vibration* 49.2 (1976), pp. 221–230. DOI: 10.1016/0022-460X(76)90498-3.

[197] *PCB Model 288D01 Data Sheet*. Nov. 2018.

[198] B. Peherstorfer, K. Willcox, and M. Gunzburger. "Survey of Multifidelity Methods in Uncertainty Propagation, Inference, and Optimization." In: *SIAM Review* 60.3 (2018), pp. 550–591. DOI: 10.1137/16M1082469.

[199] B. Peherstorfer, S. Zimmer, and H.-J. Bungartz. "Model Reduction with the Reduced Basis Method and Sparse Grids." In: *Sparse Grids and Applications*. Ed. by J. Garcke and M. Griebel. Vol. 88. Lecture Notes in Computational Science and Engineering. Berlin, Heidelberg: Springer, 2012, pp. 223–242. ISBN: 978-3-642-31702-6. DOI: 10.1007/978-3-642-31703-3_11.

[200] L. Pernebo and L. Silverman. "Model Reduction via Balanced State Space Representations." In: *IEEE Transactions on Automatic Control* 27.2 (1982), pp. 382–387. DOI: 10.1109/TAC.1982.1102945.

[201] A. W. Phillips and R. J. Allemang. "An Overview of MIMO-FRF Excitation/Averaging/Processing Techniques." In: *Journal of Sound and Vibration* 262.3 (2003), pp. 651–675. DOI: 10.1016/S0022-460X(03)00116-0.

[202] L. Pillage and R. Rohrer. "Asymptotic Waveform Evaluation for Timing Analysis." In: *IEEE Transactions on Computer-Aided Design of Integrated Circuits and Systems* 9.4 (1990), pp. 352–366. DOI: 10.1109/43.45867.

[203] M. J. D. Powell. “A Fast Algorithm for Nonlinearly Constrained Optimization Calculations.” In: *Numerical Analysis*. Ed. by G. A. Watson. Vol. 630. Lecture Notes in Mathematics. Berlin, Heidelberg: Springer, 1978, pp. 144–157. ISBN: 978-3-540-35972-2. DOI: 10.1007/BFb0067703.

[204] M. J. D. Powell. “Variable Metric Methods for Constrained Optimization.” In: *Mathematical Programming the State of the Art: Bonn 1982*. Ed. by A. Bachem, B. Korte, and M. Grötschel. Berlin, Heidelberg: Springer, 1983, pp. 288–311. ISBN: 978-3-642-68874-4. DOI: 10.1007/978-3-642-68874-4_12.

[205] C. E. Rasmussen and C. K. I. Williams. *Gaussian Processes for Machine Learning*. Adaptive Computation and Machine Learning. Cambridge, MA, USA: MIT Press, 2006. ISBN: 978-0-262-18253-9. DOI: 10.7551/mitpress/3206.001.0001.

[206] K. Rasmussen. *Calibration of Artificial Mastoids and Impedance Transducers*. Tech. rep. PL-15. Copenhagen: Danish Primary Labratory of Acoustics, Technical University of Denmark, 2000.

[207] T. Reis and T. Stykel. “Balanced Truncation Model Reduction of Second-Order Systems.” In: *Mathematical and Computer Modelling of Dynamical Systems* 14.5 (2008), pp. 391–406. DOI: 10.1080/13873950701844170.

[208] D. J. Rixen. “How Measurement Inaccuracies Induce Spurious Peaks in Frequency Based Substructuring.” In: *Proceedings of the XXVI International Modal Analysis Conference*. Orlando, FL, USA, 2008, pp. 1–15.

[209] D. J. Rixen. “A Dual Craig–Bampton Method for Dynamic Substructuring.” In: *Journal of Computational and Applied Mathematics* 168.1-2 (2004), pp. 383–391. DOI: 10.1016/j.cam.2003.12.014.

[210] T. D. Rossing, ed. *Springer Handbook of Acoustics*. 2nd ed. New York, NY: Springer, 2014. ISBN: 978-1-4939-0755-7. DOI: 10.1007/978-1-4939-0755-7.

[211] S. Rubin. “Improved Component-Mode Representation for Structural Dynamic Analysis.” In: *AIAA Journal* 13.8 (1975), pp. 995–1006. DOI: 10.2514/3.60497.

[212] A. Ruhe. “The Rational Krylov Algorithm for Nonsymmetric Eigenvalue Problems. III: Complex Shifts for Real Matrices.” In: *BIT Numerical Mathematics* 34.1 (Mar. 1994), pp. 165–176. DOI: 10.1007/BF01935024.

[213] Y. Saad. *Iterative Methods for Sparse Linear Systems*. 2nd ed. Other Titles in Applied Mathematics. Philadelphia, PA, USA: Society for Industrial and Applied Mathematics, 2003. ISBN: 978-0-89871-800-3. DOI: 10.1137/1.9780898718003.

[214] B. Salimbahrami, B. Lohmann, T. Bechtold, and J. Korvink. “A Two-Sided Arnoldi Algorithm with Stopping Criterion and MIMO Selection Procedure.” In: *Mathematical and Computer Modelling of Dynamical Systems* 11.1 (2005), pp. 79–93. DOI: 10.1080/13873950500052595.

[215] B. Salimbahrami, B. Lohmann, and A. Bunse-Gerstner. “Passive Reduced Order Modelling of Second-Order Systems.” In: *Mathematical and Computer Modelling of Dynamical Systems* 14.5 (2008), pp. 407–420. DOI: 10.1080/13873950701844279.

[216] B. Salimbahrami and B. Lohmann. *Krylov Subspace Methods in Linear Model Order Reduction: Introduction and Invariance Properties*. Tech. rep. Bremen: Institute of Automation, University of Bremen, 2002.

[217] S. B. Salimbahrami. “Structure Preserving Order Reduction of Large Scale Second Order Models.” PhD thesis. München: Technische Universität München, 2005.

[218] A. Saltelli, M. Ratto, T. Andres, F. Campolongo, J. Cariboni, D. Gatelli, M. Saisana, and S. Tarantola, eds. *Global Sensitivity Analysis: The Primer*. Chichester, England: Wiley, 2008. ISBN: 978-0-470-05997-5. DOI: 10.1002/9780470725184.

[219] G. Sandberg, P.-A. Wernberg, and P. Davidsson. “Fundamentals of Fluid-Structure Interaction.” In: *Computational Aspects of Structural Acoustics and Vibration*. Ed. by G. Sandberg and R. Ohayon. Vol. 505. CISM International Centre for Mechanical Sciences. Vienna: Springer, 2008, pp. 23–101. ISBN: 978-3-211-89651-8. DOI: 10.1007/978-3-211-89651-8_2.

[220] C. Schaal, J. Ebert, J. Bös, and T. Melz. “Relation Between Structural Intensity-Based Scalars and Sound Radiation Using the Example of Plate-Rib Models.” In: *Journal of Vibration and Acoustics* 138.4 (2016), p. 041011. DOI: 10.1115/1.4033339.

[221] I. Schur. “On Power Series Which Are Bounded in the Interior of the Unit Circle. I.” In: *I. Schur Methods in Operator Theory and Signal Processing*. Ed. by I. Gohberg and I. Gohberg. Vol. 18. Operator Theory: Advances and Applications. Basel: Birkhäuser, 1986, pp. 31–59. ISBN: 978-3-0348-5483-2. DOI: 10.1007/978-3-0348-5483-2_3.

[222] H. A. Schwarz. *Gesammelte Mathematische Abhandlungen: Erster Band*. 1890. ISBN: 978-3-642-50665-9. DOI: 10.1007/978-3-642-50665-9.

[223] D. A. Scott, L. P. Dickinson, and T. J. Bell. “Traceable Calibration of Impedance Heads and Artificial Mastoids.” In: *Measurement Science and Technology* 26.12 (2015), p. 125013. DOI: 10.1088/0957-0233/26/12/125013.

[224] S. Sen. “Reduced-Basis Approximation and *A Posteriori* Error Estimation for Many-Parameter Heat Conduction Problems.” In: *Numerical Heat Transfer, Part B: Fundamentals* 54.5 (2008), pp. 369–389. DOI: 10.1080/10407790802424204.

[225] P. J. Shorter and R. S. Langley. “Vibro-Acoustic Analysis of Complex Systems.” In: *Journal of Sound and Vibration* 288.3 (2005), pp. 669–699. DOI: 10.1016/j.jsv.2005.07.010.

[226] S. Sicklinger and R. Ullmann. “Structural Power as an Acoustic Design Criterion for the Early Phase of Product Design.” In: *Proceedings of ISMA2018 Including USD2018*. Leuven, Belgium, 2018.

[227] S. A. Sicklinger. “Stabilized Co-Simulation of Coupled Problems Including Fields and Signals.” PhD thesis. München: Technische Universität München, 2014.

[228] H. D. Simon. “Analysis of the Symmetric Lanczos Algorithm with Reorthogonalization Methods.” In: *Linear Algebra and its Applications* 61 (1984), pp. 101–131. DOI: 10.1016/0024-3795(84)90025-9.

[229] R. Singh and S. Kim. “Examination of Multi-Dimensional Vibration Isolation Measures and Their Correlation to Sound Radiation over a Broad Frequency Range.” In: *Journal of Sound and Vibration* 262.3 (2003), pp. 419–455. DOI: 10.1016/S0022-460X(03)00105-6.

[230] L. Sirovich. “Turbolence and the Dynamics of Coherent Structures Part I: Coherent Structures.” In: *Quarterly of Applied Mathematics* 45.3 (1987), pp. 561–571.

[231] P. Sjövall, T. McKelvey, and T. Abrahamsson. “Constrained State–Space System Identification with Application to Structural Dynamics.” In: *Automatica* 42.9 (2006), pp. 1539–1546. DOI: 10.1016/j.automatica.2006.04.021.

[232] D. Skoogh. *A Rational Krylov Method for Model Order Reduction*. Tech. rep. 1998-47. Göteborg: Department of Mathematics, Chalmers University of Technology, 1998.

[233] N. T. Son. “A Real Time Procedure for Affinely Dependent Parametric Model Order Reduction Using Interpolation on Grassmann Manifolds.” In: *International Journal for Numerical Methods in Engineering* 93.8 (2013), pp. 818–833. DOI: 10.1002/nme.4408.

[234] A. Soppa. “Krylov-Unterraum Basierte Modellreduktion Zur Simulation von Werkzeugmaschinen.” PhD thesis. Braunschweig: Technische Universität Carolo-Wilhelmina zu Braunschweig, 2011. DOI: 10.24355/dbbs.084-201204181039-0.

[235] D. C. Sorensen. “Implicitly Restarted Arnoldi/Lanczos Methods for Large Scale Eigenvalue Calculations.” In: *Parallel Numerical Algorithms*. Ed. by D. E. Keyes, A. Sameh, and V. Venkatakrishnan. Vol. 4. ICASE/LaRC Interdisciplinary Series in Science and Engineering. Dordrecht: Springer, 1997, pp. 119–165. ISBN: 978-94-011-5412-3. DOI: 10.1007/978-94-011-5412-3_5.

[236] T. Stykel. “Low-Rank Iterative Methods for Projected Generalized Lyapunov Equations.” In: *Electronic Transactions on Numerical Analysis* 30 (2008), pp. 187–202.

[237] R. P. Szwerc, C. B. Burroughs, S. A. Hambric, and T. E. McDevitt. “Power Flow in Coupled Bending and Longitudinal Waves in Beams.” In: *The Journal of the Acoustical Society of America* 107.6 (2000), pp. 3186–3195. DOI: 10.1121/1.429346.

[238] R. P. Szwerc and S. A. Hambric. *The Calculation and Measurement of Flexural and Longitudinal Structural Power Flow on a Tee-Shaped Beam*. Tech. rep. NSWCCD-SIG-96/014-7250. Bethesda, MD, USA: Naval Surface Warfare Ctr., 1996.

[239] M. Tadina, P. Ragnarsson, B. Pluymers, S. Donders, W. Desmet, and M. Boltezar. “On the Use of an FE Based Energy Flow Post-Processing Method for Vehicle Structural Dynamic Analysis.” In: *Proceedings of ISMA2008*. Leuven, Belgium, 2008.

[240] S. X. D. Tan and L. He. *Advanced Model Order Reduction Techniques in VLSI Design*. Cambridge: Cambridge University Press, 2007. ISBN: 978-0-511-54111-7. DOI: 10.1017/CBO9780511541117.

[241] Y.-C. Tan. “Efficient Modeling of Low- to Mid-Frequency Vibration and Power Flow in Complex Structures.” PhD thesis. Ann Arbor, MI, USA: University of Michigan, 2001.

[242] A. K. Tangirala. *Principles of System Identification: Theory and Practice*. Boca Raton: CRC Press, Taylor & Francis Group, 2015. ISBN: 978-1-4398-9599-3.

[243] G. Tanner. “Dynamical Energy Analysis—Determining Wave Energy Distributions in Vibro-Acoustical Structures in the High-Frequency Regime.” In: *Journal of Sound and Vibration* 320.4-5 (2009), pp. 1023–1038. DOI: 10.1016/j.jsv.2008.08.032.

[244] A. Thite and B. Mace. “Robust Estimation of Coupling Loss Factors from Finite Element Analysis.” In: *Journal of Sound and Vibration* 303.3-5 (2007), pp. 814–831. DOI: 10.1016/j.jsv.2007.02.004.

[245] F. Tisseur and K. Meerbergen. “The Quadratic Eigenvalue Problem.” In: *SIAM review* 43.2 (2001), pp. 235–286. DOI: 10.1137/S0036144500381988.

[246] Z. Tomljanović, C. Beattie, and S. Gugercin. “Damping Optimization of Parameter Dependent Mechanical Systems by Rational Interpolation.” In: *Advances in Computational Mathematics* 44.6 (2018), pp. 1797–1820. DOI: 10.1007/s10444-018-9605-9.

[247] A. Toselli and O. B. Widlund. *Domain Decomposition Methods–Algorithms and Theory*. Springer Series in Computational Mathematics 34. Berlin: Springer, 2005. ISBN: 978-3-540-20696-5. DOI: 10.1007/b137868.

[248] A. Troshin and M. A. Sanderson. “Structural Energy Flow in a Resilently Coupled T-shaped Beam by Wave Intensity and Mobility Approaches.” In: *Acta Acustica united with Acustica* 84.5 (1998), pp. 860–869.

[249] Z. Ugray, L. Lasdon, J. Plummer, F. Glover, J. Kelly, and R. Martí. “Scatter Search and Local NLP Solvers: A Multistart Framework for Global Optimization.” In: *INFORMS Journal on Computing* 19.3 (2007), pp. 328–340. DOI: 10.1287/ijoc.1060.0175.

[250] R. Ullmann. *A 3D Solid Beam Benchmark for Model Order Reduction*. 2020. DOI: 10.17632/cprx2kx2ws.2.

[251] R. Ullmann. *Data for: Validation of a Structure-Borne Sound Benchmark With Emphasis on Power and Phase Accuracy*. 2019. DOI: 10.17632/8MXPPTMZPN.1.

[252] R. Ullmann and S. Sicklinger. *A Two-Dimensional Structural-Acoustic Radiation Benchmark*. 2019. DOI: 10.17632/MHYK7R6V2Z.1.

[253] R. Ullmann, S. Sicklinger, M. Buchschmid, and G. Müller. “Power-Based Approach for Assessment of Structure-Borne Sound in Mechanical Networks of Vehicle Structures.” In: *Procedia Engineering* 199 (2017), pp. 1386–1391. DOI: 10.1016/j.proeng.2017.09.371.

[254] R. Ullmann, S. Sicklinger, and G. Müller. “Optimization-Based Parametric Model Order Reduction for the Application to the Frequency-Domain Analysis of Complex Systems.” In: *Model Reduction of Complex Dynamical Systems*. Ed. by P. Benner, T. Breiten, H. Faßbender, M. Hinze, T. Stykel, and R. Zimmermann. International Series of Numerical Mathematics 171. Cham: Birkhäuser, 2021, pp. 165–189. ISBN: 978-3-030-72983-7. DOI: 10.1007/978-3-030-72983-7_8.

[255] R. Ullmann, S. Sicklinger, and G. Müller. “Validation Experiment for Structural Power.” In: *Proceedings of ISMA2018 Including USD2018*. Leuven, Belgium, 2018, pp. 4293–4303.

[256] R. Ullmann, S. Sicklinger, and G. Müller. “Validation of a Uniaxial Structure-Borne Sound Benchmark with Emphasis on Power and Phase Accuracy.” In: *Journal of Sound and Vibration* 459 (2019), p. 114786. DOI: 10.1016/j.jsv.2019.05.049.

[257] E. E. Ungar. “Loss Factors of Viscoelastic Systems in Terms of Energy Concepts.” In: *The Journal of the Acoustical Society of America* 34.7 (1962), pp. 954–957. DOI: 10.1121/1.1918227.

[258] K. Urban, S. Volkwein, and O. Zeeb. “Greedy Sampling Using Nonlinear Optimization.” In: *Reduced Order Methods for Modeling and Computational Reduction*. Ed. by A. Quarteroni and G. Rozza. MS&A - Modeling, Simulation and Applications 9. Cham: Springer, 2014, pp. 137–157. ISBN: 978-3-319-02090-7. DOI: 10.1007/978-3-319-02090-7_5.

[259] A. van de Walle. “The Power of Model Order Reduction in Vibroacoustics and Its Applications in Model-Based Sensing.” PhD thesis. Leuven, Belgium: KU Leuven, 2018.

[260] M. Van Der Seijs. “Experimental Dynamic Substructuring.” PhD thesis. Delft, Netherlands: Delft University of Technology, 2016. DOI: 10.4233/uuid:28b31294-8d53-49eb-b108-284b63edf670.

[261] P. Van Dooren, K. Gallivan, and P.-A. Absil. “H2-Optimal Model Reduction of MIMO Systems.” In: *Applied Mathematics Letters* 21.12 (2008), pp. 1267–1273. DOI: 10.1016/j.aml.2007.09.015.

[262] S. van Ophem. “Novel Reduction Techniques for Exterior Vibro-Acoustic Models and Their Use in Model-Based Sensing and Identification.” PhD thesis. Leuven, Belgium: KU Leuven, 2019.

[263] A. Vandendorpe and P. V. Dooren. “Krylov Techniques for Model Reduction of Second-Order Systems.” 2004.

[264] A. Varga. “Enhanced Modal Approach for Model Reduction.” In: *Mathematical Modelling of Systems* 1.2 (1995), pp. 91–105. DOI: 10.1080/13873959508837010.

[265] J. W. Verheij. “Cross Spectral Density Methods for Measuring Structure Borne Power Flow on Beams and Pipes.” In: *Journal of Sound and Vibration* 70.1 (1980), pp. 133–138. DOI: 10.1016/0022-460X(80)90559-3.

[266] N. Vlahopoulos and X. Zhao. “Basic Development of Hybrid Finite Element Method for Midfrequency Structural Vibrations.” In: *AIAA Journal* 37.11 (1999), pp. 1495–1505. DOI: 10.2514/2.629.

[267] S. N. Voormeeren, D. de Klerk, and D. J. Rixen. “Uncertainty Quantification in Experimental Frequency Based Substructuring.” In: *Mechanical Systems and Signal Processing* 24.1 (2010), pp. 106–118. DOI: 10.1016/j.ymssp.2009.01.016.

[268] S. N. Voormeeren, P. L. C. van der Valk, and D. J. Rixen. “A Truly Hybrid Approach to Substructuring Problems Using Mixed Assembly and Implicit Solving Strategies.” In: *Linking Models and Experiments, Volume 2*. Ed. by T. Proulx. Conference Proceedings of the Society for Experimental Mechanics Series. New York, NY: Springer, 2011, pp. 329–347. ISBN: 978-1-4419-9305-2. DOI: 10.1007/978-1-4419-9305-2_23.

[269] S. N. Voormeeren. “Dynamic Substructuring Methodologies for Integrated Dynamic Analysis of Wind Turbines.” PhD thesis. Delft, Netherlands: Delft University of Technology, 2012. DOI: 10.4233/uuid:f45f0548-d5ec-46aa-be7e-7f1c2b57590d.

[270] H. F. Walker. “Implementation of the GMRES Method Using Householder Transformations.” In: *SIAM Journal on Scientific and Statistical Computing* 9.1 (1988), pp. 152–163. DOI: 10.1137/0909010.

[271] T. Weisser, E. Foltête, N. Bouhaddi, and L.-O. Gonidou. “A Power Flow Mode Approach Dedicated to Structural Interface Dynamic Characterization.” In: *Journal of Sound and Vibration* 334 (2015), pp. 202–218. DOI: 10.1016/j.jsv.2014.09.012.

[272] E. G. Williams, H. D. Dardy, and R. G. Fink. “A Technique for Measurement of Structure-borne Intensity in Plates.” In: *The Journal of the Acoustical Society of America* 78.6 (1985), pp. 2061–2068. DOI: 10.1121/1.392663.

[273] M. R. Wohlers. *Lumped and Distributed Passive Networks: A Generalized and Advanced Viewpoint*. New York, NY, USA: Academic Press, 1969. ISBN: 978-1-4831-9621-3. DOI: 10.1016/C2013-0-07706-7.

[274] J. C. Wohlever and R. J. Bernhard. “Mechanical Energy Flow Models of Rods and Beams.” In: *Journal of Sound and Vibration* 153.1 (1992), pp. 1–19. DOI: 10.1016/0022-460X(92)90623-6.

[275] S. Wyatt. “Issues in Interpolatory Model Reduction: Inexact Solves, Second-order Systems and DAEs.” PhD thesis. Blacksburg, VA, USA: Virginia Polytechnic Institute and State University, 2012.

[276] X. D. Xu, H. P. Lee, C. Lu, and J. Y. Guo. “Streamline Representation for Structural Intensity Fields.” In: *Journal of Sound and Vibration* 280.1-2 (2005), pp. 449–454. DOI: 10.1016/j.jsv.2004.02.008.

[277] Y. Yue, L. Feng, and P. Benner. “An Adaptive Pole-Matching Method for Interpolating Reduced-Order Models.” In: *arXiv:1908.00820 [cs, math]* (2019). arXiv: 1908.00820 [cs, math].

[278] Y. Yue, L. Feng, and P. Benner. “Reduced-Order Modelling of Parametric Systems via Interpolation of Heterogeneous Surrogates.” In: *Advanced Modeling and Simulation in Engineering Sciences* 6.1 (2019), p. 10. DOI: 10.1186/s40323-019-0134-y.

[279] Y. Yue and K. Meerbergen. “Accelerating Optimization of Parametric Linear Systems by Model Order Reduction.” In: *SIAM Journal on Optimization* 23.2 (2013), pp. 1344–1370. DOI: 10.1137/120869171.

[280] Z. B. Zabinsky. “Random Search Algorithms.” In: *Wiley Encyclopedia of Operations Research and Management Science*. Hoboken, NJ, USA: Wiley, 2011, eorms0704. ISBN: 978-0-470-40053-1. DOI: 10.1002/9780470400531.eorms0704.

[281] M. J. Zahr and C. Farhat. “Progressive Construction of a Parametric Reduced-Order Model for PDE-constrained Optimization.” In: *International Journal for Numerical Methods in Engineering* 102.5 (2015), pp. 1111–1135. DOI: 10.1002/nme.4770. arXiv: 1407.7618.

[282] C. Zenger. “Sparse Grids.” In: *Parallel Algorithms for Partial Differential Equations*. Ed. by W. Hackbusch. Notes on Numerical Fluid Mechanics. Kiel: Vieweg, 1991, pp. 241–251. ISBN: 3-528-07631-3.

[283] O. C. Zienkiewicz, R. L. Taylor, and J. Z. Zhu. *The Finite Element Method: Its Basis and Fundamentals*. Seventh edition. Oxford, United Kingdom: Butterworth-Heinemann, 2013. ISBN: 978-1-85617-633-0. DOI: 10.1016/C2009-0-24909-9.

[284] M. Zimmermann and J. E. von Hoessle. “Computing Solution Spaces for Robust Design.” In: *International Journal for Numerical Methods in Engineering* 94.3 (2013), pp. 290–307. DOI: 10.1002/nme.4450.